Simulation of turbulent flames relevant to spark-ignition engines

Irufan Ahmed

Hughes Hall

University of Cambridge

A dissertation submitted for the degree of

Doctor of Philosophy

January 2014

Declaration

This dissertation is the result of my own work and includes nothing which is the outcome of work done in collaboration except where specifically indicated in the text. This dissertation has not been submitted in any form for another qualification to this or any other university. Information derived from the published and unpublished work of others has been referenced in the text.

This dissertation contains approximately 46,000 words and includes 52 figures.

Irufan Ahmed
April 14$^{\text{th}}$, 2014

Keywords: computational fluid dynamics, turbulent combustion, spark-ignition engines

To my parents

Acknowledgements

I would like to express my gratitude towards my supervisor, Professor N. Swaminathan, for introducing me to the fascinating world of computational combustion. His patience, encouragement and guidance throughout the course of this work contributed to the successful completion of this thesis. I would also like to thank Professors Forman Williams, Ken Bray and Stewart Cant for their insightful comments regarding this work.

Special thanks to Dr Yuri Wright, Ms Stéphanie Schlatter and Mr Jann Koch from ETH Zürich for the STAR-CD setup and for providing the computational mesh used to simulate the internal combustion engine. I am also thankful for the assistance I received from Dr Hemanth Kolla regarding the in-house CFD code, and Mr Karl Bass from CD-adapco for his technical support on STAR-CD.

Many others have contributed to the success of this work, including colleagues from the Hopkinson laboratory with whom I have had numerous interesting and fruitful discussions. In addition, the computing help I received from Mr Peter Benie and the staff at the Cambridge High Performance Computing Service is gratefully acknowledged.

This work would not have been possible without the generous financial support from my uncle, Mr Hussain Abdullah. I would also like to acknowledge the conference grants I received from the Cambridge University Engineering Department, the Combustion Institute and Hughes Hall. The financial support I received from Tokyo Institute of Technology to participate in the ACEEES forum is gratefully acknowledged.

Abstract

Combustion research currently aims to reduce emissions, whilst improving the fuel economy. Burning fuel in excess of air, or *lean-burn* combustion, is a promising alternative to conventional combustion, and can achieve these requirements simultaneously. However, lean-burn combustion poses new challenges, especially for internal combustion (IC) engines. Therefore, models used to predict such combustion have to be reliable, accurate and robust.

In this work, the flamelet approach in the Reynolds-Averaged Navier-Stokes framework, is used to simulate flames relevant to spark-ignition IC engines. A central quantity in the current modelling approach is the scalar dissipation rate, which represents coupling between reaction and diffusion, as well as the flame front dynamics.

In the first part of this thesis, the predictive ability of two reaction rate closures, viz. strained and unstrained flamelet models, are assessed through a series of experimental test cases. These cases are: spherically propagating methane- and hydrogen-air flames and combustion in a closed vessel. In addition to these models, simpler algebraic closures are also used for comparison.

It is shown that the strained flamelet model can predict unconfined, spherically propagating methane-air flames reasonably well. By comparing spherical flame results with planar flames, under identical thermochemical and turbulence conditions, it is shown that the turbulent flame speed of spherical flames are 10 to 20% higher than that of planar flames, whilst the mean reaction rates are less influenced by the flame geometry.

Growth of the flame brush thickness in unsteady spherical flames have been attributed to turbulent diffusion in past studies. However, the present analyses revealed that the dominant cause for this increase is the heat-release induced convective effects, which is a novel observation.

Unlike methane-air flames, hydrogen-air flames have non-unity Lewis numbers. Hence, a novel two degrees of freedom approach, using two progress variables, is used to describe the thermochemistry of hydrogen-air flames. Again, it is shown that the strained flamelet model is able to predict the experimental flame growth for stoichiometric hydrogen-air flames. However, none of the models used in this work were able to predict lean hydrogen-air flames. This is because these flames are thermo-diffusively unstable and the current approach is inadequate to represent them.

When combustion takes place inside a closed vessel, the compression of the end gases by the propagating flame causes the pressure to rise. This is more representative of real IC engines, where intermittent combustion takes place. The combustion models are implemented in a commercial computational fluid dynamics (CFD) code, STAR-CD, and it is shown that both strained and unstrained flamelet models are able to predict the experimental pressure rise in a closed vessel.

In the final part of this work, a spark-ignition engine is simulated in STAR-CD using the flamelet model verified for simpler geometries. It is shown that this model, together with a skeletal mechanism for iso-octane, compares reasonably well with experimental cylinder pressure rise. Results obtained from this model are compared with two models available in STAR-CD. These models require some level of tuning to match the experiments, whereas the modelling approach used in this work does not involve any tunable parameters.

Contents

List of Figures

Nomenclature

Roman Symbols

A	– Flame surface area
	– Flame speed coefficient for s_T
c	Progress variable
C_3, C_4, K_c^*	Constants in the model for $\tilde{\epsilon}_c$
t_c	Chemical time
Q_k	Conditional mean of species k
C_p	Mixture specific heat capacity
C_pk	Specific heat capacity of species k
D	Molecular diffusivity
Da	Damköhler number
D_c	Diffusivity of the progress variable
$\boldsymbol{V}_k$	Diffusion velocity of species k
$\boldsymbol{x}$	Spatial vector
s_d	Displacement speed of $\tilde{c}$ iso-contour
s'_d	Displacement speed of c iso-contour
E_i	Ignition energy
E	Total energy
$\boldsymbol{q}$	Energy flux
h_k	Total enthalpy of species k
$h_{s,k}$	Sensible enthalpy of species k
r_f	Flame radius
K	Stretch factor
G	Non-reacting scalar used in the level set approach
Q	Heat release
$\mathbf{I}$	Identity matrix
k	Turbulent kinetic energy
Ka	Karlovitz number

Le	Lewis number
$D_{\mathcal{L}}$	Markstein diffusivity
m	Mass
m_f	Fuel mass
Y_k	Mass fraction of species k
M	– Mixture molecular weight
	– Number of reactions
N	Number of species
N_c	Instantaneous scalar dissipation rate of c
$\boldsymbol{n}$	Unit normal vector to the flame
p_∞	Atmospheric pressure
p	Hydrostatic pressure
Q_j	Progress rate of reaction j
Q_{LHV}	Lower heating value
r	Radial distance
Re_t	Turbulence Reynolds number
R_u	Ideal gas constant
Sc	Schmidt number
s_L^0	Unstrained laminar flame speed
a	Flame strain rate
s_{ij}	Strain rate tensor
T	Absolute temperature
D_{th}	Thermal diffusivity
t	Time
$\mathbf{T}$	Transport vector in turbulent kinetic energy equation
s_t	Flame propagation speed
s_t	Turbulent flame speed
u_t	Turbulent burning velocity
$\boldsymbol{u}$	Velocity vector
$\boldsymbol{f}_k$	Volume force acting on species k
W_k	Atomic weight of species k

Calligraphic Symbols

$\mathcal{L}$	Markstein length

$\mathcal{P}_k$	Turbulence production term
$\mathcal{R}$	Flame surface radius

Greek Symbols

β'	Constant in $\tilde{\epsilon}_c$ model
δ_L^0	Laminar thermal thickness
δ_t	Turbulent flame brush thickness
ϵ_c	Scalar dissipation rate of c
ε	Dissipation rate of turbulent kinetic energy
κ_c	Flame curvature
κ	Flame stretch rate
γ	Specific heat ratio
η_k	Kolmogorov length scale
δ	Chemical length scale, Zeldövich flame thickness
Λ	Turbulence integral length scale
λ	– Heat diffusion coefficient
	– air-to-fuel ratio
μ	Dynamic viscosity
μ_t	Eddy viscosity
ν	Kinematic viscosity
ν_t	Turbulent diffusivity
Ω	Angular velocity
Φ	Equivalence ratio
Ψ	General scalar property
ψ	Sample space variable for N
ρ	Fluid density
Σ	Flame surface density
τ	Heat release parameter
τ_k	Kolmogorov time scale
$\boldsymbol{\tau}$	Viscous stress tensor
τ_t	Turbulence time scale
θ	Crank angle
τ_i	Ignition delay time
u'_k	Kolmogorov velocity scale

$\dot{\omega}$	Specific dissipation rate
$\dot{\omega}_c$	Mass reaction rate of c
$\dot{\omega}_T$	Combustion heat release rate
ζ	Sample space variable for c

Superscripts

$''$	Favre fluctuation
$\tilde{}$	Favre mean
$+$	Normalised using planar laminar flame quantities
$'$	rms of Reynolds fluctuation

Subscripts

b	Burnt mixture value
j	Refers to a particular reaction
k	Refers to a particular species
L	Laminar quantity
t	Turbulent quantity
u	Unburnt mixture value

Acronyms

BDC	Bottom dead centre
BMEP	Brake mean effective pressure
BML	Bray-Moss-Libby
CA	Crank angle
CFD	Computational fluid dynamics
CFM	Coherent flame model
CMC	Conditional moment closure
DISI	Direct-injection spark-ignition
DNS	Direct numerical simulation
EBU	Eddy break-up
ECFM	Extended CFM
EGR	Exhaust gas recirculation
FSD	Flame surface density
FVM	Finite volume method
GDI	Gasoline direct injection
HCCI	Homogeneous charge compression ignition

HRR	Heat release rate
IC	Internal combustion
IVO	Intake valve opening
KPP	Kolmogorov-Petrovskii-Piskunov
LES	Large-eddy simulation
LHS	Left hand side
LHV	Lower heating value
MARS	Monotone advection and reconstruction scheme
pdf	Probability density function
PFI	Port fuel injection
RANS	Reynolds-averaged Navier-Stokes
RHS	Right hand side
rms	Root mean square
rpm	Revolutions per minute
SDR	Scalar dissipation rate
SI	Spark-ignition
TDC	Top dead centre
URANS	Unsteady RANS

1. Introduction

Combustion is mankind's oldest technology and it is one of the main contributors to the technological progress that we see today. Combustion is ubiquitous, since majority of energy conversion for transportation, power generation and domestic heating is from the burning of a fuel in the presence of an oxidiser. Most combustion processes use fossil fuels, which contributed to 81% share of the global energy consumption in 2010 (IEA, 2011).

Fossil fuels are particularly attractive for the transportation sector, with 93% of all fuels used for transport in 2010 being based on fossil fuels and it is predicted to account for 83% share in 2035 (IEA, 2011). Most motor vehicles today use reciprocating internal combustion (IC) engines, which burn fossil fuels to convert chemical energy stored in the fuel to mechanical energy.

Combustion of fossil fuels for energy conversion is not without problems. Pollutants such as unburnt hydrocarbons, oxides of nitrogen, carbon monoxide, sulphur oxides and soot are formed as unwanted by-products when fossil fuels are burnt. In addition, combustion is the major anthropogenic contributor to CO_2 concentrations in the atmosphere; combustion of fossil fuels in industrial, domestic, energy and transportation sectors contributed to 71% of the total greenhouse gas emissions in 2004 (IPCC, 2007). These issues are compounded by the fact that fossil fuel resources are finite. Therefore, it is imperative that we improve combustion efficiency and reduce emissions.

Conventional combustion technologies are unable to simultaneously increase efficiency and reduce emissions. Burning fuel in the presence of excess air, known as *fuel-lean* combustion, can achieve both requirements (Dunn-Rankin et al., 2008; Swaminathan and Bray, 2011), but it poses new challenges, especially for IC engines (Urata and Taylor, 2011). In the last half-century, there have been a drive to reduce emissions and to achieve better fuel efficiency. This is an area where improvements are still being made, despite having a long history of development. For example, new engine types, such as the homogeneous charge compression ignition (HCCI) engine, which burn lean, have been shown to provide improvements in fuel economy and reduced emissions (Drake and Haworth, 2007).

Such improvements are only possible when fundamental processes that take place during combustion are clearly understood. In the last few decades, combustion science has shifted from a field based on empiricism to one that is quantitative (Bilger et al., 2005). These fundamental studies are used to develop combustion models that can be used to design and develop efficient and clean combustion devices.

1.1 Combustion research

It is convenient to classify gaseous combustion according to the extent of mixing: *premixed* or *non-premixed*. In premixed flames, fuel and oxidiser are mixed homogeneously before combustion. Lean-burn gas turbines for power generation and spark-ignition (SI) IC engines are typical examples of this type of combustion. In non-premixed or 'diffusion flames', the fuel and oxidiser are transported separately into the reaction zones by diffusion. Aero-engine gas turbines and diesel engines are typical examples of non-premixed combustion. It is often the case in practical systems that fuel and air is not completely mixed, leading to *partially* premixed combustion. For example, fuel is injected directly into the combustion chamber in a gasoline direct-injection (GDI) engine, which does not give sufficient time and space for it to mix with air completely.

These subdivisions of combustion systems are important for modelling purposes, since the flame behaviour in these conditions are radically different. Only premixed combustion is considered in this work; however, due to the multifaceted nature of combustion research, it is impractical to present a complete background review on premixed combustion research. Instead, a general introduction to research relevant to this work is provided.

Virtually all combustion in practical devices takes place in turbulent flows. Turbulence is extremely complex even in non-reacting situations and the inclusion of chemical reactions introduces additional complexities in studying such flows. The greatest challenge associated with turbulent combustion is understanding the interaction between turbulence and combustion over a broad range of time and length scales (Bray, 1996). Thus, to a large extent, our fundamental understanding of combustion phenomena remains limited, which makes it difficult to

develop robust combustion models that can be used to design new combustion technologies.

Damköhler (1940) explained in his pioneering work that, in turbulent premixed flames, large-scale eddies wrinkle the flame surface without altering the internal flame structure, whereas small-scale eddies affect the reactive-diffusive structure. This understanding of the effect of turbulence on the flame structure lead to the identification of various regimes of turbulent combustion, where the turbulence time and length scales are used to obtain non-dimensional numbers to separate different regimes. A description of relevant background theory on turbulent premixed flames, including the combustion regime diagram of Borghi (1985) is given in section 2.4.

The regime diagram is useful for combustion modelling because it can identify relative scales for flow and combustion and thus the validity, in a broad sense, of a particular combustion model invoking some assumptions among these scales. The local flame structure that can be determined using the regime diagram can in turn give useful information on the turbulence-chemistry interactions.

One of the popular flame configurations for experimental investigation of premixed combustion is the outwardly propagating spherical flames. These experiments are usually conducted in spherical bombs (Andrews et al., 1975) or in wind tunnels (Hainsworth, 1985), where turbulence is generated using fans and grids respectively. These flames are representative of flames in SI engines and have been used to increase our fundamental understanding of the ignition process (Shy et al., 2008). Furthermore, turbulent spherical flames can be used to study accidental explosions of vapour clouds in the atmosphere (Baker et al., 1983).

An important quantity for turbulent premixed flames is the turbulent flame speed. On a practical level, flame speed determines how quickly a mixture will be burnt. However, due to flame wrinkling being geometry dependent, it may not be possible to get a geometry-independent turbulent flame speed, which explains the large scatter for measured flame speeds (Driscoll, 2008). Turbulent flame speed can be also be influenced by thermodiffusive effects of the mixture, which can be explained using the flame stretch theory (Law and Sung, 2000). Furthermore, unequal thermal and mass diffusivities could make the flame thermodiffusively

unstable. An example of one such flame is the lean hydrogen-air flame, which according to the stretch theory, is unstable when it is positively stretched (Law and Sung, 2000).

Three distinctly different numerical paradigms exist for turbulent combustion simulation; namely direct numerical simulations (DNS), large-eddy simulations (LES) and Reynolds-averaged Navier-Stokes (RANS) simulations. There are advantages and disadvantages associated with each of these simulation paradigms and the choice depends on the level of detail required from them. Essentials of these different paradigms of computational fluid dynamics (CFD) for reacting flows are presented in section 2.2.

1.2 Combustion modelling

Direct solution of the equations describing reacting flows is computationally expensive and it is necessary to use either averaged (RANS) or filtered (LES) forms of the non-linear governing equations for practical applications. Simulation of reacting flows using both RANS and LES require combustion modelling, which makes it an active area of research. The main objective of combustion modelling is to develop closure models for the mean chemical source terms that appear in the averaged/filtered equations.

These source terms cannot be described using simple averaging techniques, and physical analysis based on the comparison between chemical and turbulent time scales have to be used (Veynante and Vervisch, 2002). In a review article, Veynante and Vervisch (2002) described that most combustion models are developed according to three different approaches: geometrical analysis, turbulent mixing and one-point statistics. A challenge in all these approaches is to close unknown terms, such as the flame surface-density, scalar dissipation rate, and the probability density functions (Poinsot and Veynante, 2005).

Combustion models used in LES are similar to those developed earlier for RANS (Pitsch, 2006). The models developed for premixed combustion can be broadly categorised into flamelet and non-flamelet approaches. Most models currently in use are based on the flamelet concept. In this concept, the flame is assumed to be thin compared with the smallest scales of turbulence and it can

be thought of as an interface between hot products and cold reactants. Then one can assume that the turbulent flame is made up of an ensemble of laminar flames (Williams, 1975). For premixed flames, the reaction diffusion balance is well represented by this flamelet approach and are computationally more economical than non-flamelet approaches (Cant and Mastorakos, 2008).

Combustion models have already been used for a wide range of turbulent premixed applications in the RANS context; the applications mentioned here are not intended to be exhaustive. For example, the well-known Bray-Moss-Libby (BML) model (Bray et al., 1985) and its variants have been used for applications ranging from stagnation flames (Bray et al., 1998) to SI engines (Abu-Orf and Cant, 2000). The Coherent Flame Model (CFM) has been used for Bunsen burner flames (Prasad and Gore, 1999) as well as in IC engines (Boudier et al., 1992). The level set approach or G-equation has also been used to simulate these flames (Schneider et al., 2005; Ewald and Peters, 2007). The transported probability density function (pdf) approach has been used to simulate spherical flames (Pope and Cheng, 1986) and Bunsen burner flames (Hack and Jenny, 2013). More recently, the conditional moment closure (CMC) method, which was originally developed for non-premixed flames, has been used to simulate Bunsen burner flames (Amzin et al., 2012; Amzin and Swaminathan, 2013). A brief description of these models is given in section 2.5 and detailed description can be found in the review articles of Peters (1986) and Veynante and Vervisch (2002).

1.3 Objectives of this study

Combustion models implemented in CFD codes are now used as engine design tools. However, the desired results of such simulations rely heavily on the accuracy, fidelity and robustness of the combustion model used. These models should be able to handle a range of engine operating conditions that may change the combustion characteristics. In this regard, combustion models based on the underlying physics of the turbulence-chemistry interaction have a clear advantage over empirical or semi-empirical models.

The overall aim of this work is to use one such modelling framework, developed by Kolla and Swaminathan (2010*a*), to simulate intermittent combustion in

the RANS context. Kolla and Swaminathan (2010*b*) have validated this approach for continuous combustion. This modelling framework is based on the flamelet concept, where scalar dissipation rate (SDR) that measure the decay rate of scalar fluctuations by turbulent micromixing, is a central quantity. Kolla and Swaminathan (2010*a*) introduced two closure models for the reaction source terms, viz. unstrained and strained flamelet models. For this approach to be useful in designing IC engines, it needs to be accurate, robust, and computationally economical. Furthermore, the model must be easily implemented in multi-dimensional CFD codes. Therefore, the objectives of this study are:

1. To validate the SDR based models for spherically propagating flames that are formed in spark-ignition engines. Validation is to be done for methane- and hydrogen-air flames, by comparing with available experimental data. These fuels have different thermochemical properties that influence their dynamic behaviours. In order to simulate spherically propagating flames, an in-house CFD code originally written in Cartesian coordinates is to be modified for spherical coordinates.

2. To identify the effect of flame geometry on flame propagation, by comparing spherical flame results with those of planar flames. The objective here is to determine the effect of global mean curvature on flame propagation.

3. To study the effect of turbulence on flame propagation for both methane- and hydrogen-air flames. Two key quantities that are used to analyse this effect are the turbulent flame speed and thickness.

4. To implement the combustion model in a commercially available CFD code, STAR-CD and to validate the model for intermittent combustion. The experimental case to be used for validation is a closed combustion vessel with swirl. Unlike spherically symmetric cases above, this closed volume leads to a large pressure rise due to combustion, and is more representative of IC engines.

5. To use the modelling framework to simulate combustion in a practical SI engine.

1.4 Thesis outline

Chapter 2 of this thesis describes the background theory on turbulent premixed flames relevant for this work. This includes the governing equations for turbulent reacting flows, description of various numerical paradigms, brief description of laminar premixed flames and combustion submodels used for turbulent premixed flames.

Chapter 3 presents details of the in-house CFD code used to simulate outwardly propagating spherical flames. The governing equations written in spherical coordinates are presented, along with the numerical details for simulating such flames. The CFD code presented here is used to address objectives 1, 2 and 3 listed in the previous section.

Model validation for methane-air spherical flames is presented in Chapter 4. In addition, geometry and turbulence effects on flame propagation, noted in objectives 2 and 3, are investigated. Similarly, details of hydrogen-air flames are presented in Chapter 5. The influence of turbulence on flame propagation is explored for both spherical methane- and hydrogen-air flames.

Implementation of the combustion models in STAR-CD and the simulation of intermittent combustion are presented in Chapter 6. This chapter addresses objective 4 outlined in the previous section, where differences between the modelling approach used for this case and the constant pressure cases simulated in the previous chapters are also highlighted. Finally in Chapter 7, the modelling framework is used to simulate a practical SI engine. This thesis concludes with Chapter 8, listing the main outcomes from this work and recommendations for future work

2. Background on turbulent premixed combustion

This chapter presents background information on turbulent premixed combustion relevant to this work. Governing equations used to describe turbulent reacting flows are described first. This is followed by a description of laminar premixed flames, which is an important pre-requisite for turbulent premixed flame modelling. The next section describes various combustion modelling techniques used to simulate turbulent premixed flames. This chapter ends with the modelling approach used in this work, which is based on the scalar dissipation rate.

2.1 Governing equations

The instantaneous governing equations for a multi-component reacting flow of ideal-gas mixtures with N species and M reactions are given by [for example see Williams (1985a)]:

Mass:

$$\frac{\partial \rho}{\partial t} + \nabla \cdot (\rho \boldsymbol{u}) = 0. \tag{2.1}$$

Momentum:

$$\frac{\partial \rho \boldsymbol{u}}{\partial t} + \nabla \cdot (\rho \boldsymbol{u}\boldsymbol{u}) = -\nabla p + \nabla \cdot \boldsymbol{\tau} + \rho \sum_{k=1}^{N} Y_k \boldsymbol{f}_k. \tag{2.2}$$

where Y_k is the mass fraction of species k and $\boldsymbol{f}_k$ is the volume force acting on species k. The viscous stress tensor in the momentum equation is given by:

$$\boldsymbol{\tau} = \mu \left[\nabla \boldsymbol{u} + (\nabla \boldsymbol{u})^{\mathrm{T}} \right] - \frac{2}{3} \mu (\nabla \cdot \boldsymbol{u}) \mathbf{I}, \tag{2.3}$$

where μ is the dynamic viscosity and $\mathbf{I}$ is the 3×3 identity matrix.

Energy:

$$\frac{\partial \rho E}{\partial t} + \nabla \cdot (\rho \boldsymbol{u} E) = \dot{\omega}_T + \nabla \cdot (\boldsymbol{\tau} \cdot \boldsymbol{u}) - \nabla \cdot \boldsymbol{q} + \rho \sum_{k=1}^{N} Y_k \boldsymbol{f}_k \cdot (\boldsymbol{u} + \boldsymbol{V}_k), \quad (2.4)$$

where the total non-chemical internal energy, E, is given by

$$E = e_s + \frac{1}{2} (\boldsymbol{u} \cdot \boldsymbol{u}), \quad (2.5)$$

which includes the sensible energy, e_s. The energy flux, $\boldsymbol{q}$, in Eq. (2.4) is given by:

$$\boldsymbol{q} = -\lambda \nabla T + \rho \sum_{k=1}^{N} h_{s,k} Y_k \boldsymbol{V}_k, \quad (2.6)$$

where λ is the heat diffusion coefficient, $h_{s,k}$ is the sensible enthalpy of species k, Y_k is the mass fraction of species k and $\boldsymbol{V}_k$ is the diffusion velocity of species k. The combustion heat release, $\dot{\omega}_T$, appearing in Eq. (2.4) is given by:

$$\dot{\omega}_T = -\sum_{k=1}^{N} \Delta h^o_{f,k} \dot{\omega}_k, \quad (2.7)$$

where $\Delta h^o_{f,k}$ is the mass enthalpy of formation of species k at temperature T_0. The total rate of mass production by chemical reactions is given by: $\dot{\omega}_k = \sum_{j=1}^{M} \dot{\omega}_{kj} = W_k \sum_{j=1}^{M} \nu_{kj} \mathrm{Q}_j$, with W_k being the atomic weight of species k, $\nu_{kj} = \nu''_{kj} - \nu'_{kj}$ denotes the difference in molar stoichiometric coefficients of species k in reaction j and Q_j is the reaction j progress rate. The energy equation given in Eq. (2.4) can also be written in terms of total sensible enthalpy:

$$\frac{\partial \rho h}{\partial t} + \nabla \cdot (\rho \boldsymbol{u} h) = \frac{\partial p}{\partial t} + \dot{\omega}_T + \boldsymbol{\tau} : \nabla \boldsymbol{u} - \nabla \cdot \boldsymbol{q} + \rho \sum_{k=1}^{N} Y_k \boldsymbol{f}_k \cdot (\boldsymbol{u} + \boldsymbol{V}_k). \quad (2.8)$$

where

$$h = \int_{T_0}^{T} C_p \, \mathrm{d}T + \frac{1}{2}(\boldsymbol{u} \cdot \boldsymbol{u}) \quad \text{and} \quad C_p = \sum_{k=1}^{N} C_{pk} Y_k. \tag{2.9}$$

Species:

$$\frac{\partial \rho Y_k}{\partial t} + \nabla \cdot \left[\rho \left(\boldsymbol{u} + \boldsymbol{V}_k\right) Y_k\right] = \dot{\omega}_k, \quad k = 1, \ldots, N, \tag{2.10}$$

where chemical reaction sources, $\dot{\omega}_k$, are obtained using chemical kinetics as functions of species concentrations, temperature and pressure. The Eqs. (2.1), (2.2), (2.4) and (2.10) constitute a system of equations for a reacting flow problem with $N + 5$ dependent variables. Rest of the variables can be related to these using the state equation:

$$p = \rho R_u T \sum_{k=1}^{N} \frac{Y_k}{W_k}. \tag{2.11}$$

In principal, the governing equations give above can be solved numerically, however, for practical simulations certain simplifications have to be made. In this work, the following phenomena are neglected to simplify these equations, which have been used in many previous studies (Pierce, 2005).

- flame acoustic interactions
- heating due to viscous dissipation
- diffusion due to pressure gradients
- volume forces
- thermal radiation

The governing equations given in this section are valid for premixed and non-premixed combustion. If one uses detailed chemical kinetic mechanisms, which typically involve tens of species with hundreds of reactions, the dimensionality

of the problem can be large. Furthermore, these equations are numerically stiff owing to the disparity between the timescales associated with different chemical reactions. Only premixed combustion is considered in this work, and the simplification described in the following section is often made to simplify the thermochemistry.

2.1.1 Thermochemistry in premixed combustion

For premixed flames, instead of solving for all the reactive species, the problem can be made tractable by using a reaction progress variable, c. This progress variable can then represent all the concentrations and temperature in the system. For adiabatic flows with unity Lewis number (Le $= \lambda/\rho C_p D$, i.e. equal mass and temperature diffusivities), the progress variable can be related to temperature by

$$c = \frac{T - T_u}{T_b - T_u}, \tag{2.12}$$

where the subscript u and b denote the initial conditions in the unburnt and burnt mixtures respectively. Alternatively, the progress variable can be defined in terms of mass fractions. It can be seen that $c = 1$ in burnt products and $c = 0$ in unburnt gases. For adiabatic flows, assuming uniform pressure with various gas species having similar molecular weights, one can use the state equation [Eq (2.11)] to write density and temperature in terms of the instantaneous progress variable (Bray et al., 1985)

$$\rho = \frac{\rho_u}{1 + \tau c}, \quad T = T_u(1 - \tau c), \tag{2.13}$$

where ρ_u and T_u are the density and temperature within the unburnt gases respectively and $\tau = T_b/T_u - 1 = \rho_u/\rho_b - 1$ is the *heat release parameter*. One can obtain the following transport equation for the instantaneous progress variable by taking the temperature transport equation and substituting the definition of the progress variable given in Eq. (2.12).

$$\frac{\partial \rho c}{\partial t} + \nabla \cdot (\rho \boldsymbol{u} c) = \nabla \cdot (\rho D_c \nabla c) + \dot{\omega}, \tag{2.14}$$

where D_c and $\dot{\omega}$ are the diffusivity and reaction rate of the progress variable, c. If all the species are assumed to have the specific heat of the mixture, C_p, then D_c is equivalent to the thermal diffusivity, D_{th}. The reaction rate of the progress variable is given by

$$\dot{\omega} = \frac{-\sum_{k=1}^{N} \Delta h_k \dot{\omega}_k}{C_p \left(T_b - T_u\right)}. \tag{2.15}$$

Note that in Eq. (2.14) the transient pressure term, $D\overline{p}/Dt$, that appears in the temperature equation has been neglected. However, this term must be retained for reciprocating engine applications.

2.2 Numerical paradigms

Most flows of practical importance are turbulent, which is caused by instabilities in the flow at large Reynolds numbers (Tennekes and Lumley, 1972). It is not possible to obtain analytical solutions to the instantaneous governing equations presented in section 2.1, and numerical methods have to be used. Various numerical paradigms exist for turbulent combustion simulations, and they are classified according to the level of detail they provide as described below.

2.2.1 Direct numerical simulation(DNS)

The direct approach of solving the turbulent flow field is called direct numerical simulation. All the relevant temporal and spatial scales are resolved in DNS, which is often referred to as numerical experiments since it does not involve any empirical constants and can reveal physical information on various processes taking place within a turbulent flow field. However, the high resolution required in DNS makes it computationally very expensive; and the computational cost increases as the cube of the flow Reynolds number (Pope, 2000). In order to reduce computational costs, earlier DNS studies were performed for 2-D problems with single-step chemistry. Three-dimensional DNS with complex chemistry have only recently become feasible for moderate Reynolds number flows (Chen, 2011). Even with the current rate of increase in computational capabilities, it is unfeasible to

simulate combustion in practical engines using DNS for the foreseeable future.

2.2.2 Large-eddy simulation (LES)

The second level for solving turbulent reacting flows numerically is the large-eddy simulations, where only the larger turbulent structures are resolved directly, while the small-scale structures are modelled. In terms of computational expense, LES lies between DNS and RANS (explained in the next section) and the computational cost of LES is proportional to $\mathrm{Re}^{9/4}$ (Hirsch, 2007). LES equations are obtained using a filtering operation, where the governing equations are averaged over the part of the spectrum that is not resolved. The general filtering operation (Leonard, 1974) is defined as

$$\overline{\phi}\left(\boldsymbol{x},t\right) = \int \phi\left(\boldsymbol{x},t\right)\, G(\boldsymbol{x}-\boldsymbol{x}')\,\mathrm{d}\boldsymbol{x}', \tag{2.16}$$

where G is the spatial filter function. The filtered governing equations for LES are similar to RANS equations. However, unlike Reynolds decomposition, the filtered residual in LES is non-zero, i.e. $\overline{\phi'} \neq 0$ (Pope, 2000). LES require combustion models since combustion takes place at the unresolved scales. It is particularly attractive for combustion applications, since it can give accurate results on complex flow fields that involve swirling flows, recirculation zones and vortical structures (Pitsch, 2006). In addition, LES can be used to study flows with inherent unsteadiness, such as in IC engines to simulate the cycle-to-cycle variability (Haworth, 1999; Rutland, 2011).

2.2.3 Reynolds-averaged Navier-Stokes equations (RANS)

The next level of numerical simulation is the Reynolds-average Navier-Stokes methodology, where the instantaneous governing equations are averaged. This averaging procedure leads to unclosed terms that need to be modelled. RANS simulations are computationally the least expensive out of the three approaches, but it only provides averaged quantities. This leads to a loss of information regarding the fluid dynamic and chemical timescales. This is acceptable for most engineering applications, since it is the statistical moments that are mostly of

interest, rather than the instantaneous quantities. It is the RANS methodology that is used for the present thesis, and in this section, the governing equations for RANS are described along with the models used to close various terms in these equations. Hence, combustion modelling becomes an integral part of this framework and various combustion models have been devised to numerically simulate combustion.

RANS governing equations

It is conventional to use Favre (density-weighted) averaging for turbulent combustion, since Reynolds averaging of variable density flows introduces products of fluctuations that require correlations for closure. However, Favre averaging allows the product $\rho\boldsymbol{u}$ to be selected as a fundamental variable instead of $\boldsymbol{u}$, in which case a product of fluctuations is not obtained (Williams, 1985*a*). Favre-average of a quantity f is defined as: $\tilde{f} = \overline{\rho f}/\overline{\rho}$, where the overbar is the usual Reynolds average. The instantaneous quantity f can be decomposed into its mass-averaged part, $\tilde{f}$, and its fluctuating part, f'', i.e. $f = \tilde{f} + f''$. From this definition, $\overline{f''} \neq 0$ but $\widetilde{f''} = 0$. Averaging Eqs. (2.1) and (2.2) and neglecting the body forces leads to:

$$\frac{\partial \overline{\rho}}{\partial t} + \nabla \cdot (\overline{\rho}\tilde{\boldsymbol{u}}) = 0, \tag{2.17}$$

$$\frac{\partial \rho\tilde{\boldsymbol{u}}}{\partial t} + \nabla \cdot (\overline{\rho}\tilde{\boldsymbol{u}}\tilde{\boldsymbol{u}}) = -\nabla\overline{p} - \nabla \cdot (\overline{\rho\boldsymbol{u}''\boldsymbol{u}''}) + \nabla \cdot \overline{\boldsymbol{\tau}}, \tag{2.18}$$

where the term $\nabla \cdot (\overline{\rho\boldsymbol{u}''\boldsymbol{u}''})$ is the Reynolds stress tensor. The Favre-averaged viscous stress tensor is given by:

$$\overline{\boldsymbol{\tau}} = \mu\left[\nabla\tilde{\boldsymbol{u}} + (\nabla\tilde{\boldsymbol{u}})^{\mathrm{T}}\right] - \frac{2}{3}\mu(\nabla \cdot \tilde{\boldsymbol{u}})\mathbf{I}. \tag{2.19}$$

The progress variable, c, is used to make the problem tractable and the transport equation for Favre-averaged progress variable, $\tilde{c}$, is given by

$$\frac{\partial \overline{\rho}\tilde{c}}{\partial t} + \nabla \cdot \overline{\rho}\tilde{\boldsymbol{u}}\tilde{c} = \nabla \cdot \left(\overline{\rho D_c \nabla\tilde{c}} - \overline{\rho\boldsymbol{u}''c''}\right) + \overline{\dot{\omega}}, \tag{2.20}$$

where the molecular diffusion term is usually neglected for high Reynolds number flows.

Turbulent kinetic energy

Appearance of Reynolds stresses in the Favre-averaged momentum equation [Eq. (2.18)] leads to the *closure* problem (Pope, 2000), which requires closure models if one were to solve the above equations. Most turbulence models are based on a equation for the turbulent kinetic energy.

Turbulent kinetic energy per unit mass, k, is defined as: $k = (1/2)\,(\overline{\boldsymbol{u}' \cdot \boldsymbol{u}'})$, where $\boldsymbol{u}'$ denotes the three-dimensional velocity fluctuations. It is known that turbulence is statistically isotropic at small scales, which implies that velocity in the three coordinate directions are equal. Hence, the turbulent kinetic energy is given by: $k = (3/2)\,\overline{u'^2}$. For compressible flows, the exact Favre-averaged turbulent kinetic energy equation is given by [for example see Wilcox (1993)]:

$$\frac{\partial \overline{\rho}\tilde{k}}{\partial t} + \nabla \cdot (\overline{\rho}\tilde{\boldsymbol{u}}\tilde{k}) = -\nabla \cdot \mathbf{T} + \mathcal{P}_k - \overline{\rho}\tilde{\varepsilon} - \overline{\boldsymbol{u}''}\nabla\overline{p} + \overline{p'\nabla \cdot \boldsymbol{u}''}, \tag{2.21}$$

where the production term $\mathcal{P}_k$ is given by

$$\mathcal{P}_k = -\overline{\rho(\boldsymbol{u}''\boldsymbol{u}'')}{:}\nabla\tilde{\boldsymbol{u}}. \tag{2.22}$$

and the transport term, $\mathbf{T}$ is given by

$$\mathbf{T} = \frac{1}{2}\overline{\rho\boldsymbol{u}''\,(\boldsymbol{u}'' \cdot \boldsymbol{u}'')} + \overline{p'\boldsymbol{u}''} - 2\overline{\rho\nu\boldsymbol{u}'' \cdot \boldsymbol{s}}, \tag{2.23}$$

where the strain-rate tensor is given by

$$\overline{\boldsymbol{s}} = \frac{1}{2}\left[\nabla\tilde{\boldsymbol{u}} + (\nabla\tilde{\boldsymbol{u}})^T\right]. \tag{2.24}$$

and the dissipation rate is given by

$$\tilde{\varepsilon} = \overline{\nu\,(\nabla\boldsymbol{u}'' : \nabla\boldsymbol{u}'')}. \tag{2.25}$$

The fifth and sixth terms on the RHS of Eq. (2.21) are the *pressure work* and

pressure dilatation terms which do not have an analog in the incompressible equation for turbulent kinetic energy. The production, dissipation and turbulent transport terms in Eq. (2.21) are unclosed. In addition, closure models need to be provided for the pressure work and pressure dilatation terms.

Turbulent scales

One of the characteristic features of high Reynolds number flows is the existence of different length scales. Richardson (1922) first introduced the idea of the *energy cascade* where kinetic energy that enters the largest scales of motion are transferred to successively smaller scales until it is dissipated at the smallest scales by the action of viscous processes.

This dissipation of turbulent kinetic energy occurs at a rate determined by large-scale dynamics of turbulence. An important estimate of this dissipation rate is given by (Taylor, 1935*a*)

$$\varepsilon \sim \frac{u'^3}{\Lambda}, \tag{2.26}$$

where Λ is the integral length scale. Therefore, the small-scale structures of turbulence can be parametrised using this *dissipation rate per unit mass*, ε, and the kinematic viscosity, ν, which can be used to obtain the following *Kolmogorov microscales*:

$$\eta_k = \left(\frac{\nu^3}{\varepsilon}\right)^{1/4}, \quad \tau_k = \left(\frac{\nu}{\varepsilon}\right)^{1/2}, \quad u'_k = (\nu\varepsilon)^{1/4}. \tag{2.27}$$

It can be shown that these Kolmogorov scales correspond to the smallest eddies in a turbulent flow (Pope, 2000). Before proceeding to a discussion of turbulent combustion models, it is helpful to look at some results from laminar premixed flames, which are described in the next section.

2.3 Characteristics of laminar premixed flames

Study of laminar premixed flames is a necessary pre-requisite for turbulent premixed flames. Various characteristics of laminar premixed flames are presented in this section, which are essential for the turbulent combustion model used in this work.

2.3.1 Flame thickness

Laminar flame thickness, δ, is a characteristic quantity for laminar premixed flames. It is also important from a modelling perspective, since it can be used as a reference length scale for the flame and can control the mesh resolution (Poinsot and Veynante, 2005). From scaling laws, the thickness of the laminar premixed flame can be obtained as (Göttgens et al., 1992):

$$\delta = \frac{\lambda_u}{\rho_u C_p s_L^0}, \tag{2.28}$$

where all the values are evaluated in the unburnt gases, s_L^0 is the unstretched laminar flame speed, which is used as a reference speed for all combustion studies (Poinsot and Veynante, 2005). If the Prandlt number, $\mathrm{Pr} = \nu/\alpha$, and the Schmidt number, $\mathrm{Sc} = \nu/D$, are assumed to be unity and the reactive scalars have the same diffusion coefficient, D, then the flame thickness given in Eq. (2.28) can be written as

$$\delta = \frac{D}{s_L^0}. \tag{2.29}$$

Laminar flame thickness is often referred to as the Zeldovich thickness. The flame thickness based on the temperature profile, called the *thermal thickness*, is defined as (Spalding, 1955):

$$\delta_L^0 = (T_b - T_u)/(\partial T/\partial x)_{\max}, \tag{2.30}$$

which can only be determined if the temperature gradient is known. A thickness close to the thermal thickness has been defined using correlations (Blint, 1986)

as

$$\delta_L^b = 2\delta(1+\tau)^{0.7} \simeq \delta_L^0. \tag{2.31}$$

2.3.2 Flame speed

Propagation is the most important characteristic of premixed flames, since it determines fuel consumption rate and heat release. Propagation rate of laminar premixed flames is determined by the laminar burning velocity, s_L^0, which is the velocity with which the flame moves relative to the unburnt reactants. The direction of propagation is locally normal to the flame itself and towards the reactants. This laminar flame speed can also be used to parameterise premixed flame phenomena such as extinction, flashback, blowoff and turbulent flame propagation (Law, 2006).

Laminar flame speed measurement

A number of experimental techniques are used to measure s_L^0. For example, Bunsen-type burners can be used to determine the flow velocity at the burner exit, usually using various imaging techniques of the flame surface. A useful research tool in studying laminar premixed flames is the flat-flame burner (Williams, 1985*a*), where the flow is stabilised over a porous plate in a flow. Stagnation point flames are a type of flat-flame and is often used to study laminar flames (Poinsot and Veynante, 2005). Furthermore, spherical flames, obtained either by igniting a combustible mixture in a closed chamber or by using the soap-bubble method (Williams, 1985*a*) are also used. Most experimental techniques used to measure the laminar flame speed suffer from stretch, which needs to be subtracted from the measured laminar flame speeds to determine a stretch-free flame speed (Law, 2006).

2.3.3 Flame stretch

Non-uniformities in the flow can cause the flame front to be strained and curved. The resulting fractional rate of change of the flame surface area is collectively

called the *flame stretch*, which is defined as (Williams, 1985*a*)

$$\kappa = \frac{1}{A}\frac{\mathrm{d}A}{\mathrm{d}t}, \tag{2.32}$$

where A is the flame surface element. Candel and Poinsot (1990) derived the following expression for the flame stretch in terms of strain rate and curvature.

$$\kappa = -\boldsymbol{nn}{:}\nabla\boldsymbol{u} + \nabla\cdot\boldsymbol{u} + s'_d(\nabla\cdot\boldsymbol{n}), \tag{2.33}$$

where $\boldsymbol{u}$ is the local flow velocity, s'_d is the speed with which the flame front propagates normal to the background fluid, called the *displacement speed* and is given as (Jenkins et al., 2006)

$$s'_d = \left.\frac{\dot{\omega} + \nabla\cdot(\rho D\nabla c)}{\rho|\nabla c|}\right|_{c=c^*}. \tag{2.34}$$

The unit normal vector to the flame front is given as $\boldsymbol{n}$ in Eq. (2.33). This unit normal vector points towards the unburnt gases, which can be defined in terms of the reaction progress variable as

$$\boldsymbol{n} = -\frac{\nabla c}{|\nabla c|}, \tag{2.35}$$

where the negative sign is included because the convention is for $\boldsymbol{n}$ to be positive when it is pointing towards the burnt side (Law, 2006), i.e. a positive curvature is when it is convex to the fresh gases. Thus, an outwardly propagating spherical flame has positive curvature. The three terms on the RHS of Eq. (2.33) are: normal strain rate tensor, volumetric expansion of the fluid and the flame curvature, respectively. The curvature term can be written in terms of the principal radii of curvature as (Rutland and Trouvé, 1993)

$$s'_d\nabla\cdot\boldsymbol{n} = \pm s'_d\left(\frac{1}{\mathcal{R}_1} + \frac{1}{\mathcal{R}_2}\right), \tag{2.36}$$

where $\pm$ is used to indicate outwardly $(+)$ and inwardly propagating $(-)$ flames and $\mathcal{R}_1 = \mathcal{R}_2$ for a sphere. As the flame propagates the stretching of an expanding

flame becomes weaker; whereas it becomes stronger for an imploding flame (Law, 2006).

Effect of flame stretch

Flame stretch is important in practical flames; examples include the negatively stretched ($\kappa < 0$) Bunsen burner flame and the positively stretched ($\kappa > 0$) outwardly propagating spherical flame. Since flame stretch is a characteristic property of the flame it should be related to other physicochemical characteristics such as flame speed and temperature.

Matalon and Matkowsky (1982) used the method of matched asymptotic expansions to show the response of the flame speed to stretch. It was found that for moderate rates of strain and curvature with large activation energy, the normal flame speed is directly proportional to the flame stretch. Studies such as those by Matalon and Matkowsky (1982) and Clavin and Williams (1982) obtained the following expression for s_L

$$s_L = s_L^0 - \mathcal{L}\kappa, \tag{2.37}$$

where $\mathcal{L}$ is the Markstein length, which is proportional to the laminar flame thickness, δ (Peters, 2000). This equation implies that the flame speed changes linearly with stretch. Thus, Markstein length can also be used to characterise a laminar flame (Clavin, 1985). However, if the stretch was intensified, the above Markstein relation would not hold. Therefore, one cannot always use the flame stretch to parameterise the flame structure.

Experimental and numerical studies have also been conducted to determine the effect of flame stretch. Hassan et al. (1998*a*) carried out experimental investigations to determine the properties of outwardly propagating spherical laminar premixed flames and compared the results with numerical simulations. The results of their study showed that there is a significant effect of the stretch for the flames considered.

2.4 Regimes in turbulent premixed combustion

In his pioneering work, Damköhler described how large-scale turbulence acts to wrinkle the flame without changing the internal structure, whereas small-scale eddies affect the transport processes within the flame. Therefore, in order to build a model for turbulent combustion it is necessary to consider the physical characteristic of the flame as well as the various time and length scales of the turbulent combustion process. For example, a flame with holes will not be treated in the same way as a continuous flame front (Meneveau and Poinsot, 1991). Such an analysis can be used to obtain a combustion *regime diagram* that shows the regimes as function of various non-dimensional numbers.

The turbulence Reynolds number, Re_t, is used to characterise the ratio of inertial to viscous effects of the turbulent flow. The turbulence Damköhler number, Da_t, compares the turbulent large-eddy turn-over timescale to the chemical timescale of the laminar flame. In addition, turbulent Karlovitz number, Ka, is also defined for premixed combustion, which is a ratio of laminar flame chemical timescale to the Kolmogorov timescale. These non-dimensional variables are given as:

$$\mathrm{Re}_t = \frac{u'}{s_L^0}\frac{\Lambda}{\delta}, \quad \mathrm{Da}_t = \frac{s_L^0}{u'}\frac{\Lambda}{\delta}, \quad \mathrm{Ka} = \frac{u_k'}{s_L^0}\frac{\delta}{\eta_k}. \tag{2.38}$$

where η_k is the Kolmogorov length scale and u_k' is the Kolmogorov velocity scale. Definitions of the dissipation rate given in Eq. (2.26), the Kolmogorov length scale and unity flame Reynolds number can be used to obtain the following equivalent definitions for the Karlovitz number (Poinsot and Veynante, 2005):

$$\mathrm{Ka} = \frac{(u'/s_L^0)^{3/2}}{(\Lambda/\delta)^{1/2}} = \frac{(\varepsilon\delta)^{1/2}}{{s_L^0}^{3/2}} = \left(\frac{\delta}{\eta_k}\right)^2 = \frac{(\varepsilon/\nu)^{1/2}}{s_L^0/\delta}. \tag{2.39}$$

The regime diagram introduced by Peters (1999), which is shown in Figure 2.1, includes five different regimes of premixed combustion. The dimensionless groups used to plot the diagram are: u'/s_L^0 and Λ/δ, which respectively represents the velocity scales in the flow and the flame, and the size of the turbulent eddies that

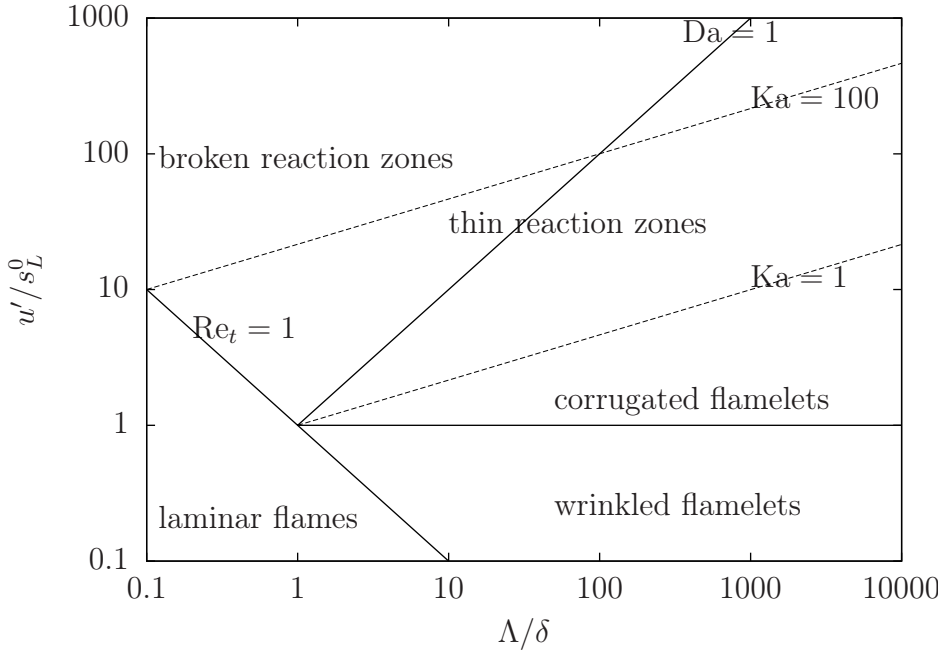

Figure 2.1: Regime diagram for turbulent premixed combustion (Peters, 1999).

interacts with the flame.

Laminar flames exist for low Reynolds numbers (Re $<$ 1) and two laminar flamelet regimes exist when Re $\gg$ 1, Da $\gg$ 1 and Ka $\ll$ 1. Laminar flamelet concept means that the turbulent flame can be thought of as an ensemble of stretched laminar flamelets (Peters, 2000), i.e. the local flame structure is the same as that of a laminar flame. This allows the separation of chemistry from turbulence, where laminar flame theory can be used to determine the reaction rate and transport. The global properties of the flow can then be computed using usual turbulence modelling techniques. Most models developed for turbulent premixed combustion use this existence of laminar flamelets (Cant and Mastorakos, 2008).

In the flamelet regimes, fast-chemistry is assumed and the flow consists of a burnt phase and an unburnt phase, separated by a flame surface made up of laminar flamelets. In the *wrinkled flamelets* regime, the laminar flame propagation overwhelms the flame front corrugation by turbulence. The flame surface becomes more wrinkled when the turbulence intensity increases, creating pockets in the flame surface. Flames in this region are called *corrugated flamelets*.

Unlike the flamelet regimes, in the *thin reaction zone*, the turbulent eddies of size η_k enter the preheat zone (since $\eta_k < \delta$). However, these eddies do not enter the inner layer as η_k is still larger than the inner layer thickness δ (Peters, 2000). Thus, the reaction zone still has the laminar flame structure, and the laminar burning velocity remains well defined.

The above description of various combustion regimes explains why the premixed laminar flame theory is needed for turbulent combustion models. Even though such diagrams are highly qualitative, it provides a useful reference for comparison between modelled and computed flames. In the broken reaction zones, the turbulent eddies are smaller than the inner layer thickness and can therefore influence the chemical reactions in the inner layer causing local flame extinctions. The resulting flame does not have a laminar flame structure and will not be considered further in this study. The commonly used premixed combustion models are described in the following section, including the model used in the present work.

2.5 Premixed combustion sub-models

The main objective of turbulent combustion modelling is to provide closure for the mean reaction rate term, $\overline{\dot{\omega}}$, appearing in Eq. (2.20). A detailed description of these combustion models is beyond the scope of this work [see for example Veynante and Vervisch (2002)], and only a brief overview of Reynolds-averaged sub-models for turbulent premixed combustion is given here.

2.5.1 Eddy Break-Up (EBU) model

This classical model for the mean reaction rate, first proposed by Spalding (1971), is based on phenomenological analysis, assuming $\mathrm{Re} \gg 1$ and $\mathrm{Da} \gg 1$. The reaction zone is described as pockets of burnt and unburnt gases and the mixing of these pockets by turbulent eddies controls the reaction rate. The reaction rate

according to this model is given as:

$$\overline{\dot{\omega}} = -C_{\mathrm{EBU}}\overline{\rho}\frac{\tilde{\epsilon}}{\tilde{k}}\sqrt{\widetilde{c''^2}}, \tag{2.40}$$

where the model constant C_{EBU} is of the order unity. Large values of Re and Da imply that the combustion is in the flamelets regime, with the flame infinitely thin and the reaction assumed to be fast. Thus one could estimate the variance as $\widetilde{c''^2} = \tilde{c}(1-\tilde{c})$. The biggest limitation of the Eddy Break-Up model in its original form is that chemical kinetics is not taken into account. Even though EBU-like models are one of the simplest reaction rate models, they do not represent the physics of the problem and the fast chemistry assumption leads to overprediction of reaction rates. A variant of this approach, called the eddy dissipation concept, is developed to include complex chemical kinetics.

2.5.2 Bray-Moss-Libby (BML) modelling

This flamelet model is based on statistics of the progress variable for thermochemical closure (Bray et al., 1985). The main assumption for this model is that the turbulent flame is thin and its structure is not disturbed by turbulent structures in the surrounding fluid. The probability density function (pdf) of the progress variable is then a sum contributions from fresh gases, burnt mixtures and reacting mixtures, written as:

$$\overline{p}(c;\boldsymbol{x},t) = \alpha(\boldsymbol{x},t)\delta(\zeta) + \beta(\boldsymbol{x},t)\delta(1-\zeta) + \gamma(\boldsymbol{x},t)f(\zeta;\boldsymbol{x},t), \tag{2.41}$$

where $\alpha(\boldsymbol{x},t)$, $\beta(\boldsymbol{x},t)$ and $\gamma(\boldsymbol{x},t)$ respectively denote the probability of finding the reactants and products and reacting mixture, at position $\boldsymbol{x}$ and at time t. Dirac δ functions $\delta(\zeta)$ and $\delta(1-\zeta)$ are used to denote the fresh ($c=0$) and fully burnt ($c=1$) gases respectively. When the flame front is taken to be thin (i.e. $\mathrm{Re} \gg 1$ and $\mathrm{Da} \gg 1$), the probability of finding the reacting gas is negligible (i.e. $\gamma \ll 1$). When the normalisation condition is then applied to the pdf in

Eq. (2.41), the following condition is obtained:

$$\alpha(\boldsymbol{x};t) + \beta(\boldsymbol{x};t) = 1. \tag{2.42}$$

The coefficients α and β can be determined as a function of the Favre-averaged progress variable, $\tilde{c}$, as follows:

$$\overline{\rho}\tilde{c} = \int_0^1 \rho(\zeta)\,\zeta\,p\,(\zeta)\;\mathrm{d}\zeta = \rho_b\beta, \tag{2.43}$$

where ρ_b is the burnt gas density. Using the heat release parameter, τ, one obtains $\rho_u = \overline{\rho}(1+\tau\tilde{c})$ and the probabilities α and β become:

$$\alpha = \frac{1-\tilde{c}}{1+\tau\tilde{c}}, \quad \beta = \frac{(1+\tau)\tilde{c}}{1+\tau\tilde{c}}. \tag{2.44}$$

This means that the thermochemical state of the mixture can be determined by $\tilde{c}$, which can be obtained from its transport equation. When γ is neglected one could obtain $\widetilde{c''^2}$, this result is used in several models for premixed combustion, including the EBU model. The consequence of this being that only the conservation equation for the mean progress variable is needed together with the fluid dynamics equations in solving a turbulent premixed combustion problem.

A gradient transport hypothesis is sometimes used to close the turbulent scalar flux term, $\widetilde{\boldsymbol{u}''c''}$, appearing in Eq. (2.20). BML formulation can be used to express the turbulent fluxes as

$$\overline{\rho}\widetilde{\boldsymbol{u}''c''} = \overline{\rho}\tilde{c}(1-\tilde{c})(\overline{\boldsymbol{u}}_b - \overline{\boldsymbol{u}}_u), \tag{2.45}$$

where $\overline{\boldsymbol{u}}_u$ and $\overline{\boldsymbol{u}}_b$ are the conditional mean velocities in unburnt and burnt gases respectively. For a steady planar flame the mean velocity increases towards the burnt gas ($\overline{u_b} > \overline{u_u}$) and $\overline{\rho}\widetilde{\boldsymbol{u}''c''} > 0$. This contradicts with the classical gradient transport assumption:

$$\overline{\rho}\widetilde{\boldsymbol{u}''c''} = -\frac{\mu_t}{\mathrm{Sc}_c}\nabla\tilde{c}. \tag{2.46}$$

Therefore, the BML model is able to predict the countergradient diffusion phe-

nomena, which has been observed both experimentally (Libby and Bray, 1981) and numerically (Veynante et al., 1997). Countergradient gradient diffusion yield a negative turbulent diffusivity, which mainly arises when the local pressure forces accelerate burnt and unburnt mixtures differentially due to their density difference.

The BML formulation can also be used to obtain relations between Reynolds-averaged and Favre-averaged values of c as (Bray, 1980):

$$\overline{c} = \frac{(1+\tau)\tilde{c}}{1+\tau\tilde{c}}. \tag{2.47}$$

The above analysis cannot be used to determine the mean reaction rate term, $\overline{\dot{\omega}}$. This is because the flamelet model assumption makes the probability of finding reacting gas negligible and alternative modelling approaches are required to estimate this term.

One such estimation proposed by Bray (1979) was obtained by analysing transport equations for $\tilde{c}$ and $\widetilde{c''^2}$ to show that the mean reaction rate is proportional to the mean scalar dissipation rate, $\tilde{\epsilon}_c = \overline{\rho\alpha_c\left(\nabla c'' \cdot \nabla c''\right)}/\overline{\rho}$.

$$\overline{\dot{\omega}} = \frac{2}{2C_m - 1}\overline{\rho}\tilde{\epsilon}_c, \tag{2.48}$$

where C_m is given by

$$C_m = \frac{\int_0^1 \zeta\,\dot{\omega}(\zeta)\,p(\zeta)\,\mathrm{d}\zeta}{\int_0^1 \dot{\omega}(\zeta)\,p(\zeta)\,\mathrm{d}\zeta}, \tag{2.49}$$

which typically varies between 0.7 and 0.8 for hydrocarbon-air flames (Swaminathan and Bray, 2005) and values of C_m for hydrogen-air mixtures at various equivalence ratios have been reported by Rogerson and Swaminathan (2007). Since Eq. (2.48) shows a direct link between the reaction rate and the scalar dissipation rate, physically correct modelling of the scalar dissipation rate will enable one to determine the reaction rate. However, the closure for the mean scalar dissipation rate is challenging for premixed flames (Kolla and Swaminathan, 2010*a*). Using the classical model for the mean scalar dissipation rate, $\tilde{\epsilon}_c \simeq \widetilde{c''^2}/\tau_t$, where the turbulence time scale is estimated as $\tau_t = \tilde{k}/\tilde{\varepsilon}$, will recover the EBU model.

Another approach to close the mean reaction rate term is based on the crossing frequency of the flame front at a given point (Bray et al., 1984). The mean reaction rate is then expressed as the product of the flame crossing frequency, ν_f, and the reaction rate per flame crossing, $\dot{\omega}_f$: $\overline{\dot{\omega}} = \dot{\omega}_f \nu_f$. By treating the progress variable signal as a telegraphic signal one can write: $\nu_f = 2\overline{c}(1-\overline{c})/\hat{T}$, where the $\hat{T}$ is the mean period of a telegraphic signal, which can be estimated as the turbulence time scale, τ_t. The Reynolds-averaged progress variable, $\overline{c}$ can be obtained from Eq. (2.47). The reaction rate per flame crossing can be expressed as (Bray et al., 1984): $\dot{\omega}_f = \rho_u s_L^0 / |\sigma_f|$, where $|\sigma_f|$ is a flamelet orientation factor.

2.5.3 Flame surface density (FSD) modelling

This widely used flamelet approach is based on the earlier coherent flame model (CFM) of Marble and Broadwell (1977). In this model, the mean reaction rate is taken as the product of reaction rate per unit flame area and the flame surface area per unity volume, Σ, which is known as the flame surface density (Marble and Broadwell, 1977): $\overline{\dot{\omega}} = \rho_u \langle s_c \rangle_s \Sigma$, where s_c is the flame consumption speed and $\langle\,\rangle_s$ denotes averaging over the flame surface. The stretching of the flame surface by turbulent eddies can influence the flame propagation speed and it is useful to write $\langle s_c \rangle_s = s_L^0 I_0$ (Bray, 1990), where I_0 is a stretch factor that takes into account the effects of stretch on s_L. This approach is attractive because the turbulence-combustion interaction is modelled by the flame surface density, Σ, which can be separated from complex chemistry effects incorporated into s_L^0 and I_0.

Two main approaches are used to close Σ; in one method an algebraic expression is used (Bray et al., 1984), and in the other method a modelled balanced equation (Pope, 1988; Candel and Poinsot, 1990) is solved. A simple algebraic model is given as (Bray and Swaminathan, 2006)

$$\Sigma \delta_L^0 \simeq \frac{2C_{D_c}}{(2C_m - 1)} \frac{\overline{\rho}}{\rho_u} \left(1 + \frac{2}{3} C_{\varepsilon_c} s_L^0 \frac{1}{\sqrt{\tilde{k}}}\right) \left(1 + \frac{C_D \tilde{\varepsilon} \delta_L^0}{C_{D_c} \tilde{k} s_L^0}\right) \widetilde{c''^2}, \tag{2.50}$$

where the three model parameters are of order unity. An exact balance equation for Σ written after Favre decomposition is given as (Pope, 1988; Candel and

Poinsot, 1990):

$$\frac{\partial \Sigma}{\partial t} + \nabla \cdot \langle \boldsymbol{u} \rangle_s \Sigma = \Sigma \langle \nabla_T \cdot \tilde{\boldsymbol{u}} + \nabla_T \cdot \boldsymbol{u}'' + \nabla_T \cdot (s_d' \hat{\boldsymbol{n}}) \rangle_s - \Sigma \nabla \cdot \langle \boldsymbol{u}'' \rangle_s - \Sigma \nabla \cdot \langle s_d' \hat{\boldsymbol{n}} \rangle_s, \tag{2.51}$$

where s_d' is the displacement speed of the surface relative to the unburnt mixture and $\hat{\boldsymbol{n}}$ is the unit normal vector to the flame front pointing towards the fresh gases. This balance equation for the flame surface density is not closed and modelling is required to close various terms. Such modelling has been the subject of many past studies [see Veynante and Vervisch (2002) for a summary of such studies]. One such modelled transport equation is given as (Boudier et al., 1992)

$$\frac{\partial \Sigma}{\partial t} + \nabla \cdot (\boldsymbol{u}\Sigma) - \nabla \cdot \left(\frac{\nu_t}{\sigma_\Sigma} \nabla \Sigma \right) = \alpha \kappa \Sigma - \beta \frac{\omega_L \left(1 + a\sqrt{k}/s_L^0 \right)}{\overline{\rho} \overline{Y}_f} \Sigma^2, \tag{2.52}$$

where ω_L is the rate of fuel per unit flame area, $\overline{Y}_f$ is the mean fuel mass fraction and α, a, β and σ_Σ are model parameters.

2.5.4 The level set approach (G-equation)

In this approach, the flame surface is represented by a *level set* of a non-reacting scalar, G, at $G(\boldsymbol{x}, t) = G_0$, where G_0 is the value at the flame front. This approach is suitable to model corrugated flamelets and thin reaction zone regimes (Peters, 2000). The original form of the G-equation introduced by Williams (1985*b*) is given as

$$\frac{\partial G}{\partial t} + \boldsymbol{u} \cdot \nabla G = s_d' |\nabla G|. \tag{2.53}$$

The above equation is modified by first including the stretch effects through the displacement speed (Matalon and Matkowsky, 1982):

$$s_d' = s_L^0 - s_L^0 \mathcal{L} \kappa_c - a\mathcal{L}, \tag{2.54}$$

where $a = -\boldsymbol{n} \cdot \nabla \boldsymbol{u} \cdot \boldsymbol{n}$ is the strain rate and $\kappa_c = \nabla \cdot \boldsymbol{n}$ is the flame curvature. The flame normal vector is given by $\boldsymbol{n} = -\nabla G/|\nabla G|$. Substitution of Eq. (2.54) into Eq. (2.53) gives the modified G-equation:

$$\frac{\partial G}{\partial t} + \boldsymbol{u} \cdot \nabla G = s_L^0 |\nabla G| - D_{\mathcal{L}} \kappa_c |\nabla| - a\mathcal{L}|\nabla G|, \tag{2.55}$$

where $D_{\mathcal{L}} = s_L^0 \mathcal{L}$ is the Markstein diffusivity. This equation is only valid for corrugated flamelets regime. The G-equation for thin reaction zones regime is given by Peters (1999)

$$\frac{\partial G}{\partial t} + \boldsymbol{u} \cdot \nabla G = (s_n + s_r)|\nabla G| - D\kappa_c |\nabla G|, \tag{2.56}$$

where s_r and s_n are the reaction and normal diffusion component to the displacement speed s_d' and $-D\kappa_c$ is the tangential diffusion component. Transport equations for $\tilde{G}$ and $\widetilde{G''^2}$ have been developed (Peters, 1992, 1999) for RANS simulations of turbulent combustion, where the transport equation for $\tilde{G}$ is given by

$$\frac{\partial \tilde{G}}{\partial t} + \tilde{\boldsymbol{u}} \cdot \nabla \tilde{G} = s_T |\nabla \tilde{G}| - D\kappa_c |\nabla \tilde{G}|. \tag{2.57}$$

This equation requires a model for the turbulent flame speed, s_T, which is usually of the general form (Peters, 1999)

$$s_T = s_L^0 \left[1 + A \left(u'/s_L^0\right)^n\right], \tag{2.58}$$

where n is around 0.7 (Williams, 1985a).

This level set approach removes the complexities involved with counter-gradient diffusion since turbulent transport terms normal to the flame front do not appear in the balance equations for G. In addition, this approach does not require a closure model for a chemical source term since, by definition, G is a non-reactive scalar. However, it has been noted by Williams (2001) that this approach is strictly valid for wrinkled flamelets.

2.5.5 Conditional moment closure (CMC)

The models presented so far are based on conventional averages. In turbulent reacting flows, when conventional averaging is used, the large spatial and temporal fluctuations of scalar quantities makes it difficult to obtain accurate closures for the mean reaction rate (Borghi, 1974). To overcome this issue, Klimenko (1990) and Bilger (1993), independently derived a model for non-premixed turbulent combustion, where the averages of the reactive scalars are conditioned on the mixture fraction. This conditional averaging makes the fluctuations around the mean smaller. Klimenko and Bilger (1999) later proposed an extension of this conditional moment closure (CMC) method to premixed combustion, where conditioning is done with the progress variable, c. Recently, Amzin et al. (2012) successfully applied the CMC method to premixed combustion of a pilot stabilised Bunsen flame.

The conditional mean of a scalar, k, is given as: $Q_k \equiv \langle Y_k | c = \zeta \rangle \equiv \langle Y_k | \zeta \rangle$, where the angled brackets denote ensemble averaging, ζ is the sample space variable of c and Y_k is a reactive scalar. Transport equations for the conditional mean scalar values, Q_k are obtained by substituting $Y_k(\boldsymbol{x}, t) = Q_k(c; \boldsymbol{x}, t) + y_k(\boldsymbol{x}, t)$ into the instantaneous equation for the reactive scalars [for example Eq. (2.10)] (Bilger, 1993). Alternatively, one could obtain the same equation by using the joint pdf transport equation (Klimenko, 1990). For premixed flames the conditional moment closure equation can be written as (Klimenko and Bilger, 1999; Swaminathan and Bilger, 2001*a*)

$$\begin{aligned}\langle \rho | \zeta \rangle \frac{\partial Q_k}{\partial t} + \langle \rho \boldsymbol{u} | \zeta \rangle \cdot \nabla Q_k - \frac{\mathrm{Le}_c}{\mathrm{Le}_k} \langle \rho N_{c,k} | \zeta \rangle \frac{\partial^2 Q_k}{\partial \zeta^2} \\ = \langle \rho \dot{\omega}_k | \zeta \rangle - \langle \rho \dot{\omega} | \zeta \rangle \frac{\partial Q_k}{\partial \zeta} - \frac{1}{\tilde{p}\,(\zeta)} \nabla \cdot \left[\langle \rho \boldsymbol{u}'' Y_k'' | \zeta \rangle \, \tilde{p}\,(\zeta) \right] + e_{Q_k}, \end{aligned} \quad (2.59)$$

where Le_k is the Lewis number of species k, $\tilde{p}$ is the Favre pdf of c and $\dot{\omega}_k$ and $\dot{\omega}$ are given by Eqs. (2.10) and (2.14) respectively. The instantaneous scalar dissipation rate of species k is defined as $N_{c,k} = D_k \left(\nabla c \cdot \nabla c \right)$. The symbol e_{Q_k} is

defined as (Swaminathan and Bilger, 2001*a*)

$$e_{Q_k} \equiv \nabla \cdot (\rho D_k \nabla Q_k) + \left\langle \rho D_k \nabla c \cdot \nabla \frac{\partial Q_k}{\partial \zeta} \right\rangle + \left\langle \frac{\partial Q_k}{\partial \zeta} \nabla \cdot \left[(1 - \mathrm{Le}_k)\, \rho D_k \nabla c | \zeta \right] \right\rangle . \tag{2.60}$$

The terms $\langle \rho \boldsymbol{u}'' Y'' | \zeta \rangle$, $\tilde{p}(\zeta)$, $\langle \rho \boldsymbol{u} | \zeta \rangle$, $\langle \dot{\omega}_k | \zeta \rangle$ and $\langle N_{c,k} | \zeta \rangle$ need to be modelled and various closure models have been discussed by Klimenko and Bilger (1999) and Swaminathan and Bilger (2001*a*). The closure of the conditional mean scalar dissipation rate, $\langle N_{c,k} | \zeta \rangle$, is linked to the unconditional mean scalar dissipation rate, $\tilde{\epsilon}_c$ (Swaminathan and Bilger, 2001*b*). Modelling of this unconditional mean scalar dissipation rate is discussed in section 2.5.8.

The sound theoretical basis for CMC equations means that, when compared with closure models based on phenomenology or physical analyses, it is expected to give improved predictions for species with slow time scales, such as pollutants (Klimenko and Bilger, 1999). In addition, CMC may be valid for all regimes of premixed combustion since no explicit approximations are made on the influence of turbulent eddies on the flame structure (Amzin et al., 2012). However, one of the drawbacks of CMC is that it is more expensive than the flamelet methods described earlier, since the number of transport equations that need to be solved are equal to $(N+1)$ times the number of points in the conditioning variable space. Note that here N refers to the number of species and is not to be confused with the instantaneous scalar dissipation rate N_c.

2.5.6 Transported pdf approach

In this approach, statistical methods based on the stochastic nature of turbulence are used to calculate turbulent reacting flows. A pdf can be used to determine the likelihood of finding a particular solution, given certain physical conditions of the flow at a given time. A complete statistical description of a turbulent reacting flow can be obtained by defining the joint pdf for the velocity components and the thermochemical variables (Pope, 1985). If the pdfs of the thermochemical

variables are known, the mean reaction rate can be obtained from

$$\overline{\dot{\omega}} = \int_{\underline{\psi}} \dot{\omega}\, \tilde{p}(\underline{\psi}; \boldsymbol{x}, t)\, \mathrm{d}\underline{\psi}, \tag{2.61}$$

where $\underline{\psi} = (Y_1, Y_2, \ldots, Y_N, T)$ is the scalar field vector that represent the species mass fractions of N species in addition to temperature and $\tilde{p}(\underline{\psi}; \boldsymbol{x}, t)$ is the Favre-averaged joint pdf of this scalar field, $\underline{\psi}$. This statistical description of the stochastic flow field is applicable to premixed, non-premixed and partially premixed combustion (Borghi, 1988).

The following exact evolution equation for the joint pdf $\tilde{p}(\underline{\psi})$ (for ease of notation the dependence of $\boldsymbol{x}$ and t is omitted) has been derived by Dopazo and O'Brien (1974) and Pope (1976) [the details of this derivation can be found in O'Brien (1980)].

$$\begin{aligned} &\frac{\partial}{\partial t}\left[\overline{\rho}\tilde{p}(\underline{\psi})\right] + \nabla\cdot\left[\overline{\rho}\tilde{\boldsymbol{u}}\tilde{p}(\underline{\psi})\right] + \sum_{\alpha=1}^{N}\frac{\partial}{\partial\psi_\alpha}\left[\dot{\omega}_\alpha(\underline{\psi})\overline{\rho}\tilde{p}(\underline{\psi})\right] \\ &\qquad = -\nabla\cdot\left[\overline{\rho}\langle\boldsymbol{u}''|\underline{\psi}\rangle\tilde{p}(\underline{\psi})\right] + \sum_{\alpha=1}^{N}\frac{\partial}{\partial\psi_\alpha}\left[\langle\nabla\cdot(\boldsymbol{J}_\alpha|\underline{\psi})\rangle\tilde{p}(\underline{\psi})\right], \end{aligned} \tag{2.62}$$

where $\dot{\omega}_\alpha$ and $\boldsymbol{J}_\alpha$ respectively represent the reaction per unit volume and the molecular diffusive flux of species α. The unsteady, convection and chemical source production terms (the three terms on the LHS of the equation) are closed. This exact form of the chemical source term implies that finite chemistry can be implemented in the calculations without the need to define the flame structure, which is the main reason why the transported pdf approach is attractive for reacting flows (Jones, 2002). The turbulent flux term and the micromixing term on the RHS of this equation are unclosed.

Jones (2002) notes that the classical closure problem of turbulent combustion has been transferred mathematically from the mean reaction term in moment closures to the micromixing terms in the pdf closures. The turbulent transport term can be modelled using gradient transport assumptions and the standard $k-\varepsilon$ model has been used to obtain the turbulent flow field (Pope, 1985). Alternatively, one could use the velocity-composition joint pdf, $p(\boldsymbol{u}, \underline{\psi}; \boldsymbol{x}, t)$, which makes the

turbulent diffusion term exact and no turbulence model is required. However, this introduces further unknowns into the pdf transport equation (Pope, 1985). Many models have been proposed for the micromixing term [see for example Haworth and Pope (2011) for a discussion of these models].

Solving the pdf transport equation by conventional numerical methods is expensive and alternatives such as the *Monte-Carlo* method applied for turbulent reacting flows (Pope, 1981) have to be used. In such methods the computational cost of the problem increases only linearly with the dimensionality of the pdf. However, the transported pdf methods are still more complex and time-consuming compared to the moment methods and its practical use in industrial applications is limited (Poinsot and Veynante, 2005).

2.5.7 Presumed pdf approach

In general, the pdf, $\tilde{p}(\underline{\psi}; \boldsymbol{x}, t)$, in Eq. (2.61) can take any shape. However, in some combustion problems, certain similarities can be seen in the pdf functions (Poinsot and Veynante, 2005). This is the motivation behind presuming a certain shape for the pdf. In this approach the pdf shapes are parametrised using moments, which are obtained from their balance equations (Borghi, 1988). It can be easily envisaged that this method is much less time-consuming than solving the pdf transport equation, and therefore more suitable for three-dimensional flow calculations of industrial problems. An important point to note here is that the presumed pdf approach is only applicable to cases where the scalar fluctuations are small, therefore, its applicability is only limited to premixed combustion or non-premixed flames with fast chemical reactions (Borghi, 1988).

The BML formulation described in section 2.5.2 is one such example of a presumed pdf model where a bimodal pdf is used. The shape of the presumed pdf determines the number of scalar moments balance equations that need to be solved. For the BML formulation only the first moments, $\tilde{c}$, is required. In contrast the popular pdf shape, β-function pdf, requires the first two moments, $\tilde{c}$ and $\widetilde{c''^2}$.

Presumed pdf approach can also be used for the level set formulation. For example, if the non-reactive scalar G is assumed to be well-defined and well-

behaved outside the surface, $G(\boldsymbol{x}, t) = G_0$, then a pdf, $p(G; \boldsymbol{x}, t)$, can be defined for G. According to the presumed pdf approach, the first two moments of G obtained from their balance equations can be used to parametrise and calculate $p(G; \boldsymbol{x}, t)$ (Peters, 2000). In comparison with the transported pdf approach, both the BML and G-equation formulations have: i) reduced the dimensionality of the problem by considering only the progress variable (in case of the BML model) and the scalar G (in G-equation formulation) to describe the thermochemical state of the problem and ii) used a presumed pdf approach, which is not only less costly computationally but also separates the complex chemistry from fluid dynamics.

In premixed flames, the reaction rate can be closed using the presumed pdf approach as

$$\overline{\dot{\omega}} = \int \dot{\omega}(\zeta)\, p(\zeta)\, \mathrm{d}\zeta, \tag{2.63}$$

where the function $\dot{\omega}(\zeta)$ is obtained using canonical laminar flame calculations having the same thermochemical attributes as that of the turbulent flame. In the above formulation, it is assumed that the flame structure is undisturbed by turbulent eddies. The fluid dynamic stretch effects can be included using (Bradley, 1992)

$$\overline{\dot{\omega}} = \int p(\kappa)\, \mathrm{d}\kappa \int \dot{\omega}(\zeta)\, p(\zeta)\, \mathrm{d}\zeta, \tag{2.64}$$

where statistical independence of ζ and κ has been assumed. Recently, Kolla and Swaminathan (2010*a*) used the scalar dissipation rate to parametrise flamelet stretch effects. This method is described in the following section.

2.5.8 Scalar dissipation rate (SDR) based modelling

In order to understand the physical significance of scalar dissipation rate, it is helpful to look at the transport equation of the progress variable variance, $\widetilde{c''^2}$. These fluctuations represent inhomogeneities and intermittencies (Veynante and Vervisch, 2002). One can obtain a transport equation for the scalar variance as follows: first subtract the Favre-averaged transport equation for the progress

variable [Eq. (2.20)] from its instantaneous equation [Eq. (2.14)] to obtain an equation for c''. Then multiply this equation by $2c''$ and average the result to obtain the following exact transport equation for $\widetilde{c''^2}$ [see for example Veynante and Vervisch (2002)]

$$\frac{\partial \overline{\rho}\widetilde{c''^2}}{\partial t} + \nabla \cdot (\overline{\rho}\widetilde{\boldsymbol{u}}\widetilde{c''^2}) = \underbrace{\nabla \cdot \left(\overline{\rho D_c \nabla c''^2}\right) + 2\overline{c''\nabla \cdot (\rho D_c \nabla \widetilde{c})}}_{\text{molecular diffusion}} - \underbrace{\nabla \cdot (\overline{\rho \boldsymbol{u}'' c''^2})}_{\text{turbulent transport}} - \underbrace{2(\overline{\rho \boldsymbol{u}'' c''}) \cdot \nabla \widetilde{c}}_{\text{production}} + \underbrace{2\overline{\dot{\omega}'' c''}}_{\text{reaction}} - \underbrace{2\overline{\rho D_c (\nabla c'' \cdot \nabla c'')}}_{\text{dissipation}}. \quad (2.65)$$

Note that in the above equation, the 'production term' may take negative values (i.e. act as a sink term) in the case of countergradient flames. The last term in the above equation is unclosed and it is known as the mean scalar dissipation rate $\widetilde{\epsilon}_c$. It can be written as

$$\overline{\rho}\widetilde{\epsilon}_c = \overline{\rho D_c \nabla c'' \cdot \nabla c''}. \quad (2.66)$$

Scalar dissipation rate measures the decay rate of scalar fluctuations by turbulent micromixing. It can be used to determine the mixing rate at the molecular level, since a well-mixed fluid does not have any fluctuations (Cant and Mastorakos, 2008). By taking the average of the instantaneous dissipation rate, N, it can be shown that (Veynante and Vervisch, 2002)

$$\overline{\rho N} = \overline{\rho D_c \nabla c \cdot \nabla c} = \overline{\rho D_c} \nabla \widetilde{c} \cdot \nabla \widetilde{c} + \overline{2\rho D_c \nabla c''} \cdot \nabla \widetilde{c} + \overline{\rho D_c \nabla c'' \cdot \nabla c''}. \quad (2.67)$$

The assumption, $\overline{\rho N} \approx \overline{\rho}\widetilde{\epsilon}_c$, can be made since gradients of the fluctuations are much larger than the gradients of the mean progress variable.

It is the micromixing between burnt products and unburnt reactants that sustains combustion in premixed flames. For example, Eq. (2.65) clearly shows the coupling between turbulent mixing ($\tilde{\epsilon}_c$) and chemical reaction ($\overline{\dot{\omega}'' c''}$). Since turbulent mixing also leads to dissipation of scalar fluctuations, the scalar dissipation rate is an important quantity in turbulent premixed combustion (Libby and Bray, 1980) and appears directly or indirectly in most combustion submodels (Veynante and Vervisch, 2002).

In addition to having unclosed reaction rate terms, $\overline{\dot{\omega}}$ and $\overline{\dot{\omega}''c''}$, the mean scalar dissipation rate, $\tilde{\epsilon}_c$, term is also unclosed. This poses an additional challenge in using Eq. (2.65) to solve premixed combustion problems. It is known that the modelling of $\tilde{\epsilon}_c$ is challenging for premixed flames (Mantel and Borghi, 1994; Mantel and Bilger, 1995; Swaminathan and Bray, 2005). Such a model should include the interaction between turbulence, chemical reaction and molecular diffusion, and the earlier models that only used the turbulence time scale were inadequate in capturing the correct physics (Swaminathan and Bray, 2005).

Mean scalar dissipation rate closure

Swaminathan and Bray (2005) derived the following exact equation for the mean scalar dissipation rate, $\tilde{\epsilon}_c$

$$\overline{\rho}\frac{\partial\widetilde{\epsilon}_c}{\partial t} + \overline{\rho}\widetilde{\boldsymbol{u}}\cdot\nabla\widetilde{\epsilon}_c = \underbrace{\overline{\nabla\cdot(\rho D_c\nabla\epsilon_c)}}_{D_1} - \underbrace{2\overline{\rho {D_c}^2\left[\nabla\left(\nabla c''\right)\right]^2}}_{D_2} + T_1 + T_2 + T_3 + T_4, \tag{2.68}$$

$$T_1 = \underbrace{-\nabla\cdot\overline{(\rho\boldsymbol{u}''\epsilon_c)}}_{T_{11}} - \underbrace{2\overline{\rho D_c\boldsymbol{u}''\cdot\nabla c''}(\nabla(\nabla\widetilde{c}))}_{T_{12}},$$

$$T_2 = 2\overline{\rho\epsilon_c\nabla\cdot\boldsymbol{u}},$$

$$T_3 = \underbrace{-2(\overline{\rho D_c\nabla\boldsymbol{u}''\cdot\nabla c''})\nabla\widetilde{c}}_{T_{31}} - \underbrace{2\overline{\rho D_c\nabla c''\cdot\nabla\boldsymbol{u}''\cdot\nabla c''}}_{T_{32}} - \underbrace{2(\overline{\rho D_c\nabla c''\cdot\nabla c''})\nabla\cdot\widetilde{\boldsymbol{u}}}_{T_{33}},$$

$$T_4 = 2\overline{D_c\nabla c''\cdot\nabla\dot{\omega}''},$$

when the diffusivity D_c has a weak dependence on temperature. The LHS represents unsteady and convective terms. Molecular diffusion and dissipation are denoted by D_1 and D_2 respectively. Turbulent transport of $\tilde{\epsilon}_c$ is denoted by T_1. The dilatation term is denoted by T_2, which was shown to be significant at all Da using an order of magnitude analysis by Swaminathan and Bray (2005). This term was absent in the earlier exact equation derived by Borghi and co-workers (Borghi, 1990; Mantel and Borghi, 1994; Mura and Borghi, 2003), where they used a constant density approximation. Influences of the interaction between turbu-

lence and scalar concentration is denoted by T_3, while the influence of chemical reactions is denoted by T_4.

Details of this transport equation as well as the results obtained from a number of studies using this equation were summarised by Chakraborty et al. (2011). This exact equation, together with necessary DNS data validations, facilitated the derivation of an accurate algebraic model for the mean scalar dissipation rate, $\tilde{\epsilon}_c$, by Kolla et al. (2009). In deriving this model, Kolla et al. (2009) used closure models proposed by Chakraborty et al. (2008) for the leading order terms of Eq. (2.68), when the Damköhler number is large. This model is written as

$$\tilde{\epsilon}_c \simeq \frac{1}{\beta'}\left[(2K_c^* - \tau C_4)\frac{s_L^0}{\delta_L^0} + C_3\frac{\tilde{\varepsilon}}{\tilde{k}}\right]\widetilde{c''^2}, \tag{2.69}$$

Various model parameters are: $\beta' = 6.7$, $C_3 = 1.5\sqrt{\mathrm{Ka}}/(1+\sqrt{\mathrm{Ka}})$ and $C_4 = 1.1/(1+\mathrm{Ka})^{0.4}$. The model constant, K_c^*, depends on the thermochemistry of the mixture, and it is chosen such that its sensitivity to internal flame front structure is small (Kolla et al., 2009). Values of K_c^* for hydrocarbon and hydrogen-air flames at different equivalence ratios have been calculated by Rogerson and Swaminathan (2007). These parameters are specified to satisfy certain physical aspects of turbulence-flame interaction (Kolla et al., 2009; Kolla and Swaminathan, 2011) and cannot be changed arbitrarily. In this work three different reaction rate closures that uses the mean scalar dissipation rate model will be used. These models are given in section 3.2.

3. Numerical setup for spherical flame simulation

One of the objectives of this work, as outlined in section 1.3, is to validate combustion models based on the scalar dissipation rate for spherically propagating flames. These flames are of both fundamental and practical relevance, and can be found in a number of engineering devices as well as in accidental explosions of vapour clouds released into the atmosphere. This chapter discusses the numerical method used to simulate such flames.

In this work, an in-house CFD code that was previously used to study freely propagating planar flames, is modified to study spherically propagating flames. Governing equations written in spherical coordinates are implemented in the code. These spherical equations are given in section 3.1. The algebraic model for $\tilde{\epsilon}_c$ given in Eq. (2.69) is used in this work. A modification to this model is proposed in section 3.2, which includes the mean curvature effects for a spherical flame.

Spherical flames simulated in this work are computed using three different models: strained, unstrained and algebraic flamelet models. These models were explained in section 2.5 and some additional details are discussed here. Both unstrained and strained flamelet models require a flamelet library that will be accessed during the CFD simulations. The generation of these flamelet libraries is described in section 3.3.

Description of the CFD code, including the numerical schemes, initial and boundary conditions are given in section 3.4. The CFD code developed here is used to simulate spherically propagating methane- and hydrogen-air flames, which are presented in Chapters 4 and 5 respectively. Note that the description of the reaction rate models and the flamelet library generation is relevant not only to these spherical flames, but also to other cases simulated in this work.

3.1 Governing equations and modelling

The unsteady RANS (URANS) approach is used to simulate spherical turbulent explosions. These flames are assumed to be spherically symmetric, which results in considerable simplification, since only the radial terms in the governing equations written in (r, θ, ϕ) coordinates need to be retained.

The Favre-averaged, RANS equations given in section 2.2.3 can be written for a spherically symmetric flow field (see Appendix A on how the spherically symmetric radial momentum equation is obtained). Continuity and radial momentum conservation are then given by

$$\frac{\partial \overline{\rho}}{\partial t} + \frac{1}{r^2}\frac{\partial r^2 \overline{\rho}\tilde{u}_r}{\partial r} = 0, \tag{3.1}$$

$$\begin{aligned}\frac{\partial \overline{\rho}\tilde{u}_r}{\partial t} + \frac{1}{r^2}\frac{\partial}{\partial r}\left[r^2\,\overline{\rho}\tilde{u}_r^2\right] = &-\frac{\partial \overline{p}}{\partial r} + \frac{1}{r^2}\frac{\partial}{\partial r}\left[r^2\left(\overline{\tau}_{rr} - \overline{\rho u_r''^2}\right)\right] \\ &- \frac{\left(\overline{\tau}_{\theta\theta} - \overline{\rho u_\theta''^2} + \overline{\tau}_{\phi\phi} - \overline{\rho u_\phi''^2}\right)}{r},\end{aligned} \tag{3.2}$$

where $\overline{\tau}_{rr}, \overline{\tau}_{\theta\theta}$ and $\overline{\tau}_{\phi\phi}$ denote the normal components of the viscous stress tensor in the respective directions. The centrifugal forces per unit volume arising from the Reynolds stresses in θ and ϕ directions are $\overline{\rho u_\theta''^2}/r$ and $\overline{\rho u_\phi''^2}/r$ respectively, which do not vanish even in the spherically symmetric case. Thus, they must be retained as their contributions are significant in the earlier period of flame development (small r).

The progress variable equation [Eq. (2.20)] can be written for high Reynolds number flows as

$$\frac{\partial \overline{\rho}\,\tilde{c}}{\partial t} + \frac{1}{r^2}\frac{\partial}{\partial r}\left(r^2 \overline{\rho}\,\tilde{u}_r \tilde{c}\right) = \frac{1}{r^2}\frac{\partial}{\partial r}\left\{r^2\left[\left(\alpha_c + \frac{\mu_t}{\mathrm{Sc}_c}\right)\frac{\partial \tilde{c}}{\partial r}\right]\right\} + \overline{\dot{\omega}}, \tag{3.3}$$

where $\overline{\dot{\omega}}$ is the mean rate of production of $\tilde{c}$ per unit volume, which is modelled using the flamelet models to be explained in section 3.2. The following transport

equation for the progress variable variance, $\widetilde{c''^2}$

$$\frac{\partial \overline{\rho}\,\widetilde{c''^2}}{\partial t} + \frac{1}{r^2}\frac{\partial}{\partial r}\left(r^2\overline{\rho}\tilde{u}_r\widetilde{c''^2}\right) = \frac{1}{r^2}\frac{\partial}{\partial r}\left\{r^2\left[\left(\alpha_c + \frac{\mu_t}{\mathrm{Sc}_c}\right)\frac{\partial \widetilde{c''^2}}{\partial r}\right]\right\} + 2\frac{\mu_t}{\mathrm{Sc}_c}\frac{\partial \tilde{c}}{\partial r}^2 - 2\overline{\rho}\tilde{\epsilon}_c + 2\overline{\dot{\omega}''c''}, \tag{3.4}$$

is also included in the simulation. The mean scalar dissipation rate, $\tilde{\epsilon}_c$, is closed using the model given in Eq. (2.69). In the next section, a modification to this model is proposed to simulate spherical flames. The mean density is calculated using the equation of state written as $\overline{\rho} = \rho_u/\left(1+\tau\tilde{c}\right)$.

Uncertainties related to turbulence modelling is minimised in these spherical flame simulations by using the $\tilde{k}$-$\tilde{\varepsilon}$ equations (Jones and Launder, 1972) given by

$$\frac{\partial \overline{\rho}\,\tilde{k}}{\partial t} + \frac{1}{r^2}\frac{\partial}{\partial r}\left[r^2\,\overline{\rho}\,\tilde{u}_r\tilde{k}\right] = \frac{1}{r^2}\frac{\partial}{\partial r}\left\{r^2\left[\left(\mu + \frac{\mu_t}{\mathrm{Sc}_k}\right)\frac{\partial \tilde{k}}{\partial r}\right]\right\} - \overline{\rho u_r''^2}\left(\frac{\partial \tilde{u}_r}{\partial r}\right) - \left(\overline{\rho u_\theta''^2} + \overline{\rho u_\phi''^2}\right)\frac{\tilde{u}_r}{r} - \overline{u_r''}\frac{\partial \overline{p}}{\partial r} + \overline{p'\frac{1}{r^2}\frac{\partial\left(r^2u_r''\right)}{\partial r}} - \overline{\rho}\tilde{\varepsilon}, \tag{3.5}$$

$$\frac{\partial \overline{\rho}\,\tilde{\varepsilon}}{\partial t} + \frac{1}{r^2}\frac{\partial}{\partial r}\left[r^2(\overline{\rho}\,\tilde{u}_r\tilde{\varepsilon})\right] = \frac{1}{r^2}\frac{\partial}{\partial r}\left\{r^2\left[\left(\mu + \frac{\mu_t}{\mathrm{Sc}_\varepsilon}\right)\frac{\partial \tilde{\varepsilon}}{\partial r}\right]\right\} - C_{\varepsilon 1}\frac{\tilde{\varepsilon}}{\tilde{k}}\left[\overline{\rho u_r''^2}\left(\frac{\partial \tilde{u}_r}{\partial r}\right) + \left(\overline{\rho u_\theta''^2} + \overline{\rho u_\phi''^2}\right)\frac{\tilde{u}_r}{r} - \overline{u_r''}\frac{\partial \overline{p}}{\partial r}\right] - C_{\varepsilon 2}\overline{\rho}\frac{\tilde{\varepsilon}^2}{\tilde{k}}, \tag{3.6}$$

where μ and μ_t represent the molecular and eddy viscosities respectively. The model constants are $C_{\epsilon 1} = 1.44$, $C_{\epsilon 2} = 1.92$ and $\mathrm{Sc}_k = \mathrm{Sc}_\epsilon = 1$. The compressible form of these equations are written above (Wilcox, 1993), where the second and third terms appearing on the RHS of Eq. (3.5) represent the production of $\tilde{k}$ by the gradients of mean velocity. The next two terms respectively represent the effects of mean pressure gradient and pressure-dilatation. The dissipation of $\tilde{k}$ is represented by the last term of Eq. (3.5). Reynolds stresses are modelled using

the eddy-viscosity hypothesis as

$$\overline{\rho u_r''^2} = -2\mu_t \frac{\partial \tilde{u}_r}{\partial r} + \frac{2}{3}\mu_t \left[\frac{1}{r^2}\frac{\partial}{\partial r}\left(r^2 \tilde{u}_r\right)\right] + \frac{2}{3}\overline{\rho}\tilde{k}, \tag{3.7}$$

$$\overline{\rho u_\theta''^2} = \overline{\rho u_\phi''^2} = -2\mu_t \frac{\tilde{u}_r}{r} + \frac{2}{3}\mu_t \left[\frac{1}{r^2}\frac{\partial}{\partial r}\left(r^2 \tilde{u}_r\right)\right] + \frac{2}{3}\overline{\rho}\tilde{k}. \tag{3.8}$$

If one uses an anisotropic turbulence model then $\overline{\rho u_\theta''^2}$ and $\overline{\rho u_\phi''^2}$ will be different. The pressure work and pressure-dilatation terms are often neglected or combined with the diffusive term in reacting flow simulations, while these are modelled explicitly in this study. The pressure-dilatation is modelled as $\overline{p'(1/r^2)\left[\partial(r^2 u_r'')/\partial r\right]} = 1/2\tilde{c}\left(\tau s_L^0\right)^2 \overline{\dot{\omega}}$ (Zhang and Rutland, 1995). The average of u'' in the pressure work term is modelled (Libby, 1985) as $\overline{\boldsymbol{u}''} = \widetilde{\boldsymbol{u}''c''}\tau/\left(1+\tau\tilde{c}\right)$, where the turbulent scalar flux $\widetilde{\boldsymbol{u}''c''}$ is modelled using the classical gradient transport. It is well known that this scalar flux can be counter-gradient in premixed flames, which can be included in simulations using second order closures. However, the gradient model is used in this work for the sake of simplicity and its validity can be evaluated from the experimental comparisons to be shown in Chapters 4 and 5. Although it is ideal to include the pressure-dilatation effect in both $\tilde{k}$ and $\tilde{\varepsilon}$ equations it is included only in $\tilde{k}$ equation following many previous studies (Bray et al., 1985; Jones, 1994; Kolla and Swaminathan, 2010*a*). Also, the effects of these terms may be small for open flames (Swaminathan and Bray, 2011).

3.2 Reaction rate closures

The mean reaction rate, $\overline{\dot{\omega}}$, is modelled using the scalar dissipation rate based approach described in section 2.5.8. Three different reaction rate closures that uses the mean scalar dissipation rate modelling approach are described in this section.

First is the algebraic model of Bray (1979), which was given in Eq. (2.48). For this model, the source term in the progress variable variance, $\widetilde{c''^2}$, equation is given as: $\overline{\dot{\omega}''c''} = (C_m - \tilde{c})\overline{\dot{\omega}}$. This model does not involve complex chemical kinetics and, therefore, finite rate chemistry effects cannot be taken into account.

Note that the mean scalar dissipation rate model of Kolla et al. (2009) [given in Eq. (2.69)] is used in this study because it is simple and satisfies the realisability condition ($\tilde{\epsilon}_c \geq 0$).

The second model is an unstrained flamelet model, where the reaction rate closure is given by Eq. (2.63). The pdf, $p(\zeta)$, in this equation is usually presumed to be a β-function, which requires both $\tilde{c}$ and $\widetilde{c''^2}$. Detailed chemistry can be used to obtain, $\dot{\omega}(\zeta)$ from laminar flame calculations. This model does not involve $\tilde{\epsilon}_c$ explicitly, however, in RANS calculations involving the use of this model, one also need to solve the variance equation, which includes $\tilde{\epsilon}_c$ as a source term. For this model, the unclosed source term $\overline{\dot{\omega}''c''}$ in the $\widetilde{c''^2}$ is given by

$$\overline{\dot{\omega}''c''} = \int_0^1 \zeta \dot{\omega}_0(\zeta) p(\zeta)\, \mathrm{d}\zeta - \overline{\dot{\omega}}\tilde{c}. \tag{3.9}$$

For given values of $\tilde{c}$ and $\widetilde{c''^2}$ one can build a look-up table or flamelet library for $\overline{\dot{\omega}}$ and other required quantities using laminar flame solutions. This look-up table is accessed during turbulent flame simulations to obtain the source terms required for Eqs. (2.20) and (2.65).

The third model is a strained flamelet model proposed by Kolla and Swaminathan (2010*a*). In this model, the flamelets are parametrised using the scalar dissipation rate. This model is described briefly here and elaborate detail can be found in Kolla and Swaminathan (2010*a*). The flamelets, which are freely propagating laminar flames and those established in opposing flows of reactant and product, are parametrised using $\tilde{\epsilon}_c$. The mean reaction rate is given by

$$\overline{\dot{\omega}} = \int_0^1 \left[\int_{N_1}^{N_2} \dot{\omega}(\zeta, \psi)\, p(\psi|\zeta)\, \mathrm{d}\psi \right] p(\zeta)\, \mathrm{d}\zeta, \tag{3.10}$$

where ζ and ψ are the sample space variables for c and the instantaneous scalar dissipation rate, N_c, respectively. The reaction rate of flamelets, $\dot{\omega}(\zeta, \psi)$, and the integration limits N_1 and N_2 are obtained using results of fully burning and almost extinguished flamelets. As with the unstrained flamelet model, complex chemistry can be used in the look-up table generation.

The presumed shapes for the pdfs, $p(\zeta)$ and $p(\psi|\zeta)$, are specified using the β and lognormal functions respectively. Lognormal function for $p(\psi|\zeta)$ requires the

conditional mean and variance of the natural logarithm of the conditional scalar dissipation rate, i.e. $\ln(N_c|\zeta)$. The log-normal pdf is given by

$$p(\psi|\zeta) = \frac{1}{(\psi|\zeta)\,\sigma\sqrt{2\pi}} \exp\left\{ \frac{1}{2\sigma^2} \left[\ln(\psi|\zeta) - \mu^2 \right] \right\} \tag{3.11}$$

where the mean and variance of $\ln(N_c|\zeta)$ are denoted by μ and σ^2 respectively. These quantities are related to the conditional mean, $\langle N_c|c=\zeta\rangle$ and conditional variance, G_N^2, of the scalar dissipation rate via $\langle N_c|\zeta\rangle = \exp(\mu + 0.5\sigma^2)$ and $G_N^2 = \langle N_c|\zeta\rangle^2 (\exp\sigma^2 - 1)$. These dissipation related quantities are obtained following the method described by Kolla and Swaminathan (2010*a*), where they used the assumption that effects of strain rate on the progress variable gradient are primarily felt in the inner reaction zone (denoted by ζ^*). This enables one to approximate the scalar dissipation rate for a given strain rate, a, as: $N_c(\zeta, a)\, f(\zeta)$. Kolla and Swaminathan (2010*a*) showed that $f(\zeta)$ curves for various strain rates collapse well in the region of the flame where chemical reactions dominate. Using these approximations, they obtained the following expression for the conditional mean scalar dissipation rate

$$\langle N_c|\zeta\rangle \approx \frac{\tilde{\epsilon}_c f(\zeta)}{\int_0^1 f(\zeta)\widetilde{P}\,\mathrm{d}\zeta}. \tag{3.12}$$

The source term, $\overline{\dot{\omega}''c''}$, using the strained flamelet model is given by

$$\overline{\dot{\omega}''c''} = \int_0^1 \zeta\langle\dot{\omega}|\zeta\rangle p(\zeta)\,\mathrm{d}\zeta - \overline{\dot{\omega}}\tilde{c}. \tag{3.13}$$

where the conditional reaction rate, $\langle\dot{\omega}|\zeta\rangle$ is given by the integral in the square brackets of Eq. (3.10). The look-up table built for this model is three-dimensional, where the source terms are a function of $\tilde{c}$, $\widetilde{c''^2}$ and $\tilde{\epsilon}_c$.

All three models require an algebraic closure for the mean scalar dissipation rate, $\tilde{\epsilon}_c$. The model proposed by Kolla et al. (2009) [Eq. (2.69)] includes the effects of curvature induced stretch on flamelets and various important effects of turbulence and its interaction with chemical reaction and molecular diffusion. The parameter β' specifically represent the flamelet curvature induced effects.

However, a spherical flame brush also experiences stretch due to its mean curvature, which is absent in a planar case. This particular effect is not included in Eq. (2.69), and thus an additional correction can be included based on the analysis of Chakraborty et al. (2010). This revised model written as

$$\tilde{\epsilon}_c \simeq \frac{1}{\beta'}\left\{\left[2K_c^* - \tau C_4\left(1 - \frac{D_u}{s_L^0}\nabla\cdot\boldsymbol{n}\right)\right]\frac{s_L^0}{\delta_L^0} + C_3\frac{\tilde{\varepsilon}}{\tilde{k}}\right\}\widetilde{c''^2}, \tag{3.14}$$

is obtained through a leading order balance analysis, similar to Kolla et al. (2009), using the models proposed by Chakraborty et al. (2010). The normal vector in Eq. (3.14) is defined as $\boldsymbol{n} = -\nabla\tilde{c}/|\nabla\tilde{c}|$. The major difference between the models in Eqs. (2.69) and (3.14) is the contribution of flame brush curvature $\nabla\cdot\boldsymbol{n}$. Note that the revised model in Eq. (3.14) is *unconditionally realisable* for explosion but the realisability condition imposes a minimum radius for implosion. Both models in Eqs. (2.69) and (3.14) are used in this study to understand the extent of influence of $\nabla\cdot\boldsymbol{n}$.

Both the unstrained and the strained flamelet models require flamelet libraries, which are generated from laminar flame calculations. The generation of these libraries is described in the next section.

3.3 Flamelet library generation

Details of flamelet library generation for both strained and unstrained flamelets are described in this section. Note that a similar procedure is used to generate all the flamelet libraries used in this work.

3.3.1 Unstrained flamelet model

Chemistry can be separated from fluid mechanics in flamelet models and the flamelet libraries are generated *a priori*. This makes it computationally economical to use detailed chemistry in turbulent combustion simulations. Before proceeding with the flamelet library generation it is important to ensure that the chemical mechanism can predict laminar flame speeds found in the literature.

For the unstrained flamelet model given in Eq. (2.63), one needs to calculate

freely propagating laminar premixed flames for a particular fuel-air mixture at a given equivalence ratio and thermodynamic conditions. These laminar flames are calculated using CHEMKIN's PREMIX code (Kee et al., 1985), which gives the instantaneous reaction rate, $\dot{\omega}(\zeta)$, as a function of the progress variable, c. Since the unstrained flamelet library is two-dimensional, a bilinear interpolation with $\tilde{c}$ and $\widetilde{c''^2}$ is used during the CFD simulations to obtain source terms, $\overline{\dot{\omega}}$ and $\overline{\dot{\omega}''c''}$.

3.3.2 Strained flamelet model

As described in section 3.2, the strained flamelet model requires the calculation of both freely propagating and reactant-to-product (RtP) counterflow laminar flames. These counterflow flames are calculated using CHEMKIN's OPPDIF code (Lutz et al., 1997).

Figure 3.1(a) shows the normalised reaction rate of the progress variable, $\dot{\omega}^+ = \dot{\omega}\,(\delta_L^0/\rho_u s_L^0)$, for various normalised strain rates, a^+, plotted against the normalised distance from the stagnation plane. The plot shown in this figure

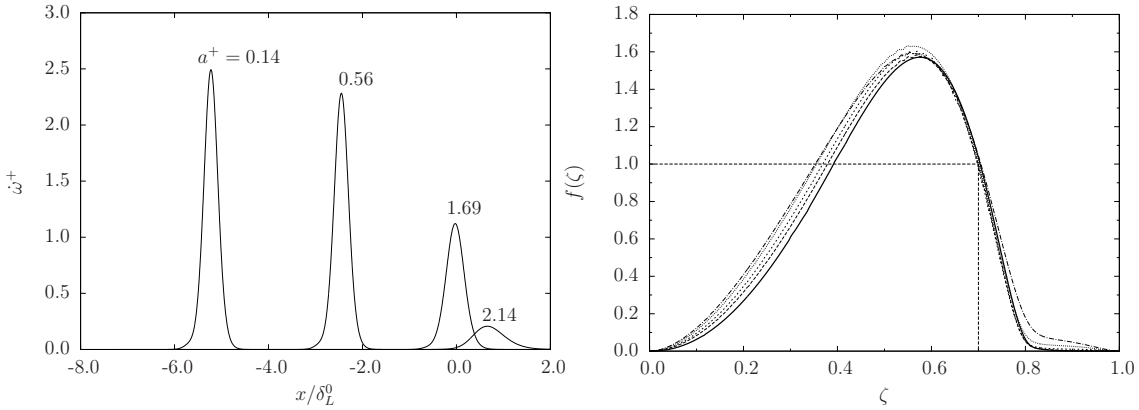

Figure 3.1: Reactant-to-product, stoichiometric methane-air flame: (a) Reaction rate of the progress variable, $\dot{\omega}^+$ for various strain rates, a^+, plotted against the distance from the stagnation plane. All quantities in this figure are normalised; (b) curves of $f(\zeta)$ up to the point the reaction zone reaches the stagnation plane (unstrained, freely propagating flame is shown as a solid line).

is for a stoichiometric methane-air flame. The values of the unburnt mixture

density, ρ_u, laminar flame thermal thickness, δ_L^0, and the unstrained laminar flame speed, s_L^0, for this mixture are obtained from freely propagating laminar flame calculations.

In this figure, the location at which $x = 0$ is defined as the stagnation plane, where the region $x < 0$ corresponds to reactants and $x > 0$ corresponds to products. This figure shows that increasing the strain rate reduces the reaction rate and moves the flame towards the product stream. Also, the flame reaches the stagnation plane at a strain rate of roughly 1602 1/s. Further increasing the strain rate reduces the reaction until extinction takes place.

Figure 3.1(b) shows curves for $f(\zeta) \approx N_c(\zeta)/N_c(\zeta^*)$ for this flame at various rates of strain (solid line in this figure is for the unstrained, freely propagating flame). Here the inner reaction zone, $\zeta^* \approx 0.7$, and a good collapse of these curves is obtained in the region where the chemical reactions dominate. As already described in section 3.2, this collapse in $f(\zeta)$ helps to simplify the calculation of the conditional mean scalar dissipation rate given in Eq. (3.12).

In order to calculate the mean reaction rate using the strained flamelet formulation, one needs to understand the response of the reaction rate to strain through changes in the scalar dissipation rate. Figures 3.2(a) and 3.2(b) show the plots of $\dot{\omega}^+$ vs. N_c^+ for methane-air flames with $\Phi = 1.0$ and $\Phi = 1.1$ respectively. Note that the superscript + is to denote a quantity that is normalised using laminar flame values (i.e. laminar flame speed and thickness). Each symbol on this figure corresponds to a particular laminar flame calculation, with the maximum reaction rate value given by the unstrained, freely propagating flame. It is interesting to note that even though these flames have Lewis numbers close to unity, the response of the reaction rate to strain is considerably different. For the stoichiometric case the variation of $\dot{\omega}^+$ vs. N_c^+ is single-valued whereas for $\Phi = 1.1$ it is multi-valued. Kolla and Swaminathan (2010*a*) described how the integral given in Eq. (3.10) could be evaluated for a multi-valued function, such as the one shown in Figure 3.2(b). This multi-valued behaviour of $\dot{\omega}^+$ with N_c^+ is an indication that there exist a higher and a lower burning rate in the domain $\psi \in |N_1, N_2|$, here the integration limits, N_1 and N_2, corresponds to unstrained flame value and the extinction limit respectively, while the intermediate value is given by N_0. Unlike the unstrained flamelet model, the look-up table for this

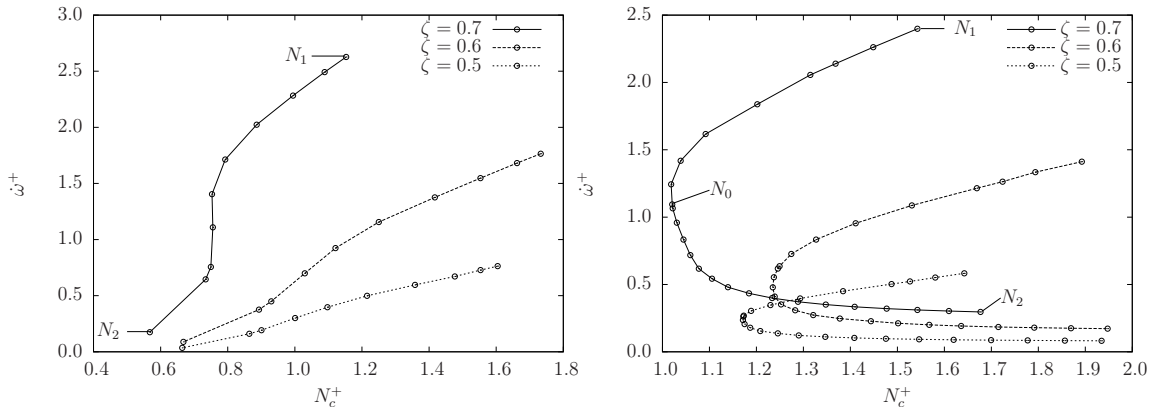

Figure 3.2: Curves of $\dot{\omega}^+$ vs. N_c^+ conditioned on the progress variable, ζ for two cases: (a) stoichiometric methane-air flame and (b) methane-air flame with $\Phi = 1.1$.

model is three-dimensional involving $\tilde{c}$ and $\widetilde{c''^2}$ and $\tilde{\epsilon}_c$. Therefore a tri-linear interpolation is used during the CFD simulations.

3.4 Computational approach

The governing equations given in section 3.1 can be written in the following standard form for a transported scalar property, Ψ

$$\frac{\partial}{\partial t}\left(\overline{\rho}\Psi\right) + \frac{1}{r^2}\frac{\partial}{\partial r}\left(r^2\overline{\rho}\tilde{u}_r\Psi\right) - \frac{1}{r^2}\frac{\partial}{\partial r}\left(\Gamma_\Psi\frac{\partial\Psi}{\partial r}\right) = S_\Psi. \tag{3.15}$$

The values of Ψ, Γ_Φ and S_Φ for the modelled governing equations are given in Table 3.1 (refer to Appendix A to see how the radial momentum equation is cast in the form given in this table).

These equations are discretised using the finite volume method (FVM). Power law scheme of Patankar (1980) is used for spatial discretisation and the implicit backward Euler method is used for time-stepping. The pressure-velocity coupling is through the SIMPLER approach of Patankar (1980) and the set of discrete algebraic equations are solved iteratively.

Table 3.1: Diffusion coefficients and source terms in the generalised conservation law for all the governing equations

Ψ	Γ_Ψ	S_Ψ
1	0	0
$\tilde{u}_r$	$\frac{4}{3}(\mu+\mu_t)$	$\frac{\partial \overline{p}}{\partial r}-\frac{\partial}{\partial r}\left(\frac{2}{3}\overline{\rho}\tilde{k}\right)-\frac{1}{r}\left[\frac{\partial \Gamma_\Psi}{\partial r}+2\frac{\Gamma_\Psi}{r}\right]\tilde{u}_r$
$\tilde{k}$	$\mu+\frac{\mu_t}{\mathrm{Sc}_k}$	$-\frac{2}{3}\left(\frac{\partial \tilde{u}_r}{\partial r}+2\frac{u_r}{r}\right)\overline{\rho}\tilde{k}+\frac{4}{3}\mu_t\left(\frac{\partial \tilde{u}_r}{\partial r}-\frac{\tilde{u}_r}{r}\right)^2-\overline{\rho}\tilde{\varepsilon}+\frac{\mu_t}{\overline{\rho}\mathrm{Sc}_c}\frac{\partial \tilde{c}}{\partial r}\left(\frac{\tau}{1+\tau\tilde{c}}\right)\frac{\partial \overline{p}}{\partial r}+\frac{1}{2}\tilde{c}(\tau s_L^0)^2\overline{\dot{\omega}}$
$\tilde{\varepsilon}$	$\mu+\frac{\mu_t}{\mathrm{Sc}_\varepsilon}$	$-C_{\varepsilon 1}\frac{\tilde{\varepsilon}}{\tilde{k}}\left[\frac{2}{3}\left(\frac{\partial \tilde{u}_r}{\partial r}+2\frac{u_r}{r}\right)\overline{\rho}\tilde{k}-\frac{4}{3}\mu_t\left(\frac{\partial \tilde{u}_r}{\partial r}-\frac{\tilde{u}_r}{r}\right)^2-\frac{\mu_t}{\overline{\rho}\mathrm{Sc}_c}\frac{\partial \tilde{c}}{\partial r}\left(\frac{\tau}{1+\tau\tilde{c}}\right)\frac{\partial \overline{p}}{\partial r}\right]-C_{\varepsilon 2}\overline{\rho}\frac{\tilde{\varepsilon}^2}{\tilde{k}}$
$\tilde{c}$	$\alpha_c+\frac{\mu_t}{\mathrm{Sc}_c}$	$\overline{\dot{\omega}}$
$\widetilde{c''^2}$	$\alpha_c+\frac{\mu_t}{\mathrm{Sc}_c}$	$2\frac{\mu_t}{\mathrm{Sc}_c}\left(\frac{\partial \tilde{c}}{\partial r}\right)^2-2\overline{\rho}\epsilon_c+2\overline{\dot{\omega}''c''}$

3.4.1 Initial and boundary conditions

Length of the computational domain depend on the ratio of turbulence integral length scale, Λ, to the Zeldovich thickness, δ, so that the simulated flames remain within the domain for the simulation period. The number of grid points are chosen such that there are at least 10 points inside $\min(\Lambda, \delta_t)$ for a uniform grid spacing. The turbulent flame brush thickness is given by $\delta_t \equiv 1/|\partial\tilde{c}/\partial r|_{\max}$. The size of time-step is chosen to be 0.1 μs, which ensures the resolution of reaction, diffusion and convection time scales and satisfies the numerical stability conditions for the chosen grid, turbulence and thermochemical conditions.

The initial spatial variation of $\tilde{c}$ having 0 in the unburnt and 1 in the burnt mixtures is chosen after few tests to minimise the initial transients for the given turbulence and thermochemical conditions. This saves computational time required to attain a "steady propagation" state. The initial $\tilde{u}$, $\overline{\rho}$ and $\overline{p}$ are specified to be consistent with the initial $\tilde{c}$ variation. It is straightforward to specify the boundary conditions for the planar flames as has been done in many earlier studies (Corvellec et al., 1999, 2000; Swaminathan and Bray, 2005; Kolla and Swaminathan, 2010*a*). Assuming that the flame propagates radially outward the

following boundary conditions are obtained at $r = 0$:

$$\tilde{u}_r(0,t) = \frac{\partial \tilde{c}}{\partial r}(0,t) = \frac{\partial \widetilde{c''^2}}{\partial r}(0,t) = \frac{\partial \tilde{k}}{\partial r}(0,t) = \frac{\partial \tilde{\varepsilon}}{\partial r}(0,t) = 0. \tag{3.16}$$

Similarly, the boundary conditions applied at $r = R$ (at the end of the domain) are:

$$\frac{\partial \tilde{u}_r}{\partial r}(R,t) = \frac{\partial \tilde{k}}{\partial r}(R,t) = \frac{\partial \tilde{\varepsilon}}{\partial r}(R,t) = 0, \quad \tilde{c}(R,t) = \widetilde{c''^2}(R,t) = 0, \quad \overline{p}(R,t) = p_\infty. \tag{3.17}$$

The values of turbulent kinetic energy, $\tilde{k}$, and its dissipation rate, $\tilde{\varepsilon}$, obtained using the chosen value of u' and Λ are used to specify their initial conditions. As noted in the beginning of this chapter, governing equations written in spherical coordinates are implemented in an existing in-house CFD code. Before proceeding with turbulent combustion simulations, it is necessary to validate this code for simple, non-reacting flow cases; this is discussed in Appendix B.

4. Spherical methane-air flames

Simulation of statistically spherical, methane-air flames using the scalar dissipation rate based modelling approach is presented in this chapter. The predictive ability of the unstrained and strained flamelet models described in section 3.2 is assessed by comparing with experimental data. In addition, a simple algebraic closure for the mean reaction rate is also used for comparison. Simulations of spherical and planar flames at various turbulence intensities are used to obtain the effect of geometry and turbulence on flame propagation.

4.1 Introduction

Expanding statistically spherical flame in turbulent environment is a canonically important configuration and its investigation helps us to enhance our understanding of combustion in practical devices such as the spark ignited IC engine, modern stratified charge engines and accidental explosions of fuel vapour cloud. Although it is a classical problem our current understanding is not fully satisfactory and complete.

When a combustible mixture cloud is ignited at the centre, a laminar flame kernel is initiated and it develops into a turbulent spherical flame. During this evolution, the flame front is stretched due to its time varying curvature and flow straining acting on it. In addition to these effects on the flame front, the flame brush experiences stretch due to its curvature in this geometry. The effects of stretch on laminar flame speed was explained in section 2.3.3.

Practical combustion systems involve turbulence invariably and hence turbulent spherical flames have been studied using various experimental configurations such as fan-stirred bombs involving stationary turbulence (Andrews et al., 1975; Abdel-Gayed et al., 1984; Bradley et al., 1994; Lawes et al., 2012), bombs with decaying grid turbulence (Checkel and Thomas, 1994) and wind tunnels with grid turbulence (Hainsworth, 1985; Renou et al., 2002) to address the influence of turbulence on spherical flame propagation. Beretta et al. (1983) and Hainsworth (1985) have shown that the turbulent spherical flames initially expand as a lam-

inar flame and then it is exposed gradually to a wide range of length and time scales of turbulence, resulting in flame wrinkling thereby leading to an increase in the burning velocity that is larger than the laminar value (Abdel-Gayed et al., 1987). Additional flame wrinkling can arise in thermo-diffusively unstable flames (of reactant mixtures with negative Markstein number). The flame wrinkling was shown to increase with pressure and for mixtures with negative Markstein numbers (Haq et al., 2002). The tendency to greater flame wrinkling, resulting in faster flame propagation and high flame front curvature for mixtures with low Lewis number (thermo-diffusively unstable mixtures), is also known (Renou et al., 2000).

As a spherical flame brush expands its thickness increases, with significant amount of unburnt gas inside the flame brush (Beretta et al., 1983; Abdel-Gayed et al., 1988). This poses a challenge to define the turbulent burning velocity since its definition relies on the correct choice of an associated flame radius. One way to define this radius is to equate the volume of unburnt gas inside the flame brush to that of burnt gas outside the flame brush (Bradley et al., 2003). The mass burning velocity defined using this radius is equal to the velocity of turbulent entrainment of unburnt gas into the flame brush. The flame propagation model using this entrainment concept has been developed in several past studies (Blizard and Keck, 1974; Tabaczynski et al., 1980; Groff, 1987; Bradley et al., 1994). Alternatively, flame area enhancement due to turbulence has also been considered using a vortex tube model (Ashurst et al., 1994) and an exponential growth of flame surface area (Ashurst, 1995) to study expanding spherical flames. These studies treated the flame surface to be a passive surface which is not fully satisfactory. An analogy to the laminar flame theory has also been used to study turbulent spherical flame growth rate involving a turbulent Markstein number (Lipatnikov and Chomiak, 2004). These studies have helped to develop some understanding of spherical flame propagation within the scope defined by the assumptions used in their development.

The three numerical paradigms described in section 2.2 have been used to simulate spherical flames. DNS studies were initially aimed to address ignition related issues (Baum and Poinsot, 1995; Poinsot et al., 1995) using a single irreversible reaction in two-dimensional turbulence. Some of these limitations were

relaxed in later DNS studies on spherical flames (Kaminski et al., 2000; Jenkins and Cant, 2002; Jenkins et al., 2006; Klein et al., 2006, 2008; Albin and D'Angelo, 2012; Thévenin et al., 2002; Thévenin, 2005; van Oijen et al., 2005) and these studies predominantly addressed flame surface density related modelling issues.

LES has recently been used to study ignition and propagation of turbulent spherical flames (Nwagwe et al., 2000; Tabor and Weller, 2004; Fureby, 2005; Colin and Truffin, 2011; Lecocq et al., 2011). Combustion models based on sub-grid scale wrinkling factor (Nwagwe et al., 2000; Tabor and Weller, 2004; Fureby, 2005) and flame surface density (FSD) transport equation (Colin and Truffin, 2011) have been used in conjunction with simplified chemistry in the past to compute spherical flames of the Leeds bomb experiments. These studies showed a good comparison with experimental data. Recently, a combustion modelling approach combining the FSD and presumed pdf concepts has been used (Lecocq et al., 2011) to calculate the spherical flame propagation in weak turbulence (Renou et al., 2000) showing a good comparison.

RANS calculations of spherical turbulent flames of Hainsworth (1985) were done by Schmid et al. (1998) using a turbulent flame speed closure. A similar approach was also used by Lipatnikov and Chomiak (2000) to study turbulent spherical flames in various configurations. A transported joint velocity-scalar pdf approach was used by Pope and Cheng (1986) to compute the spherical flames of Hainsworth (1985) and showed a very good agreement with the measurements.

In this work, the RANS methodology is used to study the propagation of turbulent premixed spherical and planar flames. Reaction rate closure is provided by the models described in section 3.2, which are based on the scalar dissipation rate of a progress variable. The progress variable is calculated using temperature, given by Eq. (2.12). The main objectives of this work are:

1. To assess the predictive ability of the various scalar dissipation rate based models described in section 3.2; secondly,

2. To contrast flame propagation mechanisms in spherical and planar cases and to elucidate the underlying physics.

Numerical method, including the combustion models have been described in Chapter 3. The detailed chemical mechanism, GRI-Mech 3.0 (Smith et al.,

accessed 10th November 2013), is used for combustion kinetics of methane-air mixture. This chapter is organised as follows: the experimental test case for validation and various computational cases considered are described in section 4.2. The simulation results are presented and discussed in section 4.3. The main conclusions from this study are summarised in the last section.

4.2 Test Flames

The numerical method described in Chapter 3 is used to study the influence of turbulence and thermochemical conditions on the evolution of expanding spherical flames. Simulation results are also used to elucidate the difference in the propagation of planar and spherical flames. Before discussing the conditions of the flames considered here, an experimental case used to validate the numerical models is described briefly.

4.2.1 Validation case

Spherical flames established in wind tunnel turbulence by Hainsworth (1985) are considered for model validation purpose. This wind tunnel turbulence generated using perforated plates was homogeneous and isotropic, and the methane-air mixture having equivalence ratios of $\Phi = 1.1$ and 0.8 were experimentally investigated. For reasons to be discussed in section 4.3.1, $\Phi = 1.1$ mixture is considered for this study and its thermochemical characteristics along with the experimental conditions at ignition are given in Table 4.1. The flame was ignited using a spark downstream of the perforated plate and it was convected downstream by the mean flow as it evolves in an approximately spherical shape. Temporal changes of position and radius of this flame were recorded using high-speed schlieren movies and it has been suggested that this flame is representative of combustion in spark-ignition engines (Pope, 1987). This flame was also considered in earlier computational studies (Pope and Cheng, 1986; Schmid et al., 1998; Lipatnikov and Chomiak, 2000).

Table 4.1: Experimental conditions for $\Phi = 1.1$ flame of Hainsworth (1985)

Parameter	Value
s_L^0	0.43 m/s
δ_L^0	0.0408 cm
δ	0.00565 cm
$r_{f,0}$	0.15 cm
τ	5.25
u'	1.93 m/s
Λ	0.838 cm
p_0	0.1 MPa
T_0	298 K

4.2.2 Flames for further analysis

Spherical flames propagating outwardly in nearly homogeneous isotropic turbulence field in an unconfined space are considered. Boundary conditions discussed earlier in section 3.4 describe this problem. The influences of combustion on turbulence are also included in the simulation by solving the $\tilde{k}$-$\tilde{\varepsilon}$ equation. A stoichiometric methane-air mixture at 298 K and atmospheric pressure is considered for these flames. Since this mixture has unity Lewis number, the influence of turbulence on the flame propagation can be studied without the added complexity of differential diffusion, which could amplify the stretch-induced effects. Furthermore, this mixture was considered in an earlier study addressing the turbulence effects on the propagation of statistically planar flames (Kolla and Swaminathan, 2010*a*). Thus, the behaviour of spherical flames can be compared directly to planar flames to understand the geometry effects. The thermochemical characteristics of this mixture are, $s_L^0 = 0.4$ m/s, $\delta_L^0 = 0.41$ mm, $\tau = 6.48$ and $\delta = 0.047$ mm.

The turbulent combustion conditions of 8 flames simulated in this study are shown in Figure 4.1. Two different values for the stretch factor, as defined by Abdel-Gayed et al. (1987), $K = 0.157\,(u'/s_L^0)^2\,\mathrm{Re}_t^{-0.5} = 0.157$ and 1 are considered. The turbulence Reynolds number was given earlier in Eq. (2.38). The flames with the smaller stretch value have the Karlovitz number, $\mathrm{Ka} = (u'/s_L^0)^2\,\mathrm{Re}_t^{-0.5}$, of unity and they are located at the upper limit of the corrugated flamelets regime.

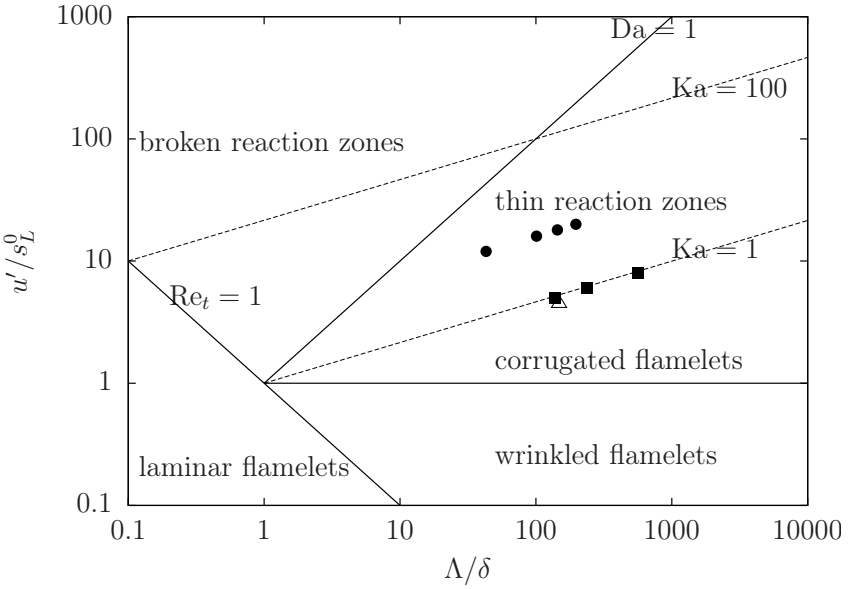

Figure 4.1: Regime diagram of turbulent premixed combustion (Peters, 1999) with the flame conditions considered for this study. The filled symbols correspond to two flame stretch parameters: $K = 0.15$ (•) and $K = 1.0$ (■) and the open triangle (△) is for the experimental case of Hainsworth (1985).

The other case with larger K value is in the thin reaction zones regime as shown in Figure 4.1. These particular values for K are chosen so that the combustion conditions remain the same for the current spherical and planar flames of Kolla and Swaminathan (2010*a*). For the three flames with $K = 0.15$, the values of u'/s_L^0 are 5, 6 and 8, and these values are 12, 16, 18, and 20 for the other cases with $K = 1$. It is also to be noted that the experimental flame of Hainsworth (1985) is in the corrugated flamelets regime for the conditions noted in Table 4.1.

4.3 Results

Computational results of spherically expanding flames under a wide range of turbulence conditions are analysed in this section. Validation of the computational models are discussed first. Then, the influence of turbulence on the propagation of spherical flames are explored using the seven test flames and they are compared with corresponding planar flames to understand the geometry effects.

4.3.1 Model validation

Figure 4.2(a) shows the temporal variation of the flame brush radius measured using high speed schlieren techniques for $\Phi = 1.1$ mixture in two sets of experiments (Hainsworth, 1985). Since schlieren images show the burnt side and mark the regions with strong density gradients, the flame radius reported in the experiment is taken to be the leading edge of the flame brush (Bradley et al., 2000, 2011). For comparison purposes, the location at which $\tilde{c} = 0.05$, is taken to be the leading edge in the simulated flames. As one expects, this radius grows with time as in Figure 4.2(a), where radius is normalised using its initial value, $r_{f,0}$ in Table 4.1, and time is normalised using the laminar flame time or chemical time, $t_c = \delta_L^0/s_L^0$, (see Table 4.1). The bottom two curves, marked for laminar flames, represent the evolution of the initial flame kernel if it evolves as a laminar spherical flame. This laminar evolution can be computed simply by considering mass conservation, $\mathrm{d}\, m_b/\mathrm{d}t = \rho_u\, s_L\, A$, for the burnt gas mass, m_b, inside the kernel having a surface area of A. This simplifies to $\mathrm{d}r_f/\mathrm{d}t = (\rho_u/\rho_b)s_L$ for a spherical kernel. If one takes $s_L = s_L^0$, ignoring stretch effects on the laminar flame propagation, then r_f grows linearly with t and this line passes through the experimental data for $t^+ \leq 2$. This suggests that the initial evolution is laminar and it may be uninfluenced by the stretch effects induced by flow straining and curvature. This is supported by the result shown for stretched laminar flame in Figure 4.2(a) (the bottom-most curve). Stretch effects are included in the above mass conservation equation by using Eq. (2.37), where stretch rate, $\kappa = 2(\mathrm{d}\ln r_f/\mathrm{d}t)$, and $\mathcal{L}$ is the Markstein length scale for the chosen mixture. This length scale is computed as 0.89 mm using Eq. (2.109) of Poinsot and Veynante (2005), which is close to the value reported by Bradley et al. (1996). The comparison of unstretched and stretched laminar flame results to the experimental data suggests the following: it was clearly noted by Hainsworth (1985) that the mixture of $\Phi = 1.1$ is thermodiffusively stable and there are no cell formation on the flame surface. Hence, the increase in the burning rate is purely due to turbulence. As the initial laminar flame grows, it is exposed to progressively wider range of scales, which would increase the surface area through flame wrinkling. This results in increased burning rate as has been noted in earlier studies (Beretta

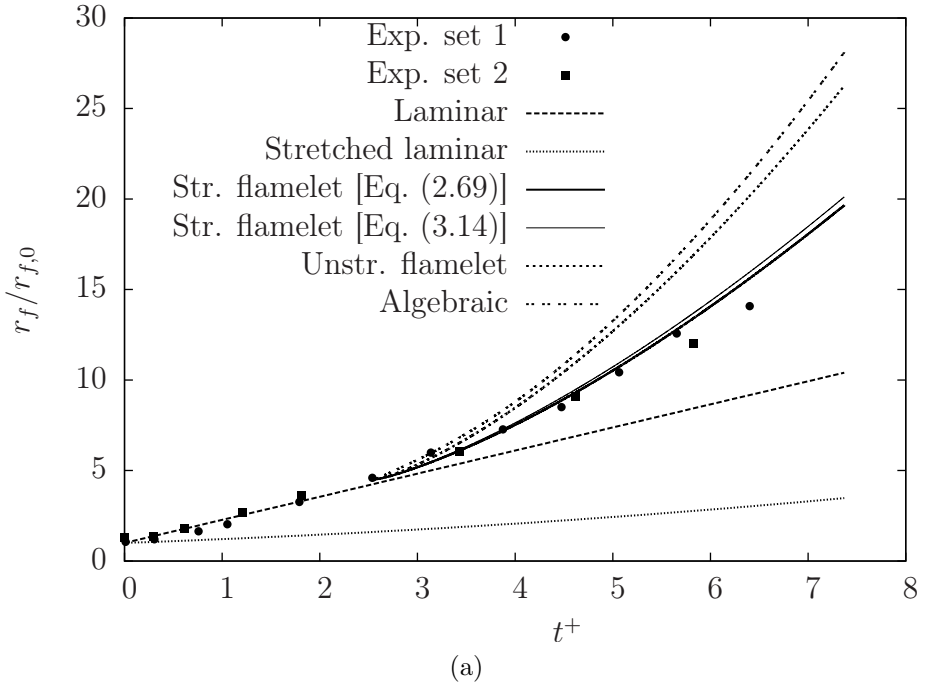

(a)

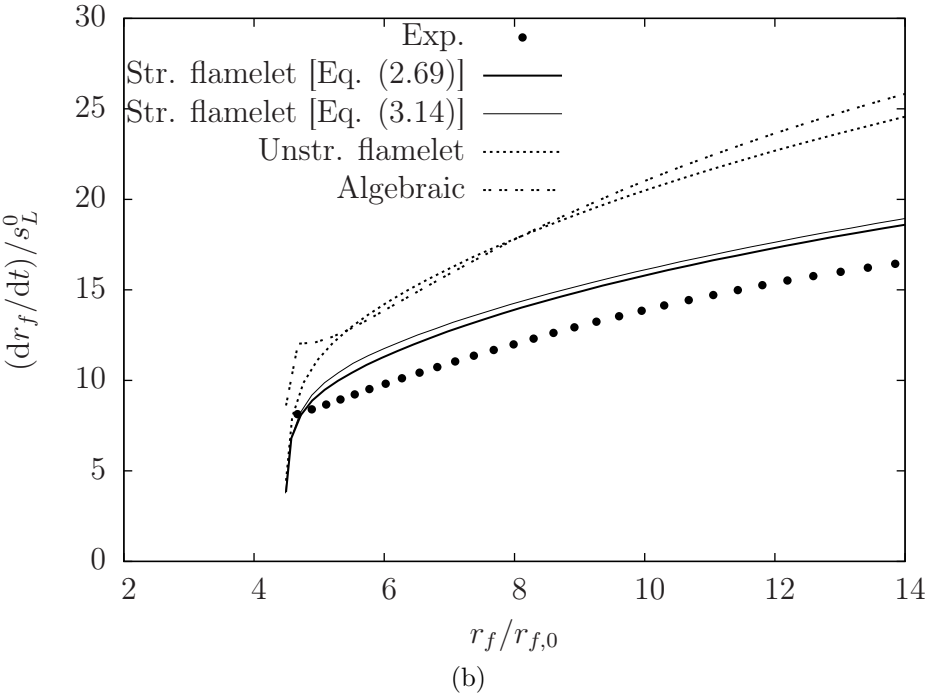

(b)

Figure 4.2: Comparison of numerical and experimental (Hainsworth, 1985) results: (a) radius as a function of time and (b) flame propagation speed as a function of radius.

et al., 1983; Hainsworth, 1985). It is possible that this increase is compensated by the stretch-induced negative effect, resulting in a growth rate similar to that of freely propagating spherical laminar flame for about $t^+ \leq 2$. Beyond this time, the effects of flame wrinkling produced by turbulence overwhelms the stretch effect, producing a smooth departure from the freely propagating spherical laminar flame as seen in Figure 4.2(a).

When the flame kernel is much smaller than the turbulence integral length scale, it will simply be convected by the large-scale eddy and the flame-turbulence interaction is limited to a small part of the wide spectrum of turbulence scales and thus RANS combustion modelling may not hold. This leads to some ambiguity in using turbulent combustion modelling to simulate the transition from laminar to turbulent growth using this approach. This has been recognised by Pope (1987), and so, a joint velocity-scalar pdf approach was chosen by Pope and Cheng (1986) to simulate this experimental flame from $t^+ = 0$, showing a good comparison with measurements over the whole period of the experiment. Thus, the experimentally measured flame radius at $t^+ \approx 2.5$ obeying this condition is chosen as the initial flame radius for the simulation. This flame radius departs from the laminar result by about 5% as shown in Figure 4.2(a). Thus, the turbulent flame results start from $t^+ \approx 2.5$ in this figure.

The URANS approach along with the $\tilde{k}$-$\tilde{\varepsilon}$ model was also used in earlier studies employing an empirical mean reaction rate model based on turbulent flame speed closure (Schmid et al., 1998) and a time dependent mean reaction rate closure with a laminar-like source (Lipatnikov and Chomiak, 2000). The later study also excluded momentum equation in the analysis.

The difficulties noted previously, due to the relative size of the flame and turbulence integral length scale and further reasonings given below, means that only the $\Phi = 1.1$ flame from the experiments of Hainsworth (1985) can be simulated in this study. Also, the lean methane-air mixture is thermo-diffusively unstable (weakly) and this effect must be taken into account in the combustion modelling approach. It is unclear at this time how to include these effects into RANS combustion modelling. As shown in Figure 4.1, the conditions of the experimental flames are in the corrugated flamelets regime, whether one can ignore the thermodiffusive instabilities, however weak they may be, and their influence on flame

propagation is an open question.

The turbulent flame results are shown for three different combustion models in Figure 4.2(a). The algebraic model in Eq. (2.48) overpredicts the flame growth as one would expect because this model assumes fast chemistry resulting in faster burning. The unstrained flamelet model in Eq. (2.63) includes finite rate chemistry effects but assumes the flame front to be a freely propagating laminar flame and thus excludes the local stretch effects on the flame front. Thus, the flame growth rate is overpredicted by this model as well, but the level of overprediction is reduced when compared with the algebraic model case. The values of r_f computed using the strained flamelet model given by Eq. (3.10) agree well with the measured values as shown in Figure 4.2(a) for the following reason. In premixed flames, the local balance among reaction, diffusion and fluid dynamic effects determines the local scalar gradient magnitude which is directly related to the scalar dissipation rate. The stretch effects from turbulence are due to straining and curvature and both of these will directly influence the scalar gradient. Thus, using the scalar gradient to parametrise the flamelets seems prudent for spherical flames as it has been shown earlier for planar flames (Kolla and Swaminathan, 2010*a*). The relative behaviour of the three combustion models shown here for the statistically spherical flame is similar to the observation of Kolla and Swaminathan (2010*a*) for statistically planar flames. Also, the use of equation (3.14) to include the curvature of the flame brush shows negligible effect on the growth of the flame as in Figure 4.2(a) and for this reason Eq. (2.69) will be used for further analyses of spherical flames to be discussed below, unless mentioned otherwise.

There is some uncertainty in choosing the initial flame radius for the computations, as noted earlier. Thus, the variation of normalised propagation speed, $(\mathrm{d}r_f/\mathrm{d}t)/s_L^0$, with the normalised radius is shown in Figure 4.2(b). The computational results are about 12% larger than the values derived from the experimental results, and this level of difference is acceptable. A best-fit cubic curve for the two sets of experimental data for $t > 2.4$ ms given in Figure 4.2(a) is used to calculate $\mathrm{d}r_f/\mathrm{d}t$ for the experimental result.

4.3.2 Spherical and planar flames comparison

The flame geometry effect on the propagation and consumption speeds of turbulent premixed flames is investigated in this section using the results of spherical and planar flames simulated in this study. The planar flame results computed in this study were observed to be very close to those reported by Kolla and Swaminathan (2010*a*). All the flames investigated in this section are simulated for a period of about 8 ms. Typical time evolution of these two, planar and spherical, flames is shown in Figure 4.3 by plotting the spatial variation of $\tilde{c}$ at various times. The spatial position, x', shown in this figure is a Galilean transformed, $x' = x - \tilde{\boldsymbol{u}}_b t$, because the burnt side velocity, $\tilde{\boldsymbol{u}}_b$, is different in the planar and spherical cases. This allows a direct comparison between these two flames. The burnt side velocity is zero in the spherical case and it is negative in the planar case.

The initial variation is shown by dashed lines and the profiles are shown for a period of 8 ms ($t^+ \approx 7.8$) at an interval of 2 ms. These flames have $u'/s_L^0 = 6$ and $K = 0.15$, and the same thermochemical parameters because they are stoichiometric CH_4-air mixture. These flames propagate from left to right in Figure 4.3 and they are computed in the Cartesian and spherical coordinate systems respectively. This flame pair is used to demonstrate the flame geometry effects because the relative behaviours shown and discussed in this section hold for other cases considered, unless noted otherwise.

In Figure 4.3 the profile at 8 ms is plotted using symbolled lines to show the grid resolution. For all the cases the grid resolution was defined such that there are at least 10 points within the integral length scale. This figure also shows that the planar flame reaches a nearly steady propagation speed after some initial transients, but the spherical flame does not seem to suggest a steady value for its propagation speed [shown in Figure 4.3(b) by the increasing gap between consecutive iso-contour profiles]. As the spherical flame grows outwardly, the leading surface area increases, resulting in increased burning rate, which can be seen clearly by plotting the temporal variation of the propagation speed of an iso-value, $\tilde{c} = c_1$. This speed is extracted from the computed time variation of

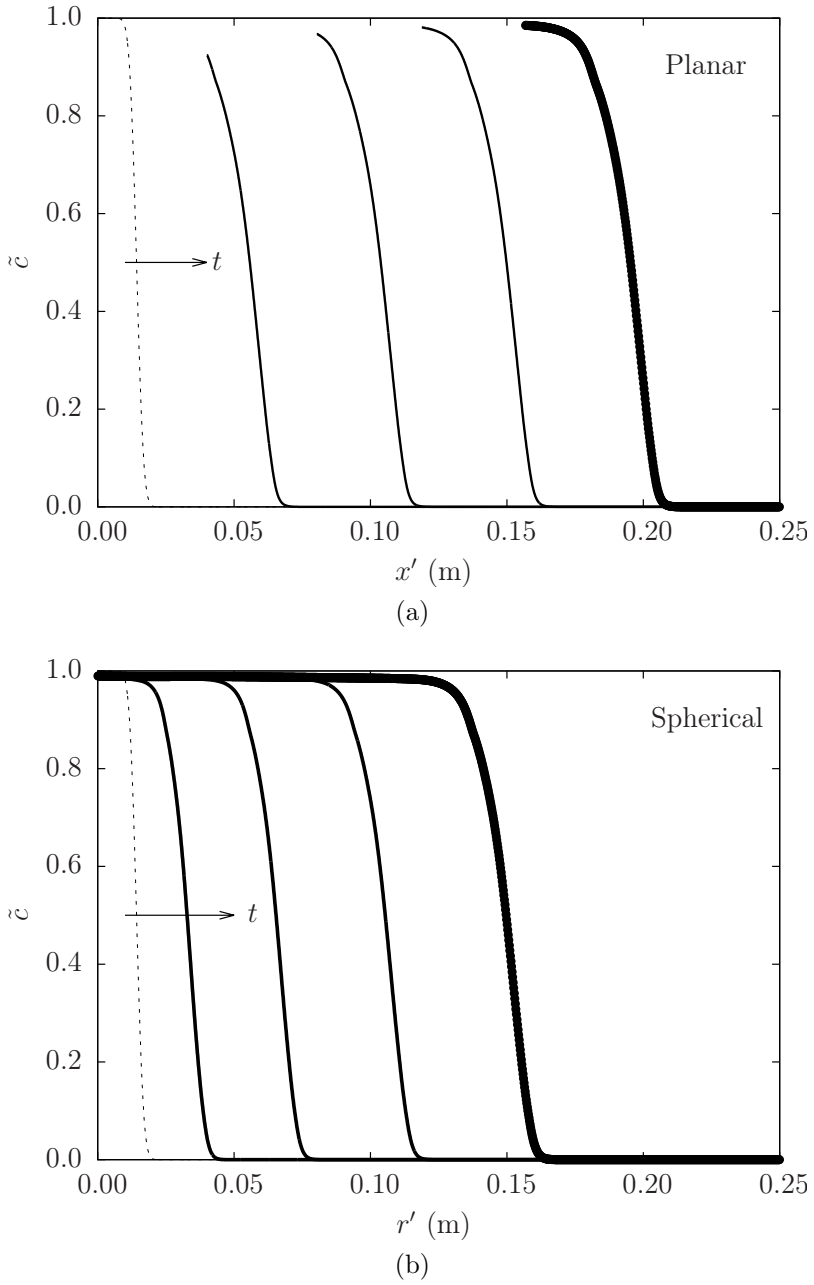

Figure 4.3: Spatial variation of $\tilde{c}$ at five different times, 0 to 8 ms at an interval of 2 ms, in (a) planar and (b) spherical flames having $u'/s_L^0 = 6$ and $K = 0.15$. Dashed lines show the variation at $t = 0$.

the spatial position $x\,(c_1)$ or $r\,(c_1)$ through

$$\frac{\mathrm{d}\boldsymbol{x}(c_1)}{\mathrm{d}t} \cdot \boldsymbol{n} = \tilde{\boldsymbol{u}} \cdot \boldsymbol{n} + s_d, \tag{4.1}$$

where $\tilde{\boldsymbol{u}}$ is the fluid velocity and s_d is the displacement speed of the $\tilde{c}$ iso-level in its normal, $\boldsymbol{n}$, direction due to its relative movement created by combined effects of mean reaction rate, turbulent flux and molecular diffusion. Note the difference between this displacement speed and the one defined in section 2.3.3, which was defined for instantaneous c. For the rest of this work, the displacement speed will be defined with respect to Favre-averaged progress variable, $\tilde{c}$. The effect of molecular diffusion can be neglected in high-Reynolds number turbulent flows and the displacement speed can then be written as

$$s_d = \underbrace{\frac{1}{r^2}\frac{\partial}{\partial r}\left[r^2\left(\frac{\mu_t}{\mathrm{Sc}_c}\frac{\partial \tilde{c}}{\partial r}\right)\right] \Big/ \left(\overline{\rho}\left|\frac{\partial \tilde{c}}{\partial r}\right|\right)}_{s_d^T} + \underbrace{\overline{\dot{\omega}} \Big/ \left(\overline{\rho}\left|\frac{\partial \tilde{c}}{\partial r}\right|\right)}_{s_d^r}, \tag{4.2}$$

using the mean progress variable equation, Eq. (3.3). It is understood that all the quantities on the right hand side of Eq. (4.2) must be evaluated at $\tilde{c} = c_1$. A corresponding equation can also be written in the Cartesian system. The displacement speed of the leading edge, $s_d\,(\tilde{c} = 0.05)$, is referred as the turbulent flame speed in the latter part of this section. The equality in Eq. (4.1) is verified using the computational results since the three terms can be evaluated individually.

Figure 4.4 shows the temporal variation of the propagation speed, s_p, with respect to the burnt mixture computed from $\mathrm{d}x'/\mathrm{d}t$ for the iso-levels. The results with low and high turbulence levels are shown respectively in Figures 4.4(a) and 4.4(b). This propagation speed is normalised using the unstrained planar laminar flame speed and the time is normalised using the respective integral time scale of the turbulence in the reactants, t_e. This normalised time is related to t^+ through $t^* = t^+\,(t_c/t_e)$. After going through some initial transients for $t^+ \sim 2$ to 2.5, all the iso-levels converge to a nearly constant propagation speed that depends on the value of u'/s_L^0 for the planar flames, and a small decrease with t^* suggest the persistence of the initial transients. On the other hand, the propagation speed increases with t^*, and different iso-levels are travelling at different speeds

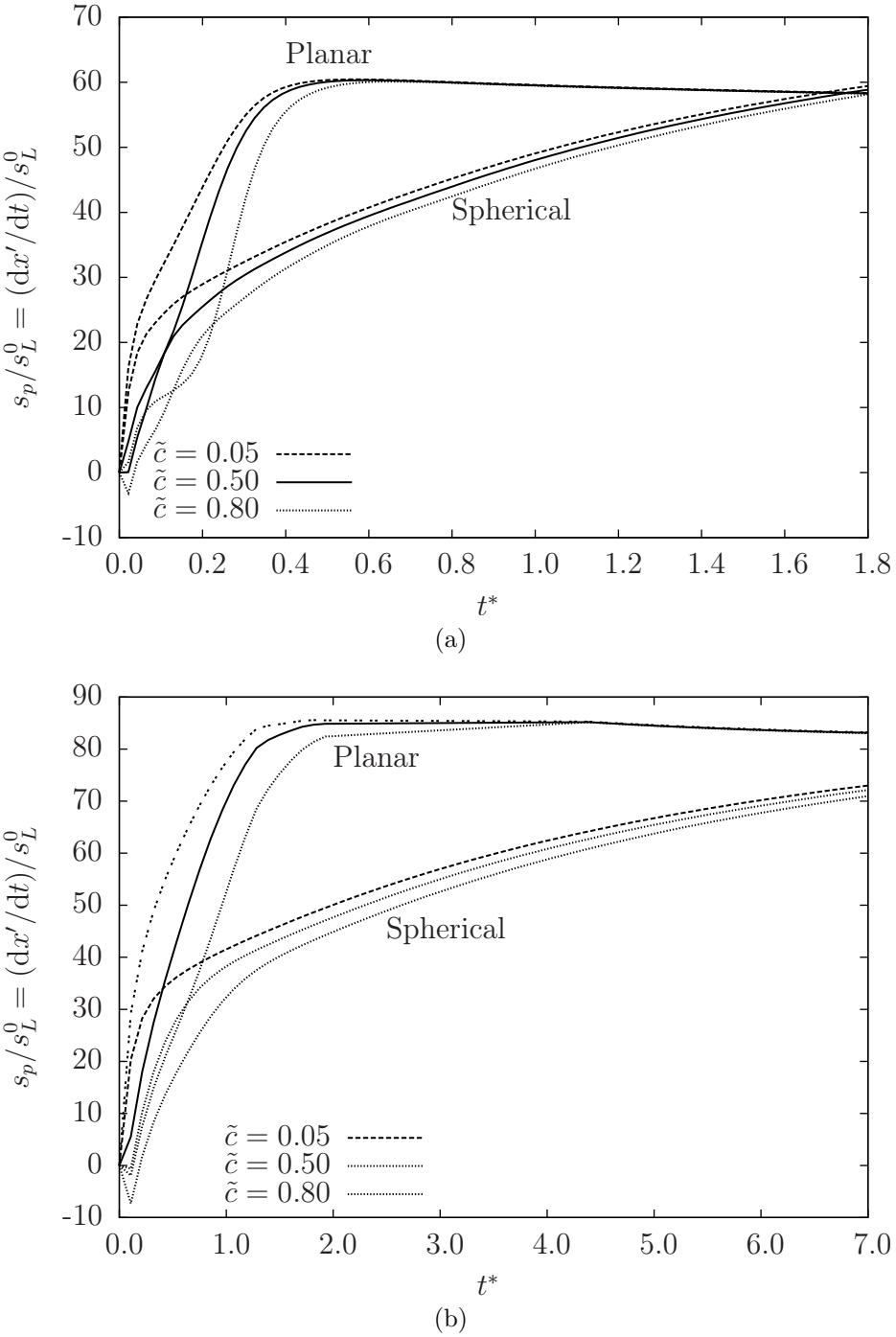

Figure 4.4: Temporal variation of propagation speed of $\tilde{c}$ iso-levels in planar and spherical turbulent flames for (a) $u'/s_L^0 = 6$ and $K = 0.15$, and (b) $u'/s_L^0 = 18$ and $K = 1$. Results are shown for three different iso-levels.

in spherical flames. The larger values seen in the early period for the planar flame is because of the high $\tilde{\boldsymbol{u}}_b$. The continuous growth in the spherical cases is because of the continuous increase in the burning surface area. Further discussion on this point is postponed until section 4.4.

The iso-levels with lower $\tilde{c}$ values are moving more quickly compared to those with greater values in the spherical cases. This relative behaviour can be seen clearly by plotting the variation of the propagation speed in Eq. (4.1) across the flame brush at a given instant. This variation is shown in Figure 4.5(a) for both planar and spherical flames at $t = 5$ ms. The results are shown for two combustion conditions, $u'/s_L^0 = 20$ and $K = 1$ and $u'/s_L^0 = 6$ and $K = 0.15$. A gradual decrease of the normalised propagation speed across the spherical flame brush is seen, and this decrease is about 9 to 12%, depending on the value of u'/s_L^0 (larger decrease for greater u'/s_L^0). It is to be noted that the values of the propagation speed are divided by 2 for $u'/s_L^0 = 20$ cases to fit within the scale shown in Figure 4.5(a). The statistically planar flames (open symbols) do not show any decrease across their flame brushes, except for the sharp change near the burnt side, which is for an obvious reason. The large scatter seen at $\tilde{c} = 0$ is due to sharp variation of s_d over a small range of $\tilde{c}$ near the unburnt side of the flame brush.

Typical variations of the two components, $\tilde{\boldsymbol{u}}/s_L^0$ and s_d/s_L^0, across the flame brush are shown in Figure 4.5(b) for the $u'/s_L^0 = 6$ case at $t = 5$ ms. The results for planar and spherical flames are shown respectively with dashed and solid lines and using the corresponding symbol in Figure 4.5(a). The displacement speed is calculated using Eq. (4.2). The following observations can be made from this figures: (1) The normalised $\tilde{u}$ and s_d have the same sign in the spherical case, whereas they have opposite signs in the planar case. This implies that the fluid and $\tilde{c}$ iso-level move in opposite directions in planar flames, unlike in spherical flames. (2) The values of s_d/s_L^0 and $\tilde{u}/s_L^0$ near the leading edge of the spherical flame is much larger than in the planar flame. On the burnt side, the planar flames have larger values. It is to be noted that the fluid velocity shown here is because of heat-release effects, since $\tilde{u}\,(\tilde{c} = 0)$ and the velocity gradient at the burnt side are specified to be zero for the planar flames as noted earlier in Subsection 3.4. Thus, the flow acceleration across the flame brush gives a large flow velocity on

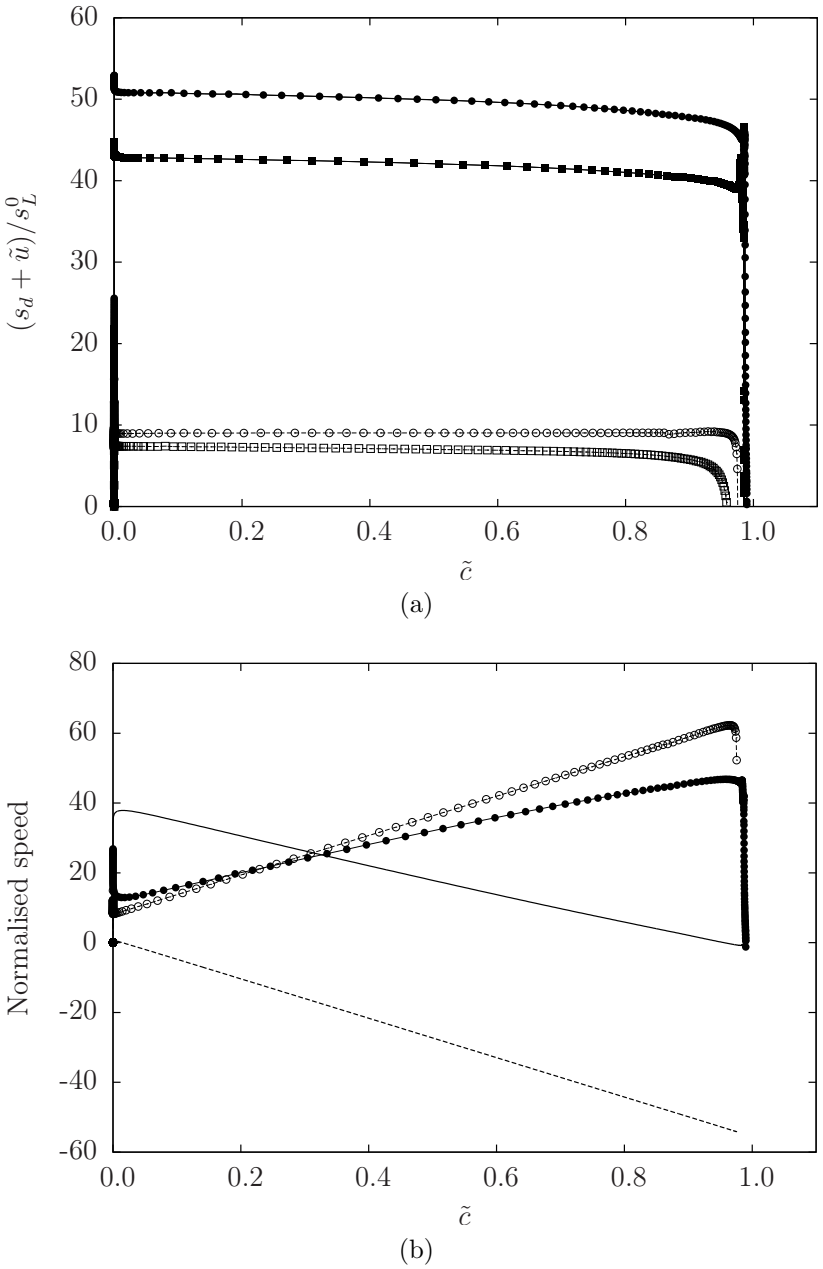

Figure 4.5: Variation of propagation speed across the flame brush is shown in (a) for planar (open symbols and dashed lines) and spherical (closed symbols and solid lines) flames with $u'/s_L^0 = 6$ and $K = 0.15$ (circle), and $u'/s_L^0 = 20$ and $K = 1$ (square) at $t^+ = 4.88$ ($t = 5$ ms). The two components, s_d (symboled lines) and $\tilde{u}$ (lines), are shown in (b) for the $u'/s_L^0 = 6$ case.

the burnt side of the planar flame brush as it is well known and this is clear in Figure 4.5(b).

In the spherical case, the burnt mixture and the unburnt mixture at large radial distance are at rest and thus the flame-induced velocity has to decay to zero on both sides of the flame brush. These behaviours, especially on the unburnt side, are unclear in Figure 4.5(b). Thus, the spatial variation of $(\tilde{u}/s_L^0)$ at $t = 5$ ms is shown in Figure 4.6, where the distance is normalised using the turbulence integral length scale, Λ. The peak flow velocity occurs near the leading edge of

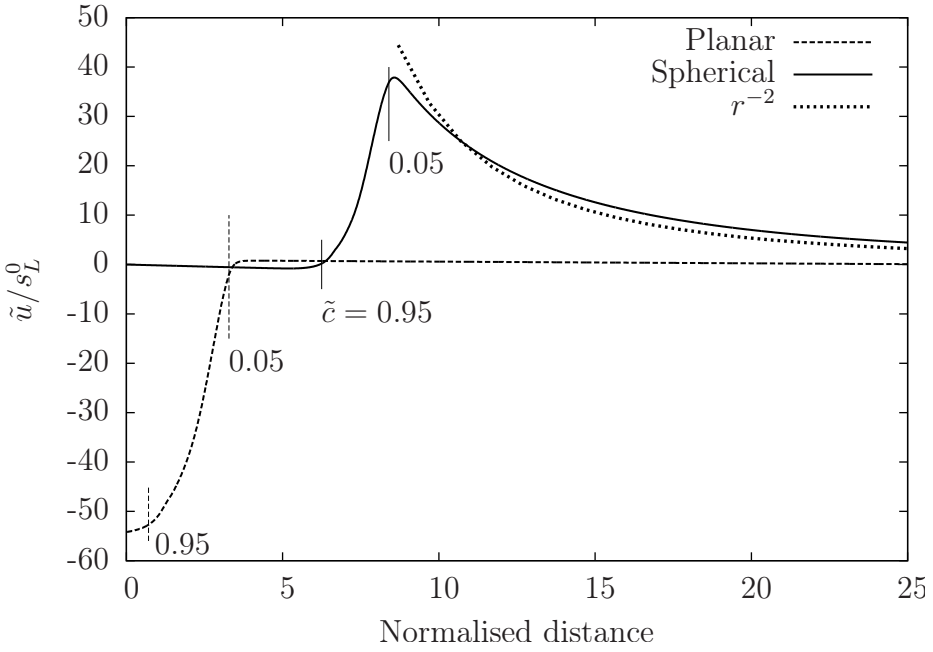

Figure 4.6: Spatial variation of $\tilde{u}/s_L^0$ at $t^+ = 4.88$ for the cases with $u'/s_L^0 = 6$ and $K = 0.15$. The locations of $\tilde{c} = 0.05$ and 0.95 in the respective flames are marked to indicate the flame brush sizes. The r^{-2} decay of mean velocity is also plotted.

the spherical flame brush and it decays to zero as r^{-2} in the unburnt mixture. Also, the flame brush thickness as marked roughly in Figure 4.6 is relatively smaller for the spherical case compared to the planar flame.

The time evolution of the flame brush thickness normalised by the laminar flame thermal thickness, δ_t/δ_L^0, is plotted in Figure 4.7. The flame brush thickness is defined in two ways, one is using the maximum gradient of $\tilde{c}$ (shown as

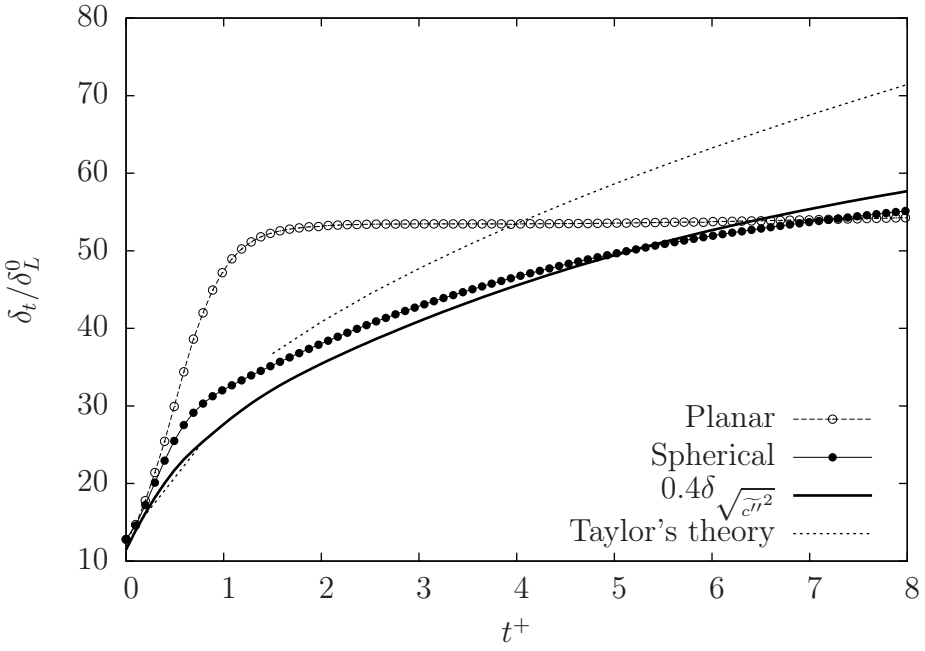

Figure 4.7: Evolution of flame brush thickness with time in flames with $u'/s_L^0 = 18$ and $K = 1$.

symboled lines in Figure 4.7) and another one is using the variance, $\widetilde{c''^2}$ (shown as a solid line). This second thickness is defined as the thickness over which rms value drops to 5% of its maximum value to be consistent with Taylor's theory of turbulent dispersion (Taylor, 1935*b*). Note that this variance thickness is also scaled to fit in the scale shown in Figure 4.7. These results are discussed fully in section 4.4. The planar flame reaches a steady value, dictated by the turbulence and thermochemical conditions, after $t^+ \approx 2.6$, whereas there is no such steady-state value for the spherical flame, and its thickness keeps growing with time, which is well known in the literature. This relative behaviour is the same in other flames investigated in this study.

From the results discussed so far, it seems that this continuous growth is because the burnt side of the flame is advancing slowly compared to the leading edge. This difference can be seen clearly for Figure 4.4 for $\tilde{c} = 0.05$ and 0.8 [also see Figure 4.5(a)]. It is obvious from the discussion that the fluid velocity at the leading edge is larger as shown in Figures 4.4-4.6 and it acts together

with the displacement speed in the spherical case. Based on these results, a simple schematic diagram can be drawn as shown in Figure 4.8 to represent the difference in the physical mechanisms influencing the propagation of statistically planar and spherical flames. Note the difference in directions of flow, $\tilde{u}$, and flame displacement speeds, s_d, between spherical and planar cases.

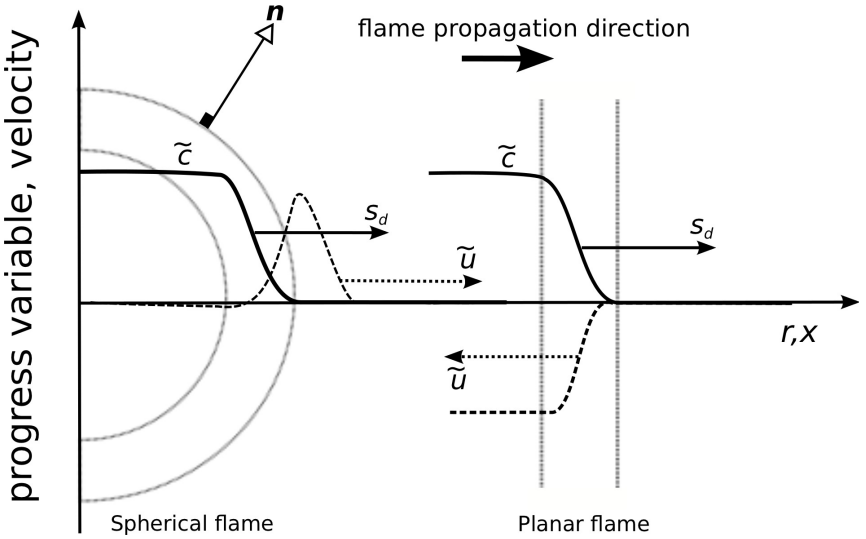

Figure 4.8: Schematic diagrams showing the propagation mechanism in a statistically planar and spherical flames. Dashed and solid arrows represent the flow and iso-level displacement directions respectively.

Behaviour of s_d

From the discussion in the previous section, it is evident that δ_t will influence the flame displacement speed. As noted in Eq. (4.2), the s_d has two (reaction and turbulent flux), components and their typical variations across the flame brush are shown in Figure 4.9 for two instances, $t^+ = 4.88$ in Figure 4.9(a) and 8 in Figure 4.9(b). The reaction rate contribution can be written as $(s_d^r/s_L^0) = \overline{\dot{\omega}}^+ (1 + \tau\tilde{c}) / |\partial\tilde{c}/\partial r^+|$. Thus, the behaviour of (s_d^r/s_L^0) with $\tilde{c}$ is expected to be approximately linear according to $(1 + \tau\tilde{c})$ because the variations of $\overline{\dot{\omega}}^+$ and $|\partial\tilde{c}/\partial r^+|$ with $\tilde{c}$ would be similar. This observation explains the variations of (s_d^r/s_L^0) shown in Figure 4.9. The difference between the planar and spherical flames predominantly comes from $1/|\partial\tilde{c}/\partial r^+|$, which is related to δ_t shown in

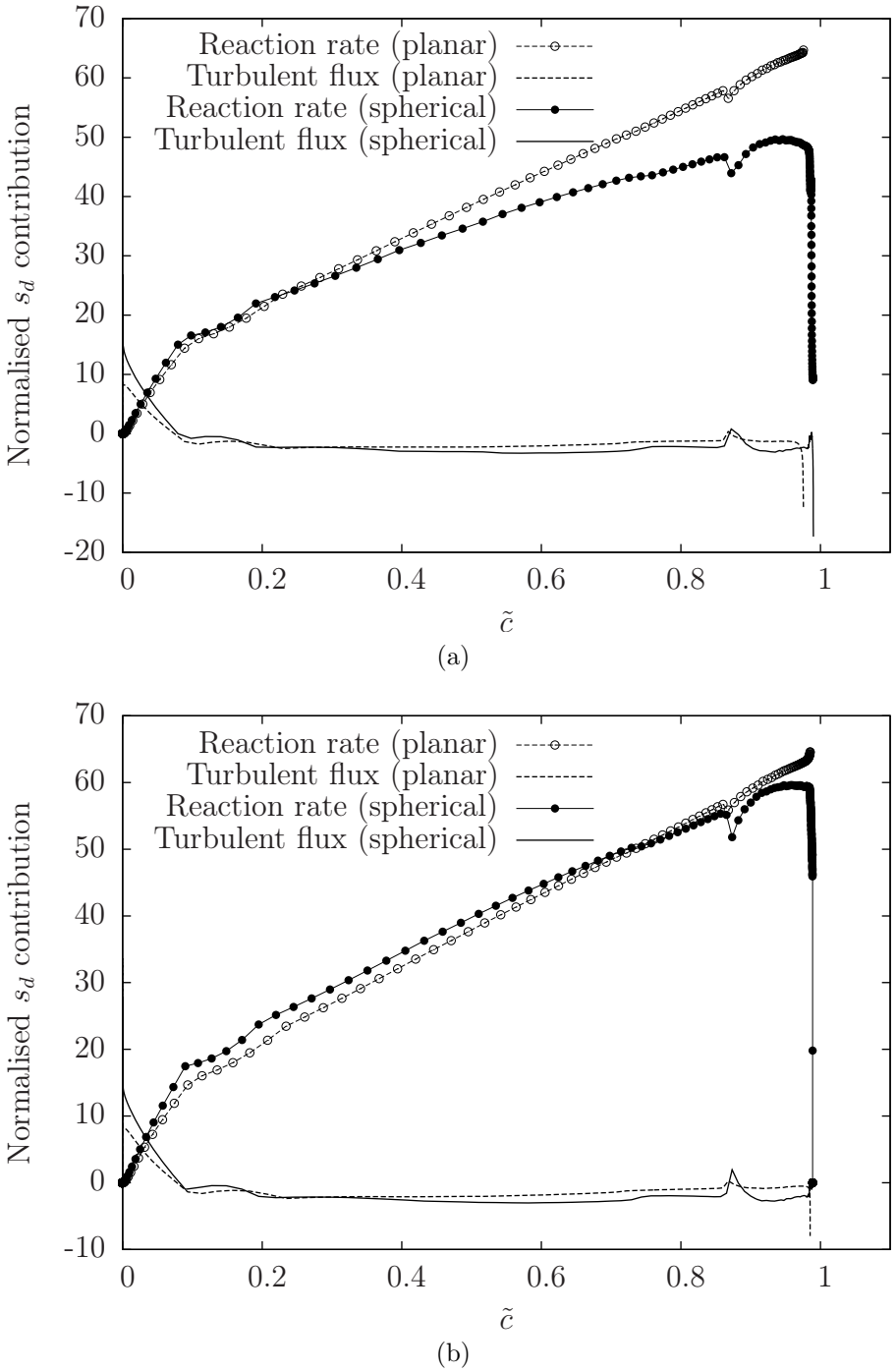

Figure 4.9: Reaction rate and turbulent flux contributions to (s_d/s_L^0) for both planar and spherical flames with $u'/s_L^0 = 6$ and $K = 0.15$ at: (a) $t^* = 1.14$ $(t^+ = 4.88)$ and (b) $t^* = 1.87$ $(t^+ = 8)$.

Figure 4.7. The planar flame is thicker at $t^+ = 4.88$ and thus (s_d^r/s_L^0) is larger compared to the spherical flame, and the value of this displacement speed is about the same at $t^+ = 8$ because δ_t is nearly equal for these two flames.

The difference in the mean reaction rate variation is observed to be small in Figure 4.10 and this relative behaviour is also observed in other flames considered for this study. Also,the inset shows that the maximum value of the normalised mean reaction rate does not vary much over the wide range of turbulence conditions of both planar and spherical flames considered in this study. The values of $\overline{\dot{\omega}}^+_{\max}$ differ by a small amount between the planar and spherical flames. These behaviours of $\overline{\dot{\omega}}^+$ is observed to hold after the initial transient. The reduced sensitivity of $\overline{\dot{\omega}}^+$ to the turbulence level and the flame geometry has also been reported in a direct numerical simulation study (Dunstan et al., 2012) by considering oblique and planar turbulent premixed flames established in a range of turbulence conditions.

The turbulent flux contribution, s_d^T, to (s_d/s_L^0) decreases across the flame brush as shown in Figure 4.9. This is an expected behaviour for the planar flames. To understand its behaviour in spherical flames and for the difference seen near the leading edge, one can expand the first term of Eq. (4.2). This will identify an extra term of $2\mu_t(\partial\tilde{c}/\partial r)/(r\,\mathrm{Sc}_c)$ in spherical flames, which will increase as $\tilde{c}$ increases in outwardly propagating flames. Since $(\partial\tilde{c}/\partial r)$ is negative for these flames, this extra term contributes negatively leading to a decrease of s_d^T as $\tilde{c}$ increases. The flux contribution near the leading edge is larger in the spherical case because of the additional increase in $\partial^2\tilde{c}/\partial r^2$ resulting from the flame geometry. Thus, the difference in the s_d of spherical and planar flames comes predominantly from the turbulent scalar flux. This is seen clearly in Figure 4.9, specifically at the leading edge. The influence of turbulence on the leading edge displacement speed and the consumption speed is discussed in the next subsection.

Turbulent flame speed comparison

The displacement speed of flame brush leading edge is defined as the turbulent flame speed, s_t. This quantity is of interest for theoretical investigation of turbulent flames and the influence of flame geometry on this quantity is of consid-

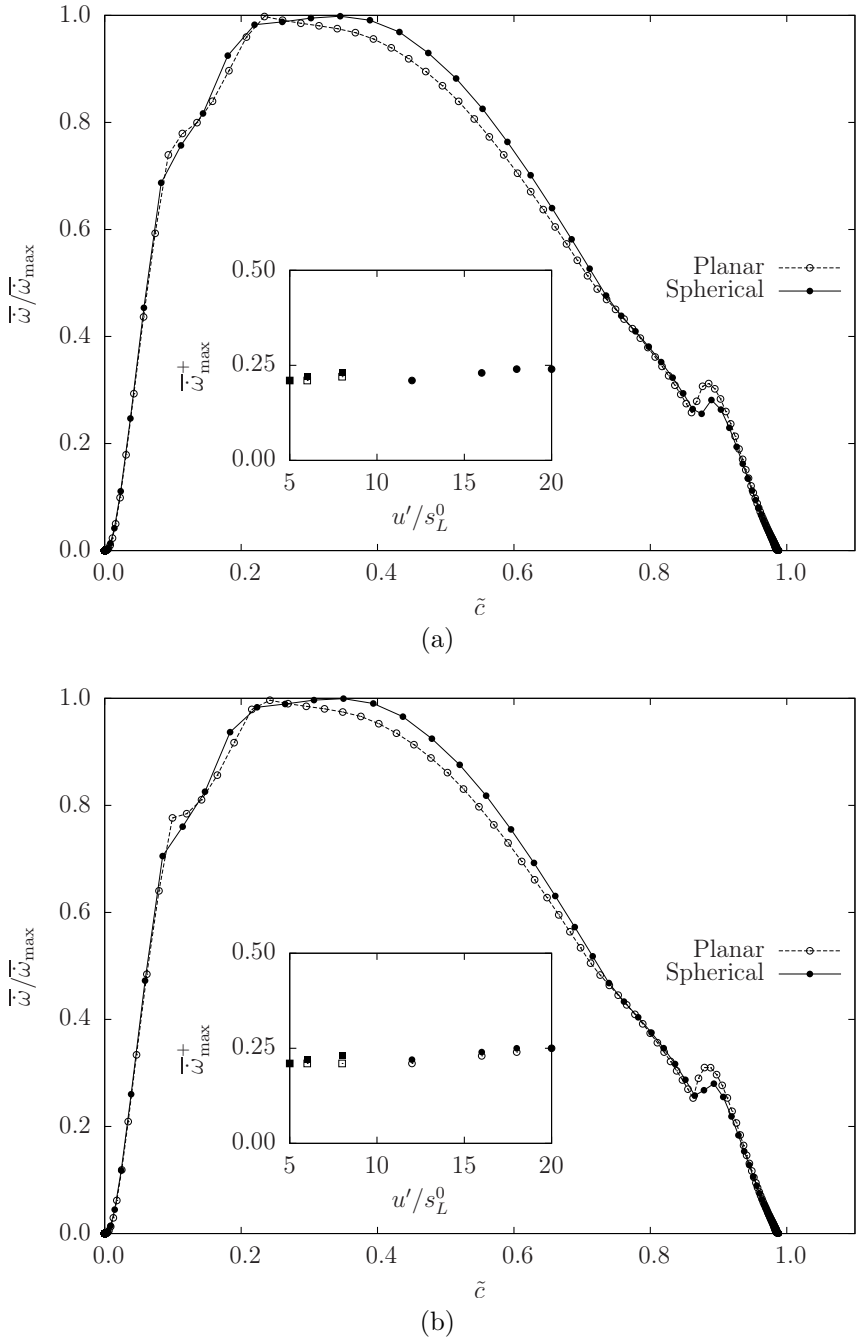

Figure 4.10: Variation of normalised mean reaction rate across the flame brush for both planar and spherical flames, with $u'/s^0_L = 6$ and $K = 0.15$ at $t^+ = 8$, at (a) $t^+ = 4.88$ and (b) $t^+ = 8$, and the insets show the variation of $\overline{\dot{\omega}}^+_{\max}$ with (u'/s^0_L) for the various flames considered in this study, where $\overline{\dot{\omega}}^+ = \overline{\dot{\omega}}\delta^0_L/(\rho_u\, s^0_L)$.

erable interest for turbulent combustion modelling (Driscoll, 2008). It has been suggested recently that s_t is weakly sensitive to the flame geometry among freely propagating planar, strained planar and rod stabilised oblique turbulent premixed flames (Dunstan et al., 2012). It must be noted that there is no "stationary value" for s_t in the spherical flames as for the planar flames.

The variation of s_t/s_L^0 with the turbulence Reynolds number is shown in Figures 4.11(a) and 4.12(a), and its variation with u'/s_L^0 is shown as the inset. The turbulent flame speed of the spherical flames is always larger than the corresponding planar flame value for a given turbulence condition by about 10 to 20% and the greater value is due to the turbulent scalar flux contribution at the leading edge as noted in the previous subsection. The results in the inset clearly suggests an approximate relation $s_t \sim u'$ when the value of the stretch factor, K is kept constant. This relation was noted by Bray (1990) in his theoretical analysis using the Bray-Moss-Libby model. Lipatnikov and Chomiak (2002) analysed a number of experimental flames to show that $s_t \sim u'^q$, with $0.5 \leq q \leq 1$. This increase in s_t with u' is generally believed to be due to turbulent eddies increasing the flame surface area by stretching and contorting it (Lipatnikov and Chomiak, 2002).

The increase in s_t with u' is sharp for the high Damköhler number cases (low K) and the values of the slopes, obtained using the best linear fit, are about 6.3 and 5.1 respectively for the spherical and planar cases. These values become three time smaller for the cases with high stretch, however the relative difference in s_t between the spherical and planar flames remains almost the same. The computed variations with Re_t shown in Figures 4.11(a) and 4.12(a) suggest a relation $s_t/s_L^0 \simeq B\,\mathrm{Re}_t^n$ with $0.57 \leq n \leq 0.58$. The curves of least square fits shown in the figure for both the spherical and planar flames suggest that $B = 0.20$ for the spherical and 0.18 for the planar flames. The approximate square root dependence on the turbulence Reynolds number observed here is similar to that reported by Chaudhuri et al. (2012) for the *propagation speed* of spherical and Bunsen flames of methane-air mixtures which are thermodiffusively stable and do not include Darrieus-Landau instability. The approximate square root dependence observed in this study is consistent with the classical analysis of Damköhler for the thin reaction zone combustion through a hypothesis $s_t \sim \sqrt{D_t/t_c}$, where D_t is the turbulent diffusivity, which is similar to $s_L^0 \sim \sqrt{D/t_c}$, where D is the

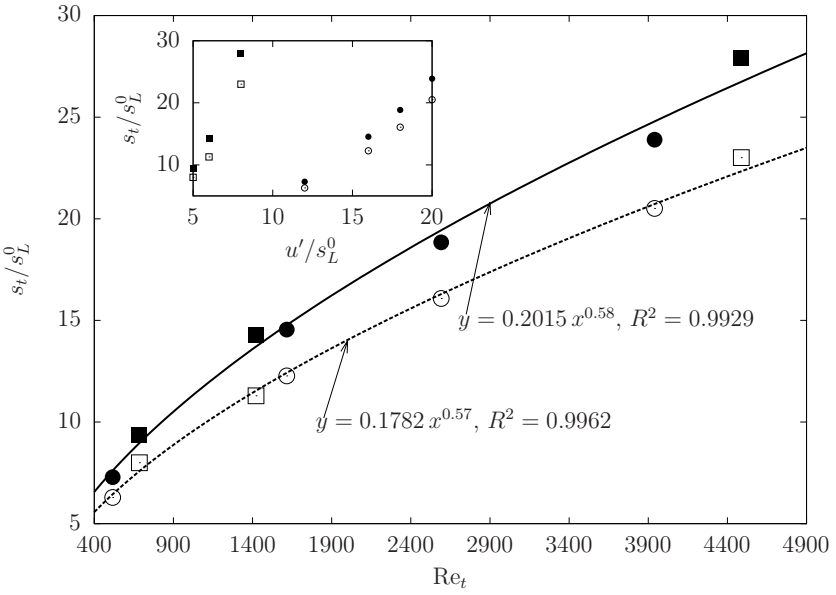

(a)

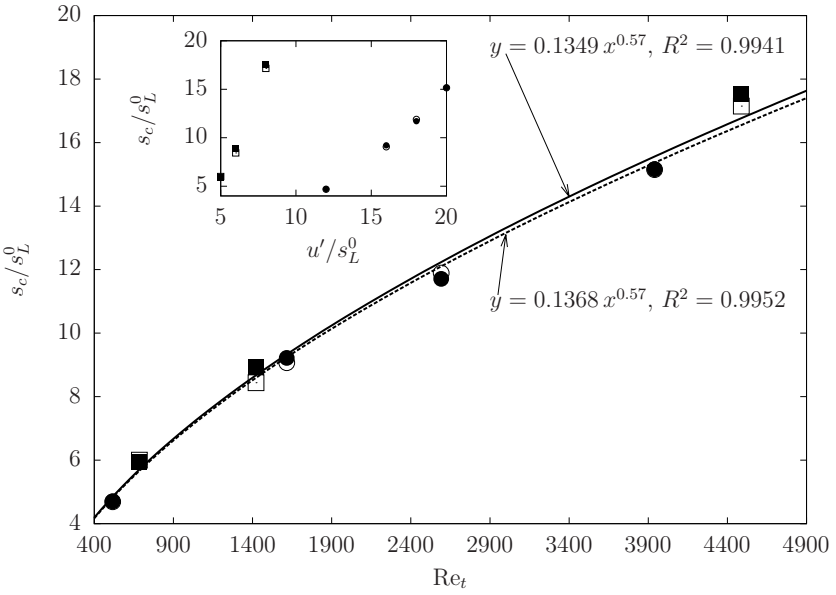

(b)

Figure 4.11: Planar (open symbols) and spherical (closed) flame speeds for the cases simulated in this study are plotted against the turbulence Reynolds number. The inset shows the variation with u'/s_L^0. All flame speeds are taken at $t^+ = 8$ ($t =$ 8.2 ms) in (a) normalised turbulent flame speed and (b) normalised consumption speed. The symbols correspond to those shown in Figure 4.1.

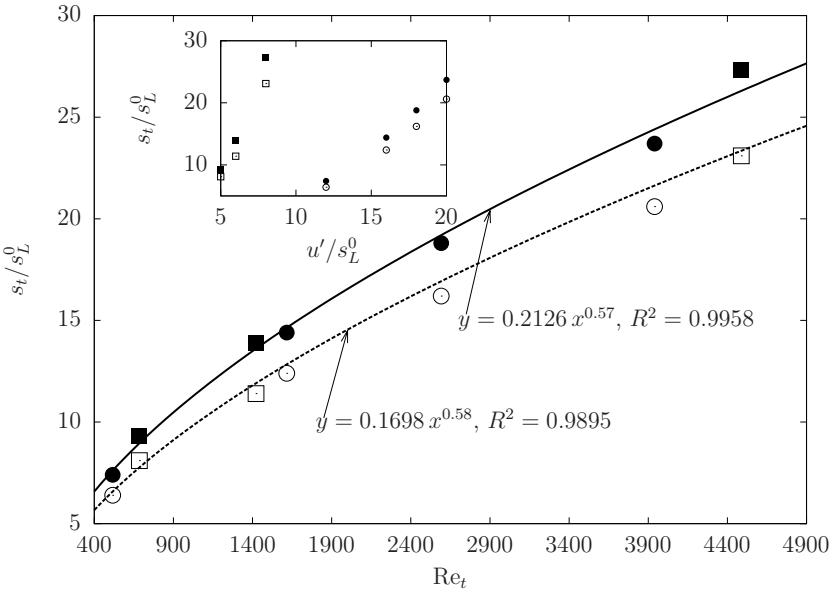

(a)

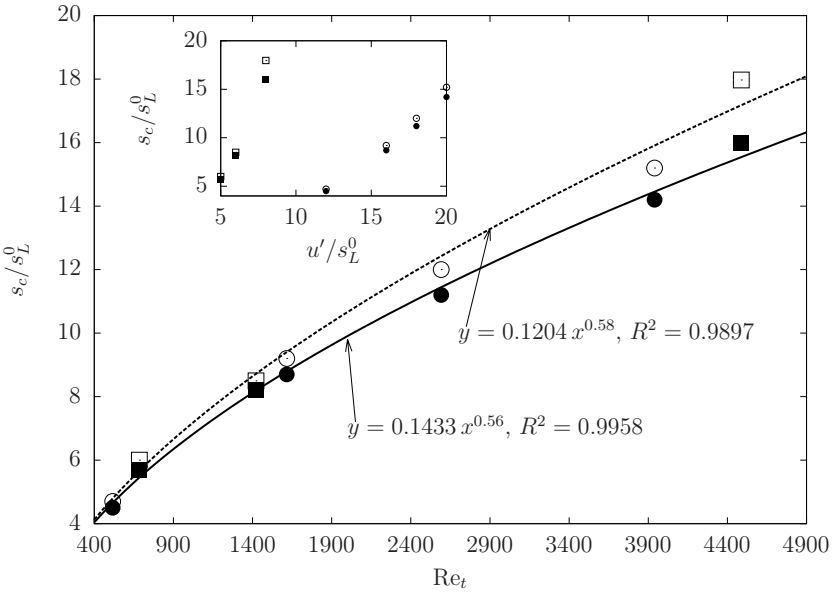

(b)

Figure 4.12: Planar (open symbols) and spherical (closed) flame speeds for the cases simulated in this study are plotted against the turbulence Reynolds number. The inset shows the variation with u'/s_L^0. All flame speeds are taken at $t^+ = 5.86$ ($t = 6$ ms) in (a) normalised turbulent flame speed and (b) normalised consumption speed. The symbols correspond to those shown in Figure 4.1.

molecular diffusivity, in the laminar flame theory (Peters, 1999). The results of this study suggests that the flame geometry does not impart influence on this scaling relation for turbulent flames.

Figure 4.11(b) and 4.12(b) show the consumption speed variation at $t^+ = 4.88$ and 8 respectively. This speed is defined as

$$s_c = \frac{1}{\rho_u} \int_0^1 \frac{\overline{\dot{\omega}}}{|\partial \tilde{c}/\partial r|} \, \mathrm{d}\tilde{c} \qquad = \int_0^1 \frac{s_d^r}{(1+\tau\tilde{c})} \, \mathrm{d}\tilde{c}. \tag{4.3}$$

The latter part is obtained using s_d^r defined in Eq. 4.2 and thus the consumption speed is the reactive component of the density-weighted displacement speed integrated across the flame brush. As noted in the previous subsection, the difference between the planar and spherical flames comes predominantly through $\partial\tilde{c}/\partial r$ and the mean reaction rate is less influenced by the flame geometry. This gives the variation of s_c/s_L^0 with Re_t similar to s_t/s_L^0; however the magnitude of s_c is smaller than s_t as shown in Figures 4.11 and 4.12. The difference in the consumption speeds of the planar and spherical flames at $t^+ = 8$ is very small because the flame brush thickness is nearly equal, as shown in Figure 4.7.

4.4 Discussion

The results discussed in the previous section suggest that the flame brush leading-edge displacement speed, which will be referred to as the turbulent flame speed in this work, is larger for spherical flames compared to planar flames. The propagation speed, which is the sum of fluid velocity and the displacement speed, of the leading edge grows continuously with time in spherical flames, while it reaches a nearly constant value in planar flames. The increasing difference between the propagation speeds of the leading and trailing edges in spherical flames yields a continuous growth of its flame brush thickness. This growth is usually attributed to turbulent diffusion in the past studies, which is different from the physical explanation. The aim of this section is to shed more light on these observations.

The Kolmogorov-Petrovskii-Piskunov (KPP) analysis applied to multidimensional premixed in high-Reynolds number turbulent flow gave an expression for

the turbulent flame speed as (Kolla et al., 2010)

$$s_t = 2\sqrt{\frac{\nu_t}{\rho_u \mathrm{Sc}_c}\left(\frac{\partial\overline{\dot{\omega}}}{\partial\tilde{c}}\right)_{\tilde{c}=0}} + \left(\frac{\nu_t}{R\mathrm{Sc}_c}\right)_{\tilde{c}=0}, \tag{4.4}$$

where ν_t is the eddy viscosity and R is the radius of the leading edge. Figure 4.10 shows that the quantities $\left(\partial\overline{\dot{\omega}}/\partial\tilde{c}\right)_{\tilde{c}=0}$ in the planar and spherical flames are almost identical and the influence of flame brush curvature, R^{-1}, is responsible for the larger value of s_t observed in Figures 4.11 and 4.12. One expects that this contribution will decrease as R becomes very large and s_t of the spherical flame will reach the planar flame value eventually. This limiting behaviour is not observed in the simulation studied here because of their finite domain size and computational time. One requires a much larger computational domain than those considered in this study.

The Favre-averaged fluid velocity at the leading edge of a turbulent spherical flame is larger than at its trailing edge as shown in Figure 4.8. The maximum value of this velocity will increase with time because of a continuous increase in mass burning rate resulting from the growth of the leading surface area. This increase, indeed observed in this study, results in a continuous acceleration of the leading edge of spherical flames unlike in planar flames. Thus, a transition from turbulent deflagration to a detonation can occur eventually if the conditions are right. This transition is aggravated if the spherical flame propagates in a closed vessel under appropriate conditions.

The spatial or temporal variation of flame brush thickness has been studied in many earlier investigations and the results are summarised by Lipatnikov and Chomiak (2002, 2005) and an increase in the thickness with time or distance has been observed in these studies. Furthermore, Lipatnikov and Chomiak (2005) showed that the evolution of the measured flame brush thickness is well predicted by Taylor's theory of turbulent diffusion for a passive scalar (Taylor, 1935*b*). This theory predicts a linear growth in t for the rms displacement of a fluctuating passive scalar iso-surface when t is smaller than the turbulent eddy turn over time t_e, and this growth becomes $\sqrt{t}$ when t is very much larger than t_e. Analysis using direct numerical simulation date of turbulent "V" flames offered good support

for this (Minamoto et al., 2011; Dunstan et al., 2012) theory, suggesting that the turbulent diffusion plays a predominant role on the growth of the flame brush thickness. The applicability of this theory to the spherical flames studied here is tested in Figure 4.7, which is typical for the flames studied here. As noted earlier in section 4.3.2, the solid line denotes the temporal variation of $\delta_{\sqrt{\widetilde{c''^2}}}$, a thickness over which $\sqrt{\widetilde{c''^2}}$ drops to 5% of its maximum value. This variation is similar to δ_t as shown in Figure 4.7. The values predicted by Taylor's theory are also shown in that figure. The gap in the theoretical curve is intentional to mark some transition from linear to square root dependence. This result suggests that the variations of δ_t and $\delta_{\sqrt{\widetilde{c''^2}}}$ do not follow the turbulent diffusion theory, except for a very short initial period. The relative gap between the theoretical curve and δ_t in the spherical flame is controlled by the propagation mechanisms governed by chemical reaction, convection and turbulent diffusion. The role of turbulent diffusion for the growth of δ_t seems secondary compared to the convection because of the fluid velocity induced by the chemical reaction.

4.5 Summary

Spherically expanding and statistically planar turbulent premixed flames of methane-air mixtures are simulated using the URANS approach. The mean chemical reaction rate is modelled using strained and unstrained flamelet models and the algebraic model of Bray (1979). The unstrained flamelet model requires $\tilde{c}$ and $\widetilde{c''^2}$ for its computation, while the strained flamelet model (Kolla and Swaminathan, 2010*a*) uses the mean scalar dissipation rate, $\tilde{\epsilon}_c$, in addition to $\tilde{c}$ and $\widetilde{c''^2}$. The values of $\tilde{c}$ and $\widetilde{c''^2}$ are obtained by solving their transport equations and the mean dissipation rate is obtained using two algebraic models. These models are obtained by balancing the leading order terms of the transport equation for the mean scalar dissipation rate. One of this algebraic model was proposed in an earlier study (Kolla et al., 2009) for statistically planar flames and the second model includes the effects of mean curvature. The turbulence is modelled using the k-ε equations.

These models are first validated by computing a spherical methane-air flame

investigated experimentally in an earlier study (Hainsworth, 1985). A good comparison between the computed and measured flame ball growth rate is observed for the strained flamelet model and the other two combustion submodels yield a faster growth.

Statistically planar and spherical flames, fourteen flames in total, experiencing low and high turbulence stretch rates are computed using strained flamelet model and these flames are analysed in detail to understand the influence of geometry on their propagation. For the conditions investigated in this study, including curvature corrections in the algebraic model for $\tilde{\epsilon}_c$ did not influence the flame propagation. Detailed analyses of the computed flames showed that the advancement of the leading edge is aided by the local fluid velocity in the spherical case. In the planar flames, the directions for the fluid flow and the advancing leading edge are opposite. The planar flame showed a steady propagation once a balance between the local flow and displacement speeds is achieved for a given turbulence conditions. The spherical flames accelerated continuously because of the compounded effects of flow and leading edge displacement. This continuous acceleration cause the heat-release induced convective effects to be dominant for the growth of the flame brush thickness.

The flame geometry is observed to influence the magnitude of turbulent scalar flux at the leading edge, spherical flames showing larger magnitude compared to the planar flames for a given turbulence and thermochemical conditions. The mean reaction rate is found to be less influenced by the flame geometry. Thus, the influence of flame geometry on the turbulent flame speed, leading edge displacement speed, is observed to result from the contribution of the turbulence scalar flux. The turbulent flame speed, s_t, of the spherical flames is observed to be 10 to 20% greater than the corresponding planar flame values for the conditions investigated in this study. For a constant value of turbulence stretch rate, $s_t \sim u'$ as noted by Bray (1990) and this scaling is observed for both planar and spherical flames. The values of s_t, normalised by the laminar flame speed, for the 14 flames computed in this study scales as Re_t^n with $0.57 \leq n \leq 0.58$. This scaling is consistent with the classical analysis of Damköhler. The consumption speed also shows a similar scaling with Re_t. The results presented in this chapter is encouraging in using scalar dissipation rate based models to simulate turbulent

combustion in spark-ignition engines, which involve expanding flame balls.

The numerical method used in this chapter is used to simulate hydrogen-air spherical flames in the following chapter.

5. Spherical hydrogen-air flames

Results from the simulation hydrogen-air spherical flames are presented in this chapter. The numerical method described in Chapter 3 is used to simulate these flames. Application of this numerical method for hydrocarbon flames has been explained in the preceding chapter. The main aim of this chapter is to assess the predictive ability of the scalar dissipation rate based combustion models in simulating hydrogen-air flames, which have non-unity Lewis numbers. In addition, the effect of turbulence on the propagation of hydrogen-air flames is investigated, and results obtained for hydrogen-air flames are compared with those of methane-air flames obtained in Chapter 4.

5.1 Introduction

The envisaged depletion of fossil fuel resources and a need to reduce pollutants emission from combustion have led to a surge in finding alternative energy sources. Hydrogen is considered as a potential future energy carrier with many benefits over the current hydrocarbon fuels (DeLuchi, 1989; Ogden, 1999; Balat, 2008). In particular, good combustion characteristics of hydrogen make it an attractive fuel for internal combustion engines (White et al., 2006; Verhelst and Wallner, 2009). Hydrogen has certain favourable combustion properties such as wide flammable range and large burning velocity, which render hydrogen as an ideal additive to improve combustion characteristics of new and bio-derived hydrocarbon fuels (Bauer and Forest, 2001). Also, fundamental understanding of hydrogen combustion is important from safety view points; for example, generation and accumulation of hydrogen in nuclear reactors (Stohl et al., 2012) and rupturing of a pressurised hydrogen storage tank can lead to explosions.

A spherically expanding flame is commonly used to investigate fundamental characteristics of hydrogen-air combustion from various view points and these studies related to internal combustion engines (Verhelst and Wallner, 2009) and safety aspects (Kumar et al., 1989; Molkov et al., 2007) have been reviewed in the past. In earlier experimental studies the influence of fluid dynamic stretch, κ, on

the laminar flame speed, s_L^0, were ignored. This influence is given in Eq. (2.37) for small values of κ and the Markstein length scale $\mathcal{L}$ can be positive or negative (Law and Sung, 2000). For a spherical flame with radius r_f, the stretch rate is defined as: $\kappa = (2/r_f)(\mathrm{d}r_f/\mathrm{d}t)$ (Law and Sung, 2000). Later studies (Dowdy et al., 1990; Kwon et al., 1992*a*; Aung et al., 1998; Kwon and Faeth, 2001; Tse et al., 2000; Kwon et al., 2002; Verhelst, 2005; Verhelst et al., 2005) showed that the stretch effects must be included in the analysis to explain the presence of cellular instabilities observed in experiments of lean hydrogen-air spherical flames. The additional flame area resulting from this instability led to an increase in s_L, implying a negative $\mathcal{L}$ for thermo-diffusively unstable lean hydrogen-air mixtures. The stoichiometric and rich mixtures showed positive $\mathcal{L}$.

Since the thermo-diffusive instabilities result from differential and/or preferential diffusion phenomena, the Lewis number is typically used to identify thermo-diffusively unstable mixtures. Lewis number is typically less than unity for lean hydrogen-air mixtures (Law and Sung, 2000) and these flames are more susceptible to cellular instability (Tse et al., 2000; Verhelst et al., 2005; Bradley et al., 2007; Kitagawa et al., 2008). A review of these studies on thermo-diffusive instabilities can be found in Matalon (2007).

Similar to methane-air flames considered in Chapter 4, turbulent spherical hydrogen-air flames have been investigated using fan-stirred bombs (Wu et al., 1990; Kwon et al., 1992*b*; Aung et al., 2002; Kido et al., 2002; Kitagawa et al., 2008) and wind tunnels with grid turbulence (Renou et al., 1998, 2000) to address the role of turbulence. These studies showed that the turbulent burning velocity is increased when the reactant mixture yields thermo-diffusively unstable flames and this effect is pronounced when the turbulence is weak. Accounting for thermo-diffusive instability effects in turbulent combustion modelling is a challenging task and is still an open question although some attempts has been made in the past to include hydrodynamic instability effects (Paul and Bray, 1996). One way to account for thermo-diffusive instability effects is to use an effective Lewis number to modify the turbulent burning velocity expressions as has been done in Muppala et al. (2009) for hydrocarbon flames. An alternative approach is to include the instability effects in laminar flame speed correlations obtained using spherically expanding laminar flames and use them as input to

turbulent combustion models based on turbulent burning velocity or flame surface density (Gerke, 2007). These approaches were shown to yield a satisfactory comparison with measurements for laboratory scale flames (Muppala et al., 2009), a single-cylinder compression machine (Gerke, 2007) and spark-ignited internal combustion engines (Rakopoulos et al., 2010). Following the second approach, the thermo-diffusive effects are expected to be included when s_L^0 calculated with detailed chemistry and transport is used. This philosophy of including thermo-diffusive effects, however, does not seem to be adequate for a test case considered here as one shall see later in section 5.4.1.

The simulations are performed using the numerical approach outlined in Chapter 3. The specific objectives of this work are:

1. To assess the scalar dissipation rate based models given in section 3.2 for turbulent spherical hydrogen-air flames by comparing measured (Kitagawa et al., 2008) and computed results;

2. To compare and contrast turbulent spherical flame propagation characteristics of hydrogen- and methane-air mixtures having the same equivalence ratio and turbulence conditions.

This chapter is organised as follows. The numerical problem setup is described in the next section. Test cases used for model validation are described in section 5.3. Results from these simulations are discussed in section 5.4 along with a comparison of different reaction rate closures. The final section summarises the main learnings from these simulations.

5.2 Numerical setup

The numerical setup described in Chapter 3 is used to simulate spherical hydrogen-air flames. Application of this numerical method to simulate methane-air flames has been described in Chapter 4. In this section, the combustion modelling challenges that are unique to hydrogen-air flames are discussed.

5.2.1 Reaction rate model

Details of the modelling technique have been described in section 2.5.8 and the flamelet library generation was given in section 3.2. For hydrogen-air flames, K_c^* in the algebraic models for the mean scalar dissipation rate [Eqs. (2.69) and (3.14)] takes a value of 0.73τ for $\phi = 0.4$ and 0.66τ for $\phi = 1.0$ (Rogerson and Swaminathan, 2007).

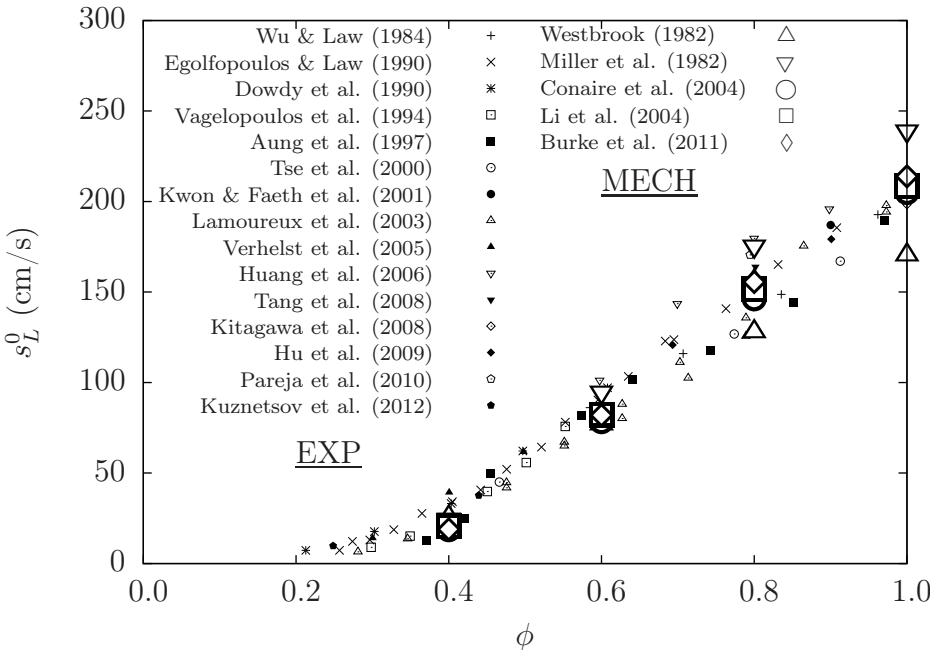

Figure 5.1: Comparison of computed and measured unstretched laminar burning velocity for various equivalence ratios. The experimental values are obtained from 15 earlier studies.

Comprehensive chemical kinetic mechanisms can be used to calculate laminar flames used in the reaction rate modelling technique described in section 3.2; a number of such mechanisms are available for hydrogen-air combustion. Figure 5.1 compares unstretched laminar burning velocity, s_L^0, computed in this study employing several such mechanisms (Westbrook, 1982; Miller, 1982; Ó Conaire et al., 2004; Li et al., 2004; Burke et al., 2011), denoted as MECH in Figure 5.1, with measured values available in the open literature (Wu and Law, 1984; Egolfopoulos and Law, 1990; Dowdy et al., 1990; Vagelopoulos et al., 1994; Aung et al., 1997;

Tse et al., 2000; Kwon and Faeth, 2001; Lamoureux et al., 2003; Verhelst et al., 2005; Huang et al., 2006; Tang et al., 2008; Kitagawa et al., 2008; Hu et al., 2009; Pareja et al., 2010; Kuznetsov et al., 2012).

These experiments, denoted as EXP in Figure 5.1, were conducted at atmospheric pressure and reactant temperature of about 300 K using various flame configurations such as outwardly propagating spherical, stagnation point and counter-flow flames. These results are shown in Figure 5.1 only for the equivalence ratio spanning from lean to stoichiometric range. There is a large scatter in the experimental data and the computational results for various chemical mechanisms used here agree quite well for lean mixtures but the values of s_L^0 obtained using the mechanisms of Westbrook (1982) and Miller (1982) are beyond the experimental scatter. The values obtained using the mechanisms of Ó Conaire et al. (2004), Li et al. (2004) and Burke et al. (2011) are in good agreement with the experimental data for $\phi = 1$ mixture. The mechanism of Li et al. (2004) is used in this study to calculate turbulent spherical flames of hydrogen-air mixture having $\phi = 0.4$ and 1. In addition, the mechanism of Westbrook (1982) is used for the strained flamelet in order to find the effect of the chemical mechanism.

Unlike the methane-air flame simulated in Chapter 4, hydrogen-air flames typically have non-unity Lewis numbers and the method used in this study to account for this effect is described next.

5.2.2 Accounting for non-unity Lewis number

One needs at least two degrees of freedom to describe the thermochemical state of a mixture with non-unity Lewis number, since the temperature and mass fraction evolve differently. Thus, two progress variables are used in this study to account for this. One is based on H_2O mass fraction normalised by its burnt side value in an unstrained laminar flame, defined as $c = c_{\mathrm{H2O}} = Y_{\mathrm{H2O}}/Y^b_{\mathrm{H2O}}$ and another one is based on temperature $c_T = (T - T_u)/(T_b - T_u)$. In this work, water vapour is used instead of H_2 for the progress variable because the Lewis number of H_2O is close to unity. It is well-known that non-unity Lewis number flames can display super-adiabatic values of temperature (Rutland and Trouvé, 1993; Chakraborty and Cant, 2005); therefore, it is questionable to use temperature based progress

variable for such cases. Indeed, such super-adiabatic behaviour was observed for the lean hydrogen-air flame simulated in this work.

The variation of c with c_T in the laminar strained and unstrained flames is shown in Figure 5.2(a). If c and c_T are identical then the variation in Figure 5.2(a)

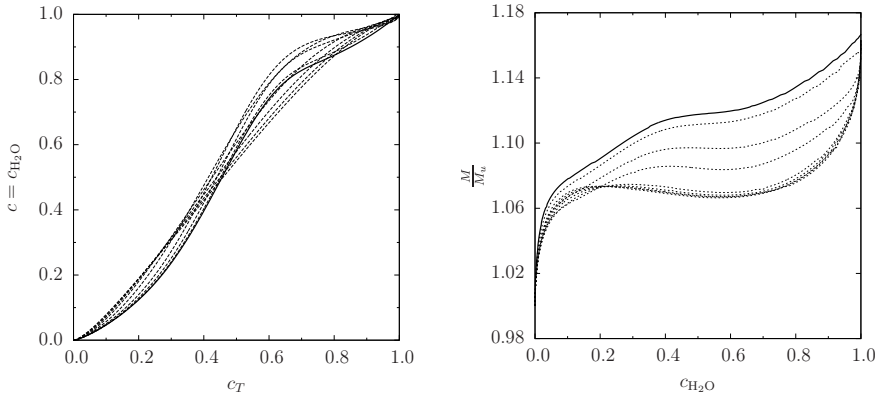

Figure 5.2: Variation of (a) $c = c_{H_2O}$ with c_T and (b) mixture molecular weight, M, normalised by its unburnt side value, across unstrained (solid line) and strained (dashed lines) flamelets.

should fall on the diagonal line and this result clearly show that the difference between these two progress variables is large on the burnt side. This is as expected and a similar observation has been made in turbulent flames as well (Chakraborty and Cant, 2009; Minamoto et al., 2011). The mixture molecular weight also changes considerably, nearly 18%, across the flamelets as shown in Figure 5.2(b). For these reasons, the mean density is calculated as

$$\frac{\overline{\rho}}{\rho_u} = \left(\frac{\overline{M}}{M_u} \right) \frac{1}{(1 + \tau\, \tilde{c}_T)}, \tag{5.1}$$

using the equation of state. The non-unity Lewis number effects on the chemical source terms is presumed to be included at the flamelets level since detailed transport and chemical kinetics are used to compute the necessary laminar flames. This is akin to the methodology used in earlier studies as noted in the introduction. Thus, two Favre-averaged progress variables, $\tilde{c}$ and $\tilde{c}_T$, and $\widetilde{c''^2}$ equations

in addition to other conservation equations are solved for the turbulent flames. Note that $\tilde{c}$ is used as an independent variable in the flamelet library generation and the chemical source terms $\overline{\dot{\omega}}_c, \overline{\dot{\omega}}_{c_T}$ and $\overline{\dot{\omega}'' c''}$ are obtained using the method described in section 3.2. As before a single variance equation corresponding to $\tilde{c}$ is solved as well. Since the molecular diffusivities are smaller than turbulent diffusivities, the difference between the $\tilde{c}$ and $\tilde{c}_T$ transport equations is only in their respective source terms.

The algebraic model for the mean scalar dissipation rate, $\tilde{\epsilon}_c$ is influenced by Lewis number (Chakraborty and Swaminathan, 2011). Using the closure models proposed by Chakraborty and Swaminathan (2011), one could modify the closure model given in Eq. (2.69). A significant difference in the results were not observed during initial tests using this modified version of $\tilde{\epsilon}_c$, hence it is not considered further.

5.3 Test flames

The numerical model of an outwardly propagating turbulent spherical flame described in the previous section is used to investigate turbulence effect on the propagation of hydrogen-air spherical flames. The results of these simulations will be compared to spherical methane-air flames presented in Chapter 4. Before discussing these test cases, experimental flames, used to assess the validity of scalar dissipation rate based combustion models for hydrogen-air mixtures, are described.

5.3.1 Experimental flame

Spherically expanding turbulent hydrogen-air flames inside a fan-stirred combustion vessel investigated by Kitagawa et al. (2008) are considered for the assessment of the reaction rate models. In these experiments, turbulent flame propagation was reported for two equivalence ratios (ϕ = 0.4 and 1) at two different initial pressures, 1 and 5 atm and an initial temperature of 300 K. Out of these cases, only the atmospheric flames are considered here for computational reasons. Thermo-chemical characteristics of these two flames are given in Table 5.1

and $\tau \neq \rho_u/\rho_b - 1$, specifically for $\phi = 1$ case, due to the variation of mixture molecular weight across the flame front as noted earlier.

Table 5.1: Thermo-chemical conditions of experimental flames (Kitagawa et al., 2008) considered for this study

ϕ	s_L^0 (m/s)	δ_L^0 (mm)	δ (mm)	ρ_u/ρ_b	τ
0.4	0.21	0.67	0.09	4.31	3.66
1.0	1.98	0.35	0.01	6.84	6.97

Two fans, continuously running during the experiments, were used to mix the reactants inside the vessel and to generate non-decaying isotropic turbulence. Experiments were conducted at two turbulence intensities and the higher turbulence case with rms of velocity fluctuations, u', of 1.59 m/s is simulated in this study. The experimentally determined turbulence integral length scale, Λ, was 10.3 mm. Since turbulence in the experiment is non-decaying, values of $\tilde{k}$ and $\tilde{\varepsilon}$ were frozen for the simulations. As with the methane-air experiments of Hainsworth (1985) described in Chapter 4, the propagation of turbulent flames was recorded using high speed schlieren photography in the experiments of Kitagawa et al. (2008) and as before the flame radius, r_f, is defined using $\tilde{c} = 0.05$ in the simulations.

5.3.2 Test cases for further analyses

Outwardly propagating turbulent spherical flames in an unconfined space are considered and the influences of heat release on turbulence are also included in these simulations by solving for $\tilde{k}$ and $\tilde{\varepsilon}$ unlike in the above experimental cases. Only stoichiometric hydrogen-air mixture at 300 K and atmospheric pressure are considered. The hydrogen-air flame results are to be compared with stoichiometric methane-air flames under the same initial pressure, temperature, and turbulence (u'/s_L^0 and Λ/δ) conditions to understand their relative behaviour. The thermo-chemical characteristics of stoichiometric methane-air flame are: $s_L^0 = 0.4$ m/s, $\delta_L^0 = 0.41$ mm, $\delta = 0.047$ mm, $\tau = 6.48$ and $\rho_u/\rho_b = 7.54$.

The conditions of the three stoichiometric hydrogen-air flames used for comparative analyses are depicted in the combustion regime diagram shown in Figure 5.3. These flames have the same stretch factor, $K = 0.157\,(u'/s_L^0)^2\,\mathrm{Re}_t^{-0.5}$

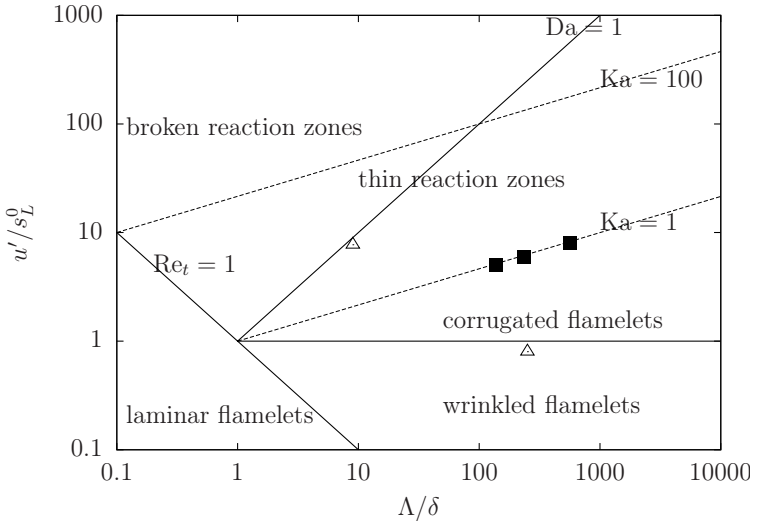

Figure 5.3: Turbulent premixed combustion regime diagram (Peters, 1999) showing the conditions of test cases for further analyses (■) and the experimental case of Kitagawa et al. (2008) (△) considered in this study.

= 0.157 (Abdel-Gayed et al., 1987), where the turbulent Reynolds number is defined as $\mathrm{Re}_t = u'\Lambda/\nu$ with ν as the kinematic viscosity of the reactant mixture. For these flames, u'/s_L^0 values are 5, 6 and 8 and the stoichiometric methane-air flames also have the same combustion conditions as those for H_2-air flames shown in Figure 5.3. All of these flames are in the border between corrugated flamelets and thin reaction zones regime. The experimental flames of Kitagawa et al. (2008) are also shown in this figure – the stoichiometric flame is near the border between wrinkled and corrugated flamelets while the lean flame with $\phi = 0.4$ is near Da = 1 line, where $\mathrm{Da} = (\Lambda/\delta)/(u'/s_L^0)$ is the Damköhler number.

5.4 Results and discussion

The computational results of spherically propagating hydrogen-air flames under a range of turbulence conditions are analysed in this section. Validation of the computational models is discussed first before presenting comparative analyses of hydrogen- and methane-air flames experiencing the same turbulent combustion conditions.

5.4.1 Validation

The amount of heat released by burning m_f amount of fuel is simply given by $Q = m_f\, Q_{\mathrm{LHV}}$, where $Q_{\mathrm{LHV}} = 120$ MJ/kg is the lower heating value of hydrogen (Verhelst and Wallner, 2009). The amount of fuel consumed by the spherical turbulent flame when its leading edge moves from a radius of $r_{f1} = 4.2$ cm to $r_{f2} = 7.74$ cm over a period of $\Delta t = 1.7$ ms is $m_f = \rho_u\, Y_{f,u} 4\pi \left(r_{f2}^3 - r_{f1}^3\right)/3$, where $Y_{f,u} = 0.028$ is the fuel mass fraction in the stoichiometric hydrogen-air mixture. The leading edge radius, r_f, is defined using $\tilde{c} = \tilde{c}_1 = 0.05$ iso-level in the simulation and the above radii and Δt are taken from one of the simulations chosen arbitrarily. The theoretical value for the heat release is 4.68 kJ and this value calculated from the results of numerical simulation using

$$Q = 4\pi \left(T_b - T_u\right) \int_t^{t+\Delta t} \left[\int_{r_{f1}}^{r_{f2}} \overline{C}_p(r,t)\, \overline{\dot{\omega}}_{c_T}(r,t)\, r^2 \ \mathrm{d}r \right] \mathrm{d}t, \tag{5.2}$$

agrees within 6% of the above value. The symbol $\overline{C}_p(r,t)$ is the mean mixture heat capacity at constant pressure. This level of agreement is acceptable in the light of various approximations made in the modelling of turbulence and combustion.

As noted earlier, two atmospheric flames, $\phi = 1$ and 0.4, of Kitagawa et al. (2008) are simulated to assess the validity of scalar dissipation rate based models for hydrogen-air combustion. The variation of turbulent flame propagation speed, u_t, with r_f was reported in Kitagawa et al. (2008) and this will be used for the validation purpose. This speed is defined as (Andrews and Bradley, 1972):

$$u_t = \frac{\overline{\rho}_b}{\rho_u} \frac{\mathrm{d}r_f}{\mathrm{d}t}, \tag{5.3}$$

where $\overline{\rho}_b$ is the mean density of the burnt gases. As with the methane-air flame results given in section 4.3, the numerical simulations give $\tilde{c}(r,t)$, and thus it is straightforward to compute u_t. Figure 5.4 compares the computed and measured u_t variation with r_f for the stoichiometric, Figure 5.4(a), and lean, Figure 5.4(b), hydrogen-air flames. The computational results are shown for three combustion models described in section 3.2. The chemical kinetics mechanism of Li et al. (2004) is used for the unstrained flamelets model in Eq. (2.63). The mechanisms

of both Li et al. (2004) (noted as mech 1 in Figure 5.4(a)) and Westbrook (1982) (mech 2) are used for the strained flamelets model in order to assess the influence of chemical kinetics. Both the algebraic and the unstrained flamelet models yield larger u_t values.

The strained flamelet model with the mechanism of Li et al. (2004) is able to capture the measured variation reasonably well, whereas the values of u_t computed using the mechanism of Westbrook (1982) are smaller as in Figure 5.4(a). This is because the mechanism of Westbrook (1982) underpredicts the laminar burning velocity, s_L^0, as was shown in section 5.2.1. This highlights the importance of choosing a chemical mechanism that gives accurate laminar flame characteristics required for the strained flamelets model. The maximum error between the measured and computed u_t values is about 5% for the strained flamelets model and this error is well within the experimental scatter of Kitagawa et al. (2008).

The variation of u_t shown in Figure 5.4 suggests that the burning velocity for the spherical flame is not constant as has been observed in many earlier studies (Kwon et al., 1992*b*; Aung et al., 2002). In turbulent flames, the mean reaction rate depends on the fuel, the equivalence ratio and local turbulent strain rate (Cant and Bray, 1989). In these flames, local fluid dynamic strain induced by turbulent eddies acts to reduce the burning rate. Amongst the models used in this study, the strained flamelets model seems to describe both the complex chemistry and the local fluid dynamic effects quite well for stoichiometric hydrogen-air flame. This flame is thermo-diffusively stable whereas the lean flame having $\phi = 0.4$ is thermo-diffusively unstable as noted by Kitagawa et al. (2008). Figure 5.4(b) compares the measured and computed u_t values for $\phi = 0.4$ flame. All the three models severely underestimate the turbulent burning velocity because these models do not include the influences of thermo-diffusive instability on the propagation of turbulent flame leading edge. Including these effects in turbulent combustion modelling is a challenging task and one way to include them may be through the use of Markstein numbers but this approach is strictly valid for small stretch rates $\kappa^+ \equiv \kappa\delta_L^0/s_L^0 \ll 1$ (Poinsot and Veynante, 2005). In the remainder of this chapter only stoichiometric hydrogen-air flames simulated using the strained flamelet model [Eq. (3.10)], will be considered for further and comparative analyses.

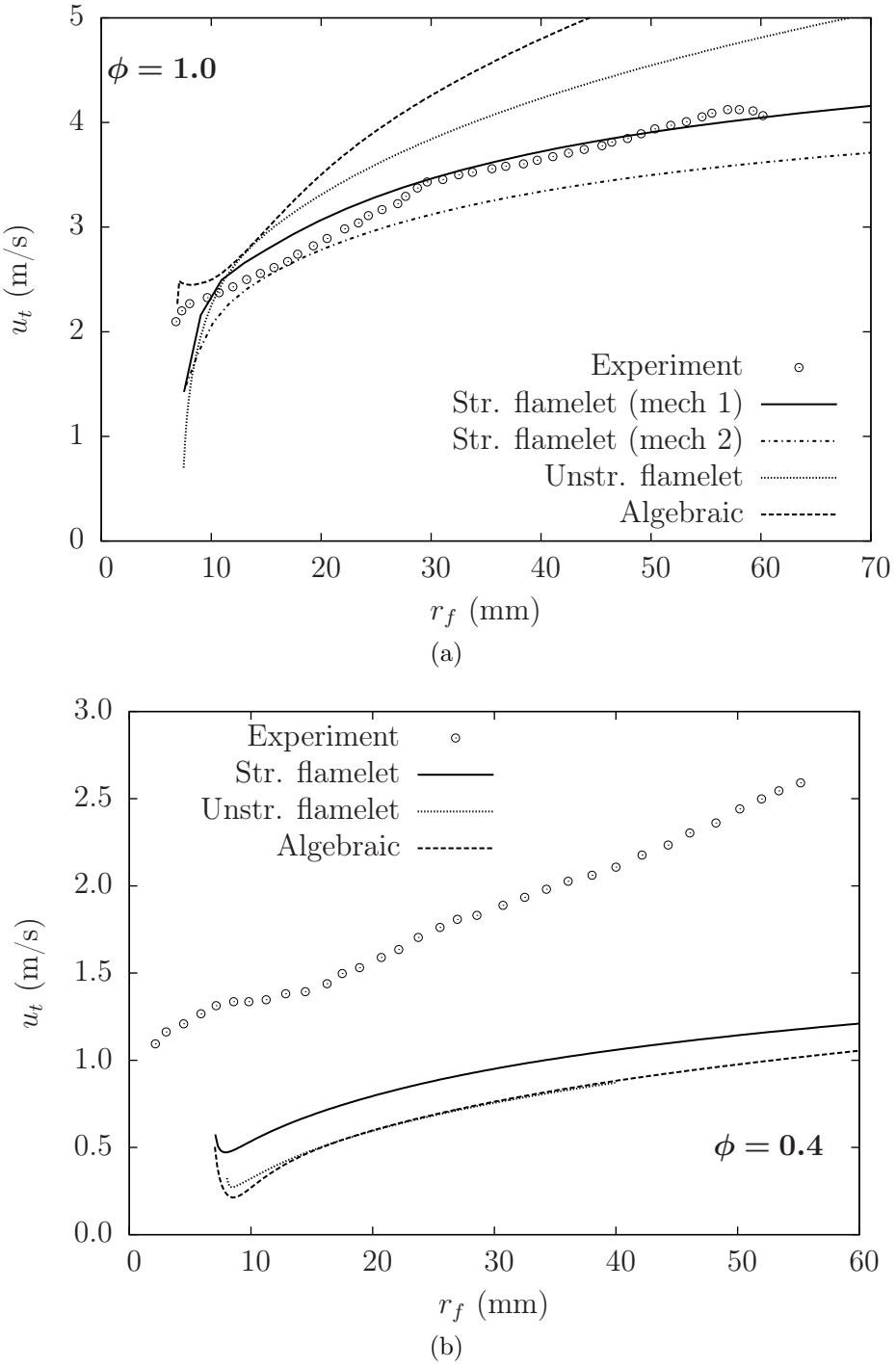

Figure 5.4: Comparison of computed and measured variation of u_t with r_f in (a) stoichiometric and (b) lean hydrogen-air flames.

5.4.2 Comparison of hydrogen- and methane-air flames

Propagation characteristics

The stoichiometric hydrogen- and methane-air spherical flames experiencing the same combustion conditions are compared in this section. Typical evolution of these flames is shown in Figure 5.5 for $u'/s_L^0 = 6$ case. Both of these flames evolve from the same initial variation of $\tilde{c}$ shown as dashed lines and the results are shown for a period of 3 ms at an equal interval of 1 ms. The symbols used for 3 ms indicates typical spatial resolution used in simulations. The stoichiometric hydrogen flames propagate faster than the methane flames, which is expected since the laminar burning velocity for the hydrogen-air mixture is larger than for the methane-air mixture.

Variation of flame radius, normalised by its initial value, with time is shown in Figure 5.6 for all 6 (3 H_2- and 3 CH_4-air) flames considered in this study. For a given combustion condition denoted by u'/s_L^0 and Λ/δ, the hydrogen flames propagate significantly (nearly 4 to 5 times) faster compared to methane-air flames. This result also shows that the increase in u', for a constant K or Ka, results in faster flame propagation for both of these fuel-air mixtures. This increase in flame propagation speed agrees with many previous studies summarised by Lipatnikov and Chomiak (2002).

Turbulent flame speed and consumption speed

The importance of the turbulent flame speed, s_t, has been described in section 4.3.2. As described in this section, s_t is defined to be the displacement speed of the flame brush leading edge, marked using $\tilde{c} = 0.05$. The displacement speed, s_d, is given in Eq. (4.1). Methane-air flame simulations in Chapter 4 have already shown that s_d is influenced directly by the mean reaction rate, turbulent flux and molecular diffusion. Note the difference in definitions of s_t and the turbulent burning velocity, u_t, given in Eq. (5.3).

Figure 5.7(a) shows the variation of normalised turbulent flame speed, s_t/s_L^0, with turbulent Reynolds number, Re_t. The results are shown for a normalised time of $t^+ = 8$ and the results for other earlier times are similar to those shown

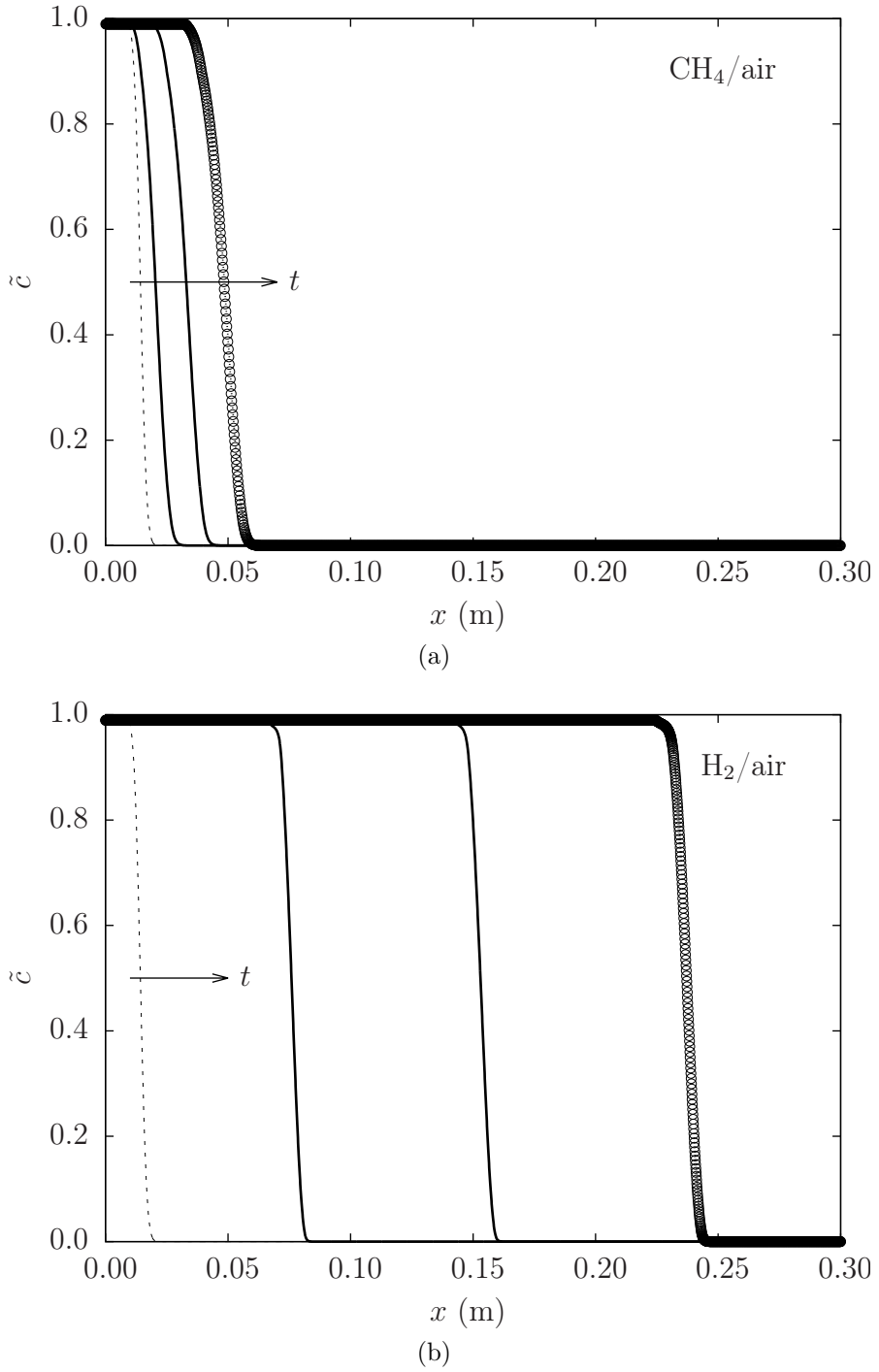

Figure 5.5: Spatial variation of $\tilde{c}$ at four instances from 0 to 3 ms at an interval of 1 ms in (a) CH_4-air and (b) H_2-air flames having $u'/s_L^0 = 6$.

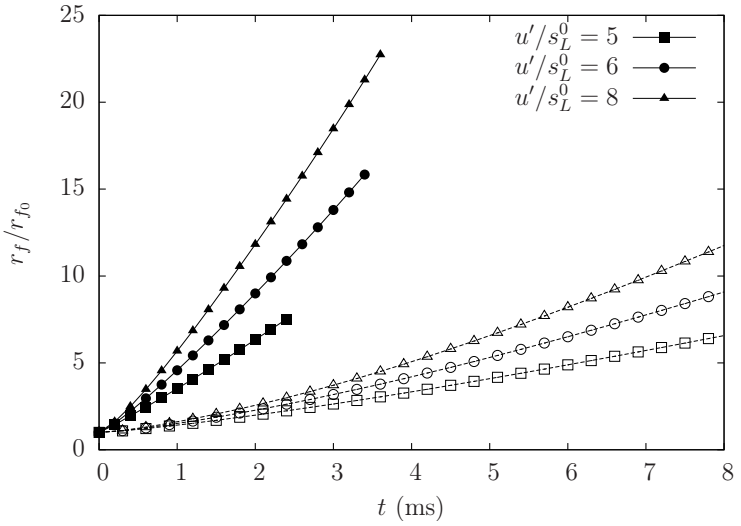

Figure 5.6: Temporal variation of normalised flame radius of CH_4-air (open symbols) and H_2-air (closed) turbulent flames at various combustion conditions.

here, as noted in section 4.3.2 for methane-air flames. The inset shows the variation of s_t/s_L^0 with u'/s_L^0, which again suggests $s_t \sim u'$. The slopes of s_t/s_L^0 versus u'/s_L^0 curves are 6.3 and 4.4 respectively for the methane- and hydrogen-air flames considered here. It was observed earlier in section 4.3.2 that this slope became steeper when the stretch factor, K, is increased.

These results suggest the same scaling relation, $s_t/s_L^0 \simeq B\mathrm{Re}_t^n$, is applicable for both flames, with $n \approx 0.5$. The least squares fit shown in the figure suggests $B = 0.21$ for the methane- and 0.16 for hydrogen-air flames. The variation of consumption speed, s_c [defined in Eq. (4.3)] with Re_t is shown in Figure 4.11(b)]. The scaling of s_c/s_L^0 with Re_t is similar to that of s_t/s_L^0, albeit with a lower magnitude. As with s_t/s_L^0, the computed values of s_c/s_L^0 are about 20% lower for hydrogen-air flames when compared with methane-air flames; this is due to the larger s_L^0 value.

Turbulent flame brush thickness

Figure 5.8 shows the temporal variation of flame brush thickness for the stoichiometric H_2-air flame with $u'/s_L^0 = 8$. The flame brush thickness is normalised using the laminar flame thermal thickness and time is normalised using the flame

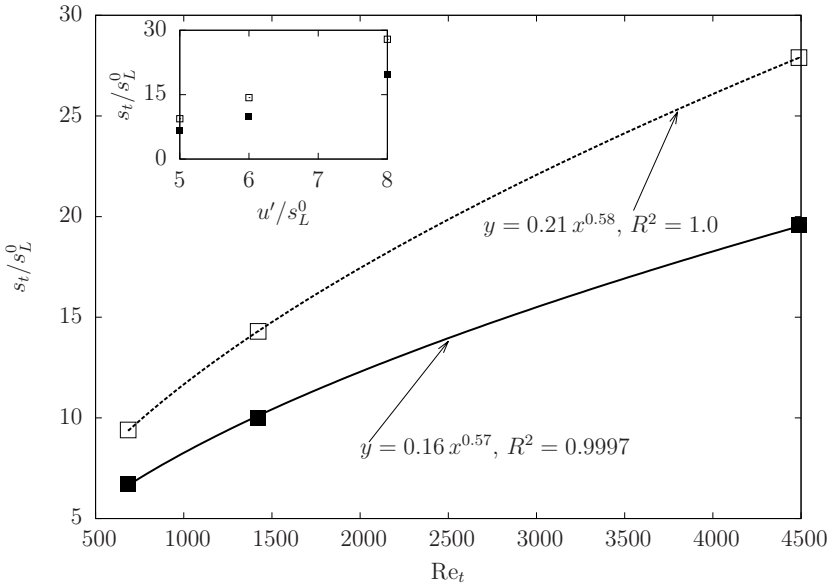

(a)

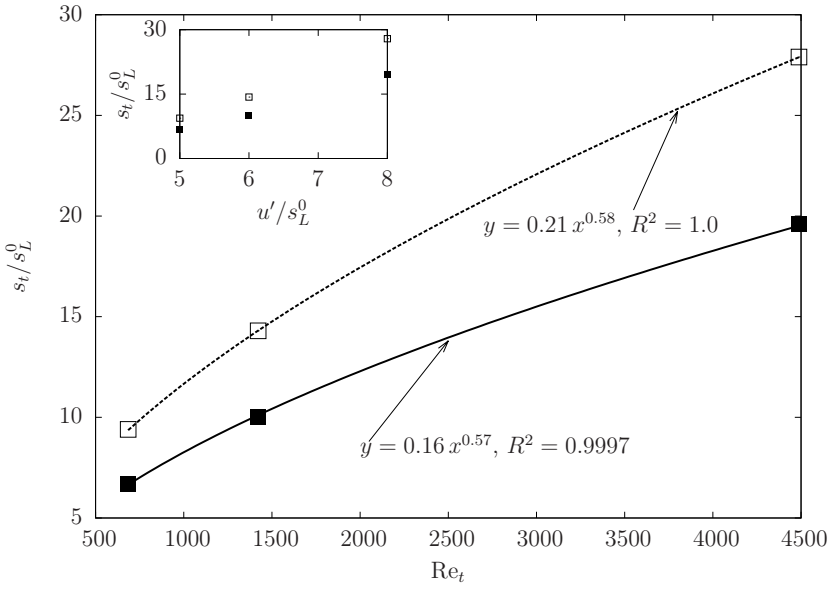

(b)

Figure 5.7: Variation of normalised turbulent (a) flame and (b) consumption speeds of H_2-air (closed symbols) and CH_4-air flames (open) with turbulence Reynolds number. The inset shows the variations with u'. The results are shown for $t^+ = 8$.

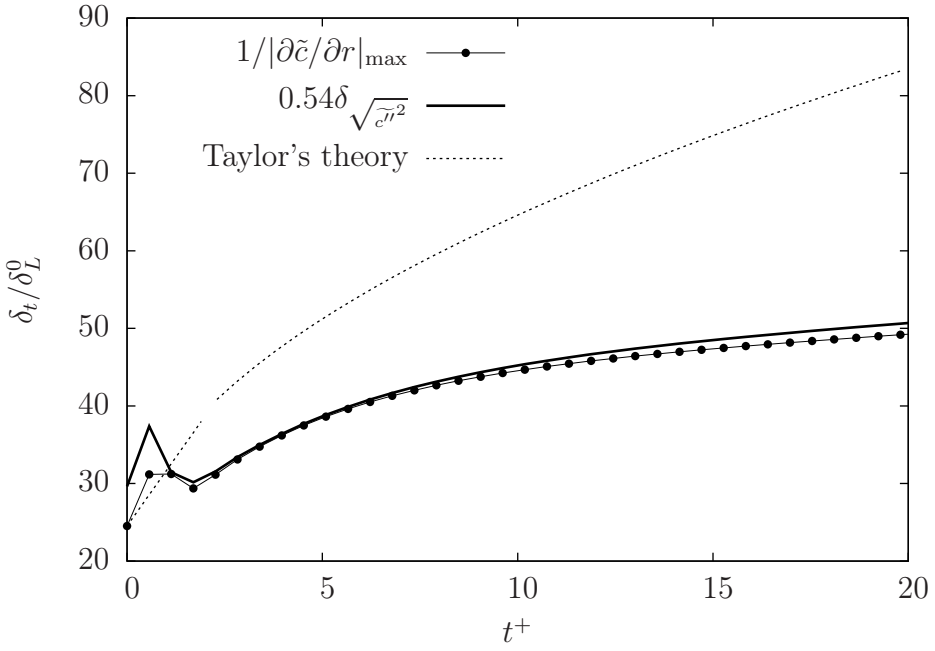

Figure 5.8: Temporal variation of normalised flame brush thickness for H_2-air flame with $u'/s_L^0 = 8$.

time, $t_c = \delta_L^0/s_L^0$. As in section 4.3.2, the turbulent flame brush thickness is calculated using the maximum gradient of $\tilde{c}$ and the variance, $\widetilde{c''^2}$ (which is scaled in Figure 5.8). After going through some initial transients, both thickness grow with time. If the turbulent diffusion plays the central role for this growth then one would expect to see a growth similar to that shown for Taylor's theory (also plotted). This theory suggests a linear variation for $t^+ \ll$ Da and a square root dependence for $t^+ \gg$ Da. It is apparent that the computed thicknesses do not follow these variations as it has been observed for methane-air flames (see section 4.3.2). Thus, it is concluded here the growth of the flame brush thickness in the stoichiometric hydrogen-air flames studied here is governed by the differential propagation of the leading and trailing edges of the flame brush as for the methane-air flames, i.e. the leading edge propagates faster compared to the trailing edge.

According to the concept of turbulent premixed combustion regimes, two flames with identical values for Λ/δ, u'/s_L^0 and τ are expected to have simi-

lar s_t/s_L^0. Although these quantities are kept to be identical for the hydrogen- and methane-air flames investigated in this work, there is a significant difference in s_t/s_L^0. The well known KPP analysis (Zeldovich et al., 1985) shows that s_t strongly depends on the rate of change of $\overline{\dot{\omega}}_c$ with respect to $\tilde{c}$, as $\tilde{c} \to 0$. This quantity not only depends on the turbulence-chemistry interaction but also on the combustion kinetics. The turbulence-chemistry interaction is expected to be predominantly the same if u'/s_L^0 and Λ/δ are kept the same. To gain an understanding of $\left(\partial\overline{\dot{\omega}}_c/\partial\tilde{c}\right)_{\tilde{c}\to 0}$, the variation of $\overline{\dot{\omega}}_c$ with $\tilde{c}$ is studied next.

Mean reaction rates

Figure 5.9(a) shows a comparison of the mean reaction rate variation across the flame brush for planar and spherical hydrogen-air flames. The mean reaction rates are normalised by the respective maximum value inside the flame brush. It was shown earlier in Figure 4.10 for methane-air flames that the normalised mean reaction rates are insensitive to geometry. The plots in Figure 5.9(a) shows that this is true even for hydrogen-air flames. Only the flame at $u'/s_L^0 = 6$ is shown in this figure but it is expected that this will hold for other flames as well.

Figure 5.9(b) shows a comparison of the normalised mean reaction rates for spherical hydrogen- and methane-air flames. The top inset in this figure, shows the maximum value of the normalised mean reaction rate, $\overline{\dot{\omega}}^+_{\mathrm{max}}$, for different turbulence conditions considered for this study. As was shown previously for methane-air flames, these results show that, the turbulence level does not have a significant effect on $\overline{\dot{\omega}}^+_{\mathrm{max}}$ for hydrogen-air flames as well. However, there is some difference in the variation of normalised reaction rate across the flame brush between the methane- and hydrogen-air mixtures. The mean reaction rate is more uniform inside the flame brush for hydrogen compared to methane. The difference between these two flames looks small for low $\tilde{c}$ values, however the bottom inset clearly shows that there is a substantial difference. The value of $\left(\partial\overline{\dot{\omega}}_c/\partial\tilde{c}\right)_{\tilde{c}\to 0}$ for the hydrogen flame can be two orders of magnitude larger than for the methane flame. This is because of the low activation temperature for hydrogen combustion. Obviously, this parameter is related to chemical kinetics of the fuel.

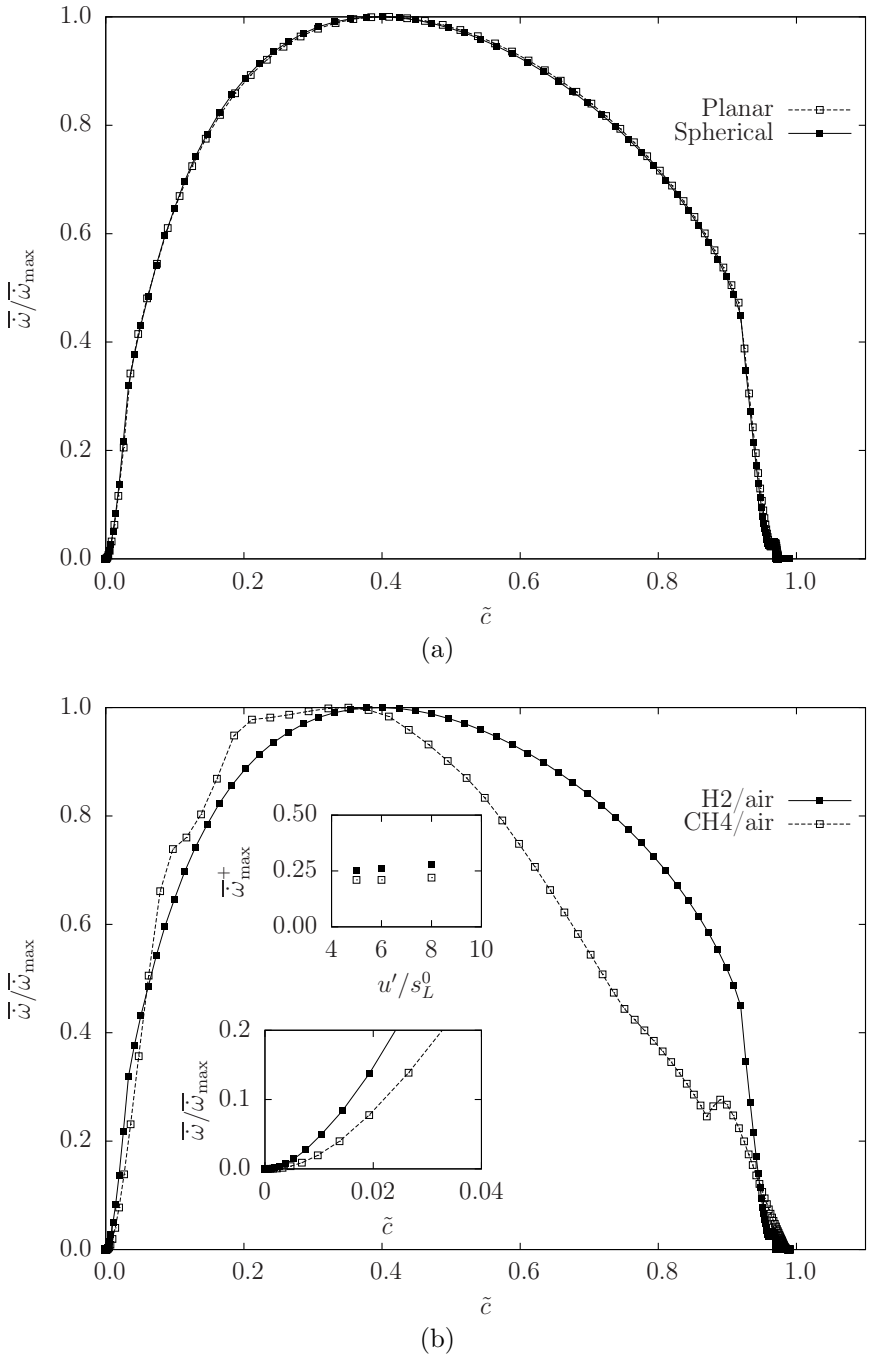

Figure 5.9: Comparison of normalised mean reaction rate for $u'/s_L^0 = 6$ at $t^+ = 8$ between (a) planar and spherical H_2-air flames and (b) H_2- and CH_4-air flames. The top inset shows the variation of $\overline{\dot{\omega}}^{+}_{\max}$, normalised as $\overline{\dot{\omega}}_{\max}\delta_L^0/(\rho_u s_L^0)$, with u'/s_L^0.

5.5 Summary

Numerical simulations of turbulent spherical hydrogen-air flames have been performed using RANS methodology employing three different reaction rate closures based on the scalar dissipation rate: an algebraic model of Bray (1979), strained and unstrained flamelets. Since the hydrogen-air mixture has non-unity Lewis number, a two progress variable approach is used in this work to account for differential evolution of temperature and mass fraction in hydrogen-air combustion. This modelling approach is assessed using the experimental data of Kitagawa et al. (2008). The measured variation of propagation speed of flame brush leading edge with flame radius is compared with the computed values for stoichiometric and a lean, $\phi = 0.4$, flames. This comparison demonstrate that the stretch effects on flamelets must be included to capture experimental measurements. The strained flamelets model is able to capture the experimental variations quite well while the unstrained flamelets and the algebraic models give faster flame propagation. Also, the results also showed that the chemical kinetics mechanism to be used in the calculation must capture the laminar flame characteristics such as burning velocity, flame thermal thickness, flame structure, etc., of the corresponding mixture well. The use of the strained flamelets modelling approach is justified for stoichiometric hydrogen-air flames as these flames are thermo-diffusively stable. The propagation speed of the lean flame, which is thermo-diffusively unstable, is underestimated by all three combustion models used in this study. It seems that the approach of including the thermo-diffusive effects in the laminar flamelets is inadequate and an alternative methodology need to be found.

The results of stoichiometric hydrogen- and methane-air spherical flames obtained using strained flamelets model are analysed comparatively to understand the relative effects of turbulence on the propagation of these flames. It is observed that for a constant value of turbulence stretch rate, $s_t \sim u'$ for hydrogen-air flames, which was shown earlier for methane-air flames. Furthermore, the normalised turbulent flame speed, s_t/s_L^0, and consumption speed, s_c/s_L^0, scale as Re_t^n, with $n \approx 0.5$ for both mixtures. However, the magnitudes of these speeds are observed to be substantially different for the stoichiometric hydrogen- and methane-air mixtures despite the fact that these H_2- and CH_4-air flames

have identical combustion conditions in terms of u'/s_L^0 and Λ/δ, implying similar turbulence-flame interactions. It is observed that this difference is related to behaviour of $\left(\partial\overline{\dot{\omega}}_c/\partial\widetilde{c}\right)_{\widetilde{c}\to 0}$, which is controlled not only by turbulence and its interaction with the flame but also by chemical kinetics. This gradient value is observed to be nearly two orders of magnitude larger for the H_2-air flame compared to the CH_4-air flame. The predominant role of differential propagation between the leading and trailing edges of the flame brush on the growth of the flame brush thickness is also observed for the hydrogen flames.

Now that the scalar dissipation rate based models have been validated for spherically propagating flames of two different fuel-air mixtures, the aim is to use these models to simulate intermittent combustion, found in internal combustion engines. Before proceeding with a simulation of a practical spark-ignition engine, a simple validation test case for intermittent combustion is carried out as explained in the next chapter.

6. Combustion in a closed vessel with swirl

Flames simulated in Chapters 4 and 5 can be considered to be unconfined and combustion is continuous, where experimental measurements were taken before compression effects due to combustion are felt by the flame. In contrast, intermittent combustion take place in IC engines due to compression of the end gases by the propagating flame. The scalar dissipation rate based models is used in this work to simulate combustion inside a closed vessel, where turbulence is generated through the swirling in-flow of premixed fuel-air mixture. This is used as simple test case for a SI engine. The simulations are performed in a commercially available CFD code called STAR-CD.

6.1 Introduction

Computations of lean flames require reliable and robust combustion models. Eddy dissipation rate based models, commonly used for internal combustion engine simulations, have a limited predictive ability as they do not include the effects of chemical kinetics. The scalar dissipation rate based flamelet models described in section 3.2 have shown to be robust for continuous combustion systems (Chapters 4 and 5).

This modelling approach is used in this chapter to simulate the experiments of Hamamoto et al. (1988). Combustion inside the closed vessel caused the pressure to increase by 10 folds in these experiments. This provides an additional challenge for the models, which were previously only used for constant pressure combustion simulations. As before, a reaction progress variable is used to describe the thermochemical system. The main objective of this work is to validate the flamelets based approach described in section 2.5.8 for combustion in closed vessel with complex flows.

6.2 Experimental test case

The experiment of Hamamoto et al. (1988) is used to assess the performance of strained and unstrained flamelet models that were used to simulate spherical flames in the preceding chapters. This experiment is more representative of real spark-ignition combustion since the compression effects caused by combustion are taken into consideration. Hamamoto et al. (1988) conducted experiments in a cylindrical combustion chamber, where swirling flow was produced by charging the fuel-air mixture tangentially in to the combustion chamber. Swirl increases the turbulence intensity, which leads to an increase in the turbulent flame burning velocity. The mixture was then spark ignited at the centre to create a propagating turbulent flame.

The combustion chamber had a diameter of 125 mm and a width of 35 mm. It was initially at a pressure of 50 kPa and was connected to a tank containing stoichiometric propane-air mixture. This fuel-air mixture in the tank was initially at room temperature, while two initial pressure conditions at 300 kPa or at 400 kPa were investigated. Only the case of 300 kPa is simulated in this work. In this case, the pressure inside the combustion chamber increased from 50 kPa to 243 kPa, once the fuel-air mixture was discharged in to the combustion chamber by opening a valve. This discharge also initially increased the temperature inside the combustion chamber, which reduced gradually due to heat loss from the walls.

Hamamoto et al. (1988) conducted experiments with various flow fields by spark igniting the mixture at different times after the valve closure. The swirling flow decayed with time, which reduced the turbulence intensity. Using the radial distribution of the mean tangential velocity an angular velocity, Ω, was calculated. In this work, $\Omega = 139.1$ rads/s case is simulated, which corresponded to $t_v = 10$ ms (i.e. the time between valve closure and spark ignition). At this time the temperature inside the combustion chamber was at 325 K.

Flame propagation was measured using high-speed schlieren photography and an ion probe. A two-dimensional laser Doppler anemometer was used to measure flow velocity. Combustion inside the vessel caused the pressure to increase due to compression and a pressure transducer was used to measure the pressure inside the combustion chamber.

6.3 Numerical setup

Numerical setup used to simulate the experimental is described in this section. The simulations are performed using STAR-CD v4.18, which is a multi-dimensional CFD code. The URANS approach is used in this work, where the equations solved in the code are given in section 2.2.3. The numerical method used in this chapter is similar to the setup described in Chapter 3 and only the differences are highlighted in this section.

6.3.1 Flamelet table generation

The look-up table generation for the flamelet models is described in this section. The method described here is similar to the one outlined in section 3.3, however, unlike the constant pressure calculations described in Chapters 4 and 5, additional dimensions have to be included to account for the change in mixture thermochemistry due to compression.

Chemical mechanism

As with the spherically symmetric cases described in Chapters 4 and 5, a detailed chemical mechanism is used to calculate freely propagating and strained laminar flames. In this work, the detailed chemical mechanism of Sung et al. (1998) is used for propane-air combustion. Figure 6.1 shows a comparison of the unstretched laminar flame speed calculated using this chemical mechanism with stoichiometric propane-air flame experimental data of Vagelopoulos et al. (1994), Hassan et al. (1998*b*) and Jomaas et al. (2005), at different pressures with $T_u = 298$ K. The comparison is reasonably good for the pressures considered in these experiments.

Effect of pressure

Compression effects from combustion cause the unburnt mixture temperature, T_u, to change with pressure, p. Therefore, a number of laminar flames at various temperatures and pressures have to be computed to cover the range of reaction rates, $\overline{\dot{\omega}}$, experienced by the turbulent flame. Furthermore, the values of s_L^0 and

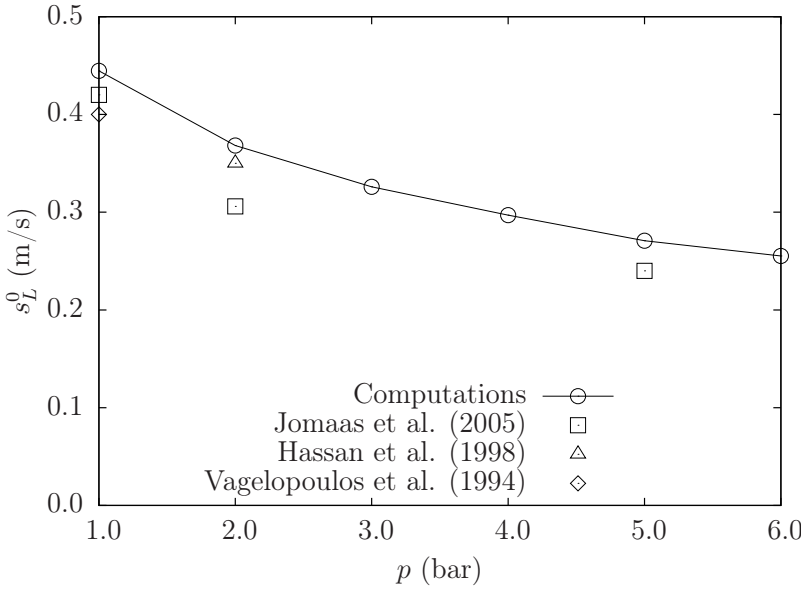

Figure 6.1: Comparison of unstretched laminar flame speed of stoichiometric propane-air mixtures from different experiments with the values predicted numerically using the detailed chemical mechanism of Sung et al. (1998).

δ_L^0 appearing in Eq. (2.69) are functions of both temperature and pressure of the unburnt reactants and will need to be tabulated.

Figure 6.2(a) shows normalised burning rates, $\dot{\omega}^+$, of steady one-dimensional planar laminar flames, plotted against distance for different pressures. Reaction rates are normalised using ρ_u, s_L^0 and δ_L^0 and the plots are shifted by x^*, the location of the peak heat release rate. This figure shows that increasing the pressure intensifies the reaction and drastically reduces the flame thickness. This figure also shows the non-linear effect of pressure on the laminar burning rate. This non-linear response of the flame to pressure means that simple scaling arguments cannot be used to extrapolate laminar flame results from a lower pressure to a higher pressure. The implication of this to flamelet library generation is that laminar flames have to be calculated for a number of initial pressures and temperatures, which increases the pre-processing time for the simulations. The effect of pressure on the laminar flame structure can be seen in Figure 6.2(b), where the spatial profiles of c are plotted for various pressures. It is evident that the gradient of the progress variable becomes steeper with increasing pressure. Due

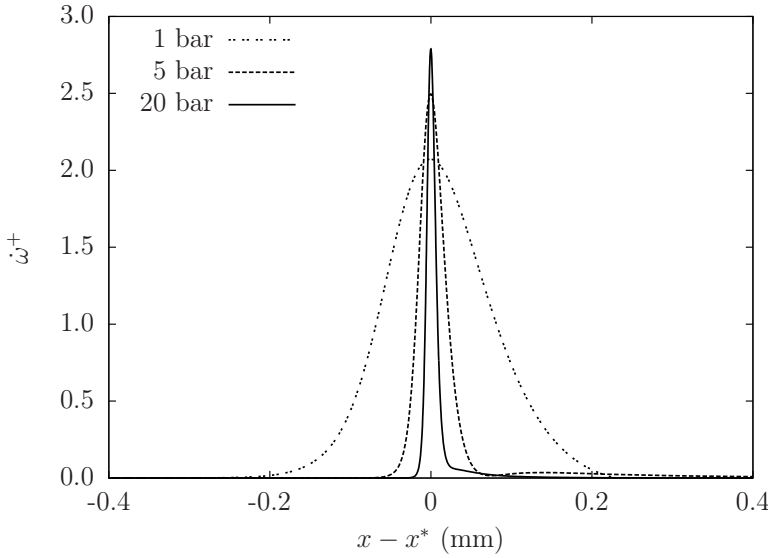

(a)

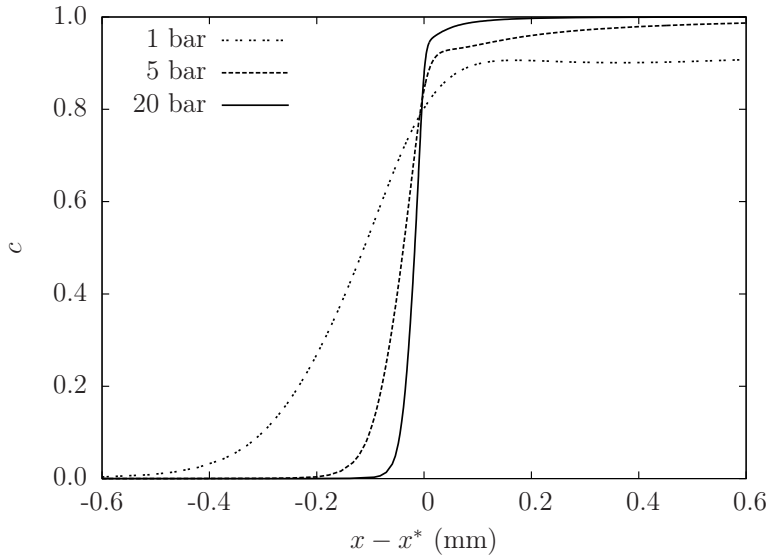

(b)

Figure 6.2: (a) Normalised reaction rate of progress variable, $\dot{\omega}^+ = \dot{\omega}\delta_L^0/\rho_u s_L^0$ plotted against distance for different pressures and $T_u = 300$ K. (b) Spatial profiles of c for different pressures. In these plots, the peak heat release location is denoted by x^*.

to reasons to be explained later, the progress variable is defined based on water vapour mass fraction.

Figure 6.3 shows the variation of the normalised maximum reaction rates, $\dot{\omega}^+_{\max}$, of laminar flames for different initial pressures and unburnt mixture temperatures. This figure shows that for a given unburnt mixture temperature, increasing the pressure increases the reaction rate. However, for a given pressure, increasing the unburnt mixture temperature reduces $\dot{\omega}^+_{\max}$. The reason for this decrease is because, s^0_L, which is used to normalise the reaction rate, increases with temperature.

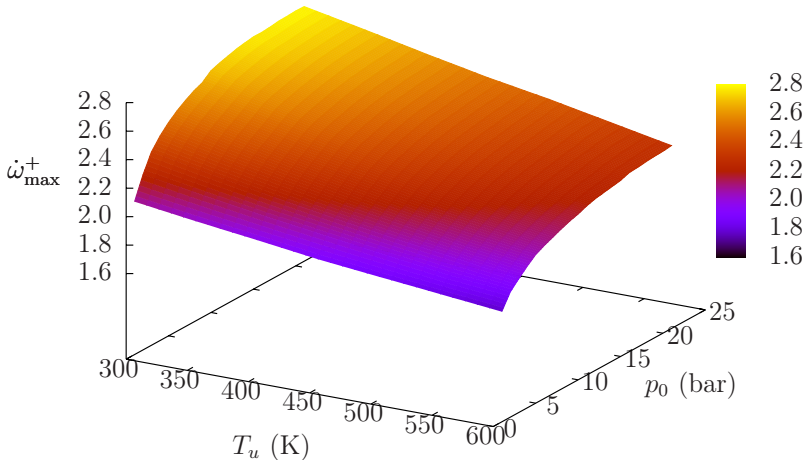

Figure 6.3: Normalised reaction rate of progress variable, $\dot{\omega}^+_{\max} = \dot{\omega}_{\max}\delta^0_L/\rho_u s^0_L$, variation with pressure and temperature.

Strained flamelet

As described in section 3.3.2, response of the reaction rate due to strain need to be determined for the strained flamelet model. Figs. 6.4(a) and 6.4(b) show the plots of $\dot{\omega}^+$ vs. N^+ for stoichiometric propane-air flames at two different pressures at unburnt mixture temperatures of 300 K. Similar plots are obtained for other temperatures, therefore, these figures show that the variation of $\dot{\omega}^+$ vs. N^+ is multi-valued and that the general shape of these curves do not change when temperature or pressure is changed and thus remains a function of the chemical properties of the fuel-air mixture.

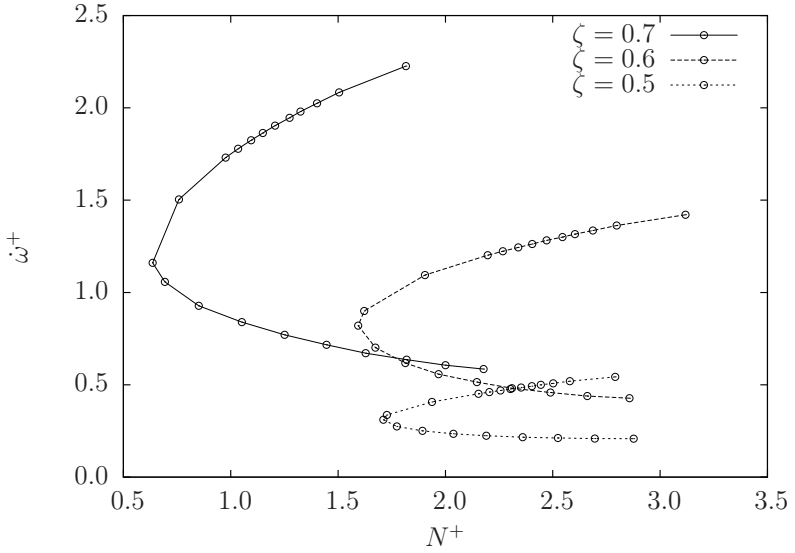

(a)

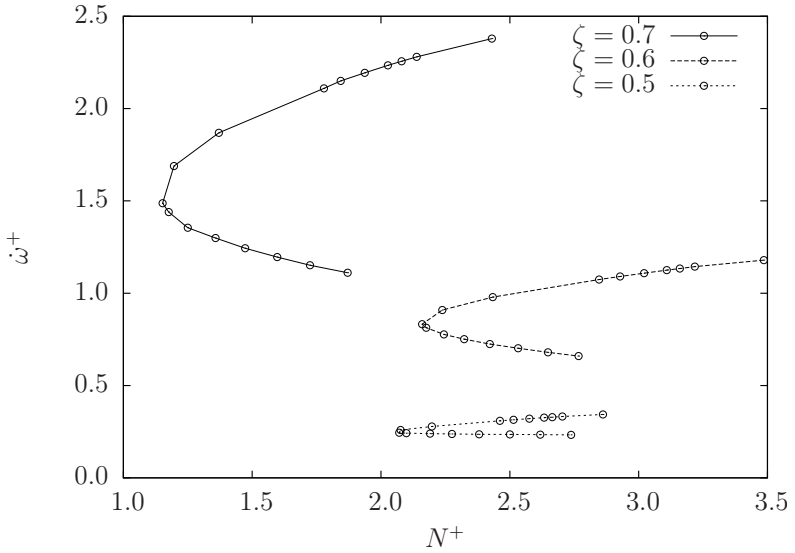

(b)

Figure 6.4: Curves of $\dot{\omega}^+$ vs. N^+ conditioned on the progress variable, ζ, for an unburnt mixture temperature of 300 K at two different pressures: (a) $p = 2$ bar and (b) $p = 5$ bar.

The collapse of $f(\zeta)$ curves for stoichiometric propane-air flames subjected to various strain rates and at different unburnt mixture temperatures and pressures are shown in Figs. 6.5(a) and 6.5(b). As with the methane-air flame shown in Figure 3.1(b), the chemical reactions dominate in the region closer to the burnt side, with $\zeta^* \approx 0.6$.

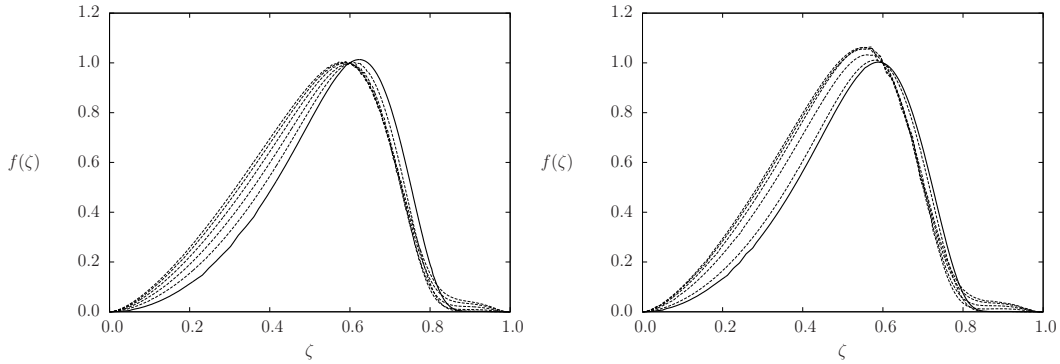

Figure 6.5: Curves of $f(\zeta)$ for stoichiometric propane-air mixture at (a) $T_u = 300$ K and $p = 11$ bar and (b) $T_u = 400$ K and $p = 8$ bar. The solid curve in these figures show the freely propagating unstrained flame.

Similar to the simulations described in Chapters 4 and 5, unstrained and strained flamelet models can be used to build a library for $\overline{\dot{\omega}}$ and other required quantities. Due to the above mentioned effect of pressure on the reaction rates, this look-up table becomes four and five dimensional respectively for unstrained and strained cases.

Choice of progress variable

In this work the progress variable is defined in terms of the mass fraction of water vapour, Y_{H_2O}, as $c = Y_{H_2O}/Y^b_{H_2O}$. This is because a progress variable based on temperature will over-define the system of equations, since an enthalpy equation is already solved. Furthermore, defining the progress variable in terms of species mass fraction removes the complexity involved in implementing the $D\overline{p}/Dt$ term that exists in the transport equation for temperature. Here c based on fuel

mass fraction is not used because of the poor resolution of $\dot{\omega}_T$ with c. Another possibility is to use the mass fraction of the combination, $CO + CO_2$.

Data given in the look-up are interpolated to obtain values required during the CFD calculations. Unburnt mixture temperature, T_u, is obtained from the simulation by assuming that the mixture is adiabatically compressed by the flame front. The look-up table is generated with a resolution of 0.01 in $\tilde{c}$, 0.02 in g, 50 K in temperature and 1 bar in pressure. For the strained flamelet, the additional dimension, ϵ_c, had a resolution of 5 1/s.

6.3.2 Model implementation

Strained and unstrained flamelet models are implemented in STAR-CD. Note that the combustion models available in STAR-CD are de-activated during the simulations. Therefore, in the current combustion model implementation, the temperature rise during combustion is achieved by including the source term due to combustion heat release, $\overline{\dot{\omega}}_T$, in the following Favre-averaged enthalpy equation

$$\frac{\partial \overline{\rho}\tilde{h}}{\partial t} + \nabla \cdot \left(\overline{\rho}\tilde{h}\tilde{\boldsymbol{u}}\right) = \frac{\partial \overline{p}}{\partial t} - \nabla \cdot \left(\overline{\boldsymbol{q}} + \overline{\rho}\widetilde{\boldsymbol{u}''h''}\right) + \overline{\boldsymbol{\tau}} : \nabla\tilde{\boldsymbol{u}} + \overline{\boldsymbol{\tau} : \nabla \boldsymbol{u}''} + \overline{\dot{\omega}}_T. \quad (6.1)$$

This source term is also calculated using strained and unstrained flamelet models. Similarly, the mean heat capacity at constant pressure, $\overline{C_p}$, is calculated using these flamelet models and its value is specified for each cell at every time step during the simulations.

As shown in section 3.1, the pressure-dilatation term, $\overline{p'\nabla \cdot u''}$, that appears in the turbulent kinetic energy is modelled in this study and this term is included in both $\tilde{k}$ and $\tilde{\omega}$ equations. Since there is no spatial gradient of pressure in the domain, the pressure work term is ignored. The flow and turbulence quantities necessary for combustion modelling are obtained from the CFD code. Additional transport equations for the progress variable, $\tilde{c}$ [Eq. (2.20)], and its variance, $\widetilde{c''^2}$ [Eq. (2.65)], are implemented using user subroutines.

6.3.3 Computational details

In this work, the $k-\omega$ SST model is chosen for turbulence closure, where ω is the specific dissipation rate. The effect of using this turbulence model is analysed in section 6.4, where the $k-\omega$ SST model is compared with $k-\epsilon$ RNG model. Standard values are used for the turbulence model coefficients, which are given in tables 6.1 and 6.2 for $k-\omega$ SST and $k-\epsilon$ RNG models respectively.

Table 6.1: Coefficients of the $k-\omega$ SST model

σ_{k1}^{ω}	1.176
σ_{k2}^{ω}	1.0
$\sigma_{\omega1}^{\omega}$	2.0
$\sigma_{\omega2}^{\omega}$	1.168
β_1	0.075
β_2	0.0828
$\beta_1^* = \beta_1^*$	0.09
κ	0.41

Table 6.2: Coefficients of the $k-\epsilon$ RNG model

C_μ	0.085
$\sigma_k = \sigma_\epsilon$	0.719
$\sigma_h = \sigma_m$	0.9
C_{ϵ_1}	1.42
C_{ϵ_2}	1.68
C_{ϵ_3}	0 or 1.42
C_{ϵ_4}	-0.387
κ	0.4
E	9.0
η_0	4.38
β	0.012

Since the combustion chamber is axisymmetric, only a one degree segment of the cylindrical domain is modelled to save computational costs. Furthermore, as spark ignition occurs at the centre of the chamber, only the top half of the cylinder is considered. Cyclic boundary conditions are imposed on the two geometrically identical faces and a symmetry boundary condition is applied at the mid-plane

where the cylinder is halved. Wall boundary conditions are applied for the top and side walls. The wall boundary is fixed at a temperature of 288 K since there was heat loss at the walls in the experiment.

The segment is one-cell thick and the grid spacing is uniform in both the axial and radial directions. The grid is refined until the solution did not show a significant change in the results and the spatial resolution in both axial and radial directions is about 0.18 mm. The size of the time-step is chosen to be 5 μs, which ensures the resolution of reaction, diffusion and convection time scales.

A certain number of cells are selected for spark ignition, which correspond to the spark gap and an ignition source term is included in the enthalpy equation. In this work the temperature is fixed at the burnt temperature, T_b, at these ignition cells during the spark duration. The ignition energy, E_i, can then be calculated using

$$E_i = \rho_u V_i C_p \left(T_b - T_u\right), \tag{6.2}$$

where V_i is the volume of ignition cells. Thus by changing the burnt temperature of the ignition cells and the volume of the cells, one could alter the ignition energy. Different ignition energy values are tested since experimental ignition data was not available. Note that the spark duration is set to one time step size. In the progress variable based approach used in this work, in addition to supplying energy for spark ignition, hot products and cold reactants need to be specified for ignition. Here values of $\tilde{c} = 1$ and $\widetilde{c''^2} = 0.25$ are prescribed for the ignition cells and $\tilde{c} = \widetilde{c''^2} = 0$ is prescribed for the rest of the domain.

The initial temperature and pressure inside the combustion chamber are 325 K and 243 kPa respectively. Radial profiles of turbulence intensity, TI, and swirling velocity, V, obtained from the experimental measurements of Hamamoto et al. (1988) are used to define the initial flow field. The integral length scale, Λ, is taken as 12.5 mm, which is 10% of the vessel diameter. The simulation results does not change significantly when this initial value of Λ is halved. Radial distribution of TI is used to calculate the turbulent kinetic energy and dissipation rate as

$$\tilde{k} = \frac{3}{2} TI^2 \quad \text{and} \quad \tilde{\varepsilon} = \frac{TI^3}{\Lambda}. \tag{6.3}$$

The governing equations are solved in STAR-CD using FVM. In this work, PISO method is chosen for the pressure-velocity coupling. The second-order MARS scheme (Asproulis, 1994) is used to discretise convective terms in the momentum and modelled turbulence equations. First-order upwind scheme is used to discretise the convective terms in enthalpy and $\tilde{c}$ and $\widetilde{c''^2}$ equations. Accuracy of temporal discretisations lie between first- and second-order, in which the discretisation scheme is based on the fully-implicit Euler scheme and explicit deferred correctors.

6.4 Results and discussion

In this section, simulation results obtained using the strained and unstrained flamelet models are compared with the experimental data of Hamamoto et al. (1988). Figure 6.6 shows these predictions, where the results from the EBU model available in STAR-CD is plotted as well. This figure shows that in the

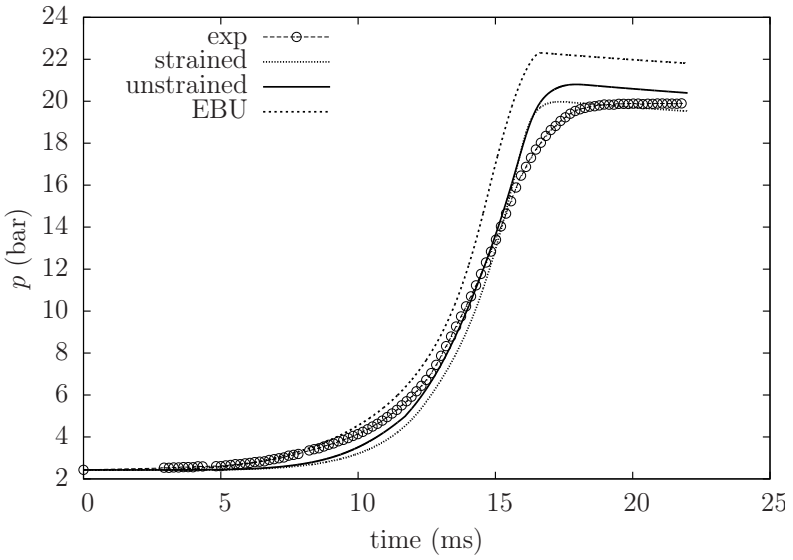

Figure 6.6: Pressure rise prediction using three different combustion models.

numerical simulations, pressure reaches a peak and then drops slightly. This drop is due to heat loss at the walls. This figure shows that the prediction from strained and unstrained flamelet models are reasonably good when compared

with the EBU model. In addition, these models are able to predict the temporal gradient of pressure, $\partial p/\partial t$, reasonably well. The predicted pressure rise from the unstrained flamelet is 5% higher than the experimental value, while the EBU model overpredicts the pressure rise by 12%.

The time taken to generate the look-up table for the strained flamelet model is considerably longer than that for the unstrained flamelet model, since a number of strained laminar flames have to be calculated for each temperature and pressure condition considered. The plots in Figure 6.6 indicate that the unstrained flame is adequate for this problem and the improvements from the strained flamelet model are marginal. Therefore, only the results obtained using the unstrained flamelet model are discussed in the rest of this chapter.

It is important to note that the strained flamelet model gave considerably improved results when compared with the unstrained flamelet model for the flames simulated in Chapters 4 and 5. Even though the experimental flames simulated in Chapter 5 were conducted in a spherical bomb, they can be considered to be unconfined, since the experimental measurements were made before a considerable pressure rise was observed and the diameter of the combustion vessel was more than three times larger than the one considered here. The experiments of Hamamoto et al. (1988) were performed in a closed vessel with pressure rise due to combustion. It is believed that confinement changes the turbulence stretching effect on the flame, since it restricts the entrainment of air and changes the turbulence response of the flame.

Figure 6.7 shows the comparison of the mean scalar dissipation rate, $\tilde{\epsilon}_c$, and the mean reaction rate, $\overline{\dot{\omega}}$, across the flame brush using simulations from both strained and unstrained flamelet models. These quantities are taken across the centre line of the computational domain at a simulation time of 10 ms. These figures show that the difference in the quantities, $\tilde{\epsilon}_c$ and $\overline{\dot{\omega}}$, obtained from the strained and unstrained flamelet models are small, which could explain the small difference in the predictions from these two models for the confined flame simulated in this work.

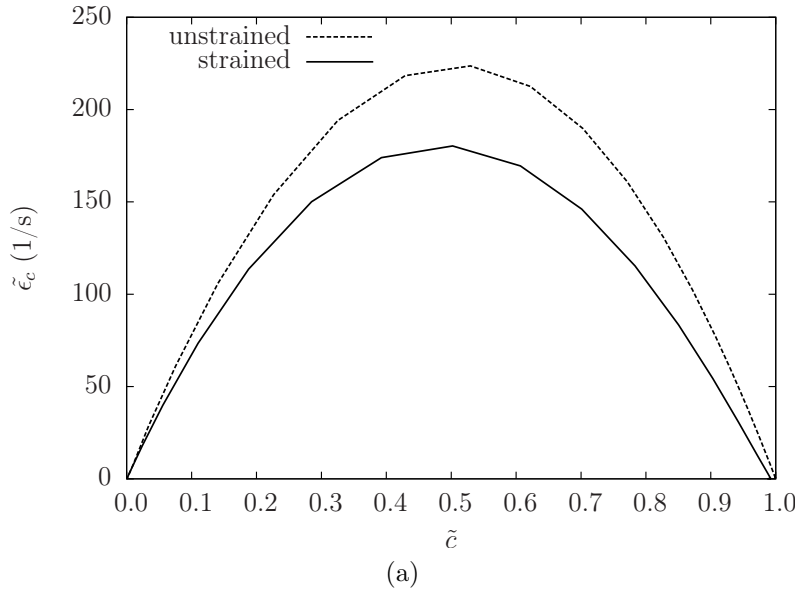

(a)

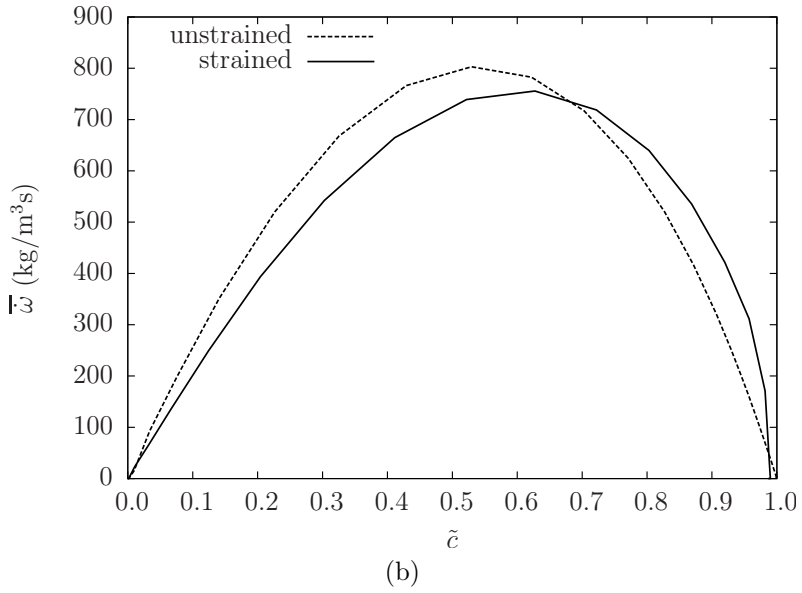

(b)

Figure 6.7: Comparison of flame quantities obtained using strained and unstrained flamelets. These quantities are taken along the centreline of the computational domain at a simulation time of 10 ms; (a) mean scalar dissipation rate, and (b) mean reaction rate.

6.4.1 Effect of ignition energy

In section 6.3 it was described that ignition is induced by depositing energy in some computational cells during the spark duration. Figure 6.8 shows the sensitivity of the ignition energy in predicting the pressure rise during combustion. This figure shows that increasing the ignition energy, E_i, to 5 mJ leads to faster burning.

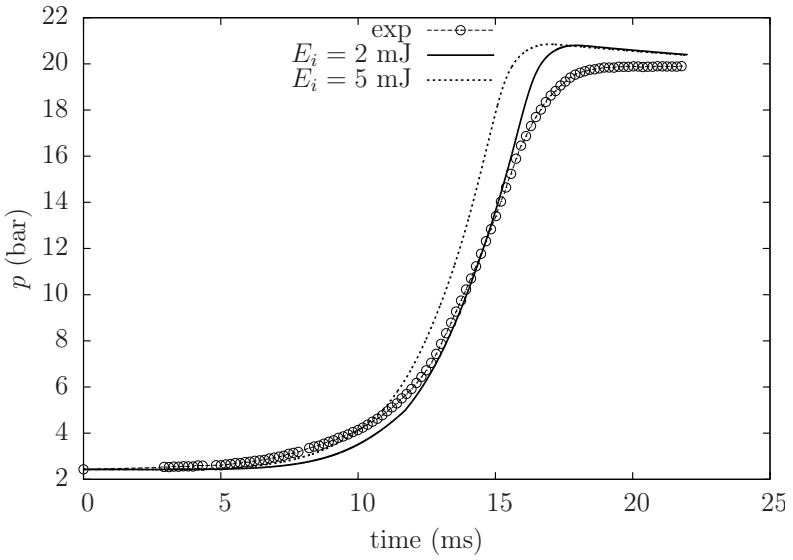

Figure 6.8: Pressure rise prediction using different ignition energy definitions.

6.4.2 Effect of turbulence model

Figure 6.9 shows the prediction using two different turbulence models, with other modelling parameters unchanged. It can be seen that flame propagation is faster when $k-\varepsilon$ RNG model is used. Applicability of the $k-\varepsilon$ model and its variants to swirling flows is questionable (Hogg and Leschziner, 1989) and could explain the poor agreement with experimental data here.

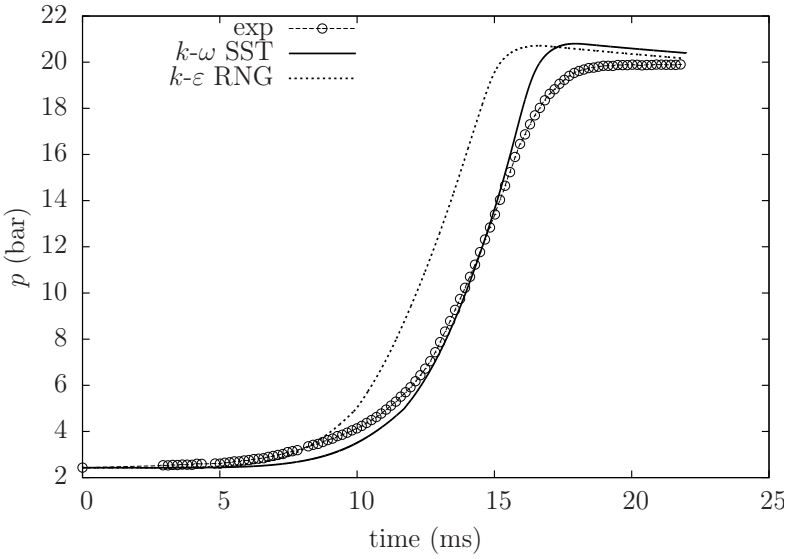

Figure 6.9: Pressure rise prediction using two different turbulence models.

6.4.3 Flame propagation

Hamamoto et al. (1988) used ion probe measurements to determine the position of the flame front, where experiments were repeated with the ion probe fixed at several locations. Measurements were also made using schlieren photographs and Hamamoto et al. (1988) reported that the two measurements coincided with each other. Therefore, similar to the previous experimental flames simulated in Chapters 4 and 5, the flame profiles reported in these experiments are taken to be the leading edge of the flame brush. For comparison purposes, the location at which $\tilde{c} = 0.05$ is taken to be the leading edge in the simulated flames. As described earlier, the progress variable, $\tilde{c}$, is defined in terms of water vapour mass fraction. Lewis number of H_2O is roughly 0.88 for stoichiometric propane-air mixture, which implies that the mass diffusivity of H_2O is higher than the thermal diffusivity. Therefore, the flame leading edge is taken as $\tilde{c} = 0.06$ for the simulation using unstrained and strained flamelet models. For the computation using the EBU model, c is taken as the normalised temperature, $c = (T - Tu)/(T_b - T_u)$, and the leading edge as $\tilde{c} = 0.05$. Figure 6.10 shows the comparison of flame propagation obtained from different models with the experimental data at seven

different time instants. It can be seen that all models predict a slower flame

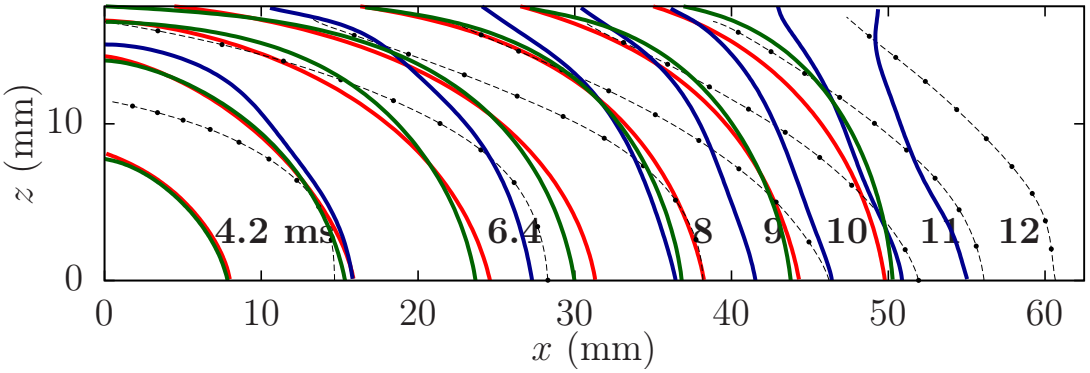

Figure 6.10: Flame propagation comparison between experimental data (dashed lines with symbols) and the predicted results from the unstrained (red lines), strained (green) and EBU (blue) models at seven different time instants.

propagation. This figure also shows that the flame brush becomes distorted at later times for the EBU model. Calculations using the unstrained and strained flamelet models are similar; however, $\tilde{c}$ contours obtained using these two models resemble the experimental flame brush more closely than with the EBU model. These contours show that the flame is initially spherical but becomes cylindrical due to the presence of the side walls.

Gas expansion within the flame induces a flow velocity. Figure 6.11 shows the time-variation of the induced radial velocity, $\tilde{u}$, for the experimental measurements and the predictions using combustion models. These quantities are taken at a radial location of $x = 50$ mm. Note that the comparisons are approximate as the experimental data were reported as ensemble-averaged velocities but the results from the numerical simulation are density-weighted averaged. Nevertheless, such comparisons can be found in the literature (Roomina and Bilger, 2001). The models are able to qualitatively predict the increase in the mean radial velocity and the time at which the peak velocity was encountered in the experiments is in agreement with the predicted values. The increase in flame velocity at the measuring location is due to the approaching flame. Once the flame passes the measuring location the velocity drops. This figure appears to show that both models are able to predict the flame arrival time, which contradicts with the

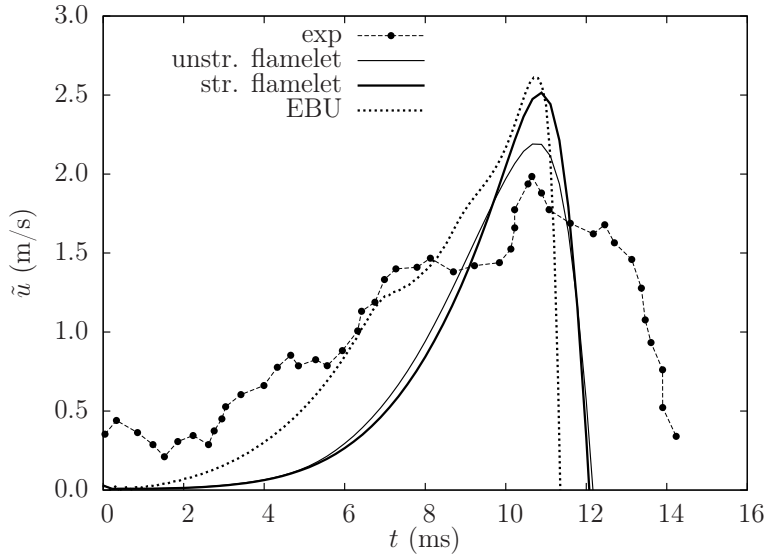

Figure 6.11: Flame induced radial velocity, $\overline{u}$, variation with time. Comparison is made between the two combustion models and the experimental data.

results shown in Figure 6.10 for the experimental part.

6.5 Summary

Predictive capability of strained and unstrained laminar flamelet models are tested inside a closed vessel with swirl. Compression effect due to combustion means that the change in the thermochemistry of the mixture needs to be included in the flamelet library generation. Therefore, compared with constant pressure cases simulated in earlier chapters, the dimensionality of the look-up tables has to be increased to include both temperature and pressure dependencies The combustion models are implemented in STAR-CD.

It is shown that both the unstrained and strained flamelet models are able to predict the experimental pressure rise reasonably well. In addition, these results are an improvement from the results of the EBU model already implemented in STAR-CD. None of the models used here are able to predict the flame propagation reported in the experiments. However, these models are able to predict the flame arrival time at a particular radial location, which appears to show a mismatch

between the results reported in the experimental study.

Results from this chapter show that the unstrained flamelet is adequate in simulating combustion of confined flames. It is believed that these results are similar because of the restriction in the air entrainment and the change in the turbulence characteristics of the flow when the flame is confined. The pre-processing time for the unstrained flamelet model is significantly shorter than the strained flamelet model, since the strained flamelet model requires the calculation of a number of strained laminar flamelets. Therefore, in the next chapter, the unstrained flamelet model is used to simulate combustion in a practical SI engine.

7. Spark-ignition engine simulation

Results from the previous chapter have shown that the unstrained flamelet model given in Eq. (2.63) is adequate to simulate intermittent combustion in closed vessels. In this chapter, this reaction rate closure is used to simulate combustion in a practical spark-ignition engine. These simulations are performed using STAR-CD and the model implementation is largely similar to the description given in Chapter 6. An overview of various closure models used in the past to simulate SI engine combustion is presented first. The results from the unstrained flamelet model are compared with two models available in STAR-CD.

7.1 Introduction

Three-dimensional CFD has become an indispensable tool in engine design, which can provide detailed information on flow and combustion inside IC engines. RANS methodology has been the industry standard, but with increasing computational power, LES is now becoming feasible. The predictive capability of both of these computational frameworks depends largely on the combustion model. This work will focus on spark-ignition gasoline engines, where the models outlined in section 2.5 are used in combustion simulation.

The widely used eddy break-up model (Spalding, 1971) is known to predict unphysically high reaction rates near the wall (Abu-Orf and Cant, 2000) and it is necessary to adjust the empirical model coefficients for different operating conditions. By simulating a research engine, Abu-Orf and Cant (2000) showed that a flamelet model, based on the BML formalism, does not suffer from this problem of flame acceleration near the walls. Drake et al. (2005) also used a modified version of the BML model to simulate stratified combustion in a spray-guided direct-injection spark-ignition (DISI) engine.

Zhao et al. (1993) used the coherent flame model (CFM) to simulate SI engine combustion. They showed that the surface production term constant in the

model needs to be calibrated for each engine. The original form of CFM has been extended to study both homogeneous and stratified combustion (Baritaud et al., 1996). This extended coherent flame model (ECFM) was used by Duclos and Zolver (1998) to investigate combustion in a DISI engine at both homogeneous and stratified conditions. In their approach, the model coefficients had to be calibrated based on previous engine data, which gave good agreement with experimental pressure measurements. Henriot et al. (1999) used ECFM, with the same model constants, to predict the experimental results in a different DISI engine. This model has been adapted to hydrogen combustion by Knop et al. (2008), where they validated the model for both port fuel injection (PFI) and DISI engines. More recently, Galloni et al. (2012) used ECFM to simulate combustion in a downsized SI engine. As with previous studies, the model constants had to be tuned depending on the engine configuration.

Weller et al. (1994) proposed a flame surface wrinkling model, in which a wrinkling factor was introduced into the transport equation of a regress variable. The model is supposed to capture the evolution of an initial laminar flame kernel into a fully turbulent flame and its subsequent propagation by using either a spectral model or a semi-empirical model for the local wrinkle factor. Using this model, Weller et al. (1994) simulated combustion in a research engine with a square piston, and was able to obtain a good match with the measured pressure histories. For these calculations, an orifice-type equation was used with some tuning to account for the leakage past the piston rings. Heel et al. (1998) used the same model to show reasonably good agreement for the same research engine for certain operating conditions. They attributed the discrepancies in some of the results to the combustion model used. Kech et al. (1998) extended this wrinkling model for DISI engines, where they showed that the model can be used for stratified combustion.

Ewald and Peters (2007) validated the G-equation modelling approach for a homogeneous charge SI engine and Tan and Reitz (2006) used this model to simulate combustion in SI engines with exhaust gas recirculation (EGR). Peters and Dekena (1999) applied the model to a hypothetical DISI engine, while Liang and Reitz (2006) validated the model for both SI and stratified DISI engines.

The transported PDF method has also been used to simulate IC engines.

For example, Taut et al. (2000) used a RANS/PDF method to simulate combustion in a two-stroke SI engine. However, the results only showed qualitative agreement with experimental measurements for the flame speed and a pressure history comparison was not shown. Haworth (2010) noted that these calculations show that the transported PDF method is feasible in simulating such complex three-dimensional combustion processes.

Most IC engine simulations in the past were done in the RANS framework, but LES is now gaining popularity. The choice between LES or RANS for IC engine simulations depends on the objectives of the study. The interaction between turbulence and combustion are more accurately captured in LES when compared with RANS. LES is particularly useful in determining cycle-to-cycle variations found in IC engines (Haworth and Jansen, 2000) but RANS is adequate if one is only interested in the statistics. The combustion models used in LES are usually extensions of the ones used in RANS. For example, Vermorel et al. (2009) used the ECFM with LES to simulate a practical SI engine. Banaeizadeh et al. (2008) used a LES/PDF method to simulate a research DISI engine.

Almost all of the above mentioned spark-ignition engine simulations were performed using single-step or reduced chemistry, which does not allow the prediction of pollutant formation (Heywood, 1988). One exception is the study of Liang and Reitz (2006), who used detailed chemical mechanism for propane to simulate the SI engine. They also simulated the gasoline DISI engine using a 21-species, 42-reaction iso-octane mechanism. Complex chemistry in CFD simulations is important for lean burn engines in which the turbulence-chemistry interactions are expected to be stronger. Chemical kinetics also play a central role in HCCI engines, and unlike the SI engine simulations above, a number of simulations with detailed chemistry can be found in the literature (Bhave et al., 2005; Zhang et al., 2005).

It is also noted that the studies mentioned above used some amount of model tuning to obtain a good match between measured and computed in-cylinder pressure with crank angle. However, if the model parameters are closely tied to the physics of the problem, then one could eliminate model tuning. Furthermore, these models should include complex kinetics that can be used to calculate pollutants such as CO and NO_x.

The objective of this work is to use the reaction rate closure model given in Eq. (2.63) to simulate combustion in a single-cylinder, four-stroke SI engine, experimentally investigated in ETH Zürich (Wright, 2013). As with the previous simulations performed in this thesis, a reaction progress variable is used to track the reaction zones. In addition, a transport equation for the progress variable variance is also solved, which includes the mean scalar dissipation rate as a sink term. In terms of combustion modelling, the homogeneous charge SI engine is simpler than the stratified combustion taking place in a DISI engine (Colin et al., 2003). However, complex turbulent-chemistry interactions take place inside the cylinder and it is a good first test for the application of the combustion model discussed here. Note that unlike many previous studies used to simulate SI engine combustion there are no tunable parameters in this modelling approach and detailed chemistry is included in this study.

This chapter is organised as follows: the test SI engine is described in section 7.2. This is followed by a description of the numerical setup, which includes the flamelet library generation. CFD simulations are performed using STAR-CD. In the results section, computations using the reaction rate closure given in Eq. (2.63) and two models available in STAR-CD are compared with experimental measurements. This chapter ends with the main conclusions of this investigation.

7.2 Engine measurements

The engine used for this work is a 250cc single cylinder, four-stroke SI engine, which was designed for Kart racing (Wright, 2013). Figure 7.1 shows the engine geometry simulated (boundary conditions shown in this figure are described in section 7.3.3), and the engine parameters are shown in Table 7.1. The spark plug is located in the middle of the four valves and is slightly off centre, while the cylinderhead has a pent-roof arrangement. Fuel is injected using a port injection system; however, fuel injection is not modelled in this work.

Engine measurements were made by researchers in ETH Zürich, where the in-cylinder pressure was measured at every 0.2° CA using a piezo-electric pressure sensor, while absolute pressure values inside the intake and exhaust ducts were measured using pressure transducers (Wright, 2013).

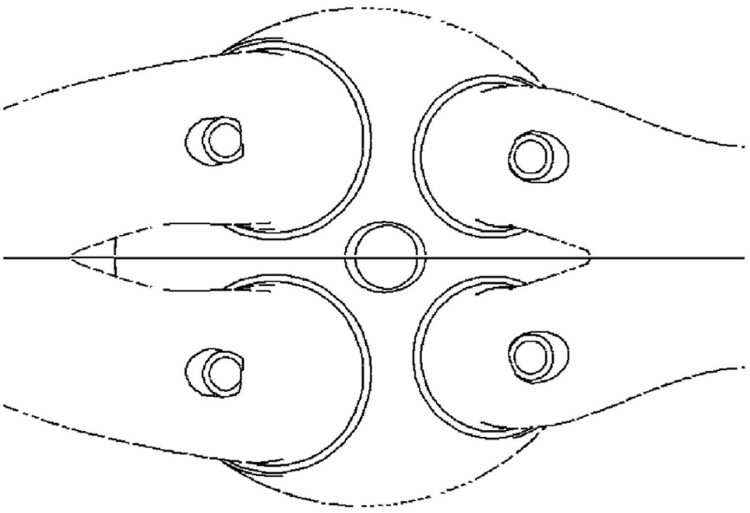

(a)

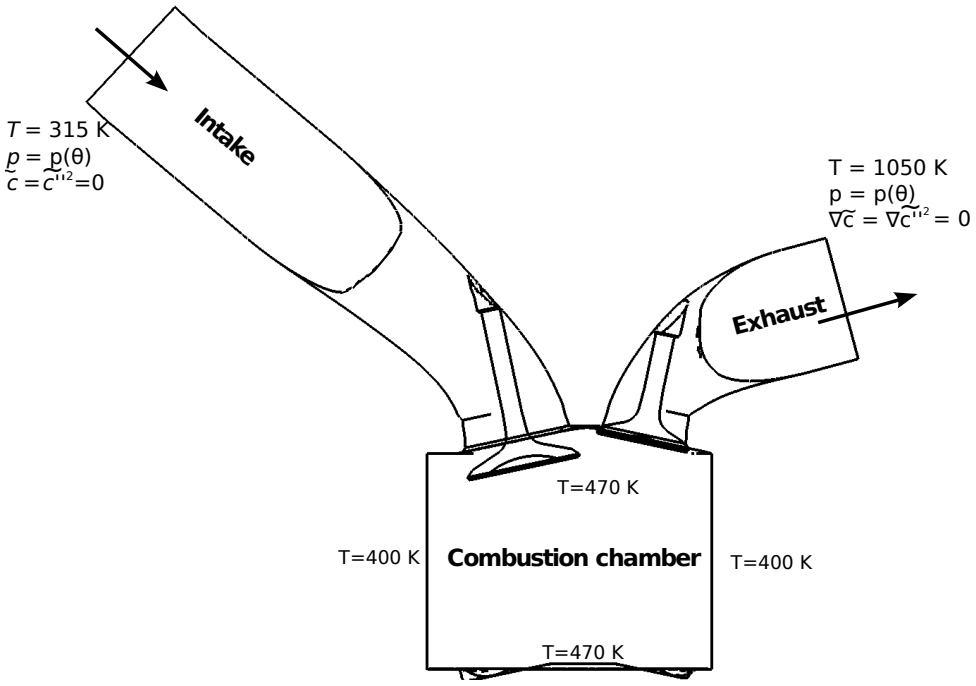

(b)

Figure 7.1: Engine geometry showing (a) top view with the symmetry axis marked and (b) side view showing the specified boundary conditions, where outlet boundary conditions are shown for a case without backflow.

Table 7.1: Engine parameters

Engine configuration	Single-cylinder, four-stroke, SI engine
Engine displacement	249.6 cm^3
Bore/Stroke	75/56.5 mm
Cylinderhead	Four valves per cylinder, pentroof
Injection	Port injected
Fuel	Standard gasoline (RON 95)
Geometric compression ratio	12.5:1

The engine was run in a range of operating conditions and 144 cycles were run for each operating point. The operating point corresponding to an engine speed of 3500 rpm with a torque of 20 Nm is considered for this work. This corresponds to a brake mean effective pressure (BMEP) of 9.9 bar and is close to engine full load. All operating conditions have a stoichiometric (i.e. air-to-fuel ratio, $\lambda = 1$), homogeneous mixture and the engine was spark ignited at 30.4° crank angle (CA) before top dead centre (TDC).

7.3 Numerical setup

Combustion simulations inside the engine are performed using STAR-CD v4.18, together with the module es-ice, which handles the moving grid for IC engine applications. The numerical setup used for the engine is similar to that of the simple geometry described in section 6.3, and additional issues related to IC engine simulations are highlighted here.

7.3.1 Flamelet library generation

Fuel-air mixture and chemical mechanisms

Gasoline fuel used in the engine is a complex mixture of several hydrocarbons, without a standard mixture composition (Ihracska et al., 2013) and currently it is not possible to represent detailed chemistry of gasoline (Pitz et al., 2007). For the computational studies carried out in this work, iso-octane is used as a substitute for gasoline, which is a single component fuel that can be used as a

gasoline surrogate (Pitz et al., 2007).

A number of detailed chemical mechanisms for iso-octane can be found in the literature. However, these detailed mechanisms involve a large number of species. For example, the detailed iso-octane mechanism of Curran et al. (2002) has 857 species and 3606 reactions. These species are also associated with large differences in their time scales, making the problem numerically stiff (Lu and Law, 2006). Therefore, for an IC engine simulation that requires a wide range of temperatures and pressures, it is unfeasible to calculate freely propagating laminar flames using these detailed mechanisms.

In order to reduce the computational effort, one could use skeletal mechanisms that have been derived from detailed mechanisms using various reduction techniques. In this work, two such mechanisms are considered. First is the skeletal mechanism of Hasse et al. (2000), which consists of 29 species and 49 reactions. The second skeletal mechanism is that of Pepiot-Desjardins and Pitsch (2008*a*), which is considerably larger as it has 109 species and 393 reactions. Note that these mechanisms are respectively denoted as mech-1 and mech-2 in this chapter.

It is necessary for these mechanisms to be able to predict experimental flame speeds for a wide range of conditions. Figure 7.2 shows the comparison of calculated stoichiometric iso-octane – air laminar flame speeds, s_L^0, for different unburnt mixture temperatures and pressures with the experimental measurements of Bradley et al. (1998); Lawes et al. (2005); Mandilas et al. (2007); Jerzembeck et al. (2009); Kelley et al. (2011) and Galmiche et al. (2012). CHEMKIN's PREMIX module (Kee et al., 1985) is used to calculate unstrained laminar flame speeds, s_L^0. In this figure, solid lines represent flame speeds computed using the mechanism of Hasse et al. (2000), while dashed lines represent values obtained using the mechanism of Pepiot-Desjardins and Pitsch (2008*a*).

Figure 7.2 shows that even though these mechanisms are able to predict experimental trends, there are significant differences between computed and measured flame speed values, especially at higher pressures. Galmiche et al. (2012) noted that current iso-octane chemical mechanisms need to be improved. It is also important to note that there are significant discrepancies in experimentally measured flame speeds. For the purposes of the present simulations, these differences between measured and computed flame speeds using the mechanisms of

Hasse et al. (2000) and Pepiot-Desjardins and Pitsch (2008*a*) are considered to be acceptable.

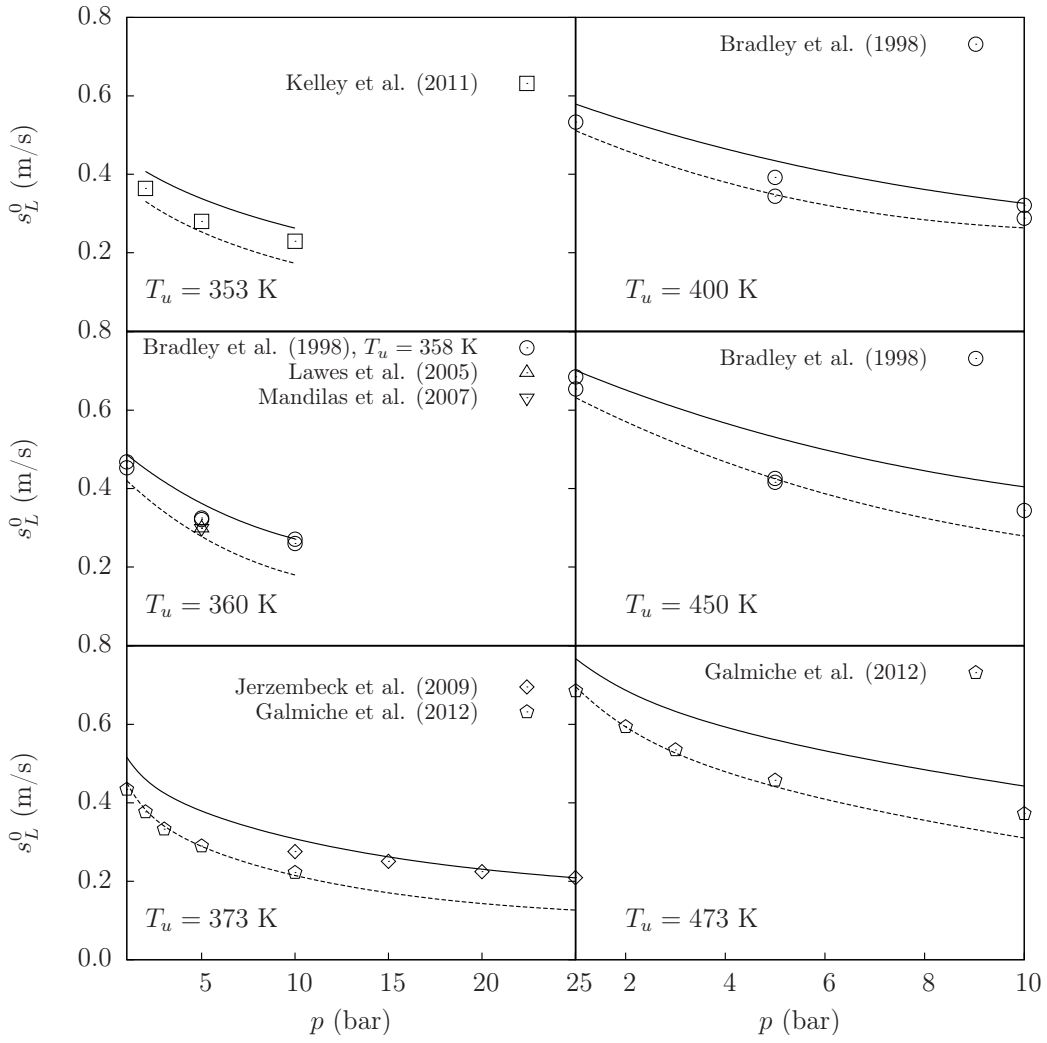

Figure 7.2: Flame speeds computed using the mechanism of Hasse et al. (2000) (solid lines, mech-1) and Pepiot-Desjardins and Pitsch (2008*a*) (dashed lines, mech-2) compared with experiments at different pressures and temperatures.

The flamelet library is generated with the progress variable defined based on water vapour mass fraction, $c = Y_{\mathrm{H_2O}}/Y^b_{\mathrm{H_2O}}$, due to reasons outlined earlier in section 6.3. It was shown in section 6.4 that the reaction rate closure expression given by Eq. (2.63) is adequate to simulate combustion in enclosed chambers

with intermittent combustion; therefore, only this closure model is compared with models implemented in STAR-CD.

Issue of auto-ignition

Beyond certain temperatures and pressures it is difficult to obtain a converged solution in PREMIX when the chemical mechanism of Pepiot-Desjardins and Pitsch (2008*a*) is used. This difficulty in convergence is also observed when the mechanism of Kelley et al. (2011) is used, which is another large skeletal mechanism. A similar observation was made by Martz et al. (2011), who showed that a steady flame solution could not be obtained at high temperatures and pressures, since at these conditions the ignition delay times, τ_i, were of the order of the characteristic flame time ($t_c = \delta_L^0 / s_L^0$).

Another surprising observation made from these laminar flame calculations is the increase in computed flame speeds with pressure, for certain unburnt mixture temperatures. This contradicts the well known negative dependence of laminar flame speed with pressure (Turns, 2000). Figure 7.3 shows the variation of com-

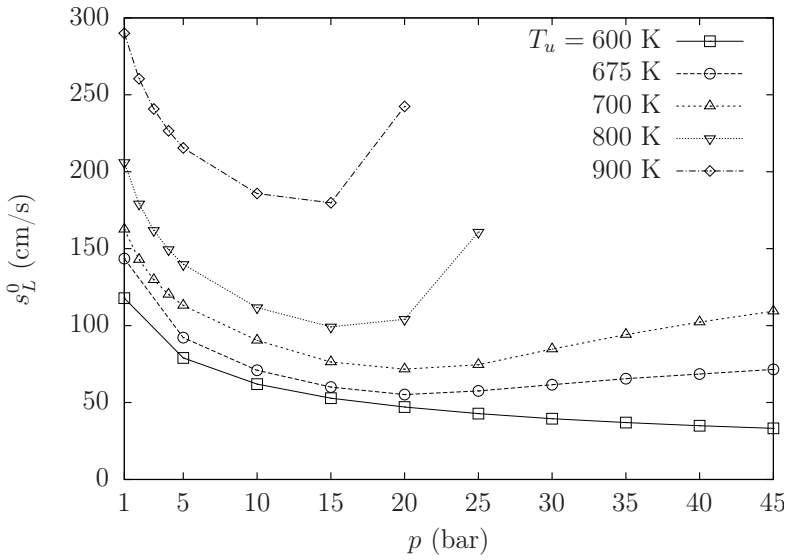

Figure 7.3: Variation of laminar flame speed with pressure for different unburnt mixture temperatures. Computations are made using the skeletal mechanism of Pepiot-Desjardins and Pitsch (2008*a*).

puted laminar speeds with pressure for different unburnt mixture temperatures. This figure shows that beyond a particular pressure for a given T_u, s_L^0 increases with pressure and this value of p reduces when T_u is increased. For example, s_L^0 starts to increase after 25 bar when $T_u = 700$ K, while it starts to increase after 20 bar when $T_u = 800$ K. Note that this increase in s_L^0 with p was only observed for $T_u \geq 675$ K. For T_u below this value, s_L^0 decreased with p as expected (for example, $T_u = 600$ K curve in Figure 7.3). The calculations for which the flame speed starts to increase with pressure are also the ones that were difficult to converge. Therefore, it is believed that this positive dependence of s_L^0 with p is due to the auto-ignition of the fuel-air mixture, in which case there is no flame speed eigenvalue.

Indeed, a recent study by Habisreuther et al. (2013) showed a similar result for stoichiometric methane-air flames, where beyond a certain temperature, the flame speed increased with pressure. They explained that this behaviour is caused by flame structure changes, induced by the ignition delay time, which is a function of T_u. They used different detailed chemical mechanisms to verify that their results are not a spurious effect of the chemical kinetic mechanism. Therefore, PREMIX calculations with the mechanism of Pepiot-Desjardins and Pitsch (2008*a*), are used to estimate ignition pressure and temperature of iso-octane, i.e. the temperature at which an increase in pressure leads to an increase in the laminar flame speed. This auto-ignition temperature variation with pressure is shown in Figure 7.4, which shows that the ignition temperature increases as the pressure is decreased. Also shown in this figure is the curve corresponding to the temperature rise resulting from adiabatic compression of a mixture initially at 300 K and 1 bar. These two curves do not intersect since auto-ignition was not observed for $T_u < 675$ K. A straight dotted line is drawn from this point to the adiabatic compression curve in Figure 7.4 to separate auto-ignition and flame regions.

With regards to the flamelet library generation, the region left of the adiabatic compression curve is of no interest as it is not possible to have such conditions inside the cylinder when the engine is running. Below the ignition temperature curve one could use a similar procedure as outlined in section 6.3.1 to generate the flamelet library since the eigenvalue of s_L^0 exists. The region bounded by

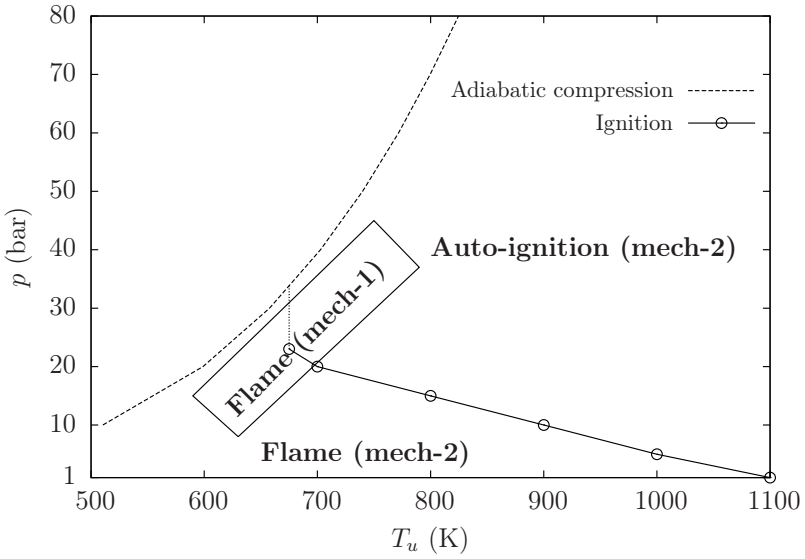

Figure 7.4: Curves showing the variation of temperature for adiabatic compression (dashed line) and the ignition temperature at a particular pressure obtained from laminar flame calculations.

the two curves in the upper right hand corner is the region where auto-ignition is expected, and in this region flame solutions cannot be found using the mechanism of Pepiot-Desjardins and Pitsch (2008*a*). The homogeneous constant-pressure module (CONP) from CHEMKIN is used to obtain the reaction rates in this region. Note that the same reaction rate closure expression, given by Eq. (2.63), is also used to build the look-up table for the auto-ignition region.

The constant-pressure reactor can also be used to determine the ignition delay time, τ_i, which is defined as the time corresponding to the maximum temperature gradient with respect to time, $\mathrm{d}T/\mathrm{d}t$. Figure 7.5 shows the variation of iso-octane ignition delay times with both temperature and pressure. In this figure, comparison is made between the values calculated numerically using the mechanism of Pepiot-Desjardins and Pitsch (2008*a*), experimental data on iso-octane auto-ignition delay times and the correlation of He et al. (2005). This figure shows that there are some discrepancies between different experiments as well as the numerical values, even though they all show the expected general trend with temperature and pressure.

An important feature of the combustion modelling approach used in this work

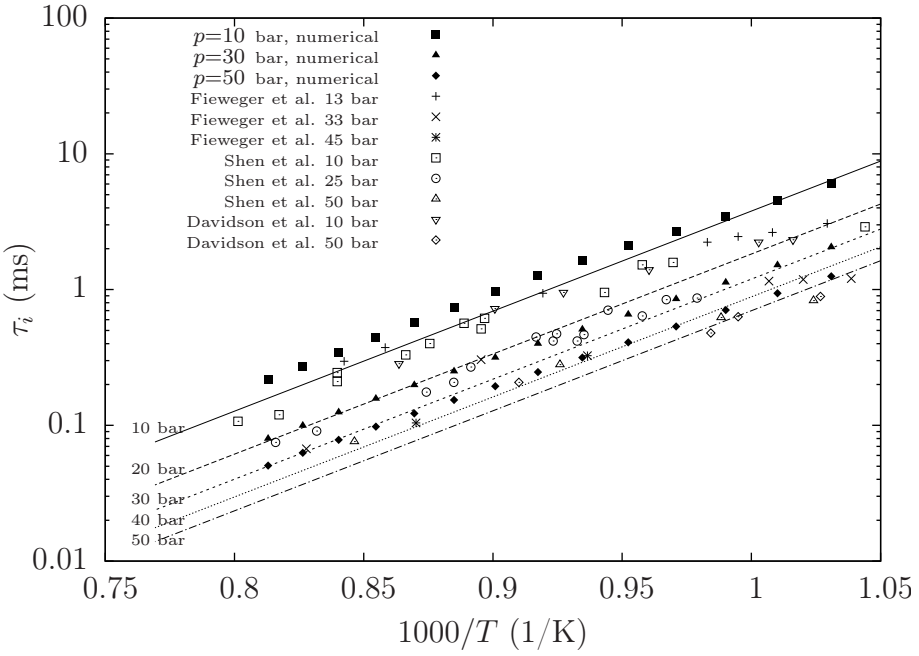

Figure 7.5: Ignition delay time variation with both temperature and pressure for iso-octane – air mixtures. Straight lines show the correlation of He et al. (2005).

is the use of the progress variable variance, $\widetilde{c''^2}$, equation [Eq. (2.65)]. This equation contains the mean scalar dissipation rate, $\tilde{\epsilon}_c$, as a sink term, which has so far been modelled using Eq. (2.69). This model contains s_L^0 and δ_L^0, which are meaningless for auto-ignition since there is no flame. Therefore, whenever conditions inside the cylinder correspond to auto-ignition as depicted by Figure 7.4, a linear relaxation model of the form, $\tilde{\epsilon}_c \simeq \left(\tilde{\varepsilon}/\tilde{k}\right) \widetilde{c''^2}$, is used for $\tilde{\epsilon}_c$.

It is important to note that the mechanism of Hasse et al. (2000) cannot be used for ignition studies. This mechanism yields flame solutions even in the auto-ignition region shown in Figure 7.4. Therefore, $\tilde{\epsilon}_c$ model given in Eq. (2.69) is used in CFD simulations involving this mechanism. Table 7.2 shows the three reaction rate closure models used in this work together with various model parameters. Note that the model parameters used in the algebraic equation for $\tilde{\epsilon}_c$ [Eq. (2.69)] cannot be changed arbitrarily and are left unchanged in these simulations. G-equation and CFM models are available in STAR-CD and only single-step chemistry is used for these two models. The model parameters in

these two models have to be tuned for a particular engine geometry and operating condition.

Table 7.2: Combustion models used in this work together with various model parameters.

Model	Parameter and value		
M1: G-equation	coefficient A in Eq. (2.58) vary between 3 to 4		
M2: CFM	a	α	β in Eq. (2.52)
	2.1	0.1	1.0
M3: Model given in Eq. (2.63)	β'	K_c^*	in Eq. (2.69)
	6.7	0.85τ	

7.3.2 Computational mesh

The engine geometry consists of the intake port (including the inlet valve), the combustion chamber (cylinder) and the exhaust port (including the exhaust valve). Only half of the geometry is used for meshing by considering the geometrical symmetry of the engine [see Figure 7.1(a)]. Computational mesh used in this work consists of unstructured hexagonal cells (Koch, 2013). The movement of the valves and the piston is handled using STAR-CD's es-ice module. To verify whether the results are independent of the grid resolution, a coarse and a fine mesh are used. Table 7.3 shows the number of cells in these two meshes at both TDC and BDC. These computational meshes were provided by researchers in ETH Zürich (Wright, 2013).

Table 7.3: Cell count of the two computational meshes.

	Coarse	Fine
Cell count at TDC	175,000	280,000
Cell count at BDC	655,000	1,080,000
Average cell size	1.2 mm	0.7 mm

7.3.3 Initial and boundary conditions

The engine events sequence is shown in Figure 7.6. Simulations are started just before the intake valve opening (IVO), which is at 420° CA before TDC. At this crank angle, cylinder and exhaust ducts contain burnt products; therefore, a temperature of 900 K is specified initially inside the cylinder. Mean pressure trace measured experimentally from 144 cycles is used to define the initial pressure inside the cylinder. Koch (2013) used these experimentally measured pressure

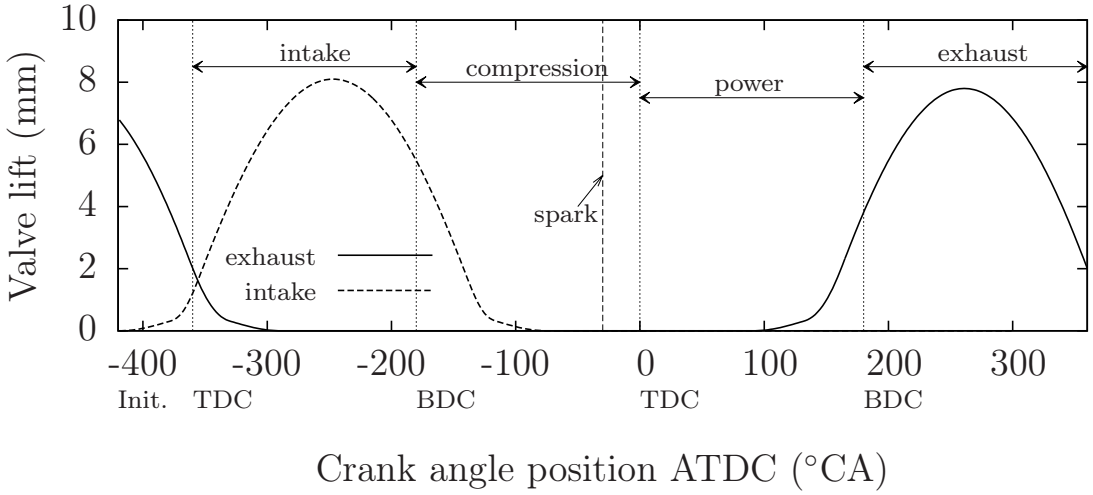

Figure 7.6: Events sequence in the engine, which shows the valve movement plotted against the crank angle.

traces as inputs to a two-zone model to calculate the heat release. Since it is difficult to measure wall temperatures in real engine setups, a sensitivity analysis was performed to determine the effect of wall temperatures on the calculated heat release rate. Koch (2013) used the two-zone model to show that the pressure trace is insensitive to wall temperatures. The assumed wall temperatures are given in Table 7.4, which are fixed during the simulations. In addition to temperature, no-slip, isothermal conditions are applied at the walls.

Pressure boundary conditions are specified for both inlet and outlet. Due to significant differences in the measured inlet and outlet pressures in a given cycle, the specified pressure boundary conditions are crank angle, θ, dependent. These crank angle dependent pressure values were obtained from the mean of 144

measured cycles (Koch, 2013). Furthermore, constant average temperatures at the inlet and outlet are prescribed, which defines the trapped mass within the cylinder. Dirichlet boundary conditions are used for the scalar variables and turbulence quantities at the inlet. For the outlet, Neumann boundary conditions are applied, where the gradients of T, $\tilde{k}$, $\tilde{\epsilon}$, $\tilde{c}$ and $\widetilde{c''^2}$ are set to zero. However, in the case of backflow, the quantities such as temperature and turbulence variables are also specified at the outlet. These boundary conditions are shown in Figure 7.1. Note that symmetry conditions are applied at the plane of symmetry.

Table 7.4: Wall temperatures

Wall	Temperature (K)
Cylinder	400
Piston crown	470
Combustion dome	470

7.3.4 Computational details

Discretisation schemes used in these simulations are similar to the ones used in Chapter 6. As before, PISO algorithm (Issa, 1986) is used for pressure-velocity coupling. A constant time step size of 0.1° CA is chosen, which resolves the reaction, convection and diffusion time scales. The k-ε RNG model (Yakhot et al., 1992; Han and Reitz, 1995) with the wall-function of Angelberger et al. (1997) is used for turbulence closure and the ignition treatment is similar to the one described in section 6.3.3, with an ignition radius of 0.5 mm and an ignition duration of 0.1° CA. Note that the same ignition radius and duration are used for the three models given in Table 7.2.

7.4 Results and discussion

Flow motion inside the cylinder at 200° and 50° crank angles before TDC are given in Figures 7.7(a) and 7.7(b) respectively. Note that 2-D cut-planes are shown in these figures to highlight the flow features. The inlet valve is already

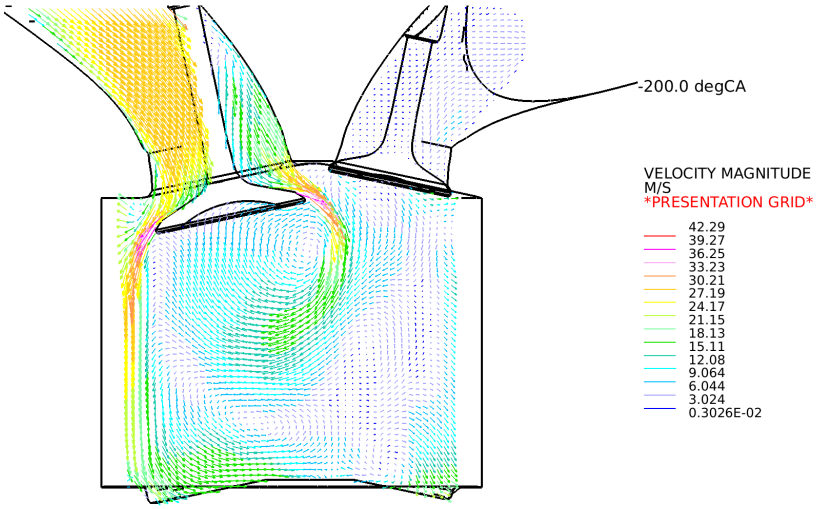

(a)

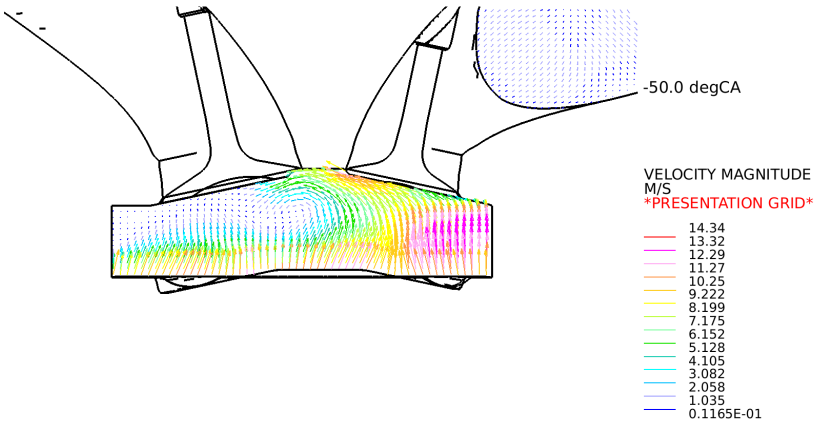

(b)

Figure 7.7: Flow motion inside the cylinder at (a) 200° and (b) 50° CA before TDC.

open at 200° (see Figure 7.6) and Figure 7.7(a) shows that a strong annular jet is created when the inlet valve is open; and two vortical structures can be identified in this figure. These vortices are compressed and quenched by the piston crown and the combustion dome as shown in Figure 7.7(b), where both valves are closed at this crank angle.

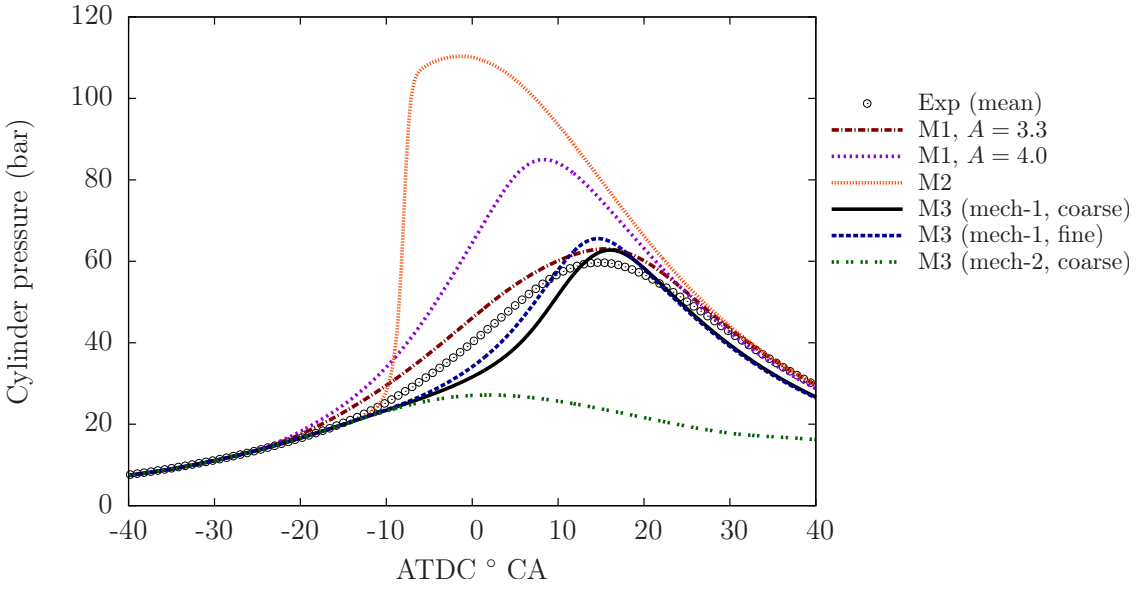

Figure 7.8: Comparison of computed results with experiment. Experimental pressure trace shown here is the mean of 144 cycles. Mech-1 and mech-2 refer to the chemical mechanisms of Pepiot-Desjardins and Pitsch (2008*a*) and Hasse et al. (2000) respectively. Two different values of the flame speed coefficient, A [see Eq. (2.58)], are shown for model M1 (Wright, 2013).

Computed and measured pressure traces are shown in Figure 7.8. This figure shows the results obtained using the reaction rate closure expression given in Eq. (2.63), which is denoted as M3 in Table 7.2, with chemical mechanisms of Hasse et al. (2000) and Pepiot-Desjardins and Pitsch (2008*a*) (denoted as mech-1 and mech-2 respectively). It can be seen that the simulation using the mechanism of Pepiot-Desjardins and Pitsch (2008*a*), in which auto-ignition is assumed to take place inside the cylinder, is unable to predict the experimental pressure rise. Computed results using model M3 and the mechanism of Hasse et al. (2000) gives a reasonable comparison with experimental results, but the initial pressure rise

shortly after ignition is underpredicted. Combustion is through flame propagation when this mechanism is used. Results from the fine mesh using this mechanism is also shown for comparison. Difference in computed peak pressures between the fine and coarse mesh is about 5%, which is considered to be acceptable, and only the coarse mesh is considered in the rest of this work. Also shown in this figure are the results from G-equation (M1) and CFM (M2). Note that the flame speed coefficient, A, in model M1 has been tuned to fit the experimental pressure curve, whereas no parameters are tuned for CFM model. This figure shows that CFM model, with default model parameters set in STAR-CD, is unable to predict the cylinder pressure rise, where the fuel-air mixture is burnt very rapidly.

Both intake and exhaust valves are closed when the mixture is spark-ignited (see Figure 7.6). Pressure traces in Figure 7.8 show that the cylinder pressure increase continuously and reaches a maximum after TDC. This is due to compression of the unburnt gas mixture by the gas-expansion from combustion. The pressure then starts to drop as the cylinder volume is increased in the expansion stroke. Therefore, pressure and temperature of the unburnt gas mixture changes during the combustion process.

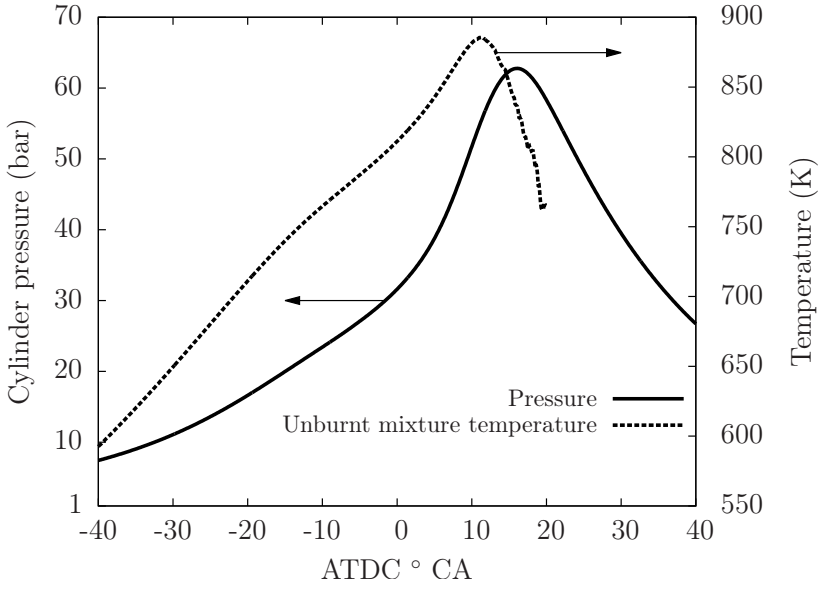

Figure 7.9: Pressure and unburnt mixture temperature variation with crank angle during the simulation.

Figure 7.9 shows the unburnt mixture temperature, T_u, and pressure variation with crank angle during the simulation. The unburnt mixture temperature is necessary to interpolate the reaction source terms from the flamelet library. It is calculated using a volume average of the unburnt cell temperatures inside the combustion chamber. The plots in Figure 7.9 are shown for model M3 using the chemical mechanism of Hasse et al. (2000). It can be seen that the maximum unburnt mixture temperature reaches around 885 K and the mixture becomes fully burnt around 20° CA after TDC.

Difference between results obtained using the chemical mechanisms of Hasse et al. (2000) and Pepiot-Desjardins and Pitsch (2008*a*) shown in Figure 7.8 is explained in the next section. It was described in section 7.3.1 that the look-up table generation is different for these two mechanisms since the mechanism of Pepiot-Desjardins and Pitsch (2008*a*) predicts auto-ignition.

7.4.1 Auto-ignition simulation

The engine is spark-ignited at 30.4° CA before TDC, where unburnt mixture temperature, T_u, near the spark location is approximately at 647 K with a pressure of 10.9 bar (see Figure 7.9). According to Figure 7.4, this corresponds to a flame solution and the flamelet library region corresponding to freely propagating laminar flame is used to obtain the source terms. However, around 15° CA before TDC, the mechanism of Pepiot-Desjardins and Pitsch (2008*a*) predicts that the mixture will be auto-ignited and from this point onwards the auto-ignition part of the flamelet library is used to calculate the source terms. When auto-ignition takes place, the scalar dissipation rate model given in Eq. (2.69) is replaced by the classical algebraic model for $\tilde{\epsilon}_c$. On the contrary, the mechanism of Hasse et al. (2000) cannot predict ignition, and the model given in Eq. (2.69) is used for simulations using this mechanism, which assumes that combustion proceeds through flame propagation.

Auto-ignition of the end gases is usually (but not always) followed by knocking. No knocking behaviour was observed during engine experiments (Wright, 2013), which makes it questionable to use auto-ignition for these simulations. The assumption that iso-octane can be used as a surrogate fuel for gasoline needs

to be considered carefully. For example, the auto-ignition behaviour of these two fuels should be similar. More complex surrogates that match the auto-ignition delay times of gasoline may need to be considered (Pitz et al., 2007; Mehl et al., 2011). Another important point to note is whether the skeletal mechanism of Pepiot-Desjardins and Pitsch (2008*a*) can predict the correct auto-ignition behaviour of a detailed mechanism. Pepiot-Desjardins and Pitsch (2008*a*) reported an average error of 10.86% for the ignition delay times. It was noted by Pepiot-Desjardins and Pitsch (2008*b*) that the error in the ignition delay time is not a monotonic function of the size of the skeletal mechanism and that a smaller error could still lead to different dynamics when compared with a detailed mechanism.

In this work, laminar flame reaction rates are computed using a constant-pressure homogeneous reactor. It is unclear whether this method can be used to obtain correct combustion characteristics for turbulent combustion. The mixture is homogeneous and turbulent mixing and micro-mixing are assumed to occur instantaneously in the constant-pressure reactor. A possible alternative is to use a partially stirred reactor (PaSR), which can handle additional non-linearities of chemistry-turbulence interactions and can serve as a good model for turbulent combustion (Correa, 1993).

These uncertainties regarding the modelling approach used for auto-ignition could explain why the closure expression given in Eq. (2.63) with the chemical mechanism of Pepiot-Desjardins and Pitsch (2008*a*) is unable to predict the correct peak pressure inside the cylinder.

7.4.2 Combustion inside the cylinder

Combustion taking place inside the cylinder at two different crank angles are shown in Figures 7.10 and 7.11, where the top cylinder view is shown with the ducts removed. These plots are obtained using model M3 and mech-1 where the progress variable (defined using water vapour mass fraction) and the mean reaction rates of water vapour are plotted. One could see how the flame propagates inside the cylinder from these two figures. Combustion can also be visualised by plotting the iso-contours of $\tilde{c}$ as shown in Figure 7.12. In this figure, the leading edge of the flame with $\tilde{c} = 0.05$ iso-contours are plotted at different crank angles.

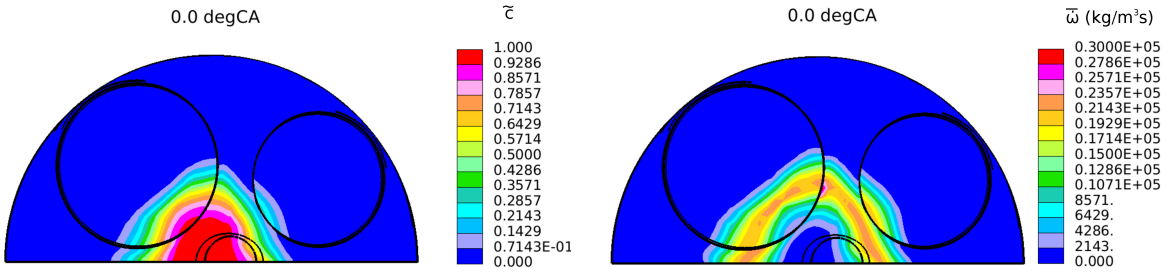

(a) (b)

Figure 7.10: Combustion at TDC: (a) progress variable, $\tilde{c}$, (b) mean reaction rate, $\overline{\dot{\omega}}$. Top view of the chamber surface is shown with holes marking the positions of the removed ducts.

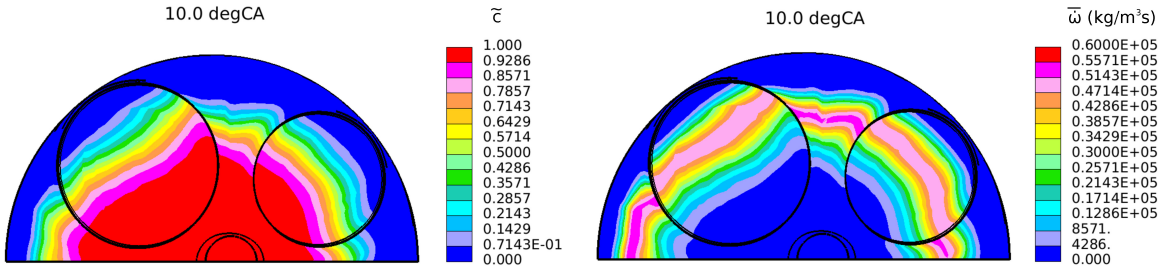

(a) (b)

Figure 7.11: Combustion at 10° CA after TDC: (a) progress variable, $\tilde{c}$ (b) mean reaction rate, $\overline{\dot{\omega}}$.

7.4.3 Heat release rate

The apparent heat release rate can be calculated from the cylinder pressure. It is equal to the difference between heat released during combustion and the heat transfer from the systems, which can be written as (Heywood, 1988)

$$\frac{\mathrm{d}Q_a}{\mathrm{d}t} = \frac{\gamma}{\gamma - 1} p \frac{\mathrm{d}V}{\mathrm{d}t} + \frac{1}{\gamma - 1} V \frac{\mathrm{d}p}{\mathrm{d}t}, \tag{7.1}$$

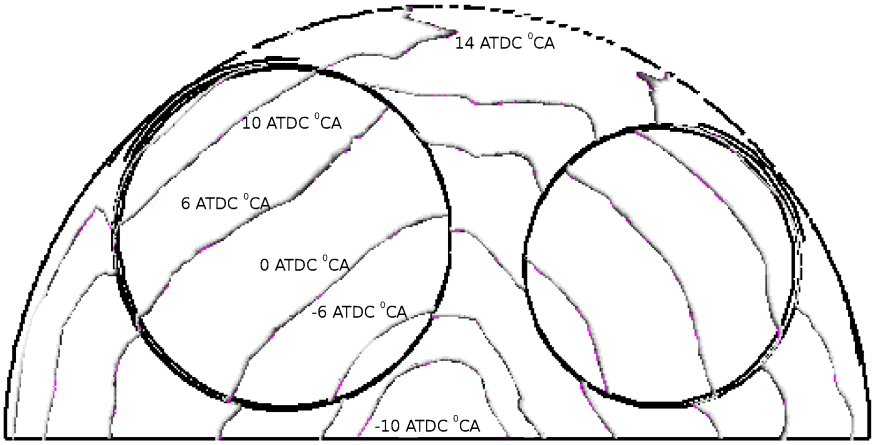

Figure 7.12: Reaction progress variable is visualised at different crank angles during combustion.

where $\mathrm{d}Q_a/\mathrm{d}t$ is the difference between heat transfer rate due to combustion, $\mathrm{d}Q_c/\mathrm{d}t$, and the wall heat-transfer rate, $\mathrm{d}Q_w/\mathrm{d}t$, γ is the ratio of specific heats and V is the cylinder volume. During CFD simulations, the heat release rate can be calculated using:

$$Q = \int_V \overline{\omega}_F Q_{\mathrm{LHV}} \, \mathrm{d}V, \tag{7.2}$$

where $\overline{\omega}_F$ is the mean reaction rate of fuel and Q_{LHV} is the lower heating value of fuel, which is 44.3 MJ/kg for iso-octane (Broustail et al., 2011). Note that Q is calculated in terms of kJ/°CA. The heat release rate, HRR, variation with crank angle is shown in Figure 7.13. This is given as a percentage of the total heat release rate if the fuel inside the cylinder is completely burnt:

$$\mathrm{HRR} = \frac{Q}{m_f Q_{\mathrm{LHV}}} \times 100. \tag{7.3}$$

where m_f is the mass of fuel inside the cylinder. The numerical results shown in Figure 7.13 are obtained using model M3 and mech-1.

This figure shows that there are considerable differences in the heat release

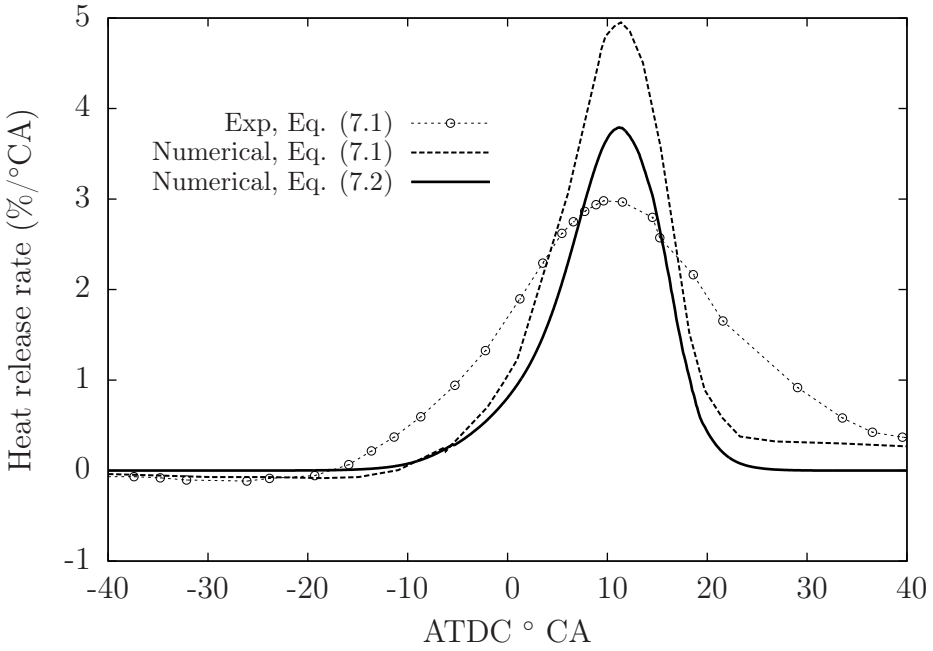

Figure 7.13: Calculated heat release rate as a function of crank angle.

rate computed using Eq. (7.1) for experimental and numerical pressure traces. Also shown on this plot is the direct calculation of the heat release rate using the CFD simulations (shown as a solid line). Unlike the results obtained using Eq. (7.1), the heat release rate obtained using Eq. (7.2) is smaller. Difference between these HRR calculations for the numerical case is because Eq. (7.1) does not use any heat-transfer models. However, even more complete methods used to calculate HRR contain several empirical approximations (Heywood, 1988) and cannot be used to compare directly with the HRR calculated numerically in CFD simulations.

Figure 7.14(a) and Figure 7.14(b) respectively show the burnt mass fraction, $x_b = m_b/m$, and burnt volume fraction, $y_b = V_b/V$, for the models used in this work as a function of the crank angle. These figures correspond to results shown in Figure 7.8 where it was shown that the fuel-air mixture is rapidly burnt when model M2 is used. Plots in Figure 7.14 show that with model M3, the mixture is completely burnt around 20° CA after TDC, which agrees with plot shown in

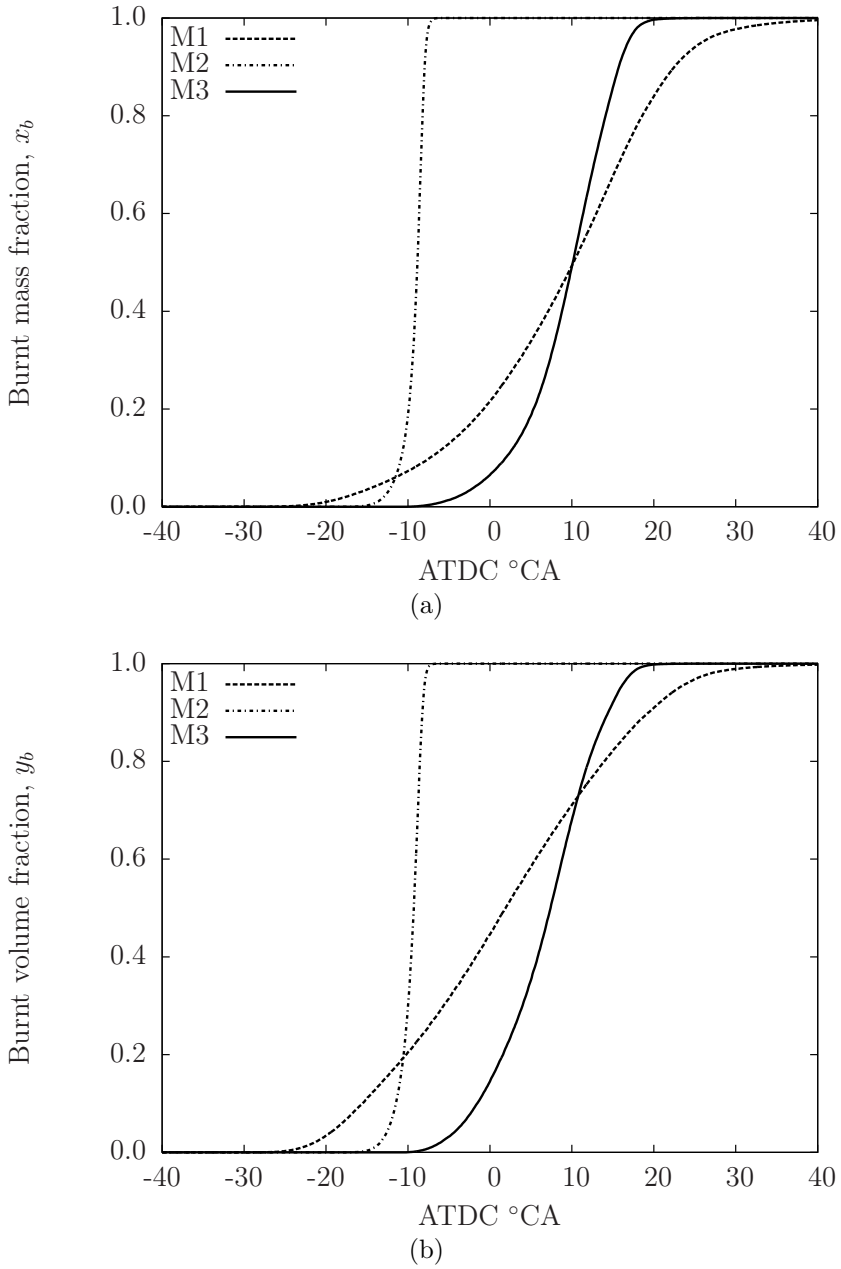

Figure 7.14: (a) Mass fraction burnt and (b) volume fraction burnt as a function of the crank angle.

Figure 7.9. The relation between x_b and y_b is given by (Heywood, 1988)

$$x_b = \left[1 + \frac{\rho_u}{\rho_b}\left(\frac{1}{y_b} - 1\right)\right]^{-1}, \tag{7.4}$$

which has a universal form (Krieger and Borman, 1966). The plot of x_b against y_b obtained using different models and the expression in Eq. (7.4) is shown in Figure 7.15. Note that the ratio $\rho_u/\rho_b = 4$ is used in Eq. (7.4), which is close to the value in most spark-ignition engine operating conditions (Heywood, 1988). Figure 7.15 shows that even though all models show the general trend as expected, none of the models follow the theoretical value. It is to be noted that for intermittent combustion, the ratio ρ_u/ρ_b will change depending on the temperature and pressure inside the cylinder.

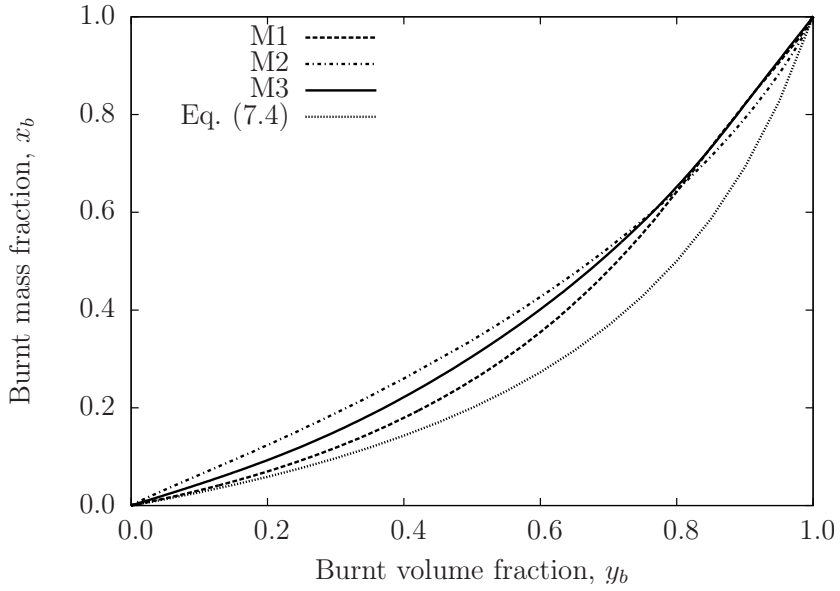

Figure 7.15: Relation between mass fraction burnt and volume fraction burnt for the three models simulated in this work and the expression given in Eq. (7.4).

7.4.4 Effect of turbulence model

Most CFD simulations of internal combustion engines are performed using some version of the widely-used k-ε model (Gosman, 1999). The standard k-ε model

(Jones and Launder, 1972) has been used by a number of researchers (Taut et al., 2000; Brandl et al., 2005). The k-ε RNG model (Yakhot et al., 1992; Han and Reitz, 1995), has also been widely used for engine flows (Cao et al., 2008; Bohbot et al., 2009). The results presented so far have been obtained using this turbulence model. Figure 7.16 shows the sensitivity of the turbulence model in obtaining the pressure trace, where the k-ε realisable model is shown to significantly change the pressure rise. This shows the importance of having correct turbulence description, especially near the spark location. The more complex Reynolds-stress model have also been used for engine flow simulations (Yang et al., 2005), however it has not been widely used, indicating that the benefits are not significant (Gosman, 1999).

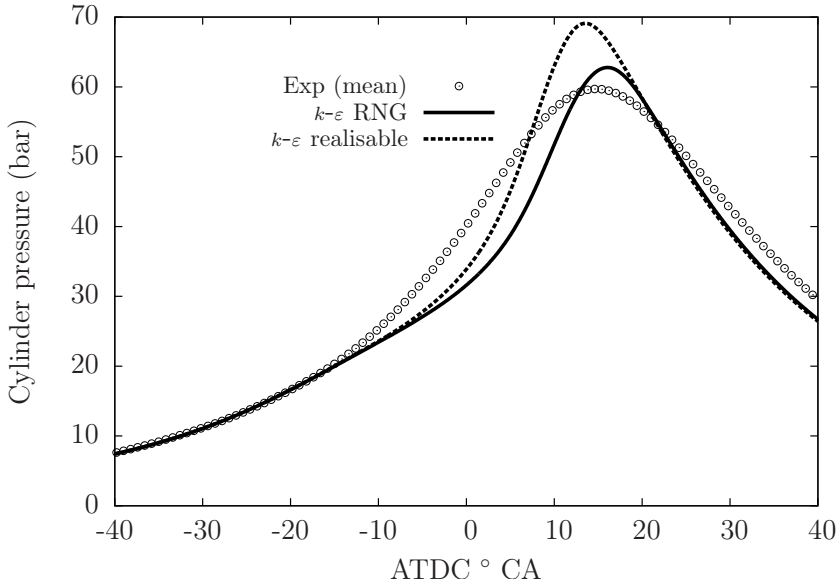

Figure 7.16: Cylinder pressure predictions using two different turbulence models.

7.5 Summary

A spark-ignition engine is simulated using the URANS methodology, with the combustion model based on the flamelet approach. In this approach, the chemical reaction rates are decoupled from CFD calculations. Two skeletal mechanisms

for iso-octane with different sizes are used in this work. The larger mechanism of Pepiot-Desjardins and Pitsch (2008*a*) predicts auto-ignition inside the cylinder after certain pressures and unburnt mixture temperatures and the modelling technique used had to account for this, whereas the smaller mechanism of Hasse et al. (2000) predicts flame propagation, where the modelling is similar to one described in previous chapters.

Results from this work show that the reaction rate closure model given in Eq. (2.63) (M3) with the mechanism of Hasse et al. (2000) gives a reasonable agreement with experimental pressure measurements. However, the mechanism of Pepiot-Desjardins and Pitsch (2008*a*), which predicts auto-ignition, is unable to give the correct pressure rise. Engine experiments did not show any knocking behaviour, which is an indication that there was no auto-ignition inside the cylinder and could explain why the auto-ignition simulation is unable to predict the experimental pressure rise. Results from model M3 are compared with G-equation and CFM models available in STAR-CD. As expected the model parameters for these two models need to be tuned for this engine operating condition, whereas the model M3 does not involve any tunable parameters. This is the first application of the modelling approach described in this thesis to internal combustion engines, and the results obtained in this chapter are encouraging to apply this flamelet based modelling approach to more complex IC engines such as DISI engines.

8. Conclusions and future work

8.1 Conclusions

A computationally economical approach is used to simulate turbulent flames relevant for spark-ignition engine combustion. This is a flamelet based approach, where the turbulent flame is assumed to be an ensemble of laminar flamelets and the chemical time scales are shorter than the turbulence time scales. A central parameter in the current modelling approach is the mean scalar dissipation rate, $\tilde{\epsilon}_c$, which appears either directly or indirectly in all turbulent combustion models. In the current work, an algebraic model for $\tilde{\epsilon}_c$ is used, which was derived based on the physics of the combustion problem (Kolla et al., 2009).

Two different closure models for the mean reaction rate, $\overline{\dot{\omega}}$, are tested: unstrained and strained flamelet models. Strained flamelet model accounts for the flame straining due to turbulence eddies. Detailed chemical mechanisms are used to generate flamelet libraries. Mean scalar dissipation rate term appears directly in the strained flamelet model, while both unstrained and strained modelling approaches require a variance equation of the progress variable, which includes $\tilde{\epsilon}_c$ as a sink term.

In the first part of this work, outwardly propagating spherically symmetric flames are simulated for both methane- and hydrogen-air mixtures. Spherical flames are found in spark-ignition engines as well as accidental explosions of vapour clouds. These simulations are performed using an in-house CFD code after modifying it for spherical coordinates.

For methane-air flames, it is shown that the strained flamelet is able to predict the experimental flame propagation of Hainsworth (1985), which were carried out in a wind tunnel with decaying turbulence. The strained flamelet model is then used to compare planar and spherical flames having the same turbulence and thermochemical conditions. It is observed that the propagation of the flame leading edge is aided by the local fluid velocity at that location for spherical flames. Whereas for planar flames the direction of fluid flow and the advancing

leading edge are in opposite directions. A novel observation from these spherical flame simulation is that the growth of the turbulent flame brush thickness is mainly due to heat-release induced convective effects and not due to turbulent diffusion. The role of turbulent diffusion for this thickness growth has been advocated in many past studies [see the review article by Lipatnikov and Chomiak (2002)].

Experiments of Kitagawa et al. (2008) are used to validate the combustion models for hydrogen-air spherical flames. These experiments were performed in a spherical bomb with fans used to generate turbulence. It is assumed that turbulence does not decay for the bomb experiments since the fans were left running during the experiments. Unlike the methane-air flames previously simulated, hydrogen-air flames do not have unity Lewis numbers. In order to overcome this issue, a two-progress variable approach is used, with one based on water vapour mass fraction and the other on temperature. As before, it is shown that the strained flamelet model is able to predict the experimental results for stoichiometric hydrogen-air flames. However, the predictions for lean hydrogen-air flames is poor, because these flames are thermo-diffusively unstable and the current numerical methodology is inadequate to deal with such flames. Further analysis of turbulent hydrogen-air flames showed that the flame response to turbulence are similar to that of methane-air flames.

Strained and unstrained flamelet models are then used to simulate intermittent combustion taking place inside a closed vessel. Here the experiments of Hamamoto et al. (1988) are used for validation. In these experiments turbulence was generated using swirling inflow of premixed fuel and air, where stoichiometric propane-air mixture was used. This is a more realistic test case for IC engine combustion and the simulations are performed using STAR-CD. Pressure rise measured in the experiment is predicted reasonably well using both strained and strained flamelet models. It is believed that flame confinement restricts the entrainment of air, which reduces the flame straining due to turbulence. This could explain why the differences in the results between unstrained and strained flamelet models are small for this case.

Therefore, only the unstrained flamelet model is used for a practical IC engine simulation, since the strained flamelet look-up table generation took significantly

longer compared with the unstrained one with a marginal gain. A single-cylinder, four-stroke SI engine experimentally investigated in ETH Zürich is simulated using STAR-CD, with iso-octane used as a gasoline surrogate. Two chemical mechanisms are tested in this work, one predicts auto-ignition for the conditions inside the cylinder whereas the other predicts flame propagation. Results obtained using the mechanism that predicts flame propagation compares reasonably well with experimental data, whereas the simulation using auto-ignition is unable to predict the correct pressure rise. It is to be noted that no knocking was observed during experimental measurements, therefore, it is unlikely that the mixture auto-ignites, which could explain why the auto-ignition simulation is unable to predict the experimental pressure rise. Unlike the combustion models available in STAR-CD, the modelling approach used in this work does not involve any tunable parameters.

8.2 Recommendations for future work

The work carried out in this study has identified the following areas for further investigations.

Spherical flame propagation: Results presented in Figure 4.4 clearly show that the propagation speed, s_p, of the spherical flame progress variable iso-contours approach that of planar flame. The domain length used in these simulations are not sufficient to simulate these flames for a longer time. It is generally believed that spherical flames will eventually propagate at the same speed as planar flames, which can be verified by running the simulation for a much longer time. This will give further fundamental insight into spherical flame propagation.

Self-similarity in spherical flames: The flame radius variation with time is given by

$$r_f(t) = R_0 + At^n \approx At^n, \tag{8.1}$$

where A and R_0 are empirical constants. Note that R_0 does not correspond to the ignition radius since self-similarity is expected to start at a later time (Gostintsev et al., 1988). The exponent, n, has been reported to fall in the range 1.25–1.5 (Gostintsev et al., 1988; Bychkov and Liberman, 1996; Pan and Fursenko, 2008). Experiments of Jomaas and Law (2009) showed that the n is around 4/3. They also showed that this value was independent of the fuel-air mixture, i.e. the chemical composition does not affect the power-law given in Eq. (8.1). By simulating spherical methane- and hydrogen-air flames given in Chapters 4 and 5 for a longer time it will be possible to determine the exponent n, which can then be compared with published data.

Accounting for thermo-diffusive effects: Results from this work indicate that including detailed chemistry in the laminar flame calculations is inadequate to simulate turbulent flames that are thermo-diffusively unstable. These effects need to be included in the turbulence models and it appears that the governing equations have to be modified to account for thermo-diffusive effects in turbulent flames.

Determining the effect of Lewis number remains an active area of combustion research. For example, Chakraborty and Cant (2011) used DNS to investigate the effect of Lewis number on flame surface density transport and proposed closure models for various terms. In addition, Lewis number effects for the progress variable and its variance equations for scalar dissipation rate based modelling have been studied and closure models have been proposed (Chakraborty and Swaminathan, 2010, 2011).

Using DNS of the G-equation, Dandekar and Collins (1995) showed that the thermo-diffusive instability analyses of Sivashinsky (1977) can be used to describe the evolution of a passive but propagative scalar G. Peters (1999) noted that the kinematic G-equation, which contains the Markstein diffusivity, must be modified to study thermo-diffusive effects. Recently, Regele et al. (2013) studied laminar flames with non-unity Lewis numbers using a progress variable equation together with an equation for the mixture fraction that includes non-unity Lewis numbers. Ranga Dinesh et al. (2013) studied non-premixed hydrogen-air flames using DNS, where they included a mixture fraction equation and two dif-

ferent progress variable equations; one based on unity Lewis number assumption and the other based on non-unity Lewis numbers. These studies indicate that the non-unity Lewis numbers have to be explicitly implemented in the turbulent simulations.

Auto-ignition of iso-octane: In this work, unburnt mixture temperature and pressure conditions for auto-ignition are determined using freely propagating flame calculations using the skeletal mechanism of Pepiot-Desjardins and Pitsch (2008*a*). These calculations can be repeated in a future study using other skeletal mechanisms that can predict ignition, to determine the effect of chemical mechanism.

Partially-stirred reactor for flamelet generation: A number of popular combustion technologies for IC engines, such as HCCI, use controlled auto-ignition. It is crucial that the laminar flame configuration used to generate the flamelet library is representative of turbulent auto-ignition. In this case a homogeneous constant-pressure reactor is used, however, one could use a partially stirred reactor which can serve as a good model for turbulent combustion.

Simulation of gasoline direct injection: Gasoline engines are moving towards direct injection, which provides a number of added benefits. However, in GDI engines the mixture is only partially premixed and the modelling approach used in this work has to be changed to account for that.

For partially premixed flames, closure models for the scalar dissipation rate of both passive and reactive scalars are required. Furthermore, one also needs to model the cross scalar dissipation rate. Algebraic models for partially premixed flames have been proposed by Ribert et al. (2005); Robin et al. (2006); Mura et al. (2007); Malkeson and Chakraborty (2010, 2011); Ruan et al. (2012). One could implement these algebraic closures in STAR-CD to simulate combustion in a spark-ignited GDI engine.

A. Spherically symmetric equations

Spherically symmetric equations for RANS can be obtained from the governing equations described in section 2.2.3. Only the momentum equation is shown here since the derivation of the rest of the equations follow a similar procedure.

A.1 Radial momentum equation

The momentum equation [Eq. (2.2)] can be written in spherical coordinates [see for example Bird et al. (2002)]. Since a spherically symmetric system is considered in this work, only the radial momentum equation needs to be considered. The Favre-averaged radial-momentum equation in conservative form can be written as

$$\begin{aligned}
&\frac{\partial \overline{\rho}\tilde{u}_r}{\partial t} + \frac{1}{r^2}\frac{\partial}{\partial r}\left[r^2(\overline{\rho}\tilde{u}_r^2)\right] + \frac{1}{r\sin\theta}\frac{\partial}{\partial \theta}\left(\overline{\rho}\tilde{u}_r\tilde{u}_\theta \sin\theta\right) + \frac{1}{r\sin\theta}\frac{\partial}{\partial \phi}\left(\overline{\rho}\tilde{u}_r\tilde{u}_\phi\right) - \overline{\rho}\frac{\tilde{u}_\theta + \tilde{u}_\phi}{r} \\
&= -\frac{\partial \overline{p}}{\partial r} + \frac{1}{r^2}\frac{\partial}{\partial r}\left[r^2\left(\overline{\tau}_{rr} - \overline{\rho u_r''^2}\right)\right] + \frac{1}{r\sin\theta}\frac{\partial}{\partial \theta}\left[\sin\theta(\overline{\tau}_{\theta r} - \overline{\rho u_\theta'' u_r''})\right] \\
&+ \frac{1}{r\sin\theta}\frac{\partial}{\partial \phi}\left(\overline{\tau}_{\phi r} - \overline{\rho u_\phi'' u_r''}\right) - \frac{(\overline{\tau}_{\theta\theta} - \overline{\rho u_\theta''^2} + \overline{\tau}_{\phi\phi} - \overline{\rho u_\phi''^2})}{r},
\end{aligned} \tag{A.1}$$

where $\tilde{u}_r$, $\tilde{u}_\theta$ and $\tilde{u}_\phi$ are the Favre-averaged velocities in the r, θ and ϕ directions respectively. For a spherically symmetric system, the following additional assumptions can be made

$$\tilde{u}_\theta = \tilde{u}_\phi = 0, \quad \tilde{u}_r = \tilde{u}_r(r), \quad \frac{\partial}{\partial \theta} = \frac{\partial}{\partial \phi} = 0, \tag{A.2}$$

to obtain the radial momentum equation [Eq. (3.2)], which is given below for convenience.

$$\frac{\partial \overline{\rho}\tilde{u}_r}{\partial t} + \frac{1}{r^2}\frac{\partial}{\partial r}\left[r^2(\overline{\rho}\tilde{u}_r^2)\right] = -\frac{\partial \overline{p}}{\partial r} + \frac{1}{r^2}\frac{\partial}{\partial r}\left[r^2\left(\overline{\tau}_{rr} - \overline{\rho u_r''^2}\right)\right] - \frac{(\overline{\tau}_{\theta\theta} - \overline{\rho u_\theta''^2} + \overline{\tau}_{\phi\phi} - \overline{\rho u_\phi''^2})}{r}. \tag{A.3}$$

The non-vanishing viscous stress tensor appearing in the above equation is given by Eq. (2.3). From this equation, the three non-vanishing stress tensors in spherical coordinates are given as

$$\overline{\tau}_{rr} = 2\mu\frac{\partial \tilde{u}_r}{\partial r} - \frac{2}{3}\mu\left[\frac{1}{r^2}\frac{\partial}{\partial r}(r^2\tilde{u}_r)\right], \tag{A.4}$$

$$\overline{\tau}_{\theta\theta} = \overline{\tau}_{\phi\phi} = 2\mu\frac{\tilde{u}_r}{r} - \frac{2}{3}\mu\left[\frac{1}{r^2}\frac{\partial}{\partial r}(r^2\tilde{u}_r)\right]. \tag{A.5}$$

Similarly the Reynolds stress terms using Boussinesq approximation are given by Eqs. (3.7) and (3.8). Substitution of these stress terms into Eq. (A.3) and term-by-term expansion gives

$$\overline{\tau}_{rr} - \overline{\rho u_r''^2} = 2(\mu+\mu_t)\frac{\partial \tilde{u}_r}{\partial r} - \frac{2}{3}(\mu+\mu_t)\left(\frac{1}{r^2}\frac{\partial}{\partial r}(r^2\tilde{u}_r)\right) - \frac{2}{3}\overline{\rho}\tilde{k}, \tag{A.6}$$

$$\frac{1}{r^2}\frac{\partial}{\partial r}\left[r^2\left(\overline{\tau}_{rr} - \overline{\rho u_r''^2}\right)\right] = \frac{1}{r^2}\frac{\partial}{\partial r}\left\{r^2\left[2(\mu+\mu_t)\frac{\partial \tilde{u}_r}{\partial r} - \frac{2}{3}(\mu+\mu_t)\left(\frac{1}{r^2}\frac{\partial}{\partial r}(r^2\tilde{u}_r)\right)\right]\right\} - \frac{1}{r^2}\frac{\partial}{\partial r}\left(r^2\frac{2}{3}\overline{\rho}\tilde{k}\right). \tag{A.7}$$

The first term on the RHS of Eq. (A.7) can be simplified as

$$\frac{1}{r^2}\frac{\partial}{\partial r}\left\{r^2\left[2(\mu+\mu_t)\frac{\partial \tilde{u}_r}{\partial r} - \frac{2}{3}(\mu+\mu_t)\left(\frac{1}{r^2}\frac{\partial}{\partial r}(r^2\tilde{u}_r)\right)\right]\right\} = \frac{1}{r^2}\frac{\partial}{\partial r}\left\{r^2\frac{4}{3}(\mu+\mu_t)\left(\frac{\partial \tilde{u}_r}{\partial r} - \frac{\tilde{u}_r}{r}\right)\right\}. \tag{A.8}$$

Therefore

$$\frac{1}{r^2}\frac{\partial}{\partial r}\left[r^2\left(\overline{\tau}_{rr}-\overline{\rho u_r''^2}\right)\right]=\frac{1}{r^2}\frac{\partial}{\partial r}\left\{r^2\frac{4}{3}(\mu+\mu_t)\left(\frac{\partial\tilde{u}_r}{\partial r}-\frac{\tilde{u}_r}{r}\right)\right\}-\frac{1}{r^2}\frac{\partial}{\partial r}\left(r^2\frac{2}{3}\overline{\rho}\tilde{k}\right). \tag{A.9}$$

Expand the last term in equation (A.3) to obtain:

$$\frac{(\overline{\tau}_{\theta\theta}-\overline{\rho u_\theta''^2}+\overline{\tau}_{\phi\phi}-\overline{\rho u_\phi''^2})}{r}=4(\mu+\mu_t)\frac{\tilde{u}_r}{r^2}-\frac{4}{3}(\mu+\mu_t)\left(\frac{1}{r^3}\frac{\partial}{\partial r}(r^2\tilde{u}_r)\right)-\frac{4}{3}\frac{\overline{\rho}\tilde{k}}{r}. \tag{A.10}$$

Now let $\Gamma=[4\,(\mu+\mu_t)]/3$. By substituting Eqs. (A.9) and (A.10) in Eq. (A.3) to obtain:

$$\frac{\partial\overline{\rho}\tilde{u}_r}{\partial t}+\frac{1}{r^2}\frac{\partial}{\partial r}\left[r^2(\overline{\rho}\tilde{u}_r^2)\right]=-\frac{\partial\overline{p}}{\partial r}+\frac{1}{r^2}\frac{\partial}{\partial r}\left(r^2\Gamma\frac{\partial\tilde{u}_r}{\partial r}\right)-\frac{1}{r^2}\frac{\partial}{\partial r}\left(r^2\Gamma\frac{\tilde{u}_r}{r}\right)-3\Gamma\frac{\tilde{u}_r}{r^2}+\frac{\Gamma}{r^3}\frac{\partial}{\partial r}(r^2\tilde{u}_r)+\frac{4}{3}\frac{\overline{\rho}\tilde{k}}{r}-\frac{1}{r^2}\frac{\partial}{\partial r}\left(r^2\frac{2}{3}\overline{\rho}\tilde{k}\right). \tag{A.11}$$

The terms on the RHS of Eq. (A.11) can be simplified further as follows:

$$\frac{4}{3}\frac{\overline{\rho}\tilde{k}}{r}-\frac{1}{r^2}\frac{\partial}{\partial r}\left(r^2\frac{2}{3}\overline{\rho}\tilde{k}\right)=-\frac{\partial}{\partial r}\left(\frac{2}{3}\overline{\rho}\tilde{k}\right), \tag{A.12}$$

and

$$-\frac{1}{r^2}\frac{\partial}{\partial r}\left(r^2\Gamma\frac{\tilde{u}_r}{r}\right)=-\frac{\partial\Gamma}{\partial r}\frac{\tilde{u}_r}{r}-\frac{\Gamma}{r}\frac{\partial\tilde{u}_r}{\partial r}-\Gamma\frac{\tilde{u}_r}{r^2} \tag{A.13}$$

$$\frac{\Gamma}{r^3}\frac{\partial}{\partial r}(r^2\tilde{u}_r)=\frac{\Gamma}{r}\frac{\partial\tilde{u}_r}{\partial r}+2\Gamma\frac{\tilde{u}_r}{r^2}. \tag{A.14}$$

Hence

$$-\frac{1}{r^2}\frac{\partial}{\partial r}\left(r^2\Gamma\frac{\tilde{u}_r}{r}\right)-3\Gamma\frac{\tilde{u}_r}{r^2}+\frac{\Gamma}{r^3}\frac{\partial}{\partial r}(r^2\tilde{u}_r)\frac{4}{3}\frac{\overline{\rho}\tilde{k}}{r}-\frac{1}{r^2}\frac{\partial}{\partial r}\left(r^2\frac{2}{3}\overline{\rho}\tilde{k}\right)$$
$$=-\frac{\partial}{\partial r}\left(\frac{2}{3}\overline{\rho}\tilde{k}\right)-\frac{\partial\Gamma}{\partial r}\frac{\tilde{u}_r}{r}-2\Gamma\frac{\tilde{u}_r}{r^2}. \tag{A.15}$$

The momentum equation can finally be written as

$$\frac{\partial\overline{\rho}\tilde{u}_r}{\partial t}+\frac{1}{r^2}\frac{\partial}{\partial r}\left[r^2(\overline{\rho}\tilde{u}_r^2)\right]=-\frac{\partial\overline{p}}{\partial r}+\frac{1}{r^2}\frac{\partial}{\partial r}\left(r^2\Gamma\frac{\partial\tilde{u}_r}{\partial r}\right)$$
$$-\frac{\partial}{\partial r}\left(\frac{2}{3}\overline{\rho}\tilde{k}\right)-\frac{1}{r}\left(\frac{\partial\Gamma}{\partial r}+\frac{2\Gamma}{r}\right)\tilde{u}_r. \tag{A.16}$$

B. Code validation

The modified in-house CFD code is validated for simple, spherically symmetric diffusion and convection problems. For the sake of simplicity, it is assumed that there is no reaction (i.e. $\overline{\dot{\omega}} = 0$) and turbulence is assumed to be frozen.

B.1 Diffusion test case

Convection is assumed to be zero in order to validate the code for pure diffusion. Then Eq. (3.3) can be written as the familiar diffusion equation

$$\frac{\partial \tilde{c}}{\partial t} = D \frac{1}{r^2} \frac{\partial^2 \tilde{c}}{\partial r^2}, \tag{B.1}$$

where diffusivity, $D = \alpha_c + \mu_t/\mathrm{Sc}_c$ and $\tilde{c}$ defined in terms of temperature as in Eq. (2.12). This parabolic PDE in r and t can be solved for a sphere with radius, R, using the method of separation of variables, assuming a solution of the form $\tilde{c}(\boldsymbol{r}, t) = R(\boldsymbol{r})T(t)$. Substituting this into Eq. (B.1), and taking the separation constant as $-\lambda^2$ gives the following two equations;

$$\nabla^2 R + \lambda^2 R = 0, \quad \frac{\mathrm{d}T}{\mathrm{d}t} + \lambda^2 D T = 0. \tag{B.2}$$

The simple solution to the time-dependent equation above is: $T(t) = Ae^{-\lambda^2 Dt}$, where A is a constant to be determined later. The first equation in Eq. (B.2) is the *Helmholtz's equation*, which for spherical symmetry (no ϕ or θ dependence) can be written as

$$\frac{1}{r^2} \frac{\mathrm{d}}{\mathrm{d}r} \left(r^2 \frac{\mathrm{d}R}{\mathrm{d}r} \right) + \lambda^2 R = 0. \tag{B.3}$$

When there is spherical symmetry it is useful to make the substitution $u = rR$. Now Eq. (B.3) can be written as:

$$\frac{\mathrm{d}^2 u}{\mathrm{d}r^2} + \lambda^2 u = 0, \tag{B.4}$$

which has the solution: $u(r) = B\sin(\lambda r) + C\cos(\lambda r)$. Hence

$$R(r) = \frac{1}{r}\left[B\sin(\lambda r) + C\cos(\lambda r)\right]. \tag{B.5}$$

Boundary and initial conditions have to be applied to obtain the constants A, B and C. Only spherical flames that propagate radially outward (explosions) are considered in this work.

Now consider a sphere with $0 < r < b$, where b is the radius of the sphere. Assuming that one is not interested in the case where an explosion started at the origin reaches the outer walls of the sphere, the temperature at the wall, at all instances of interest, can be set to T_u, which gives the boundary condition

$$\tilde{c} = 0 \quad \text{at} \quad r = b. \tag{B.6}$$

In addition, as a result of symmetry and since there is no heat influx at the centre of the sphere, an additional condition

$$\frac{\mathrm{d}\tilde{c}}{\mathrm{d}r} = 0 \quad \text{at} \quad r = 0. \tag{B.7}$$

can be set at the origin to solve the problem. The initial condition is a particular initial profile of $\tilde{c}$:

$$\tilde{c}(r, 0) = \tilde{c}_0(r). \tag{B.8}$$

Since $\tilde{c}$ has to be finite at the origin, the constant C in the solution needs to be zero. In addition, applying the boundary condition (B.6) yields the eigenvalues,

$\lambda_n = (n\pi)/b$, and the eigenfunction

$$R_n(r) = \frac{A_n}{r} \sin\left(\frac{n\pi r}{b}\right), \quad n = \pm 1, \pm 2, \pm 3, \ldots \tag{B.9}$$

A particular solution to Eq. (B.3) is then

$$\tilde{c}(r,t) = R_n(r)T(t) = \frac{A_n}{r} \sin(\lambda_n r) e^{-\lambda^2 D t}. \tag{B.10}$$

Since the diffusion equation is linear, the principle of superposition yields the following general solution

$$\tilde{c}(r,t) = \sum_{n=1}^{\infty} \frac{A_n}{r} \sin(\lambda_n r) e^{-\lambda^2 D t}. \tag{B.11}$$

Note that only the positive values of n have been taken since negative values will lead to exponential grown when $n \to \infty$. The term, $n = 0$ is omitted since it is identically zero. The coefficients A_n can now be chosen to satisfy the initial condition (B.8) to yield

$$\tilde{c}(r,0) = \tilde{c}_0(r) = \sum_{n=1}^{\infty} \frac{A_n}{r} \sin(\lambda_n r). \tag{B.12}$$

When both sides of Eq. (B.12) are multiplied by r, it can be seen that this is half-range Fourier series of $c_0(x)$ between 0 and b. Therefore A_n is given by the Fourier coefficient

$$A_n = \frac{2}{b} \int_0^b \tilde{c}_0(r') \sin\left(\frac{n\pi r'}{b}\right) r' \, \mathrm{d}r'. \tag{B.13}$$

Finally, the full solution to the problem is given by

$$\tilde{c}(r,t) = \sum_{n=1}^{\infty} \left[\frac{2}{b} \int_0^b \tilde{c}_0(r') \sin\left(\frac{n\pi r'}{b}\right) r' \, \mathrm{d}r'\right] \frac{1}{r} \sin\left(\frac{n\pi r}{b}\right) e^{-\lambda^2 D t}. \tag{B.14}$$

If the initial profile, $\tilde{c}_0(r')$, is taken as [see Figure B.1(a) for the values of r_1 and r_2]

$$\widetilde{c}_0(r') = \begin{cases} 1 & \text{for } 0 \leq r' < r_1 \\ \left(\frac{r-r_2}{r_1-r_2}\right) & \text{for } r_1 \leq r' \leq r_2 \\ 0 & \text{for } r_2 < r' \leq R \end{cases} \tag{B.15}$$

then the exact solution obtained after integration is

$$\widetilde{c}(r,t) = \sum_{n=1}^{\infty} \left\{ \frac{2}{\lambda^2 R} \left[\sin(\lambda_n r_1) + \frac{1}{r_1 - r_2} \left(r_2 \sin(\lambda_n r_2) - (2r_1 - r_2)\sin(\lambda_n r_1) + \frac{2}{\lambda_n}\left(\cos(\lambda_n r_2) - \cos(\lambda_n r_1)\right) \right) \right] \right\} \times \frac{1}{r} \sin\left(\frac{n\pi r}{R}\right) e^{-\lambda^2 D t}. \tag{B.16}$$

Figure B.1(a) shows that this analytical result at $t = 1$ s can be predicted numerically using the method outlined in this section.

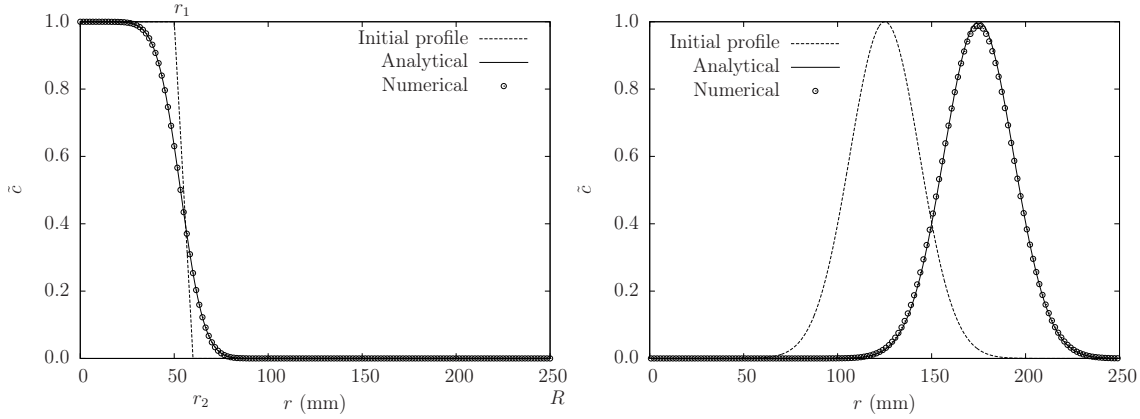

Figure B.1: Validation of numerical code for: (a) diffusion at $t = 1$ s and (b) convection at $t = 0.1$ s.

B.2 Convection test case

In the case of pure convection without heat release, Eq. (3.3) can be written as

$$\frac{\partial \tilde{c}}{\partial t} + \frac{1}{r^2}\frac{\partial}{\partial r}\left(r^2 \tilde{u}_r \tilde{c}\right) = 0, \tag{B.17}$$

which is the linear advection equation in spherical coordinates. Since $\overline{\dot{\omega}} = 0$, the heat release parameter, $\tau = 0$, thus, the convection velocity, $\tilde{u}_r$, is not a function of $\tilde{c}$. One can then think of $\tilde{c}$ as being a convected quantity, with its value at time, t, given by

$$\tilde{c}(r,t) = \tilde{c}_0(r - \tilde{u}_r t). \tag{B.18}$$

Note that if Eq. (B.17) is solved together with the momentum and pressure Poisson equation [essentially what is done in SIMPLER method (Patankar, 1980)], then the velocity $\tilde{u}_r$ will not remain constant due to the change in radius as the profile is convected. Therefore, in order to maintain a constant convection velocity, the pressure equation is not solved for this particular test problem. The results of this convection problem is shown in Figure B.1(b), which shows good agreement with the analytical result.

C. List of Publications

Journal publications

- Ahmed, I., and Swaminathan, N. 2013. Simulation of spherically expanding turbulent premixed flames. *Combust. Sci. Technol.*, **185**, 1509–1540.
- Ahmed, I., and Swaminathan, N. 2014. Simulation of turbulent explosion of hydrogen-air mixtures. *Int. J. Hydrogen Energ.*, **39**, 9562–9572.
- Ahmed, I., Swaminathan, N., Schlatter, S., and Wright, Y. M. Simulation of combustion in a closed vessel with swirl (in preparation).
- Ahmed, I., Swaminathan, N., Koch, J., and Wright, Y. M. Spark-ignition engine simulation using a flamelet based combustion model (in preparation).

Invited talks

- Swaminathan, N., and Ahmed, I. 2013. Investigation of turbulent spherical flames. *American Physical Society, 66th Annual Meeting of the APS Division of Fluid Mechanics*, November 24-26, Pittsburgh, PA, USA.

Conference publications

- Ahmed, I., and Swaminathan, N. 2011. Simulation of spherical turbulent premixed flames. *Proceedings of the 5th European Combustion Meeting*, June 28-July 1, Cardiff, UK.
- Ahmed, I., and Swaminathan, N. 2011. Effects of mean curvature on flame propagation. *Proceedings of the 23rd International Colloquium on the Dy-*

namics of Explosions and Reactive System, July 24-29, Irvine, California, USA.

- Ahmed, I., and Swaminathan, N. 2012. Simulation of spherical methane-air flames. *Proceedings of the 1st International Education Forum on Environment and Energy Science*, December 14-18, Hawaii, USA.

- Ahmed, I., Swaminathan, N., Schlatter, S., and Wright, Y. M. 2013. Simulation of swirl combustion in a closed vessel. *Proceedings of the 6th European Combustion Meeting*, June 25-28, Lund, Sweden.

References

Abdel-Gayed, R. G., Al-Khishali, K. J., and Bradley, D. 1984. Turbulent burning velocities and flame straining in explosions. *Proc. R. Soc. Lond. A*, **391** (1801), 393–414.

Abdel-Gayed, R. G., Bradley, D., and Lawes, M. 1987. Turbulent burning velocities: a general correlation in terms of straining rates. *Proc. R. Soc. Lond. A*, **414** (1847), 389–413.

Abdel-Gayed, R. G., Bradley, D., Lawes, M., and Lung, F.K-K. 1988. Premixed turbulent burning during explosions. *Proc. Combust. Inst.*, **21**, 497–504.

Abu-Orf, G. M., and Cant, R. S. 2000. A turbulent reaction rate model for premixed turbulent combustion in spark-ignition engines. *Combust. Flame*, **122** (3), 233–252.

Albin, E., and D'Angelo, Y. 2012. Assessment of the evolution equation modelling approach for three-dimensional expanding wrinkled premixed flames. *Combust. Flame*, **159**, 1932–1948.

Amzin, S., and Swaminathan, N. 2013. Computations of turbulent lean premixed combustion using conditional moment closure. *Combust. Theor. Model.*, **17**, 1125–1153.

Amzin, S., Swaminathan, N., Rogerson, J. W., and Kent, J. H. 2012. Conditional moment closure for turbulent premixed flames. *Combust. Sci. Technol.*, **184**, 1743–1767.

Andrews, G. E., and Bradley, D. 1972. The burning velocity of methane-air mixtures. *Combust. Flame*, **19** (2), 275–288.

Andrews, G. E., Bradley, D., and Lwakabamba, S. B. 1975. Measurement of turbulent burning velocity for large turbulent reynolds numbers. *Proc. Combust. Inst.*, **15**, 655–664.

Angelberger, C., Poinsot, T., and Delhay, B. 1997. Improving near-wall combustion and wall heat transfer modeling in SI engine computations. *Tech. Rep.* 972881. SAE International, Warrendale, PA, USA.

Ashurst, W. T. 1995. A simple illustration of turbulent flame ball growth. *Combust. Sci. Technol.*, **104**, 19–32.

Ashurst, W. T., Checkel, M. D., and Ting, D. S. K. 1994. The eddy structure model of turbulent flamelet propagation, the expanding spherical and steady planar cases. *Combust. Sci. Technol.*, **99**, 51–74.

Asproulis, P. 1994. High resolution numerical predictions of hypersonic flows on unstructured meshes. Ph.D., Imperial College London, London, UK.

Aung, K. T., Hassan, M. I., and Faeth, G. M. 1997. Flame stretch interactions of laminar premixed hydrogen/air flames at normal temperature and pressure. *Combust. Flame*, **109** (1-2), 1–24.

Aung, K. T., Hassan, M. I., and Faeth, G. M. 1998. Effects of pressure and nitrogen dilution on flame/stretch interactions of laminar premixed H2/O2/N2 flames. *Combust. Flame*, **112** (1-2), 1–15.

Aung, K. T., Hassan, M. I., Kwon, S., Tseng, L. K., Kwon, O. C., and Faeth, G. M. 2002. Flame/stretch interactions in laminar and turbulent premixed flames. *Combust. Sci. Technol.*, **174** (1), 61–99.

Baker, W. E., Cox, P. A., Kulesz, J. J., Strehlow, R. A., and Westine, P. S. 1983. *Explosion Hazards and Evaluation*. Elsevier, Amsterdam, Netherlands.

Balat, M. 2008. Potential importance of hydrogen as a future solution to environmental and transportation problems. *Int. J. Hydrogen Energ.*, **33** (15), 4013–4029.

Banaeizadeh, A., Afshari, A., Schock, H., and Jaberi, F. 2008. Large eddy simulations of turbulent flows in IC engines. New York, USA.

Baritaud, T. A., Duglos, J. M., and Fusco, A. 1996. Modeling turbulent combustion and pollutant formation in stratified charge SI engines. *Proc. Combust. Inst.*, **26** (2), 2627–2635.

Bauer, C. G., and Forest, T. W. 2001. Effect of hydrogen addition on the performance of methane-fueled vehicles. part i: effect on S.I. engine performance. *Int. J. Hydrogen Energ.*, **26** (1), 55–70.

Baum, M., and Poinsot, T. 1995. Effects of mean flow on premixed flame ignition. *Combust. Sci. Technol.*, **106**, 19–39.

Beretta, G. P., Rashidi, M., and Keck, J. C. 1983. Turbulent flame propagation and combustion in spark ignition engines. *Combust. Flame*, **52**, 217–245.

Bhave, A., Kraft, M., Mauss, F., Oakley, A., and Zhao, H. 2005. Evaluating the EGR-AFR operating range of a HCCI engine. *Tech. Rep.* 2005-01-0161. SAE International, Warrendale, PA.

Bilger, R. W., Pope, S. B., Bray, K. N. C., and Driscoll, J. F. 2005. Paradigms in turbulent combustion research. *Proc. Combust. Inst.*, **30**, 21–42.

Bilger, R. W. 1993. Conditional moment closure for turbulent reacting flow. *Phys. Fluids*, **A5**, 436–444.

Bird, R. B., Stewart, W. E., and Lightfoot, E. N. 2002. *Transport Phenomena*, 2nd edn. John Wiley & Sons, Inc., New York, USA.

Blint, R. J. 1986. The relationship of the laminar flame width to flame speed. *Combust. Sci. Technol.*, **49** (1), 79–92.

Blizard, N. C., and Keck, J. C. 1974. Experimental and theoretical investigation of turbulent burning model for internal combustion engines. *Tech. Rep.* 740191. SAE International, Warrendale, PA, USA.

Bohbot, J., Miche, M., Pacaud, P., and Benkenida, A. 2009. Multiscale engine simulations using a coupling of 0-d/1-d model with a 3-d combustion code. *Oil Gas Sci. Technol.*, **64**, 337–359.

Borghi, R. 1974. Chemical reactions calculations in turbulent flows: application to a co-containing turbojet plume, *Advances in geophysics volume 18B*. In Frenkiel, F. N., and Munn, R. E., (Eds.). pp. 349–365.

Borghi, R. 1985. On the Structure and Morphology of Turbulent Premixed Flames, *Recent Advances in the Aerospace Sciences*. In Casci, C., and Bruno, C., (Eds.). Plenum Press, New York, US. pp. 117–138.

Borghi, R. 1988. Turbulent combustion modelling. *Prog. Energy Combust. Sci.*, **14** (4), 245–292.

Borghi, R. 1990. Turbulent premixed combustion - further discussions on the scales of fluctuations. *Combust. Flame*, **80** (3-4), 304–312.

Boudier, P., Henriot, S., Poinsot, T., and Baritaud, T. 1992. A model for turbulent flame ignition and propagation in spark ignition engines. *Proc. Combust. Inst.*, **24** (1), 503–510.

Bradley, D. 1992. How fast can we burn? *Proc. Combust. Inst.*, **24** (1), 247–262.

Bradley, D., Gaskell, P. H., and Gu, X. J. 1996. Burning velocities, Markstein lengths, and flame quenching for spherical methane-air flames: A computational study. *Combust. Flame*, **104**, 176–198.

Bradley, D., Haq, M. Z., Hicks, R. A., Kitagawa, T., Lawes, M., Sheppard, C. G. W., and Woolley, R. 2003. Turbulent burning velocity, burned gas distribution, and associated flame surface definition. *Combust. Flame*, **133**, 415–430.

Bradley, D., Hicks, R. A., Lawes, M., Sheppard, C. G. W., and Woolley, R. 1998. The measurement of laminar burning velocities and Markstein numbers for iso-octaneAir and iso-octanen-HeptaneAir mixtures at elevated temperatures and pressures in an explosion bomb. *Combust. Flame*, **115**, 126–144.

Bradley, D., Lawes, M., Liu, K., Verhelst, S., and Woolley, R. 2007. Laminar burning velocities of lean hydrogenair mixtures at pressures up to 1.0 MPa. *Combust. Flame*, **149** (12), 162–172.

Bradley, D., Lawes, M., and Mansour, M. S. 2011. Correlation of turbulent burning velocities of ethanolair, measured in a fan-stirred bomb up to 1.2 MPa. *Combust. Flame*, **158**, 123–138.

Bradley, D., Lawes, M., Scott, M. J., and Mushi, E. M. J. 1994. Afterburning in spherical premixed turbulent explosions. *Combust. Flame*, **99**, 581–590.

Bradley, D., Sheppard, C. G. W., Woolley, R., Greenhalgh, D. A., and Lockett, R. D. 2000. The development and structure of flame instabilities and cellularity at low Markstein numbers in explosions. *Combust. Flame*, **122**, 195–209.

Brandl, A., Pfitzner, M., Mooney, J. D., Durst, B., and Kern, W. 2005. Comparison of combustion models and assessment of their applicability to the simulation of premixed turbulent combustion in IC-Engines. *Flow Turbul. Combust.*, **75**, 335–350.

Bray, K. N. C. 1996. The challenge of turbulent combustion. *Proc. Combust. Inst.*, **26**, 1–26.

Bray, K. N. C., Champion, M., and Libby, P. A. 1998. Premixed flames in stagnating turbulence part II. the mean velocities and pressure and the damköhler number. *Combust. Flame*, **112**, 635–653.

Bray, K. N. C. 1979. The interaction between turbulence and combustion. *Proc. Combust. Inst.*, **17**, 223–233.

Bray, K. N. C. 1980. pp. 115–183, *Turbulent flows with premixed reactants*. In Libby, P. A., and Williams, F. A., (Eds.). Springer-Verlag, New York, USA. pp. 115–183.

Bray, K. N. C. 1990. Studies of the turbulent burning velocity. *Proc. R. Soc. Lond. A*, **431** (1882), 315–335.

Bray, K. N. C., Libby, P. A., and Moss, J. B. 1984. Flamelet crossing frequencies and mean reaction rates in premixed turbulent combustion. *Combust. Sci. Technol.*, **41** (3), 143.

Bray, K. N. C., Libby, P. A., and Moss, J. B. 1985. Unified modeling approach for premixed turbulent combustion. 1. general formulation. *Combust. Flame*, **61**, 87–102.

Bray, K. N. C., and Swaminathan, N. 2006. Scalar dissipation and flame surface density in premixed turbulent combustion. *C. R. Mécanique*, **334**, 466–473.

Broustail, G., Seers, P., Halter, F., Morac, G., and Mounaim-Rousselle, C. 2011. Experimental determination of laminar burning velocity for butanol and ethanol iso-octane blends. *Fuel*, **90**, 1–6.

Burke, M. P., Chaos, M., Ju, Y., Dryer, F. L., and Klippenstein, S. J. 2011. Comprehensive H2/O2 kinetic model for high-pressure combustion. *Int. J. Chem. Kinet.*, **44** (7), 444–474.

Bychkov, V. V., and Liberman, M. A. 1996. Stability and the fractal structure of a spherical flame in a self-similar regime. *Phys. Rev. Let.*, **76** (15), 2814–2817.

Candel, S. M., and Poinsot, T. J. 1990. Flame stretch and the balance equation for the flame area. *Combust. Sci. Technol.*, **70** (1-3), 1–15.

Cant, R. S., and Bray, K. N. C. 1989. A theoretical model of premixed turbulent combustion in closed vessels. *Combust. Flame*, **76**, 243–263.

Cant, R. S., and Mastorakos, E. 2008. *An Introduction to Turbulent Reacting Flows*. Imperial College Press, London, UK.

Cao, L., Zhao, H., and Jiang, X. 2008. Analysis of controlled auto-ignition/HCCI combustion in a direct injection gasoline engine with single and split fuel injections. *Combust. Sci. Technol.*, **180**, 176–205.

Chakraborty, N., and Cant, R. S. 2005. Effects of strain rate and curvature on surface density function transport in turbulent premixed flames in the thin reaction zones regime. *Phys. Fluids*, **17** (6), 065108.

Chakraborty, N., and Cant, R. S. 2009. Effects of lewis number on turbulent scalar transport and its modelling in turbulent premixed flames. *Combust. Flame*, **156**, 1427–1444.

Chakraborty, N., and Cant, R. S. 2011. Effects of lewis number on flame surface density transport in turbulent premixed combustion. *Combust. Flame*, **158**, 1768–1787.

Chakraborty, N., Champion, N., Mura, A., and Swaminathan, N. 2011. 2.3 Scalar-dissipation-rate approach, *Turbulent Premixed Flames*. In Swaminathan, N., and Bray, K. N. C., (Eds.). Cambridge University Press, Cambridge, UK. pp. 74–102.

Chakraborty, N., Rogerson, J. W., and Swaminathan, N. 2008. A priori assessment of closures for scalar dissipation rate transport in turbulent premixed flames using direct numerical simulation. *Phys. Fluids*, **20** (4), 045106.

Chakraborty, N., Rogerson, J. W., and Swaminathan, N. 2010. The scalar gradient alignment statistics of flame kernels and its modelling implications for turbulent premixed combustion. *Flow Turbul. Combust.*, **85**, 25–55.

Chakraborty, N., and Swaminathan, N. 2010. Effects of lewis number on scalar dissipation transport and its modeling in turbulent premixed combustion. *Combust. Sci. Technol.*, **182**, 1201–1240.

Chakraborty, N., and Swaminathan, N. 2011. Effects of lewis number on scalar variance transport in premixed flames. *Flow Turbul. Combust.*, **87**, 261–292.

Chaudhuri, S., Wu, F., Zhu, D., and Law, C. K. 2012. Flame speed and self-similar propagation of expanding turbulent premixed flames. *Phys. Rev. Let.*, **108** (4), 044503.

Checkel, M. D., and Thomas, A. 1994. Turbulent combustion of premixed flames in closed vessels. *Combust. Flame*, **96**, 351–370.

Chen, J. H. 2011. Petascale direct numerical simulation of turbulent combustionfundamental insights towards predictive models. *Proc. Combust. Inst.*, **33**, 99–123.

Clavin, P. 1985. Dynamic behavior of premixed flame fronts in laminar and turbulent flows. *Prog. Energy Combust. Sci.*, **11**, 1–59.

Clavin, P., and Williams, F. A. 1982. Effects of molecular diffusion and of thermal expansion on the structure and dynamics of premixed flames in turbulent flows of large scale and low intensity. *J. Fluid Mech.*, **116**, 251–282.

Colin, O., Benkenida, A., and Angelberger, C. 2003. 3D modeling of mixing, ignition and combustion phenomena in highly stratified gasoline engines. *Oil Gas Sci. Technol.*, **58**, 47–62.

Colin, O., and Truffin, K. 2011. A spark ignition model for large eddy simulation based on an FSD transport equation (ISSIM-LES). *Proc. Combust. Inst.*, **33**, 3097–3104.

Correa, S. M. 1993. Turbulence-chemistry interactions in the intermediate regime of premixed combustion. *Combust. Flame*, **93**, 41–60.

Corvellec, C., Bruel, P., and Sabel'nikov, V. A. 1999. A time-accurate scheme for the calculations of unsteady reactive flows at low Mach number. *Int. J. Numer. Meth. Fl.*, **29** (2), 207227.

Corvellec, C., Bruel, P., and SabelNikov, V. A. 2000. Turbulent premixed flames in the flamelet regime: burning velocity spectral properties in the presence of countergradient diffusion. *Combust. Flame*, **120** (4), 585–588.

Curran, H. J., Gaffuri, P., Pitz, W. J., and Westbrook, C. K. 2002. A comprehensive modeling study of iso-octane oxidation. *Combust. Flame*, **129** (3), 253–280.

Damköhler, G. 1940. Der einfluß der turbulenz auf die Flammengeschwidigkeit in gasgemischen. *Z. Elektrochem., English translation NASA Techn. Mem. 1112, 1947*, **46**, 601–626.

Dandekar, A., and Collins, L. R. 1995. Effect of nonunity lewis number on premixed flame propagation through isotropic turbulence. *Combust. Flame*, **101** (4), 428–440.

DeLuchi, M. A. 1989. Hydrogen vehicles: an evaluation of fuel storage, performance, safety, environmental impacts, and cost. *Int. J. Hydrogen Energ.*, **14** (2), 81–130.

Dopazo, C., and O'Brien, E. E. 1974. An approach to the autoignition of a turbulent mixture. *Acta Astronaut*, **1** (9-10), 1239–1266.

Dowdy, D. R., Smith, D. B., Taylor, S. C., and Williams, A. 1990. The use of expanding spherical flames to determine burning velocities and stretch effects in hydrogen/air mixtures. *Proc. Combust. Inst.*, **23** (1), 325–332.

Drake, M. C., Fansler, T. D., and Lippert, A. M. 2005. Stratified-charge combustion: modeling and imaging of a spray-guided direct-injection spark-ignition engine. *Proc. Combust. Inst.*, **30** (2), 2683–2691.

Drake, M. C., and Haworth, D. C. 2007. Advanced gasoline engine development using optical diagnostics and numerical modeling. *Proc. Combust. Inst.*, **31**, 99–124.

Driscoll, J. F. 2008. Turbulent premixed combustion: Flamelet structure and its effect on turbulent burning velocities. *Prog. Energy Combust. Sci.*, **34**, 91–134.

Duclos, J.-M., and Zolver, M. 1998. 3D modeling of intake, injection and combustion in a DI-SI engine under homogeneous and stratified operating conditions. In *Int. Symp. COMODIA 98*, pp. 335–340.

Dunn-Rankin, D., Miyasato, M. M., and Pham, T. J. 2008. Introduction and Perspectives, *Lean combustion: technology and control*. In Dunn-Rankin, D., (Ed.). Elsevier, Amsterdam.

Dunstan, T. D., Swaminathan, N., and Bray, K. N. C. 2012. Influence of flame geometry on turbulent premixed flame propagation: a DNS investigation. *J. Fluid Mech.*, **709**, 191–222.

Egolfopoulos, F. N., and Law, C. K. 1990. An experimental and computational study of the burning rates of ultra-lean to moderately-rich H2/O2/N2 laminar flames with pressure variations. *Proc. Combust. Inst.*, **23**, 333–340.

Ewald, J., and Peters, N. 2007. On unsteady premixed turbulent burning velocity prediction in internal combustion engines. *Proc. Combust. Inst.*, **31**, 3051–3058.

Fureby, C. 2005. A fractal flame-wrinkling large eddy simulation model for premixed turbulent combustion. *Proc. Combust. Inst.*, **30**, 593–601.

Galloni, E., Fontana, G., and Palmaccio, R. 2012. Numerical analyses of EGR techniques in a turbocharged spark-ignition engine. *Appl. Therm. Eng.*, **39**, 95–104.

Galmiche, B., Halter, F., and Foucher, F. 2012. Effects of high pressure, high temperature and dilution on laminar burning velocities and Markstein lengths of iso-octane/air mixtures. *Combust. Flame*, **159**, 3286–3299.

Gerke, U. 2007. Numerical analysis of mixture formation and combustion in a hydrogen direct-injection internal combustion engine. Ph.D., ETH Zürich, No. 17477, Cuvillier Göttingen, Switzerland.

Gosman, A. D. 1999. State of the art of multi-dimensional modeling of engine reacting flows. *Oil Gas Sci. Technol.*, **54**, 149–159.

Gostintsev, Yu. A., Istratov, A. G., and Shulenin, Yu. V. 1988. Self-similar propagation of a free turbulent flame in mixed gas mixtures. *Combust., Expl. Shock Waves*, **24** (5), 563–569.

Göttgens, J., Mauss, F., and Peters, N. 1992. Analytic approximations of burning velocities and flame thicknesses of lean hydrogen, methane, ethylene, ethane, acetylene, and propane flames. *Proc. Combust. Inst.*, **24** (1), 129–135.

Groff, E. G. 1987. An experimental evaluation of an entrainment flame-propagation model. *Combust. Flame*, **67**, 153–162.

Habisreuther, P., Galeazzo, F. Cesar C., Prathap, C., and Zarzalis, N. 2013. Structure of laminar premixed flames of methane near the auto-ignition limit. *Combust. Flame*, **160** (12), 2770–2782.

Hack, M. L., and Jenny, P. 2013. Joint PDF closure of turbulent premixed flames. *Flow Turbul. Combust.*, **90**, 373–386.

Hainsworth, E. 1985. Study of free turbulent premixed flames. Master's thesis, Mass. Inst. Technol., Cambridge, MA, USA.

Hamamoto, Y., Tomita, E., and Izumi, M. 1988. The effect of swirl on the combustion of a homogeneous mixture in a closed vessel. *JSME Int. J., Ser. II*, **31** (1), 140–149.

Han, Z., and Reitz, R. D. 1995. Turbulence modeling of internal combustion engines using RNG - models. *Combust. Sci. Technol.*, **106**, 267–295.

Haq, M. Z., Sheppard, C. G. W., Woolley, R., Greenhalgh, D. A., and Lockett, R. D. 2002. Wrinkling and curvature of laminar and turbulent premixed flames. *Combust. Flame*, **131**, 1–15.

Hassan, M. I., Aung, K. T., and Faeth, G. M. 1998*a*. Measured and predicted properties of laminar premixed methane/air flames at various pressures. *Combust. Flame*, **115** (4), 539–550.

Hassan, M. I., Aung, K. T., Kwon, O. C., and Faeth, G. M. 1998*b*. Properties of laminar premixed hydrocarbon/air flames at various pressures. *J. Propul. Power*, **14** (4), 479–488.

Hasse, C., Bollig, M., Peters, N., and Dwyer, H. A. 2000. Quenching of laminar iso-octane flames at cold walls. *Combust. Flame*, **122**, 117–129.

Haworth, D. C. 2010. Progress in probability density function methods for turbulent reacting flows. *Prog. Energy Combust. Sci.*, **36** (2), 168–259.

Haworth, D. C., and Jansen, K. 2000. Large-eddy simulation on unstructured deforming meshes: towards reciprocating IC engines. *Comput. Fluids*, **29** (5), 493–524.

Haworth, D. C. 1999. Large-eddy simulation of in-cylinder flows. *Oil Gas Sci. Technol.*, **54**, 175–185.

Haworth, D. C., and Pope, S. B. 2011. Transported Probability Density Function Methods for Reynolds-Averaged and Large-Eddy Simulations, *Turbulent*

Combustion Modeling. In Echekki, T., and Mastorakos, E., (Eds.). Springer, Dordrecht, Netherlands. pp. 119–142.

He, X., Donovan, M. T., Zigler, B. T., Palmer, T. R., Walton, S. M., Wooldridge, M. S., and Atreya, A. 2005. An experimental and modeling study of iso-octane ignition delay times under homogeneous charge compression ignition conditions. *Combust. Flame*, **142**, 266–275.

Heel, B., Maly, R., Weller, H. G., and Gosman, A. D. 1998. Validation of SI combustion model over range of speed, load, equivalence ratio and spark timing. In *Int. Symp. COMODIA 98*, pp. 255–260.

Henriot, S., Chaouche, A., Cheve, E., and Duclos, J. M. 1999. CFD aided development of a SI-DI engine. *Oil Gas Sci. Technol.*, **54**, 279–286.

Heywood, J. B. 1988. *Fundamentals of internal combustion engines*. McGraw-Hill, New York, USA.

Hirsch, C. 2007. *Numerical Computation of Internal and External Flows: Fundamentals of Computational Fluid Dynamics*, 2nd edn. Butterworth-Heinemann, Amsterdam.

Hogg, S., and Leschziner, M. A. 1989. Computation of highly swirling confined flow with a reynolds stress turbulence model. *AIAA Journal*, **27** (1), 57–63.

Hu, E., Huang, Z., He, J., Zheng, J., and Miao, H. 2009. Measurements of laminar burning velocities and onset of cellular instabilities of methanehydrogenair flames at elevated pressures and temperatures. *Int. J. Hydrogen Energ.*, **34** (13), 5574–5584.

Huang, Z., Zhang, Y., Zeng, K., Liu, B., Wang, Q., and Jiang, D. 2006. Measurements of laminar burning velocities for natural gas-hydrogen-air mixtures. *Combust. Flame*, **146** (1-2), 302–311.

IEA. 2011. *World Energy Outlook 2011*. OECD/IEA, Paris, France.

Ihracska, B., Korakianitis, T., Ruiz, P., Emberson, D. R., Crookes, R. J., Diez, A., and Wen, D. 2013. Assessment of elliptic flame front propagation characteristics of iso-octane, gasoline, M85 and E85 in an optical engine. *Combust. Flame*.

IPCC. 2007. *Climate Change 2007: Synthesis Report*. Intergovernmental Panel on Climate Change, Geneva, Switzerland.

Issa, R. I. 1986. Solution of the implicitly discretised fluid flow equations by operator-splitting. *J. Comput. Phys.*, **62**, 40–65.

Jenkins, K. W., and Cant, R. S. 2002. Curvature effects on flame kernels in a turbulent environment. *Proc. Combust. Inst.*, **29**, 2023–2029.

Jenkins, K. W., Klein, M., Chakraborty, N., and Cant, R. S. 2006. Effects of strain rate and curvature on the propagation of a spherical flame kernel in the thin-reaction-zones regime. *Combust. Flame*, **145**, 415–434.

Jerzembeck, S., Peters, N., Pepiot-Desjardins, P., and Pitsch, H. 2009. Laminar burning velocities at high pressure for primary reference fuels and gasoline: Experimental and numerical investigation. *Combust. Flame*, **156**, 292–301.

Jomaas, G., and Law, C. K. 2009. Surface morphology and self-acceleration of expanding spherical flames. AIAA 2009-1185, American Institute of Aeronautics and Astronautics, Florida, USA.

Jomaas, G., Zheng, X. L., Zhu, D. L., and Law, C. K. 2005. Experimental determination of counterflow ignition temperatures and laminar flame speeds of C2C3 hydrocarbons at atmospheric and elevated pressures. *Proc. Combust. Inst.*, **30** (1), 193–200.

Jones, W. P, and Launder, B. E. 1972. The prediction of laminarization with a two-equation model of turbulence. *Int. J. Heat Mass Tran.*, **15**, 301–314.

Jones, W. P. 1994. Turbulence modelling and numerical solution methods for variable density and combustion flows, *Turbulent Reacting Flows*. In Libby, P. A., and Williams, F. A., (Eds.). Academic Press, London, UK. pp. 309–374.

Jones, W. P. 2002. The joint scalar probability density function, *Closure Strategies for Turbulent and Transitional Flows*. In Launder, B. E., and Sandham, N. D., (Eds.). Cambridge University Press, Cambridge, UK. pp. 582–625.

Kaminski, C. F., Hult, J., Aldén, M., Lindenmaier, S., Dreizler, A., Maas, U., and Baum, M. 2000. Spark ignition of turbulent methane/air mixtures revealed by time-resolved planar laser-induced fluorescence and direct numerical simulations. *Proc. Combust. Inst.*, **28**, 399–405.

Kech, J. M, Reissing, J., Gindele, J., and Spicher, U. 1998. Analyses of the combustion process in a direct injection gasoline engine. In *Int. Symp. COMODIA 98*, pp. 287–92.

Kee, R. J., Grcar, J. F., Smooke, M. D., and Miller, J. A. 1985. A FORTRAN program for modeling steady laminar one-dimensional premixed flames. *Tech. Rep.* SAND85-8240. Sandia National Laboratories, Livermore, CA, USA.

Kelley, A. P., Liu, W., Xin, Y. X., Smallbone, A. J., and Law, C. K. 2011. Laminar flame speeds, non-premixed stagnation ignition, and reduced mechanisms in the oxidation of iso-octane. *Proc. Combust. Inst.*, **33**, 501–508.

Kido, H., Nakahara, M., Nakashima, K., and Hashimoto, J. 2002. Influence of local flame displacement velocity on turbulent burning velocity. *Proc. Combust. Inst.*, **29** (2), 1855–1861.

Kitagawa, T., Nakahara, T., Maruyama, K., Kado, K., Hayakawa, A., and Kobayashi, S. 2008. Turbulent burning velocity of hydrogenair premixed propagating flames at elevated pressures. *Int. J. Hydrogen Energ.*, **33** (20), 5842–5849.

Klein, M., Chakraborty, N., and Cant, R. S. 2008. Effects of turbulence on self-sustained combustion in premixed flame kernels: a direct numerical simulation (DNS) study. *Flow Turbul. Combust.*, **81**, 583–607.

Klein, M., Chakraborty, N., Jenkins, K. W., and Cant, R. S. 2006. Effects of initial radius on the propagation of premixed flame kernels in a turbulent environment. *Phys. Fluids*, **18** (5), 055102.

Klimenko, A. Y., and Bilger, R. W. 1999. Conditional moment closure for turbulent combustion. *Prog. Energy Combust. Sci.*, **25** (6), 595–687.

Klimenko, A. Y. 1990. Multicomponent diffusion of various admixtures in turbulent flow. *Fluid Dyn.*, **25** (3), 327–334.

Knop, V., Benkenida, A., Jay, S., and Colin, O. 2008. Modelling of combustion and nitrogen oxide formation in hydrogen-fuelled internal combustion engines within a 3D CFD code. *Int. J. Hydrogen Energ.*, **33** (19), 5083–5097.

Koch, J. 2013. LES of a premixed SI gasoline engine with emphasis on cycle to cycle variations of the combustion process. Master's thesis, Swiss Federal Institute of Technology Zürich, Zürich, Switzerland.

Kolla, H., Rogerson, J. W., Chakraborty, N., and Swaminathan, N. 2009. Scalar dissipation rate modeling and its validation. *Combust. Sci. Technol.*, **181**, 518–535.

Kolla, H., Rogerson, J. W., and Swaminathan, N. 2010. Validation of a turbulent flame speed model across combustion regimes. *Combust. Sci. Technol.*, **182** (3), 284–308.

Kolla, H., and Swaminathan, N. 2010*a*. Strained flamelets for turbulent premixed flames, I: Formulation and planar flame results. *Combust. Flame*, **157**, 943–954.

Kolla, H., and Swaminathan, N. 2010*b*. Strained flamelets for turbulent premixed flames II: laboratory flame results. *Combust. Flame*, **157**, 1274–1289.

Kolla, H., and Swaminathan, N. 2011. Influence of turbulent scalar mixing physics on premixed flame propagation. *J. Combust.*, **2011**, 1–8.

Krieger, R. B., and Borman, G. L. 1966. The computation of apparent heat release for internal combustion engines. ASME paper 66-WA/DGP-4.

Kumar, R. K., Dewit, W. A., and Greig, D. R. 1989. Vented explosion of hydrogen-air mixtures in a large volume. *Combust. Sci. and Technol*, **66** (4-6), 251–266.

Kuznetsov, M., Kobelt, S., Grune, J., and Jordan, T. 2012. Flammability limits and laminar flame speed of hydrogenair mixtures at sub-atmospheric pressures. *Int. J. Hydrogen Energ.*, **37**, 17580–17588.

Kwon, O. C., and Faeth, G. M. 2001. Flame/stretch interactions of premixed hydrogen-fueled flames: measurements and predictions. *Combust. Flame*, **124** (4), 590–610.

Kwon, O. C., Rozenchan, G., and Law, C. K. 2002. Cellular instabilities and self-acceleration of outwardly propagating spherical flames. *Proc. Combust. Inst.*, **29** (2), 1775–1783.

Kwon, S., Tseng, L. K., and Faeth, G. M. 1992*a*. Laminar burning velocities and transition to unstable flames in H2/O2/N2 and C3H8/O2/N2 mixtures. *Combust. Flame*, **90** (34), 230–246.

Kwon, S., Wu, M. S., Driscoll, J. F., and Faeth, G. M. 1992*b*. Flame surface properties of premixed flames in isotropic turbulence: Measurements and numerical simulations. *Combust. Flame*, **88** (2), 221–238.

Lamoureux, N., Djebali-Chaumeix, N., and Paillard, C. E. 2003. Laminar flame velocity determination for H2airHeCO2 mixtures using the spherical bomb method. *Exp. Therm. Fluid Sci.*, **27** (4), 385–393.

Law, C. K. 2006. *Combustion Physics*. Cambridge University Press, Cambridge, UK.

Law, C. K., and Sung, C. J. 2000. Structure, aerodynamics, and geometry of premixed flamelets. *Prog. Energy Combust. Sci.*, **26**, 459–505.

Lawes, M., Ormsby, M. P., Sheppard, C. G. W., and Woolley, R. 2005. Variation of turbulent burning rate of methane, methanol, and iso-octane air mixtures with equivalence ratio at elevated pressure. *Combust. Sci. Technol.*, **177** (7), 1273–1289.

Lawes, M., Ormsby, M. P., Sheppard, C. G. W., and Woolley, R. 2012. The turbulent burning velocity of iso-octane/air mixtures. *Combust. Flame*, **159**, 1949–1959.

Lecocq, G., Richard, S., Colin, O., and Vervisch, L. 2011. Hybrid presumed pdf and flame surface density approaches for large-eddy simulation of premixed turbulent combustion. part 2: Early flame development after sparking. *Combust. Flame*, **158**, 1215–1226.

Leonard, A. 1974. Energy cascade in large-eddy simulations of turbulent fluid flows. *Adv. Geophys.*, **18A**, 237–248.

Li, J., Zhao, Z., Kazakov, A., and Dryer, F. L. 2004. An updated comprehensive kinetic model of hydrogen combustion. *Int. J. Chem. Kinet.*, **36** (10), 566–575.

Liang, L., and Reitz, R. D. 2006. Spark ignition engine combustion modeling using a level set method with detailed chemistry. *Tech. Rep.* SAE Paper 2006-01-0243. SAE International, Warrendale, PA, USA.

Libby, P. A. 1985. Theory of normal premixed turbulent flames revisited. *Prog. Energy Combust. Sci.*, **11**, 83–96.

Libby, P. A., and Bray, K. N. C. 1980. Implications of the laminar flamelet model in premixed turbulent combustion. *Combust. Flame*, **39** (1), 33–41.

Libby, P. A., and Bray, K. N. C. 1981. Countergradient diffusion in premixed turbulent flames. *AIAA Journal*, **19**, 205–213.

Lipatnikov, A. N., and Chomiak, J. 2000. Transient and geometrical effects in expanding turbulent flames. *Combust. Sci. Technol.*, **154**, 75–117.

Lipatnikov, A. N., and Chomiak, J. 2002. Turbulent flame speed and thickness: phenomenology, evaluation, and application in multi-dimensional simulations. *Prog. Energy Combust. Sci.*, **28**, 1–74.

Lipatnikov, A. N., and Chomiak, J. 2004. Application of the Markstein number concept to curved turbulent flames. *Combust. Sci. Technol.*, **176**, 331–358.

Lipatnikov, A. N., and Chomiak, J. 2005. Molecular transport effects on turbulent flame propagation and structure. *Prog. Energy Combust. Sci.*, **31** (1), 1–73.

Lu, T., and Law, C. K. 2006. Linear time reduction of large kinetic mechanisms with directed relation graph: n-heptane and iso-octane. *Combust. Flame*, **144**, 24–36.

Lutz, A. E., Kee, R. J., Grcar, J. F., and Rupley, F. M. 1997. OPPDIF: A fortran program for computing opposed-flow diffusion flames. *Tech. Rep.* SAND96-8243. Sandia National Laboratories, Livermore, CA, USA.

Malkeson, S. P., and Chakraborty, N. 2010. A priori direct numerical simulation assessment of algebraic models of variances and dissipation rates in the context of reynolds-averaged navier-stokes simulations for low damkhler number partially premixed combustion. *Combust. Sci. Technol.*, **182**, 960–999.

Malkeson, S. P., and Chakraborty, N. 2011. Statistical analysis of cross scalar dissipation rate transport in turbulent partially premixed flames: A direct numerical simulation study. *Flow Turbul. Combust.*, **87**, 313–349.

Mandilas, C., Ormsby, M. P., Sheppard, C. G. W., and Woolley, R. 2007. Effects of hydrogen addition on laminar and turbulent premixed methane and iso-octaneair flames. *Proc. Combust. Inst.*, **31**, 1443–1450.

Mantel, T., and Bilger, R. W. 1995. Some conditional statistics in a turbulent premixed flame derived from direct numerical simulations. *Combust. Sci. Technol.*, **110-111** (1), 393–417.

Mantel, T., and Borghi, R. 1994. A new model of premixed wrinkled flame propagation based on a scalar dissipation equation. *Combust. Flame*, **96** (4), 443–457.

Marble, F. E., and Broadwell, J. E. 1977. The coherent flame model for turbulent chemical reactions. *Tech. Rep.* TRW-9-PU. Project SQUID.

Martz, J. B., Middleton, R. J., Lavoie, G. A., Babajimopoulos, A., and Assanis, D. N. 2011. A computational study and correlation of premixed isooctaneair laminar reaction front properties under spark ignited and spark assisted compression ignition engine conditions. *Combust. Flame*, **158**, 1089–1096.

Matalon, M. 2007. Intrinsic flame instabilities in premixed and nonpremixed combustion. *Annu. Rev. Fluid. Mech.*, **39** (1), 163–191.

Matalon, M., and Matkowsky, B. J. 1982. Flames as gasdynamic discontinuities. *J. Fluid Mech.*, **124**, 239–259.

Mehl, M., Pitz, W. J., Westbrook, C. K., and Curran, H. J. 2011. Kinetic modeling of gasoline surrogate components and mixtures under engine conditions. *Proc. Combust. Inst.*, **33**, 193–200.

Meneveau, C., and Poinsot, T. 1991. Stretching and quenching of flamelets in premixed turbulent combustion. *Combust. Flame*, **86** (4), 311–332.

Miller, J. A. 1982. Toward a comprehensive chemical kinetic mechanism for the oxidation of acetylene: comparison of model predictions with results from flame and shock tube experiments. *Proc. Combust. Inst.*, **19** (1), 181–196.

Minamoto, Y., Fukushima, N., Tanahashi, M., Miyauchi, T., Dunstan, T. D., and Swaminathan, N. 2011. Effect of flow-geometry on turbulence-scalar interaction in premixed flames. *Phys. Fluids*, **23** (12), 125107.

Molkov, V. V., Makarov, D. V., and Schneider, H. 2007. Hydrogen-air deflagrations in open atmosphere: Large eddy simulation analysis of experimental data. *Int. J. Hydrogen Energ.*, **32** (13), 2198–2205.

Muppala, S. P. R., Nakahara, M., Aluri, N. K., Kido, H., Wen, J. X., and Papalexandris, M. V. 2009. Experimental and analytical investigation of the turbulent burning velocity of two-component fuel mixtures of hydrogen, methane and propane. *Int. J. Hydrogen Energ.*, **34** (22), 9258–9265.

Mura, A., and Borghi, R. 2003. Towards an extended scalar dissipation equation for turbulent premixed combustion. *Combust. Flame*, **133** (1-2), 193–196.

Mura, A., Robin, V., and Champion, M. 2007. Modeling of scalar dissipation in partially premixed turbulent flames. *Combust. Flame*, **149**, 217–224.

Nwagwe, I. K., Weller, H. G., Tabor, G. R., Gosman, A. D., Lawes, M., Sheppard, C. G. W., and Wooley, R. 2000. Measurements and large eddy simulations of turbulent premixed flame kernel growth. *Proc. Combust. Inst.*, **28**, 59–65.

Ó Conaire, M., Curran, H. J., Simmie, J. M., Pitz, W. J., and Westbrook, C. K. 2004. A comprehensive modeling study of hydrogen oxidation. *Int. J. Chem. Kinet.*, **36** (11), 603–622.

O'Brien, E. E. 1980. The probability density function (pdf) approach to reacting turbulent flows, *Turbulent Reacting Flows*. In Libby, P. A., and Williams, F. A., (Eds.). Springer-Verlag, New York. pp. 185–218.

Ogden, J. M. 1999. Prospects for building a hydrogen energy infrastructure. *Annu. Rev. Energ. Env.*, **24** (1), 227–279.

van Oijen, J. A., Groot, G. R. A., Bastiaans, R. J. M., and de Goey, L. P. H. 2005. A flamelet analysis of the burning velocity of premixed turbulent expanding flames. *Proc. Combust. Inst.*, **30**, 657–664.

Pan, K.-L., and Fursenko, R. 2008. Characteristics of cylindrical flame acceleration in outward expansion. *Phys. Fluids*, **20**, 094107.

Pareja, J., Burbano, H. J., and Ogami, Y. 2010. Measurements of the laminar burning velocity of hydrogen-air premixed flames. *Int. J. Hydrogen Energ.*, **35**, 1812–1818.

Patankar, S. V. 1980. *Numerical heat transfer and fluid flow*. Taylor and Francis Group, London, UK.

Paul, R. N., and Bray, K. N. C. 1996. Study of premixed turbulent combustion including Landau-Darrieus instability effects. *Proc. Combust. Inst.*, **26**, 259–266.

Pepiot-Desjardins, P., and Pitsch, H. 2008*a*. An automatic chemical lumping method for the reduction of large chemical kinetic mechanisms. *Combust. Theor. Model.*, **12** (6), 1089–1108.

Pepiot-Desjardins, P., and Pitsch, H. 2008*b*. An efficient error-propagation-based reduction method for large chemical kinetic mechanisms. *Combust. Flame*, **154**, 67–81.

Peters, N. 1986. Laminar flamelet concepts in turbulent combustion. *Proc. Combust. Inst.*, **21** (1), 1231–1250.

Peters, N. 1992. A spectral closure for premixed turbulent combustion in the flamelet regime. *J. Fluid Mech.*, **242**, 611–629.

Peters, N. 1999. The turbulent burning velocity for large-scale and small-scale turbulence. *J. Fluid Mech.*, **384**, 107–132.

Peters, N. 2000. *Turbulent Combustion*. Cambridge University Press, Cambridge, UK.

Peters, N., and Dekena, M. 1999. Combustion modeling with the G-equation. *Oil Gas Sci. Technol.*, **54**, 265–270.

Pierce, C. D. 2005. Progress-variable approach for large-eddy simulation of turbulent combustion. Ph.D., Stanford University, Stanford, CA, USA.

Pitsch, H. 2006. Large-eddy simulation of turbulent combustion. *Ann. Rev. Fluid Mech*, **38**, 453–482.

Pitz, W. J., Cernansky, N. P., Dryer, F. L., Egolfopoulos, F. N., Farrell, J. T., Friend, D. G., and Pitsch, H. 2007. Development of an experimental database and chemical kinetic models for surrogate gasoline fuels. *Tech. Rep.* SAE Paper 2007-01-0175. SAE International.

Poinsot, T., Candel, S., and Trouvé, A. 1995. Applications of direct numerical simulation to premixed turbulent combustion. *Prog. Energy Combust. Sci.*, **21**, 531–576.

Poinsot, T., and Veynante, D. 2005. *Theoretical and Numerical Combustion*, 2nd edn. R.T. Edwards, Inc., Philadelphia, PA, USA.

Pope, S. B. 1976. The probability approach to the modelling of turbulent reacting flows. *Combust. Flame*, **27**, 299–312.

Pope, S. B. 1981. A monte-carlo method for the pdf equations of turbulent reactive flow. *Combust. Sci. Technol.*, **25** (5-6), 159–174.

Pope, S. B. 1985. PDF methods for turbulent reactive flows. *Prog. Energy Combust. Sci.*, **11** (2), 119–192.

Pope, S. B. 1987. Turbulent premixed flames. *Ann. Rev. Fluid Mech*, **19**, 237–270.

Pope, S. B. 1988. The evolution of surfaces in turbulence. *Int. J. Eng. Sci.*, **26** (5), 445–469.

Pope, S. B. 2000. *Turbulent Flows*. Cambridge University Press, Cambridge, UK.

Pope, S. B., and Cheng, W. K. 1986. Statistical calculations of spherical turbulent flames. *Proc. Combust. Inst.*, **21**, 1473–1481.

Prasad, R. O. S., and Gore, J. P. 1999. An evaluation of flame surface density models for turbulent premixed jet flames. *Combust. Flame*, **116**, 1–14.

Rakopoulos, C. D., Kosmadakis, G. M., and Pariotis, E. G. 2010. Evaluation of a combustion model for the simulation of hydrogen spark-ignition engines using a CFD code. *Int. J. Hydrogen Energ.*, **35** (22), 12545–12560.

Ranga Dinesh, K. K. J., Jiang, X., van Oijen, J. A., Bastiaans, R. J. M., and de Goey, L. P. H. 2013. Hydrogen-enriched nonpremixed jet flames: Effects of preferential diffusion. *Int. J. Hydrogen Energ.*, **38**, 4848–4863.

Regele, J. D., Knudsen, E., Pitsch, H., and Blanquart, G. 2013. A two-equation model for non-unity lewis number differential diffusion in lean premixed laminar flames. *Combust. Flame*, **160**, 240–250.

Renou, B., Boukhalfa, A., Puechberty, D., and Trinité, M. 1998. Effects of stretch on the local structure of preely propagating premixed low-turbulent flames with various lewis numbers. *Proc. Combust. Inst.*, **27** (1), 841–847.

Renou, B., Boukhalfa, A., Puechberty, D., and Trinité, M. 2000. Local scalar flame properties of freely propagating premixed turbulent flames at various Lewis numbers. *Combust. Flame*, **123**, 507–521.

Renou, B., Mura, A., Samson, E., and Boukhalfa, A. 2002. Characterization of the local flame structure and the flame surface density for freely propagating

premixed flames at various Lewis numbers. *Combust. Sci. Technol.*, **174**, 143–179.

Ribert, G., Champion, M., Gicquel, O., Darabiha, N., and Veynante, D. 2005. Modeling nonadiabatic turbulent premixed reactive flows including tabulated chemistry. *Combust. Flame*, **141**, 271–280.

Richardson, L. F. 1922. *Weather prediction by numerical process*. Cambridge University Press, Cambridge, UK.

Robin, V., Mura, A., Champion, M., and Plion, P. 2006. A multi-dirac presumed pdf model for turbulent reactive flows with variable equivalence ratio. *Combust. Sci. Technol.*, **178**, 1843–1870.

Rogerson, J. W., and Swaminathan, N. 2007. Correlation between dilatation and scalar dissipation in turbulent premixed flames. *European Combustion Meeting*.

Roomina, M. R., and Bilger, R. W. 2001. Conditional moment closure (CMC) predictions of a turbulent methane-air jet flame. *Combust. Flame*, **125** (3), 1176–1195.

Ruan, S., Swaminathan, N., Bray, K. N. C., Mizobuchi, Y., and Takeno, T. 2012. Scalar and its dissipation in the near field of turbulent lifted jet flame. *Combust. Flame*, **159**, 591–608.

Rutland, C. J. 2011. Large-eddy simulations for internal combustion engines a review. *Int. J. Engine Res.*, **12**, 421–451.

Rutland, C. J., and Trouvé, A. 1993. Direct simulations of premixed turbulent flames with nonunity lewis numbers. *Combust. Flame*, **94** (1-2), 41–57.

Schmid, H.-P., Habisreuther, P., and Leuckel, W. 1998. A model for calculating heat release in premixed turbulent flames. *Combust. Flame*, **113**, 79–91.

Schneider, E., Sadiki, A., and Janicka, J. 2005. Modeling and 3D-simulation of the kinetic effects in the post-flame region of turbulent premixed flames based on the g-equation approach. *Flow Turbul. Combust.*, **75**, 191–216.

Shy, S. S., Shih, W. T., and Liu, C. C. 2008. More on minimum ignition energy transition for lean premixed turbulent methane combustion in flamelet and distributed regimes. *Combust. Sci. Technol.*, **180**, 1735–1747.

Sivashinsky, G. I. 1977. Nonlinear analysis of hydrodynamic instability in laminar flamesI. derivation of basic equations. *Acta Astronaut.*, **4**, 1177–1206.

Smith, G. P., Golden, D. M., Frenklach, M., Moriarty, N. W., Eiteneer, B., Goldenberg, M., Bowman, C. T., Hanson, R. K., Song, S., Gardiner Jr., W. C, Lissianski, V. V., and Qin, Z. accessed 10th November 2013. A model for calculating heat release in premixed turbulent flames. [Online] Available from: http://www.me.berkeley.edu/gri_mech/.

Spalding, D. B. 1955. *Some fundamentals of combustion*. Academic Press, Inc., New York.

Spalding, D. B. 1971. Mixing and chemical reaction in steady confined turbulent flames. *Proc. Combust. Inst.*, **13** (1), 649–657.

Stohl, A., Seibert, P., Wotawa, G., Arnold, D., Burkhart, J. F., Eckhardt, S., Tapia, C., Vargas, A., and Ysunari, T. J. 2012. Xenon-133 and caesium-137 releases into the atmosphere from the fukushima dai-ichi nuclear power plant: determination of the source term, atmospheric dispersion, and deposition. *Atmos. Chem. Phys.*, **12** (5), 2313–2343.

Sung, C. J., Li, B., Wang, H., and Law, C. K. 1998. Structure and sooting limits in counterflow methane/air and propane/air diffusion flames from 1 to 5 atmospheres. *Proc. Combust. Inst.*, **27** (1), 1523–1529.

Swaminathan, N, and Bilger, R. W. 2001*a*. Analyses of conditional moment closure for turbulent premixed flames. *Combust. Theor. Model.*, **5**, 241–260.

Swaminathan, N., and Bilger, R. W. 2001*b*. Scalar dissipation, diffusion and dilatation in turbulent h2-air premixed flames with complex chemistry. *Combust. Theor. Model.*, **5**, 429–446.

Swaminathan, N., and Bray, K. N. C. 2005. Effect of dilatation on scalar dissipation in turbulent premixed flames. *Combust. Flame*, **143**, 549–565.

Swaminathan, N., and Bray, K. N. C. 2011. Fundamentals and Challenges, *Turbulent Premixed Flames*. In Swaminathan, N., and Bray, K. N. C., (Eds.). Cambridge University Press, Cambridge, UK. pp. 1–40.

Tabaczynski, R. J., Trinker, F. H., and Shannon, B. A. S. 1980. Further refinement and validation of a turbulent flame propagation model for spark-ignition engines. *Combust. Flame*, **39**, 111–121.

Tabor, G., and Weller, H. G. 2004. Large eddy simulation of premixed turbulent combustion using flame surface wrinkling model. *Flow Turbul. Combust.*, **72**, 1–27.

Tan, Z., and Reitz, R. D. 2006. An ignition and combustion model based on the level-set method for spark ignition engine multidimensional modeling. *Combust. Flame*, **145**, 1–15.

Tang, C., Huang, Z., Jin, C., He, J., Wang, J., Wang, X., and Miao, H. 2008. Laminar burning velocities and combustion characteristics of propane-hydrogen-air premixed flames. *Int. J. Hydrogen Energ.*, **33**, 4906–4914.

Taut, C., Correa, C., Deutschmann, O., Warnatz, J., Einecke, S., Schulz, C., and Wolfrum, J. 2000. Three-dimensional modeling with monte carlo-probability density function methods and laser diagnostics of the combustion in a two-stroke engine. *Proc. Combust. Inst.*, **28**, 1153–1159.

Taylor, G. I. 1935*a*. Statistical theory of turbulence. *Proc. R. Soc. Lond. A*, **151** (873), 421–444.

Taylor, G. I. 1935*b*. Statistical theory of turbulence. *Proc. R. Soc. Lond. A*, **151** (873), 151–478.

Tennekes, H., and Lumley, J. L. 1972. *A First Course in Turbulence*. M.I.T. Press, Cambridge, MA, USA.

Thévenin, D. 2005. Three-dimensional direct simulations and structure of expanding turbulent methane flames. *Proc. Combust. Inst.*, **30**, 629–637.

Thévenin, D., Gicquel, O., De Charentenay, J., Hilbert, R., and Veynante, D. 2002. Two- versus three-dimensional direct simulations of turbulent methane flame kernels using realistic chemistry. *Proc. Combust. Inst.*, **29**, 2031–2039.

Tse, S. D., Zhu, D. L., and Law, C. K. 2000. Morphology and burning rates of expanding spherical flames in H2/O2/inert mixtures up to 60 atmospheres. *Proc. Combust. Inst.*, **28** (2), 1793–1800.

Turns, S. R. 2000. *An Introduction to Combustion: Concepts and Applications*, 2nd edn. McGraw-Hill, Boston, USA.

Urata, Y., and Taylor, A. M. K. P. 2011. 4.1 Application of lean flames in internal combustion engines, *Turbulent Premixed Flames*. In Swaminathan, N., and Bray, K. N. C., (Eds.). Cambridge University Press, Cambridge, UK. pp. 1–40.

Vagelopoulos, C. M., Egolfopoulos, F. N., and Law, C. K. 1994. Further considerations on the determination of laminar flame speeds with the counterflow twin-flame technique. *Proc. Combust. Inst.*, **25**, 1341–1347.

Verhelst, S. 2005. A study of combustion in hydrogen-fuelled internal combustion engines. Ph.D., Ghent University, Ghent, Belgium.

Verhelst, S., and Wallner, T. 2009. Hydrogen-fueled internal combustion engines. *Prog. Energ. Combust.*, **35** (6), 490–527.

Verhelst, S., Woolley, R., Lawes, M., and Sierens, R. 2005. Laminar and unstable burning velocities and Markstein lengths of hydrogenair mixtures at engine-like conditions. *Proc. Combust. Inst.*, **30** (1).

Vermorel, O., Richard, S., Colin, O., Angelberger, C., Benkenida, A., and Veynante, D. 2009. Towards the understanding of cyclic variability in a spark ignited engine using multi-cycle LES. *Combust. Flame*, **156** (8), 1525–1541.

Veynante, D., Trouvé, A., Bray, K. N. C., and Mantel, T. 1997. Gradient and counter-gradient scalar transport in turbulent premixed flames. *J. Fluid Mech.*, **332**, 263–293.

Veynante, D., and Vervisch, L. 2002. Turbulent combustion modeling. *Prog. Energy Combust. Sci.*, **28** (3), 193–266.

Weller, H. G., Uslu, S., Gosman, A. D., Maly, R. R., Herweg, R., and Heel, B. 1994. Prediction of combustion in homogeneous-charge spark-ignition engines. In *Int. Symp. COMODIA 94*, pp. 163–169.

Westbrook, C. K. 1982. Hydrogen oxidation kinetics in gaseous detonations. *Combust. Sci. Technol.*, **29** (1-2), 67–81.

White, C. M., Steeper, R. R., and Lutz, A. E. 2006. The hydrogen-fueled internal combustion engine: a technical review. *Int. J. Hydrogen Energ.*, **31** (10), 1292–1305.

Wilcox, D. C. 1993. *Turbulence Modeling for CFD*. DCW Industries, Inc, Canada.

Williams, F. A. 1975. Recent advances in theoretical descriptions of turbulent diffusion flames, *Turbulent mixing in nonreactive and reactive flows*. In Murthy, S. N. B., (Ed.). Plenum Press, New York, USA. pp. 189–208.

Williams, F. A. 1985*a*. *Combustion Theory: The Fundamental Theory of Chemically Reacting Flow Systems*, Second edn. Benjamin Cummings, Menlo Park, CA.

Williams, F. A. 1985*b*. Turbulent Combustion, *The Mathematics of Combustion*. In Buckmaster, J. D., (Ed.). SIAM, Philadelphia. pp. 97–131.

Williams, F. A. 2001. Some Recent Studies in Turbulent Combustion, *Smart Control of Turbulent Combustion*. In Yoshida, A., (Ed.). Springer-Verlag, Tokyo, Japan. pp. 1–11.

Wright, Y. M. 2013. Personal communication.

Wu, C. K., and Law, C. K. 1984. On the determination of laminar flame speeds from stretched flames. *Proc. Combust. Inst.*, **20**, 1941–1949.

Wu, M. S., Kwon, S., Driscoll, J. F., and Faeth, G. M. 1990. Turbulent premixed Hydrogen/air flames at high reynolds numbers. *Combust. Sci. Technol.*, **73** (1-3), 327–350.

Yakhot, V., Orszag, S. A., Thangam, S., Gatski, T. B., and Speziale, C. G. 1992. Development of turbulence models for shear flows by a double expansion technique. *Phys. Fluids*, **4**, 1510–1520.

Yang, S. L., Siow, Y. K., Teo, C. Y., and Hanjalic, K. 2005. A KIVA code with reynolds-stress model for engine flow simulation. *Energy*, **30**, 427–445.

Zeldovich, Ya.B., Barenblatt, G.I., Librovich, V.B., and Makhviladze, G.M. 1985. *The Mathematical Theory of Combustion and Explosions*. Consultants Bureau, New York.

Zhang, S. W., and Rutland, C. J. 1995. Premixed flame effects on turbulence and pressure-related terms. *Combust. Flame*, **102**, 447–461.

Zhang, Y. Z., Kung, E. H., and Haworth, D. C. 2005. A PDF method for multidimensional modeling of HCCI engine combustion: effects of turbulence/chemistry interactions on ignition timing and emissions. *Proc. Combust. Inst.*, **30**, 2763–2771.

Zhao, X., Matthews, R. D., and Ellzey, J. L. 1993. Three-dimensional numerical simulation of flame propagation in spark ignition engines. *Tech. Rep.* 932713. SAE International, Warrendale, PA, USA.